



**The Effects of Physical and Chemical Properties of Fly ash on the  
Manufacture of Geopolymer Foam Concretes**

A Thesis Submitted in Total Fulfilment for the Requirements of the Degree of  
Doctor of Philosophy

By

**Zuhua Zhang**

Faculty of Health, Engineering and Sciences  
University of Southern Queensland  
Australia

2014



## Abstract

The development of sustainable construction and building materials with reduced environmental footprint in both manufacturing and operational phases of the material lifecycle is attracting increased interest in the housing and construction industry worldwide. Recent innovations have led to the development of geopolymer foam concretes (GFCs), which combine the performance benefits and operational energy savings achievable through the use of lightweight foam concrete, with the cradle-to-gate emissions reductions obtained through the use of a geopolymer binder derived from fly ash.

Fly ash is a by-product of coal fired power stations, and has become a highly promising source material for geopolymer manufacture. Compared to clays, another type of usually used materials, fly ash is probably more technologically suitable as it requires less alkaline activator while providing good workability. However, fly ash particles are substantially heterogeneous in physical and chemical properties. The composition and mineralogy of fly ash have marked effects on the properties of geopolymers, such as setting behaviour. This will affect the pore structure of GFC. Unfortunately, there is very limited specification regarding feedstock utilisation in geopolymer manufacture at present. Understanding the effect of fly ash physics and chemistry on the manufacture of GFC is not only necessary for the development of commercially mature GFC technology but also important for the geopolymer technology as a whole section.

Five fly ash samples sourced from different power plants around Australia were used to manufacture geopolymer binders, enabling investigation of the relationship between the physical and chemical properties of fly ash and the mechanical properties of geopolymer products. The results showed that fly ashes from different sources exhibit substantially different physical properties. One important property is the inter-particle volume of fly ash, which largely determines the liquid requirement. The liquid requirement furthermore affects the porosity of hardened binders and their production costs. Another factor is the reaction extent of fly ash, which determines the quantity and composition of gel phases. A general trend obtained is that fly ash with higher network-modifying cations seems to possess higher reactivity.

Research by Rietveld quantitative XRD and XRF analysis found that the composition and chemistry of glassy phases play an equally important role as the quantity of these phases in affecting the reactivity of fly ash. In glassy phases, both  $\text{FeO}_4$  and  $\text{AlO}_4$  tend to randomly distribute and connect with  $\text{SiO}_4$  tetrahedra by sharing corners and this is due to the alkali/alkali earth cations, which act as charge compensators.

A reactivity index (RI) was proposed in this thesis to quantify the reactivity of fly ash under geopolymerization conditions. If pentacoordinated Fe cations are regarded as network modifiers, in addition to alkali and alkali earth cations, and by considering the contribution of specific surface area, it was found that the RI order of the studied five ashes matched well with their reactivity order. Alkaline dissolution analysis under different liquid/solid ratios supported the RI results. Additionally, dissolution analysis also showed that the crystals such as mullite and quartz were also partially dissolved, particularly in the 'impure' fly ashes, which had relatively higher concentration of network modifying cations.

The above stages of the works were very useful to understand and to obtain a strong geopolymer binder by selecting a reactive fly ash. However, GFC manufacture in the laboratory conditions showed that a fly ash suitable for making high strength solid geopolymers was not necessarily suitable for GFC manufacture. It appeared that fly ash physical properties played a more important role than fly ash chemistry in affecting the engineering performances of GFCs. Those fly ashes with lower particle density and irregular particle shape appeared best suited for the manufacture of foam geopolymers.

For a foamed paste derived from a specific fly ash, quick setting was a key property to achieve fine pore size and a homogeneous microstructure. The orthogonal array study conducted showed that slag addition was an effective method to control, and shorten the setting time of the foamed paste. The pore structure and porosity were also changed significantly and contributed to an increase in compressive strength.

Research of the characteristics of pore structure of a series of GFCs showed that the pore size distribution in GFC affected the compressive strength to a large extent, particularly for the large pores. Based on the statistical fitting and modelling, a new model was developed, called the 'large void model', which treated the porosity of critical size pores ( $>100 \mu\text{m}$ ) and total porosity separately. Two mathematical models relating the measured thermal conductivity with porosity and dry density were successfully developed. The mathematical models were proven to be able to predict the mechanical and thermal insulation properties precisely.



## Certification and Declaration

I certify that the experimental work and data reported in this thesis are original. All the work described was carried out by the author, excepted where otherwise acknowledged.

I declare that this was a USQ and industry partially funded research project, and most of the content is confidential, which has not been published. Only some of the information, including Chapter 2, Section 5.4 and Section 8.2.2 has been reported by the author in journal papers, conferences and patent documents.

I also declare that the thesis is less than 100,000 words in length, exclusive of tables, figures, references and appendices.

Student: Zuhua Zhang

Signature:

Data:

.

Principle supervisor: Hao Wang

Signature:

Data:

.

# Publications

## Book chapters

1. **Zhang Zuhua**, Wang Hao: Chapter 8: Analysing the relation between pore structure and permeability of alkali-activated binders, in Fernando Pacheco-Torgal, João Labrincha, Cristina Leonelli, Angel Palomo and Prinya Chindaprasit (Ed.) Handbook of Alkali-activated Cements, Mortars and Concretes 2014, (in press)
2. **Zhang Zuhua**, Wang Hao: Chapter 23: Alkali-activated cements for OPC concrete coating, in Fernando Pacheco-Torgal, João Labrincha, Cristina Leonelli, Angel Palomo and Prinya Chindaprasit (Ed.) Handbook of Alkali-activated Cements, Mortars and Concretes 2014, (in press)

## Journal papers

3. **Zuhua Zhang\***, John L. Provis, Andrew Reid, Hao Wang\*, Mechanical, acoustic absorption, thermal insulation and fire resistant properties of geopolymer foam concrete (GFC), Cement & Concrete Composites (submitted)
4. Tao Yang, Xiao Yao, **Zuhua Zhang\***. Quantification of chloride diffusion in fly ash-slag-based geopolymers by X-ray fluorescence (XRF). Construction and Building Materials (submitted)
5. **Zuhua Zhang\***, John L. Provis, Andrew Reid, Hao Wang\*: Fly ash-based geopolymers: the relationship between composition, pore structure and efflorescence. Cement and Concrete Research 64 (2014) 30–41.
6. Huajun Zhu, **Zuhua Zhang\***: Durability of alkali-activated fly ash concrete: Chloride penetration in pastes and mortars. Construction and Building Materials 65 (2014) 51–59
7. Tao Yang, Xiao Yao, **Zuhua Zhang\***: Geopolymer prepared with high-magnesium nickel slag: characterization of properties and microstructure. Construction and Building Materials 59 (2014) 188–194.
8. **Zuhua Zhang\***, John L. Provis, Andrew Reid, Hao Wang\*: Geopolymer foam concrete: an emerging material for sustainable construction. Construction and Building Materials 56 (2014) 113–127.
9. **Zhang, Z.\***, Zhu, Y., Reid, A., Provis J.L., Bullen, F., Wang, H.: Using fly ash to partially substitute metakaolin in geopolymer synthesis. Applied Clay Science, 2014, 88–89: 194–201.
10. Tao Yang, Xiao Yao, **Zuhua Zhang**, Huajun Zhu, Effects of NaOH solution concentration and reaction time on metakaolin geopolymerization. Journal of Nanjing University of Technology, 2013, 35 (4): 21-25. (in Chinese with English abstract)
11. H. Zhu, **Z. Zhang\***, F. Deng, Y. Cao: The effects of phase changes on the bonding property of geopolymer to hydrated cement. Construction and Building Materials 2013, 58: 124–130.
12. **Zhang, Z.\***, Wang, H., Provis, J.L., Bullen, F., Reid, A.: Quantitative kinetic and structural analysis of geopolymers. Part 2. Thermodynamics of sodium silicate activation of metakaolin; Thermochimica Acta, 2013, 565: 163–171.
13. **Zhang, Z.\***, Wang, H., Provis, J.L., Bullen, F., Reid, A., Zhu, Y.: Quantitative kinetic and structural analysis of geopolymers. Part 1. The activation of metakaolin with sodium hydroxide; Thermochimica Acta, 2012, 539: 23–33.
14. **Z. Zhang\***, H. Wang, X. Yao, Y. Zhu: Effects of halloysite in kaolin on the formation and properties of geopolymers, Cement & Concrete Composites, 2012, 34: 709–715.
15. **Zuhua Zhang\***, Xiao Yao, Hao Wang: Potential application of geopolymers as protection coatings for marine concrete III. Field experiment, Applied Clay Science 2012, (67-68): 57-60.

16. **Zhang Z**, Wang H\*, Provis JL: Quantitative study of the reactivity of fly ash in geopolymerization by FTIR. *Journal of Sustainable Cement-Based Materials*, 2012, 1(4):154-166.
17. Yang, T. Yao, X., **Zhang, Z.\***, Wang, H.: Mechanical property and structure of alkali-activated fly ash and slag blends. *Journal of Sustainable Cement-Based Materials*, 2012, 1(4): 167-178.
18. Qiang Li\*, Hao Wang, **Zuhua Zhang**, Andrew Reid: Numerical simulation of porosity on thermal properties and fire resistance of foamed concrete. *Journal of Sustainable Cement-Based Materials*, 2013, 2(1): 13-19.

### **Refereed conference papers**

19. **Zuhua Zhang**, Tao Yang, Hao Wang, et al. Inorganic polymer foams: transform from non-structural to structural upon fire. The 4th International Conference on Smart Materials and Nanotechnology in Engineering, Gold Coast, Australia, from 10 to 12 July 2013. Oral presentation.
20. **Zuhua Zhang**, Hao Wang, John L. Provis, Durability of fly ash based-geopolymers: effect of crystallization on the mechanical properties. The 8th International Symposium on Cement & Concrete (ISCC2013), Nanjing, China, from 20 to 23 September, 2013. Oral presentation.
21. **Zuhua Zhang**, John Provis, Hao Wang, The reactivity of fly ash in geopolymer synthesis: A qualification study by FTIR, the 8th Asian-Australasian Conference on Composite Materials (ACCM-8), Kuala Lumpur, Malaysia, from 6 to 9 November, 2012. Oral presentation.
22. Tao yang, Xiao Yao, Hao Wang, **Zuhua Zhang**, Effects of calcium of ground granulated blast furnace slag on the microstructure of fly ash-based geopolymer binders, the 8th Asian-Australasian Conference on Composite Materials (ACCM-8), Kuala Lumpur, Malaysia, from 6 to 9 November, 2012. Oral presentation.

### **Patent**

23. Andrew Reid, **Zuhua Zhang**, Assessment method (for precursors in used in geopolymer), in application, Australian Provisional Patent Application No. 2013900977

## Acknowledgement

I want to thank all the people who have assisted me throughout this research. In particular, I would like to acknowledge my supervisors, Prof. Hao Wang, Prof. Frank Bullen, Prof. John Provis and Mr. Andrew Reid. This is an amazing supervisor team with strong academic background on materials science, geopolymer chemistry, project management and engineering experiences. Hao gave a lot of assistances in the experimental environments and discussions on the project. Frank checked my research progress regularly and particularly at the last stage when he retired from the Dean of our faculty, he was able to spend a lot of time to help me to improve my writing skills. The discussions with Frank were always helpful. John was so helpful in examining my research results. Some of the discussions about fly ash glass chemistry were very useful. His understanding of my research and encouragements were mostly appreciated. The discussions with Andrew on a regular progress meeting base guided the research towards the application of geopolymers technology. All of their understanding, advices, encouragements and assistances were valuable resources leading to the success of this thesis.

Dr. Francisco Cardona, Dr. Friederike Eberhard, Wayne Crowell, Martin Geach, Daniel Eising and Mohan Trada gave me assistances on the experiments carried out at the Centre of Excellence in Engineered Fibre Composites (CEEFC) and the faculty. Chen Yue helped me a lot to perform the XRD testing at Nanjing University of Technology (NJUT). Thank all of you for your technical supports. Anne Reid and Steven Brown gave me the helps on the work at Halok Engineering. You are so lovely.

The support of the scholarships of IPRS and Halok Geopolymer funding are acknowledged.

I would take this opportunity to thank my wife, Yingcan Zhu, who gave me the help and encouragement in the last three years since we came to Australia. Thank you for the lasting supports for 10 years on the way of pursuing the degrees.

# Table of Contents

Abstract.....	I
Certification and Declaration.....	III
Publications.....	IV
Acknowledgement.....	VI
Table of Contents.....	VII
List of Figures.....	XI
List of Tables.....	XVI
<b>Chapter 1: Introduction.....</b>	<b>1</b>
<b>Chapter 2: Review on Geopolymer Foam Concrete: an Emerging Material for Sustainable Construction.....</b>	<b>3</b>
2.1 Introduction.....	3
2.2 Sustainability in the cement and concrete industry.....	4
2.2.1 Current status of sustainable development efforts.....	4
2.2.2 Geopolymers - alternative binders to Portland cement .....	7
2.3 Foam concrete technology.....	8
2.3.1 Composition of foam concrete.....	8
2.3.2 Properties of foam concrete.....	10
2.4 Development of geopolymer foam concrete.....	15
2.4.1 Geopolymerization.....	15
2.4.2 Important issues in geopolymer synthesis.....	15
2.4.3 Geopolymer foam concrete technology.....	19
2.4.4 Perspectives for of geopolymer foam concrete.....	24
2.5 Challenges in developing geopolymer foam concrete.....	28
2.5.1 Understanding of feedstock physics and chemistry .....	28
2.5.2 Differences between solid and foamed geopolymers.....	29
2.6 Concluding remarks.....	29
<b>Chapter 3: Research Plan and Methodology.....</b>	<b>31</b>
3.1 Introduction.....	31
3.2 Research flow chart.....	31
3.3 Materials.....	32

3.3.1 Alkali activating solutions.....	32
3.3.2 Solid materials .....	33
3.3.3 Foaming agent.....	40
3.3.4 Other materials and chemicals.....	41
3.4 Procedures.....	42
3.4.1 Characterization of raw materials.....	42
3.4.2 Geopolymer manufacture .....	47
3.4.3 Characterization of geopolymers.....	48
3.5 Concluding remarks.....	53
<b>Chapter 4: Physical Properties of Fly Ash Particles and Their Effects on the Liquid Requirement and Microstructure of Geopolymer Binders .....</b>	<b>54</b>
4.1 Introduction.....	54
4.2 Particle characteristics of the selected fly ashes .....	55
4.2.1 Chemical composition .....	55
4.2.2 Morphology and particle size.....	55
4.2.3 Surface area.....	63
4.2.4 Particle density .....	63
4.2.5 Residual carbon in the fly ashes.....	64
4.3 Liquid requirement of the selected fly ashes and the compressive strength of the derived geopolymer binders.....	66
4.3.1 Effects of particle characteristics on the liquid requirement of geopolymer pastes .....	67
4.3.2 Compressive strength of hardened binders synthesized from the fly ash.....	70
4.4 Factors affecting the mechanical properties of hardened binders.....	74
4.4.1 Microstructures of hardened products .....	74
4.4.2 Composition and quantity of geopolymeric gels .....	80
4.5 Concluding remarks .....	84
<b>Chapter 5: Glass Chemistry of Fly Ash, and Its Effects on Geopolymerization Reactivity .....</b>	<b>86</b>
5.1 Introduction.....	86
5.2 The importance of glass composition of fly ash .....	86
5.2.1 Examination of bulk composition and reactivity of fly ash.....	89
5.2.2 Determination of crystalline and amorphous components in fly ash.....	89
5.3 Reactivity index of fly ash for geopolymer manufacture.....	94
5.3.1 The development of reactivity index for fly ash.....	94

5.3.2	Dissolution of fly ashes A, B and E at high liquid/solid ratio conditions.	99
5.3.3	Dissolution of fly ash under geopolymerization conditions.....	118
5.4	FTIR analysis: a quick indicator test for reactivity of fly ash.....	120
5.4.1	FTIR analysis of fly ash.....	121
5.4.2	FTIR analysis of resultant geopolymer binders.....	132
5.5	Concluding remarks.....	134
<b>Chapter 6: Development and Investigation of Trial Manufacture of GFC.</b>		<b>135</b>
6.1	Introduction.....	135
6.2	Foam stability .....	135
6.2.1	Effect of foaming agent concentration on the foam stability .....	137
6.2.2	Effect of foam density and pH on the foam stability.....	137
6.3	Evaluation of the fly ashes for GFC manufacture.....	138
6.3.1	Workability of fresh foamed pastes .....	139
6.3.2	Segregation of foamed pastes.....	141
6.3.3	Laboratory evaluation of strength and microstructure of GFCs.....	143
6.4	Effects of composition on the phase and microstructure of GFCs .....	148
6.4.1	Orthogonal array study of composition factors.....	148
6.4.2	The effects of slag addition on the phase and pore structure of GFCs...152	
6.5	Concluding remarks.....	160
<b>Chapter 7: The Influences of Pore Structure of GFCs on the Mechanical and Thermal Insulation Properties</b>		<b>162</b>
7.1	Introduction.....	162
7.2	Characterization of pore structure in GFCs.....	162
7.2.1	Density of GFCs.....	162
7.2.2	Porosity of GFCs.....	165
7.2.3	Pore sizes and distribution .....	167
7.2.4	Pore area fraction and pore shape.....	171
7.3	Mechanical properties and pore structure.....	173
7.3.1	The effects of foam addition on phases in geopolymers.....	173
7.3.2	Relationships between porosity and compressive strength and modulus of elasticity.....	176
7.4	Modelling on the thermal insulation property of GFCs .....	185
7.4.1	Thermal conductivity measurement.....	185
7.4.2	The relationship of thermal conductivity with porosity and density.	186

7.5 Concluding remarks.....	192
<b>Chapter 8: Conclusions and Recommendations.....</b>	<b>193</b>
8.1 Conclusions.....	193
8.2 Current issues in the development and applications of GFCs.....	195
8.2.1 Shrinkage of fly ash-based GFCs.....	195
8.2.2 The potential efflorescence of GFCs .....	195
8.3 Recommendations for the future research.....	196
8.3.1 Research of the dissolution behaviour of glass phases in fly ash .....	196
8.3.2 Evaluation of the pore size effects on the strength of GFCs.....	196
8.3.3 Research of GFC shrinkage control.....	197
8.3.4 Research of the GFC efflorescence control.....	197
<b>References.....</b>	<b>198</b>
<b>Appendix .....</b>	<b>219</b>



# List of Figures

## Chapter 2

- Figure 2-1.** Global cement production and distribution. Data from (He 2010; CCM 2011; Sinoma 2011; CEMBUREAU, 2012). .....4
- Figure 2-2.** The thermal conductivity of foam concretes in comparison with solid concretes. The data by the current authors are measured using the transient plane source (TPS) method; the foam concretes are synthesised with OPC (w/c=0.5) by mechanical mixing of preformed foam; all the samples are dried in a vacuum oven at 80°C for 24 h before measuring. Data from (Newman and Owens 2003; Akthar and Evans 2010; AAC 2001; Weigler and Karl 1980; Benazzouk et al. 2008; Bentz et al. 2011).....12
- Figure 2-3.** (a) XRD patterns of metakaolin and fly ash, and (b) their alkali activation heat evolution as measured by isothermal calorimetry. Activator has SiO<sub>2</sub>/Na<sub>2</sub>O ratio of 1.4, total dissolved solids concentration of 40 wt.%; the BET surface areas of metakaolin and fly ash are 14 and 0.9 m<sup>2</sup>/g, respectively (Zhang et al. 2013).....16
- Figure 2-4.** Contour plot of compressive strength data for sodium silicate activated fly ash geopolymers (Provis et al. 2009).....18
- Figure 2-5.** (a) Digital photograph of sintered geopolymer foam, and (b) an SEM image of the pore structure of sintered product. Original figures were provided by Zhao et al. (2010) and are acknowledged.....20
- Figure 2-6.** The thermal conductivity and compressive strength of metakaolin-based foam geopolymers (air dried) (Arellano Aguilar et al. 2010).....21
- Figure 2-7.** Geopolymers foamed with different Al powder contents: C1, C2, C3 and C4 contain 5, 10, 15 and 20 mg Al powder per 100 mL activator respectively; the binders contain Si/Al=2.0; C4 produces about 70 vol% porosity; the diameter of the cylinder is 18.85 mm. All specimens cured at room temperature. Original photographs were provided by Kamseu et al. (2012) and are acknowledged.....22
- Figure 2-8.** Synthesis protocol of in situ mineral foam (a) and photography of the synthesized foams (Delair et al. 2012).....23
- Figure 2-9.** Compressive strength of different types of geopolymers before and after high temperature exposure: (a) metakaolin/slag blend-based binder and concrete, data from (Bernal et al. 2011; 2012); (b) binders derived from different fly ashes, data from (Rickard et al. 2011).....26

## Chapter 3

- Figure 3-1.** Research flow chart of this thesis.....32
- Figure 3-2.** The chemical compositions and reactive SiO<sub>2</sub> contents in the 8 collected fly ashes..35
- Figure 3-3.** The XRD patterns showing the crystalline phases in the five selected fly ashes.....38
- Figure 3-4.** Sales of GGBFS in Australia. Figure cited from (Australasian (Iron & Steel) Slag Association (ASA), 2011b).....39
- Figure 3-5.** XRD pattern of the slag used in this research. Calcium silicate, Ca<sub>3</sub>SiO<sub>5</sub> (ICSD# 81100); Mullite, Al<sub>4.75</sub> Si<sub>1.25</sub> O<sub>9.63</sub> (ICSD# 66448); Quartz (s), SiO<sub>2</sub> (ICSD# 71392 and 42498).....40
- Figure 3-6.** XRD pattern of the corundum used as the internal standard for quantitative XRD analysis by Reitveld method. Corundum, Al<sub>2</sub>O<sub>3</sub> (ICSD# 60419).....42
- Figure 3-7.** ARL 9900 Series X-ray workstation (a) and the operation principle (b).....44
- Figure 3-8.** Sketch of foam geopolymer concrete preparation.....47
- Figure 3-9.** Sketch of the Hot Disk TSP 2500 system.....48
- Figure 3-10.** Two pieces of one geopolymer mixture for thermal conductivity testing.....49
- Figure 3-11.** The optical microscopy images of the polished surface of foamed geopolymer (a);

surface coated with black ink (b); grayed photo (c) and converted into the binary format (d)....52

## Chapter 4

- Figure 4-1.** Optical images of fly ash particles (sample D). The small images on the right side emphasize specific particles: cenosphere particle (a), solid particle (b), particle formed by aggregation of finer ones (c), iron-rich particle (d) and carbon particles (e).....56
- Figure 4-2.** SEM images of the five selected fly ashes .....62
- Figure 4-3.** Cumulative particle size distributions (volume %) of fly ash samples.....62
- Figure 4-4.** Relationship between iron content and fly ash density.....64
- Figure 4-5.** Fly ashes mixed with acetone in tubes (most of the black dots are carbon particles).....65
- Figure 4-6.** Thermogravimetric analysis (TGA) of fly ashes up to 800°C.....66
- Figure 4-7.** Liquid requirement of fly ash to achieve a paste with good workability (flowability between 140 to 170 mm as measured using a cone with top and bottom diameters of 65 mm and 80 mm and height of 40 mm).....67
- Figure 4-8.** Sketch of the fly ash particles in a paste. Inter-particle volume refers to the space between packed particles, including the volume occupied by liquid layer. .... 68
- Figure 4-9.** Liquid requirement for surface wetting and the average thickness of liquid layer as a function of specific surface area.....69
- Figure 4-10.** Compressive strength of geopolymer binders at 7 d and 28 d.....71
- Figure 4-11.** Compressive strength of geopolymers synthesized with low concentration activator solution at 7 d and 28 d .....73
- Figure 4-12.** Representative SEM images of geopolymer binders (after 28 d) made by activation of fly ashes with a constant activator/ash ratio.....76
- Figure 4-13.** XRD diffraction patterns of geopolymer binders (after 28 d) made by activation of fly ashes with a constant activator/ash ratio.....76
- Figure 4-14.** Porosity of geopolymer binders as determined by MIP.....78
- Figure 4-15.** Cumulative pore size distributions of geopolymer binders as measured by MIP...79
- Figure 4-16.** Representative SEM-EDS analysis area of fracture surface of hardened binders: (a) binder A; (b) binder B; (b) binder C; (d) binder D; (e) binder E.....82
- Figure 4-17.** TGA data for the geopolymer binders at 28 d.....83

## Chapter 5

- Figure 5-1.** Pseudo-ternary composition diagram (Duxson & Provis, 2008) for the five selected fly ashes, of which reactivity is in the order A> B> C> D> E. Alkali and alkali earth oxides are summed, and represented as the total molar number of charges on the respective cations.....87
- Figure 5-2.** Rietveld refinement XRD plots showing the observed (red crosses) and calculated (red solid) patterns, and the difference between them (bottom pink line) for fly ash A (a), B (b), C (c), D (d) and E (e) mixed with 20 wt. % corundum as internal standard.....92
- Figure 5-3.** Phase diagram of the  $\text{SiO}_2/\text{FeO}\cdot\text{Fe}_2\text{O}_3$  system. Reorganized from reference (Ehrman et al. 1999).....95
- Figure 5-4.** Structure model of glass with composition of  $\text{NaFe}_{0.5}\text{Al}_{0.5}\text{Si}_2\text{O}_6$ .  $\text{SiO}_4$ ,  $\text{AlO}_4$  and  $\text{FeO}_4$  tetrahedra are represented in blue, green and black respectively.  $\text{FeO}_5$  polyhedra and Na atoms are represented in pink and yellow respectively (Weigel et al., 2008).....95
- Figure 5-5.** The relationship between surface area of fly ash and the compressive strength of derived geopolymer binders at two curing conditions. Data from (Kumar and Kumar 2011).....97
- Figure 5-6.** Typical SEM images of fly ash A particles after dissolution at 80°C for 6 h in (a) 4M KOH, (b) 4M NaOH and (c) sodium silicate solutions.....101

<b>Figure 5-7.</b> Rietveld refinement XRD plots showing the observed (red crosses) and calculated (green solid) patterns of fly ash A after dissolution by (a) 4M KOH, (b) 4M NaOH and (c) sodium silicate solutions.....	103
<b>Figure 5-8.</b> SEM-EDS analysis of fly ash A: (a) iron-rich particle dissolved by the KOH solution; (b) mullite-rich particle dissolved by the NaOH solution; (c) glass-rich particle dissolved by the sodium silicate solutions.....	105
<b>Figure 5-9.</b> Typical SEM images of fly ash B particles after dissolution at 80°C for 6 h in (a) 4M KOH, (b) 4M NaOH and (c) sodium silicate solutions.....	108
<b>Figure 5-10.</b> Rietveld refinement XRD plots showing the observed (red crosses) and calculated (green solid) patterns of fly ash B after dissolution by (a) 4M KOH, (b) 4M NaOH and (c) sodium silicate solutions.....	109
<b>Figure 5-11.</b> SEM-EDS analysis of a mullite-rich particle of fly ash B that dissolved by the NaOH solution .....	111
<b>Figure 5-12.</b> Typical SEM images of fly ash E particles after dissolution at 80°C for 6 h in (a) 4M KOH, (b) 4M NaOH and (c) sodium silicate solutions.....	113
<b>Figure 5-13.</b> Rietveld refinement XRD plots showing the observed (red crosses) and calculated (green solid) patterns of fly ash E after dissolution by (a) 4M KOH, (b) 4M NaOH and (c) sodium silicate solutions.....	114
<b>Figure 5-14.</b> Dissolution extents of fly ashes in alkaline solutions at 80°C for 6 h.....	117
<b>Figure 5-15.</b> FTIR spectra of fly ashes A (a), B (b), C (c), D (d) and E (e) before and after contacting with water for 7 days at water/ash ratios of 0.5 and 20 g/g at 25±2°C. The fly ashes were dried at 105°C for 48 h before testing.....	124
<b>Figure 5-16.</b> FTIR spectra of mullite and quartz.....	125
<b>Figure 5-17.</b> Deconvolution spectra of Si-O-T bands of fly ashes over 400-1400 cm <sup>-1</sup> .....	126
<b>Figure 5-18.</b> FTIR spectra of fly ash A (a), B (b) and E (c) dissolved in 1 M NaOH for different periods at 25°C.....	130
<b>Figure 5-19.</b> FTIR spectra of fly ash A (a), B (b) and E (c) dissolved in 4 M KOH, 4 M NaOH and 4 M NaOH + 1.3 M SiO <sub>2</sub> solutions at 80°C for 6 h.....	132
<b>Figure 5-20.</b> FTIR spectra of geopolymer samples at 7 d (a) and 28 d (b).....	133
<b>Chapter 6</b>	
<b>Figure 6-1.</b> Sketch of foam stability recording.....	136
<b>Figure 6-2.</b> Effect of the concentration of the foaming agent (active surface polypeptide-alkylene polyol) on the stability of foam.....	137
<b>Figure 6-3.</b> Effect of foam density on the stability: (a) foaming agent=2.0 wt.%; and (b) 1.5 wt.%.....	138
<b>Figure 6-4.</b> Spreadability of foamed geopolymer pastes.....	140
<b>Figure 6-5.</b> Density of freshly foamed geopolymer pastes.....	141
<b>Figure 6-6.</b> Segregation of GFCs: (a) derived from fly ash A; (b) derived from fly ash B.....	142
<b>Figure 6-7.</b> Density and compressive strength of GFCs.....	143
<b>Figure 6-8.</b> FTIR spectra of solid and foamed geopolymers at age of 28 d: (a) geopolymers from fly ash B and (b) geopolymers from fly ash E. The foam addition was 5 wt.% for GFCs.....	144
<b>Figure 6-9.</b> Deconvolution study of FTIR spectra of solid geopolymers B (a) and E (b) and foamed geopolymers B (c) and E (d).....	145
<b>Figure 6-10.</b> Pore structure of GFCs as observed by optical microscopy: (a) GFC A, (b) GFC B, (c) GFC C, (d) GFC D, and (e) GFC E. The scale bar is 1 mm.....	146
<b>Figure 6-11.</b> SEM images of (a) GFC A and (b) GFC E .....	147

<b>Figure 6-12.</b> Appearance of GFCs.....	150
<b>Figure 6-13.</b> XRD patterns of solid geopolymers containing 0 to 40 wt.% slag after 40°C×24 h oven curing plus 27 d ageing at ambient conditions. The peaks labelled as tobermorite is calcium silicate hydrates (C-S-H) with tobermorite-like structure.....	153
<b>Figure 6-14.</b> FTIR spectra of solid geopolymers containing 0 to 40 wt.% slag after 40°C×24 h oven curing plus 27 d ageing at ambient conditions.....	155
<b>Figure 6-15.</b> Appearance of top surfaces of solid geopolymers synthesised with 0 wt.% (a), 10 wt.% (b), 20 wt.% (c), 30 wt.% (d) and 40 wt.% (e) of slag and the surface after sanding (f).....	156
<b>Figure 6-16.</b> Typical optical images of GFCs with 0 wt.% (a), 20 wt.% (b), 30 wt.% (c) and 40 wt.% (d) of slag addition. The white areas are pores and the black areas are binders. The scale bar is 1mm.....	157
<b>Figure 6-17.</b> Effect of slag addition on the porosity of GFCs. (The water saturation method uses 4 samples; the image analysis method uses 2 samples with 10-20 images for each sample).....	158
<b>Figure 6-18.</b> Effect of slag addition on the initial setting time of geopolymer.....	158
<b>Figure 6-19.</b> Effects of slag addition on the pore size distribution of GFCs by IA.....	159
<b>Chapter 7</b>	
<b>Figure 7-1.</b> The difference between predicted and observed values: (a) predicted vs. observed; (b) residual analysis.....	165
<b>Figure 7-2.</b> The relationship between foam content and the air-cured density at 60 d (a) and the oven-dried density (b).....	166
<b>Figure 7-3.</b> Effects of foam content on the porosity of GFCs.....	167
<b>Figure 7-4.</b> Typical IA images of GFCs with 0 wt.% (a), 1.3 wt.% (b), 3.3 wt.% (c), 5 wt.% (d), 6.7 wt.% (e), 10 wt.% (f), 13 wt.% (g) and 16 wt.% (h) of foam addition. The white areas are pores and the black areas are geopolymer binder. The scale bar is 1 mm.....	169
<b>Figure 7-5.</b> Frequency of pores in GFCs with 0 wt.% (a), 1.3 wt.% (b), 3.3 wt.% (c), 5 wt.% (d), 6.7 wt.% (e), 10 wt.% (f), 13 wt.% (g) and 16 wt.% (h) of foam addition.....	170
<b>Figure 7-6.</b> Distribution of area fraction of pores in GFCs. The legend shows the dosage of foam addition.....	171
<b>Figure 7-7.</b> Area fraction of pores in GFCs.....	172
<b>Figure 7-8.</b> Shape factors of pores in geopolymer foams. The legend shows the dosage of foam addition.....	173
<b>Figure 7-9.</b> XRD patterns of geopolymers containing 0 to 16 wt.% of foam. Geopolymers were manufactured with a blend of 70 wt.% fly ash (E) and 30 wt.% slag.....	174
<b>Figure 7-10.</b> FTIR spectra of geopolymers containing 0 to 16 wt.% of foam. Geopolymers were manufactured with a blend of 70 wt.% fly ash and 30wt.% slag.....	175
<b>Figure 7-11.</b> Experimental data correlation with the new relationships.....	177
<b>Figure 7-12.</b> The differences between predicted values by Ryhkevitch’s and Balshin’s model and observed values.....	177
<b>Figure 7-13.</b> The predicted values of the Model1 and Model 2.....	179
<b>Figure 7-14.</b> The differences between observed and predicted values by Model 1~3.....	180
<b>Figure 7-15.</b> Representative stress-strain curves of the GFCs.....	181
<b>Figure 7-16.</b> The relationship between the modulus of the GFCs and compressive strength...	182
<b>Figure 7-17.</b> Typical IA images of GFCs with 3.3 wt% (a), 5 wt% (b), and 10 wt% (c) and 15 wt% foam addition. The scale bar is 1 mm.....	184

<b>Figure 7-18.</b> The pore size distribution and pore volume fraction of in the GFC5.0 and GFC'5.0.....	184
<b>Figure 7-19.</b> The predicting results for the five classic simplified models.....	189
<b>Figure 7-20.</b> The relationship between the porosity and thermal conductivity of GFCs .....	190
<b>Figure 7-21.</b> The relationship between the density and thermal conductivity of GFCs .....	191

# List of Tables

## Chapter 2

<b>Table 2-1:</b> Air void features achieved by different foaming methods.....	11
<b>Table 2-2:</b> Overview of fillers and foam contents used in foam concretes, and the resulting density and compressive strengths.....	13
<b>Table 2-3:</b> Summary of strength prediction models for foam concretes.....	14
<b>Table 2-4:</b> Typical curing produces used in fly ash (FA) based-geopolymer preparation in the laboratory.....	19

## Chapter 3

<b>Table 3-1:</b> D-Grade™ sodium silicate specifications.....	33
<b>Table 3-2:</b> Chemical compositions of 10 fly ashes generated in Australian power stations, wt.%. LOI is loss of ignition. Data from (Heidrich, 2003).....	34
<b>Table 3-3:</b> Composition of the mullite and quartz powder as determined by XRF, wt.%. (LOI is loss of ignition).....	41
<b>Table 3-4:</b> Dissolution conditions of fly ash.....	44

## Chapter 4

<b>Table 4-1:</b> Chemical compositions (wt.%) of fly ash as measured by XRF. LOI is loss on ignition at 1000°C. *SiO <sub>2</sub> is the reactive silica determined by the wet chemical method.....	55
<b>Table 4-2:</b> Particle characteristic parameters of fly ashes.....	63
<b>Table 4-3:</b> Surface area of the five fly ashes as determined by the BET method and the laser particle size analyser.....	63
<b>Table 4-4:</b> Particle density of fly ashes as determined by Archimedes method.....	64
<b>Table 4-5:</b> Particle density and packing density of the five fly ashes, with the inter-particle volume as estimated by subtracting the particle volume from the total volume, and the liquid required to achieve sufficient flowability of the pastes made from each ash.....	69
<b>Table 4-6:</b> Compositions of geopolymer mixtures and concentration of Si, Na <sup>+</sup> and OH <sup>-</sup> .....	71
<b>Table 4-7:</b> Compositions of geopolymer mixtures activated with lower concentration solution.....	72
<b>Table 4-8:</b> The relationship between the volume fraction of liquid in fresh mix and the porosity of hardened binders.....	79
<b>Table 4-9:</b> Composition of amorphous gels in hardened binders as determined by EDS analysis, atom %.....	82
<b>Table 4-10:</b> Gel phase of hardened geopolymer binders (28 d) as determined by dissolution of the geopolymers in 1:15 HCl solution at 25°C.....	83
<b>Table 4-11:</b> Structural water in hardened geopolymer binders (28 d) as determined by TGA and the reaction extent of the corresponding fly ash.....	84

## Chapter 5

<b>Table 5-1:</b> Normalized chemical compositions of fly ash in molar ratio terms. Only Si, Al, Ca, Mg, K and Na oxides are considered.....	87
<b>Table 5-2:</b> Crystalline and amorphous phases of the five selected fly ashes as determined by Rietveld quantitative XRD method, wt. %.....	93
<b>Table 5-3:</b> Chemical composition (wt.%) in the amorphous part of fly ash as calculated from the bulk composition and crystalline composition. 'Others' includes P <sub>2</sub> O <sub>5</sub> , SO <sub>3</sub> , trace components, and LOI.....	93

<b>Table 5-4:</b> The molar composition in the amorphous part of the fly ashes, mol %.....	96
<b>Table 5-5:</b> Composition of the iron bearing aluminosilicate glasses and the distribution of Fe <sup>3+</sup> and <sup>57</sup> Fe. Data from (Weigel et al. 2008).....	98
<b>Table 5-6:</b> The concentration of modifiers, normalised surface area (NSA) and the calculated the reactivity index (RI).....	99
<b>Table 5-7:</b> Composition (wt.%) of dissolved fly ash A by alkaline solutions at 80°C for 6 h.....	103
<b>Table 5-8:</b> Local compositions in the residual particles after dissolution, as determined by EDS analysis, atom %.....	106
<b>Table 5-9:</b> Composition (wt.%) of dissolved fly ash B by alkaline solutions at 80°C for 6 h.....	110
<b>Table 5-10:</b> Local compositions in the residual particles after dissolution, as determined by EDS analysis, atom %.....	111
<b>Table 5-11:</b> Composition (wt.%) of dissolved fly ash E by alkaline solutions at 80°C for 6 h.....	115
<b>Table 5-12:</b> Reaction extents of each phase in the dissolved fly ashes (wt.%).....	116
<b>Table 5-13:</b> Fly ash dissolution by NaOH (pH=13.7) at a liquid to solid ratio of 1000 mL/g at 40°C. Data from (Pietersen et al. 1990).....	118
<b>Table 5-14:</b> Dissolution extents (wt.%) of fly ashes A, B and E under geopolymerization conditions with the same alkalinity of activator (40°C ×24 h+ 25°C×27 d).....	119
<b>Table 5-15:</b> The relationship between the reactivity indexes of the three typical Australian fly ashes and the compressive strength of their geopolymers. Data from (Richard et al. 2011).....	120
<b>Table 5-16:</b> Assignment of the resolved bands in Figure 5-17.....	127
<b>Chapter 6</b>	
<b>Table 6-1:</b> Composition of geopolymer binders for foam concrete synthesis.....	139
<b>Table 6-2:</b> Composition of geopolymer binders for foam concrete synthesis. Metakaolin and high Ca fly ash data from (Arellano Aguilar et al. 2010) and (Bakri Abdullah et al. 2012).....	143
<b>Table 6-3:</b> Orthogonal array design of four composition factors.....	149
<b>Table 6-4:</b> Composition and strength and air-dried (AD) density of GFCs (mean of 4 samples).....	149
<b>Table 6-5:</b> Range analysis of factors affecting the strength and density.....	151
<b>Table 6-6:</b> Variance analysis of factors affecting the strength.....	151
<b>Table 6-7:</b> Modulus (Ms) and alkali content in GFCs (Na <sub>2</sub> O/solid materials mass ratio).....	151
<b>Table 6-8:</b> Composition of slag containing geopolymers and the compressive strength at 28 d, AC-Density at 28 d ageing and oven-dried (OD) density after 60 d ageing (mean of 4 samples).....	152
<b>Chapter 7</b>	
<b>Table 7-1:</b> Composition of GFCs and the workability of the foamed paste.....	163
<b>Table 7-2:</b> Effects of foam content on the density and strength (each mixture had ≥4 samples).....	163
<b>Table 7-3:</b> Fitting results of 28 d air-cured density of geopolymer foam concretes.....	164
<b>Table 7-4:</b> Porosity measured by the IA method and the standard deviation (SD) and coefficients of variation (CV) (each mixture had 2 samples).....	172
<b>Table 7-5:</b> Fitting results of equations for the strength-porosity relationship of GFCs.....	176
<b>Table 7-6:</b> Pore volumetric distribution in the GFCs (mean of 4 samples for each mix).....	178
<b>Table 7-7:</b> Fitting results of the new for the strength-porosity relationship of GFCs.....	178

<b>Table 7-8:</b> Fitting results of Model 3 for the strength-porosity relationship of GFCs.....	180
<b>Table 7-9:</b> Compression modulus of elasticity of GFCs (mean value of 4 samples of each mix).....	181
<b>Table 7-10:</b> The fitting results of models predicting modulus of elasticity.....	183
<b>Table 7-11:</b> Composition of GFCs with varied foam size and content.....	183
<b>Table 7-12:</b> Validation of the mechanical property models (each mix has $\geq 4$ samples).....	185
<b>Table 7-13:</b> Thermal conductivity of GFCs (mean of 4 values).....	186
<b>Table 7-14:</b> The five fundamental structure effective thermal conductivity models for two phase materials (Carson et al. 2005; Wang et al. 2008) .....	187
<b>Table 7-15:</b> Calculated theoretical thermal conductivity of geopolymeric gels.....	188
<b>Table 7-16:</b> Validation of the thermal conductivity models.....	191



## Chapter 1: Introduction

The housing and construction industry is a vast user of both energy and resources. Developing sustainable construction and building materials with less environmental footprint from manufacturing to operation is attracting increased interest.

Geopolymers are composed of tetrahedral silicate and aluminate units linked in a three-dimensional structure by covalent bonds, with the negative charges associated with tetrahedral Al(III) balanced by alkali cations. The geopolymers manufactured by alkali-activation of fly ash have been shown to be more sustainable alternative binders than ordinary Portland cement (OPC), in terms of reduced production energy and resource requirements and lower CO<sub>2</sub> emissions. Recent innovations have led to the development of geopolymer foam concrete (GFC), which combines the performance benefits and operational energy savings achievable through the use of lightweight foam concrete, with the cradle-to-gate emissions reductions obtained through the use of a geopolymer binder derived from fly ash.

Fabricating fly ash-based GFCs is not a simple copy of the existing OPC foam concrete production process. Normal OPC foam concrete can be manufactured with Portland cements or blended cements, which are all standardised products. The production of fly ash-based GFC uses fly ash as precursor, which is heterogeneous in physical and chemical properties. Fly ashes from different power stations, even from time to time at the same station, differ substantially in particle size, morphology and composition because of different coal powders and combustion conditions used. The effects of the nature of fly ash on the suitability for GFC manufacture are poorly understood. Besides, much of the research into the basic properties of plastic and hardened GFCs has not been previously published.

The aim of this research is to examine the physics and chemistry of fly ash and their effects on the solid and foamed geopolymers, and to understand the mechanical and thermal insulation properties of the derived GFCs.

In Chapter 2, the literature review discusses the issue of the heavy environmental footprint of the current cement and concrete industry, in terms of the large CO<sub>2</sub> emission and resource consumption. It introduces the concept of GFC as one potential solution to the global issue. As a basis for this, the current status of foam concrete technology and some fundamental physical chemical aspects of geopolymer formation are reviewed. It highlights some of the issues in the specific context of foamed lightweight geopolymer concrete production, and outlines the importance of developing more comprehensive and better understanding of the factors such as feedstock chemistry, microstructure and control of engineering properties.

In Chapter 3, the generation of fly ashes and slag in Australia and their current use are briefly reviewed. Some other materials and chemicals used in this research are outlined. The characterisation procedures for the materials and the solid and foamed geopolymers are described. In particular, the procedures for X-

ray diffraction (XRD) analysis of as-received and alkali-leached fly ashes are described in detail.

Chapter 4 characterizes the physical characteristics of the selected fly ashes and their effects on the properties of solid geopolymer binder, which is a key component for GFC manufacture. The particle size distribution, surface area, density and morphology are studied. The relationship between the inter-particle volume and the liquid requirements of the pastes are investigated for the first time. The compressive strengths of the hardened binders are studied and related to their porosity and pore size distribution.

Chapter 5 investigates the composition of the glassy and crystalline phases in the fly ashes. Based on the understanding of the different roles of cations, that are the glass network modifiers and formers, this chapter proposes a reactivity index (RI) for the quantification of fly ash reactivity in geopolymer manufacture. Dissolution experiments under different liquid/solid conditions performed in this research and by other researchers are examined to inspect the proposed index. Based on the fly ash glass chemistry, Fourier transform infrared spectroscopy (FTIR) with the spectral deconvolution technique is recommended as a quick indicator method for quantifying the reactivity.

In Chapter 6, a batch of trial GFC mixtures are manufactured at laboratory conditions and investigated. In combination with the comprehensive understanding of physics and chemistry of the fly ashes, the research answers the questions which type of fly ashes is more suitable for GFC manufacture and why. One of the most important findings is that a reactive fly ash is not more necessarily suitable for GFC manufacture. The important factors for GFC manufacture are the particle density and morphology, rather than the fly ash glass chemistry. This implies that GFC manufacture provides a very promising technology for a real 'valuable use' of fly ashes, particularly for those 'low quality' fly ashes, which are seemingly unsuitable for production of high strength geopolymer binders.

In Chapter 7, a series of GFCs with a wide range of densities and strengths are manufactured for the understanding of this type of new material. The pore features (shape, sizes and distribution and volume) are studied by image analysis. The results are correlated with the compressive strength, compression modulus and thermal conductivity through statistical-based modelling for predicting the mechanical and thermal insulation properties of the GFCs.

Chapter 8 draws the conclusions of the research undertaken in this thesis. Some problematic issues that have been noted in the GFC manufacture are mentioned. Detailed suggestions to the future work are presented for GFC production and application.

## **Chapter 2: Review on Geopolymer Foam Concrete: an Emerging Material for Sustainable Construction**

*Note: this chapter is based on the manuscript entitled “Geopolymer Foam Concrete: an Emerging Material for Sustainable Construction”, by Zuhua Zhang, John Provis, Andrew Reid and Hao Wang, published in journal of **Construction and Building Materials**, 2014.*

### **2.1 Introduction**

Over the past century, Portland cement-based concrete has become the highest-volume manufactured product on Earth, due to the versatility and generally highly reliable performance of this material, and also the widespread availability and comparatively low cost of the necessary raw materials and processing technology. However, since the widespread adoption of ‘sustainability’ as a key criterion for the assessment of materials by both the engineering community and the general public, the construction materials industry is facing increased pressure as Portland cement production is becoming perceived as unsustainable. Although the embodied energy intensity per functional unit remains lower than most other available building materials (Purnell 2012), the very large production volumes required to meet global demand lead to high sector-wide consumption of raw materials and energy, emission of greenhouse gases (GHGs), and dust pollution (Mehta 2010). Thus, the development of sustainable construction and building materials with reduced environmental footprint through both manufacturing and operational phases is currently a key focus in the global housing and construction industry.

This chapter discusses the concept of geopolymer foam concrete as one potential aspect of the global solution to this issue. As a basis for this, the current status of foam concrete technology and some fundamental physico-chemical aspects of geopolymer formation are reviewed. A geopolymer is an aluminosilicate binder formed by alkaline activation of solid alumina- and silica-containing precursor materials at or slightly above room temperature. This class of materials has emerged as one of the key alternatives to ordinary Portland cement (OPC) as a binder for concrete production in the last decades (Juenger et al. 2011).

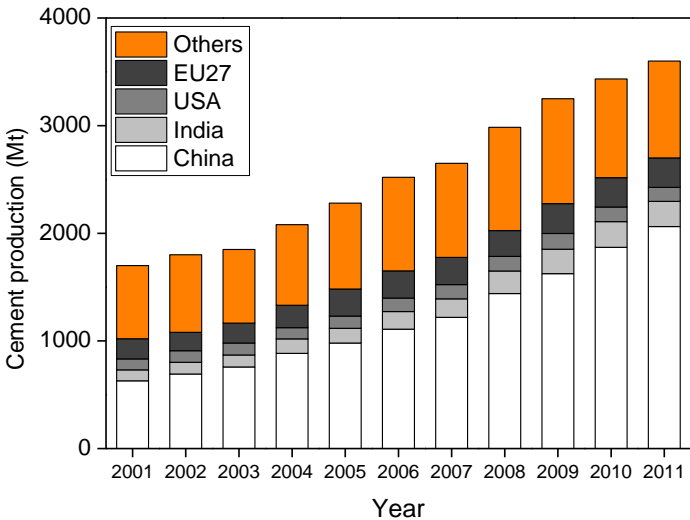
Although considerable research has been conducted on many aspects of geopolymer technology, application of this technology is not yet widespread, for both technical and non-technical reasons (Van Deventer et al. 2010; Van Deventer et al. 2012). This review highlights some of these issues in the specific context of foamed lightweight geopolymer concrete production, and outlines the importance of developing deeper and more comprehensive understanding of factors including feedstock materials chemistry, microstructure, and control of engineering properties, as part of the process of broadening the uptake of this technology.

## 2.2 Sustainability in the cement and concrete industry

### 2.2.1 Current status of sustainable development efforts

The term *sustainability* has entered prominently into public discourse since the definition of *sustainable development* in the report *Our Common Future*, also known as the *Brundtland Report*, published by the World Commission on Environment and Development (WCED) (1987). The concept of sustainable development is defined as: *'the ability to meet our current needs without compromising the ability of future generation to meet theirs'*. This definition requires consideration across all aspects of a specific industry, through raw materials supply, energy consumption and environmental impact of a material, component or structure in manufacture and in service, as well as end-of-life processing and potential reuse or recycling.

Figure 2-1 summarises the global volumes of cement production and distribution in the first decade of the 21<sup>st</sup> century.



**Figure2-1.** Global cement production and distribution. Data from (He 2010; CCM 2011; Sinoma 2011; CEMBUREAU, 2012).

A potential future shortage of low-cost raw materials is the first aspect which should be considered in the context of the cement and concrete industry, because of its huge consumption of conventional limestone-based materials. In the year 2011, the world cement production was around 3.6 billion tonnes (CEMBUREAU, 2012). This required more than 3 billion tonnes of limestone for clinker manufacturing, if considering a global average clinker factor of 0.77 (Schneider et al. 2011). Limestone supply is not inexhaustible because the transportation distance is limited for this low profit product. An example of this is the statistic given in the report *Cement Production in Vertical Shaft Kilns in China – Status and Opportunities for Improvement* (UNIDO 2006), which reads: *“1326 limestone quarries are currently known in China containing*

*approximately 56,120 million tonnes of limestone. Taking into account future growth of cement production these deposits can only maintain the need for manufacturing of cement for 59 years (other industry exploitation not taken into account)”.*

A more challenging factor related to the sustainability of this industry is its considerable energy consumption. Energy is required for clinker calcination (usually at 1400-1450°C) and grinding of raw materials, coal and clinker. The energy needed in converting raw materials to clinker accounts for the major energy requirement of the process. This strongly depends on the manufacturing plant type: inefficient long rotary kilns burning wet raw materials typically operate at a heat consumption rate of about 6 GJ/tonne clinker, while a typical modern rotary kiln needs 3.1 GJ/tonne clinker. A realistic world average specific heat consumption is estimated around 3.8 GJ/tonne clinker (Damtoft et al. 2008). The additional energy required for cement production (crushing and grinding) is about 100 kWh/tonne cement (Schneider et al. 2011). From clinker to cement product, the total energy consumption is about 3.2 GJ/t cement, assuming an average 0.77 clinker factor is used in cements (Schneider et al. 2011).

Associated with the high energy requirements of the process are high emissions. The average emission resulting from manufacturing each tonne of clinker is around 0.9 t of CO<sub>2</sub>, in which 0.53 t derives from raw materials decomposition and 0.37 t from fuel combustion (Mehta 2010). The total CO<sub>2</sub> emissions attributed to cement production contribute around 8% of global CO<sub>2</sub> emissions according to the most recent available data (Olivier et al. 2012). Portland cement production represents 74–81% of the overall CO<sub>2</sub> emissions of concrete, while aggregate production represents 13–20% (Flower and Sanjayan 2007), so the total emissions of the cement and concrete industry, as a whole sector, contribute around 10% of global anthropogenic CO<sub>2</sub> emissions.

It is quite obvious that the current cement and concrete industry has heavy impacts on the environment. However, in the next decades, cement and concrete production is expected to continue to show growth (Schneider et al. 2011). Demand for cement in industrialized nations is increasing slowly if at all, but in developing countries and regions such as India, other developing parts of Asia, the Middle East, South America and Africa it will continually increase due to the fast urbanization and associated infrastructure development. Although the per-unit CO<sub>2</sub> emissions will decrease, the sector-wide totals will grow, with major technological advances required simply to hold total emissions at current levels. Therefore, the environmental issues associated with CO<sub>2</sub> emission, limitations on natural resources, and high energy consumption will play a leading role in the sustainable development of the cement and concrete industry in the coming century.

The cement and concrete industry has been fully aware of the challenges, and has keenly focused on many positive activities over a long period toward sustainable development:

- *Saving energy/resources and reducing emissions from cement*

## *manufacturing plants*

(1) improving the energy efficiency by changing from the inefficient long rotary kilns burning wet raw materials, to modern rotary kilns which burn dry materials (Sorrentino 2011); (2) using bio-fuels such as agricultural wastes, biodegradable municipal wastes, animal wastes, paper wastes and other alternative fuels (Damtoft et al. 2008); and (3) replacing limestone with other high-calcium industrial by-products, such as metallurgical slags and red mud (Pera et al. 1997), to reduce CO<sub>2</sub> from raw materials decomposition.

- *Reducing clinker content in cement and concrete*

using more supplementary materials, such as blast furnace slag (BFS), fly ash, natural pozzolans and silica fume, in Portland cement to make blended cement, which has the potential to reduce CO<sub>2</sub> emissions approximately in proportion to the blending fraction (Bleszynski et al., 2002; Hendriks et al. 1998).

- *More precise design and use of concrete*

(1) selecting the correct concrete for specific application: using high-strength and durable concrete for infrastructure elements which usually need a high content of cement and high-grade aggregates, while using lower-strength concrete where strength is less critical, such as non-load-bearing indoor components and other non-structural applications (Ramamurthy et al. 2009); (2) recycling construction and demolition wastes to produce recycled aggregates, thus decreasing the demand for natural aggregates as well as the energy requirement for their mining and transport (Worrell et al. 1994; Corinaldesi et al. 2009); and (3) improving the durability of concretes to prolong their service life, which will greatly reduce the need for future consumption for cement and concrete in repair, retrofitting or replacement of existing structures (Tang 2006).

- *Applying new technology to make non-OPC concretes*

Alternatives which are currently available and based on known concepts include partially pre-hydrated C-S-H binders, belite-rich cements, magnesium oxy-carbonate cements, magnesium silicate cements, calcium carbonate cements, supersulfated slag cements, calcium aluminate/sulfoaluminate cements, and geopolymers (Gartner and Macphee 2011; Duxson et al. 2007; Schneider et al. 2011).

The approaches described above will undoubtedly improve the sustainability of the concrete industry as a whole. Moreover, the construction industry is paying increasing attention to the whole life-cycle aspects of construction materials as one component of the life-cycle impact of a building (Fernandez 2008). This is because the embodied energy of construction materials is only a small fraction of the total energy consumption for a building. Analysis of Australian housing

stocks and the operational energy requirements per m<sup>2</sup> of building area shows that 9.9 GJ (19.5%) is needed for manufacturing, 0.4 GJ (0.8%) is needed for construction and 40.5 GJ (79.7%) is needed for operational energy over a 50-year timeframe (Pullen 2000). Therefore, saving energy and reducing CO<sub>2</sub> emissions by using appropriately-selected concretes (or other materials) during the operational phase is critically important.

### **2.2.2 Geopolymers - alternative binders to Portland cement**

The term *geopolymer* was introduced in the 1970s by Joseph Davidovits to describe a family of alkali activated aluminosilicate binders, and later became popular to describe a larger variety of alkali activated binders (Davidovits 2008). The development of geopolymers has shifted from the original applications related to fire-resistance, toward utilisation in more general construction applications, and the research and application cases have been well reviewed in the literature (Shi et al. 2006; Provis and van Deventer 2009; van Deventer et al., 2012).

Geopolymers are composed of tetrahedral silicate and aluminosilicate units linked in a three-dimensional structure by covalent bonds, with the negative charges associated with tetrahedral Al(III) charge-balanced by alkali cations. The raw materials include two parts: reactive aluminosilicate solids, such as fly ash and calcined clays, and an alkaline activating solution, usually an alkali metal hydroxide or silicate solution. There is also interest in development of one-part geopolymer precursors (Hajimohammadi et al., 2008; Duxson and Provis 2008; Feng et al. 2012), but the materials that have been developed to date tend to have strengths which are not high enough for most construction purposes (Koloušek et al. 2007).

Geopolymers are generally reported to be much more sustainable than Portland cement, in terms of reduced production energy requirement and lower CO<sub>2</sub> emissions (Duxson et al. 2007; McLellan et al. 2011; EAEP 1999). Fly ash and calcined clay are the most two common raw materials in geopolymer synthesis for construction applications. Fly ash is an industrial waste or by-product, generated through coal-fired electricity generation. It is almost 100% profitably used in many European countries, but in many rapidly developing countries, which are consuming increasing amounts of cement as discussed above, the generation of fly ash is much higher than the current utilization rate. The utilisation of fly ash as a solid raw material does not require a major additional energy input – transportation should be considered, but little additional processing is generally needed. Calcination of clay needs a high temperature process (~750°C), but this takes place at a much lower temperature than Portland cement clinker production (~1400-1450°C), and is less energy-intensive.

The most critical ingredient in terms of the environmental footprint of a geopolymer material is the alkali activator. The production of alkalis is an energy-extensive process; for example, the embodied energy of sodium hydroxide (dry) is 14.9 GJ/t (EAEP 1999), and it is 5.4 GJ/t in sodium silicate (solution with Na<sub>2</sub>O·2SiO<sub>2</sub> content 48% by mass) (Fawer et al. 1999). The exact

energy requirements, associated with CO<sub>2</sub> emission, may vary depending on the production specific methods. However, as the content of activator is usually kept as low as possible in formulating a geopolymer, and is generally less than 10% of the total mix design, the environmental benefits of making geopolymers can appear very attractive. The CO<sub>2</sub> emission due to production of geopolymers is generally reported to be 60-80% less than cement clinker (Duxson et al. 2007; Stengel et al. 2009; McLellan et al. 2011).

However, the 'sustainability' of a geopolymer also depends significantly on many other factors. The availability of raw materials and the composition may be the two most important factors, from an industrial perspective. McLellan et al. (2011) calculated that the cost and emissions of geopolymers range from a profile where these parameters can either be much lower (approximately 72% reduction in cost and 97% reduction in greenhouse emissions) or much higher than an OPC mixture (up to approximately eight-fold cost increase and 14% increase in CO<sub>2</sub> emissions), because of the variations in transportation and composition between different geopolymer mixes analysed.

A recent innovation, geopolymer foam concrete, combines the advantages of foam concrete and geopolymer technology, and provides the opportunity to reduce the environmental footprint of construction materials in terms of raw materials, embodied CO<sub>2</sub> and operational energy in service. Before detailing the properties of this new material, it is worth to introduce the state of the art with regard to development of conventional foam concrete.

### ***2.3 Foam concrete technology***

Foam concrete is generally defined as a type of lightweight concrete that consists of a cementitious binder with a high degree of void space, with or without the addition of fine aggregate. Foam concrete was patented by Aylsworth and Dyer in 1914 and later by Bayer and Eriksson in 1923 (Valore 1961), but its application as a lightweight building material has become much more popular in the last few decades (Ramamurthy et al. 2009), as building energy efficiency has become a more widespread concern. In this paper, the term foam concrete is applied to all types of cellular concretes, regardless of the foaming and/or aeration method. The use of porous aggregates is another method which introduces air voids to improve the thermal insulation properties of the material, but falls beyond the scope of this review, which is instead focused predominantly on the development of lightweight binders.

#### **2.3.1 Composition of foam concrete**

##### **2.3.1.1 Binder**

The binder used for foam concrete is most commonly an OPC-based binder, alone or in combination with other components, giving binder types such as cement-sand, cement-lime, and rapid hardening Portland cement (Ramamurthy et al. 2009). Fly ash and GBFS are usually used as secondary cementitious components to partially replace cement (Jones and McCarthy 2005a; Wee et al. 2006), and air-cooled slag also shows some beneficial properties (Mostafa



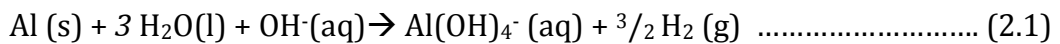
2005). For room temperature cured foam concrete, the binder phases are expected to be essentially the same as the standard hydration products of OPC or its mixtures with the same additives in dense concretes. However, in autoclaved aerated concrete, which adopts high temperature high pressure curing, the initially formed amorphous C-S-H and CH will react with Si-rich mix components to form crystalline hydrous calcium silicate phases (Mostafa 2005).

Non-cementitious fine fillers such as granitic limestone and silica fines can also be used to reduce cost, and materials such as sawdust, diatomite, and bentonite can be used as fillers to improve the workability of the fresh paste, and/or its final strength (Zawada and Mont 1998). It has also been disclosed that ground recycled glass is a good filler to reduce the cost of the products and to improve the stability of the paste (Shi et al. 2002). Expanded polystyrene granules and expanded perlite (usually in fine particles) are popular lightening fillers in foamed concrete (Laukaitis et al. 2005 Bui 2010). The amount of such non-cementitious fillers should not be higher than 50% as suggested by Spinney (1993), and particularly in the case of organic-based materials such as polystyrene, the lack of adhesion between the cement paste and the filler can give a tendency towards segregation (Chen and Liu 2004).

### 2.3.1.2 Voids

Controlling the nature, size and distribution of voids is the most critical step in production of a foam concrete, as the voids determine the density and strength of the foam concrete. Voids can be produced by two main methods: either (1) by endogenous gas generation, which can be achieved by mixing gas-releasing agents such as H<sub>2</sub>O<sub>2</sub> or fine aluminium or zinc powders in cement paste or mortar, or (2) by introducing a very large volume fraction of air bubbles, usually through the use of an organic foaming agent. Different foaming methods, as well as mixture composition and curing processes, will generate different sizes and distributions of individual bubbles in foam concrete, which will further affect the properties of the foam concrete (this aspect will be discussed in Section 3.2).

Reactive metal powders react with water and hydroxide in an alkaline environment, liberating bubbles of hydrogen gas and forming hydrolysed metal complexes. This takes place according to a reaction similar to equation (1), which is written for the case of Al, but other metals such as Zn or Si can also be used, and follow analogous reaction processes:



The bubbles lead to expansion of the cement paste or the mortar, which must have a suitable consistency to prevent their escape (Neville 2011). The dose and particle size of the metallic powder can be designed according to the target density. Autoclaved aerated concrete (AAC) is a typical product made using this method, where aluminium powder addition is around 0.05% by mass of all solid materials (Mostafa 2005).

The direct introduction of air bubbles can be achieved by a pre-foaming method, or alternatively by mixing a foam concentrate with paste or mortar using a high-

shear mixer. The pre-foaming method uses foaming agents, either synthetic surfactants (Bing et al. 2012; Çolak 2000; Huang and Liu 2001) or protein-based (Huang and Liu 2001; Kearsley and Wainwright 2002; Nambiar and Ramamurthy 2007; Othuman and Wang 2011), to make a wet foam or a dry foam. The wet foam is prepared by spraying a foaming agent solution through a fine mesh and is less stable due to the relatively larger size of the bubbles formed (diameter >1 mm). The dry foam is produced by forcing compressed air into a foaming agent solution through a foaming machine, and is more stable. The dry pre-foaming method has thus become more preferred because it needs less foaming agent than the high-shear mixing method (Ramamurthy et al. 2009).

### 2.3.1.3 Water and others

Water used in mixing of foam concretes, similar to the case of concretes in general, should be free of deleterious amounts of oil, dissolved electrolytes and/or organic materials, which would adversely affect the properties of fresh and hardened foam concretes (Fouad 2006). The quantity of water needed in a foam concrete depends on the composition of cementitious materials, filler type and workability requirements of the mixture. A common understanding, for example, is that when water absorbing fillers are used, such as expanded perlite (Hunaiti 1997), high water content is required to achieve suitable flowability. The commonly used water-cement ratios (w/c) range from 0.45 to 0.65, and may be up to 1.25 in cases with little or no superplasticiser (Ramamurthy et al. 2009).

The strength of foam concrete is mainly governed by the induced voids and the volume of evaporable water in the binder; which means that reducing w/c is generally beneficial for achieving high strength (Neville 2011). An appropriate superplasticiser in combination with mineral admixtures can decrease the water needed to achieve specified flow properties (Pan et al. 2007). Other chemical additives such as latexes and acrylics may also be used in foam concretes to improve strength or reduce permeability and absorbance (Łaźniewska-Piekarczyk and Szwabowski 2012).

However, the compatibility between foaming agents and superplasticisers or other chemical additives should be taken into consideration. Superplasticisers and other additives may contain components which are intended to have an anti-foaming function in normal concretes. For example, polyalcohol is an anti-foaming admixture that contains -OH as functional groups (Łaźniewska-Piekarczyk and Szwabowski 2012). Such active components or groups are distributed around gas bubbles, displacing foaming agent molecules and causing the breakage or coalescence of the bubbles. This means that admixtures designed for use with non-foamed concretes may have unintended effects if used indiscriminately in foamed concrete mixes.

## 2.3.2 Properties of foam concrete

### 2.3.2.1 Void features induced by different foaming methods

The pores in foam concrete, as a system, consist of gel pores, capillary pores and

air voids (Visagie and Kearsely 2002). The sizes of pores range from nanometre scale to millimetre scale, where the larger part of this range is mainly attributed to the air voids. The foaming methods, as discussed in Section 3.1.2, will influence the void features in foam concrete, including size, volume fraction and shape. Typical void features achieved by different foaming methods are shown in Table 2-1.

**Table 2-1:** Air void features achieved by different foaming methods.

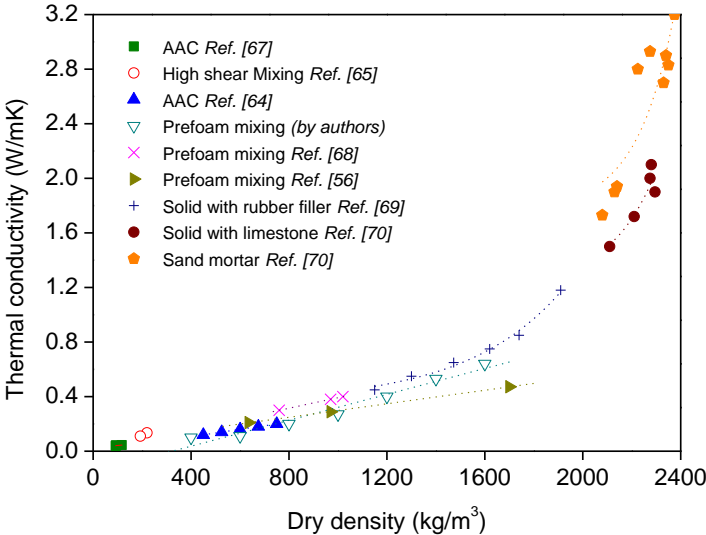
Foaming method	Diameter of air voids /mm	Volume of air voids	Shape	Density / kg/m <sup>3</sup>	Ref.
Chemical foaming: gas release	0.5-3.0	15-65%	Spherical	typical AAC: 300-800, may be as low as 100	Schober 2011; Kreft 2011; Newman 2003
Mechanical foaming: high shear mixing or pre-foaming	0.1-1.0	10-50%	Less spherical, with shape factor 1.2-1.4	400-1600	Nambiar 2007; Newman 2003; Akthar 2010

It can be seen in Table 2-1 that the void sizes in foam concrete produced by mechanical foaming are finer than those in chemically foamed concrete. The connectivity of the voids depends on the density of the mixture, regardless of the foaming method. If the density reaches a level that allows the binder to isolate individual bubbles, the voids formed are closed. Otherwise, the foam concrete has an open cell structure. For example, only AAC with density >550 kg/m<sup>3</sup> can possess a closed cell structure of air voids, because this density is required to provide sufficient paste thickness between pores (Schober 2011). Foam concretes produced by mixing the binder with preformed foams, with densities from 750 to 1500 kg/m<sup>3</sup>, can have isolated voids (Nambiar and Ramamurthy 2007). Conversely, a foam concrete with a density of 220 kg/m<sup>3</sup> shows connected voids under SEM imaging (Akthar and Evans 2010). These void features, particularly the void size and connectivity, will to a large extent determine the strength, thermal insulation and water absorption properties of the material.

### 2.3.2.2 Thermal insulation

Foam concretes are popular mainly because of their good thermal insulation properties, meaning that buildings can save operational energy, which is the major route to energy consumption over the full life cycle of a building (Pullen 2000). The thermal conductivity, as one of the most important parameters affecting thermal insulation, has been extensively reported in the literature related to these materials. This is a complex function of porosity (total fraction and size distribution), density, void liquid saturation state, binder composition, and fillers. Figure 2-2 plots the thermal conductivities of foam concretes in comparison with three solid concretes with rubber, limestone and sand as fillers. The measurement of thermal conductivity must be undertaken at a certain humidity and moisture state condition for the same batch of samples, as the

moisture in samples has a significant influence on the measurement (Ramamurthy and Narayanan 2000).



**Figure 2-2.** The thermal conductivity of foam concretes in comparison with solid concretes. The data by the current authors are measured using the transient plane source (TPS) method; the foam concretes are synthesised with OPC ( $w/c=0.5$ ) by mechanical mixing of preformed foam; all the samples are dried in a vacuum oven at 80°C for 24 h before measuring. Data from (Newman and Owens 2003; Akthar and Evans 2010; AAC 2001; Weigler and Karl 1980; Benazzouk et al. 2008; Bentz et al. 2011).

### 2.3.2.3 Mechanical properties

The key mechanical properties of interest in the discussion of foam concretes include compressive strength and modulus of elasticity. Parameters affecting the mechanical properties of foam concrete include the filler type and fraction,  $w/c$ , and curing procedure, as well as the size and distribution of air voids.

Table 2-2 presents an overview of compressive strengths of foam concretes for various mixtures as reported in the literature. Compressive strength is usually between 1 and 10 MPa in the density range 360-1400 kg/m<sup>3</sup>, while the modulus of elasticity is generally between 1.7 and 3.5 GPa (Neville 2011).

**Table 2-2.** Overview of fillers and foam contents used in foam concretes, and the resulting density and compressive strengths

Filler type	Foaming		W/C	Density/kg/m <sup>3</sup>	Compressive Strength/MPa	Ref.
	Method <sup>a</sup>	Volume ratio <sup>b</sup>				
<i>Sand</i>						
Fine sand	M-P	0.39-0.11	0.6-0.8	1300-1900	1.8-16.7	Tam 1987
Sand	M-PD	0.47-0.25	0.3-0.4	800-1320	2-10	Nambiar 2006b
Sand	C-Al			Moist-cured Autoclaved	7.4-7.9 12-14	Narayanan 2000a
Sand	M-PD	0.25-0.17	0.5	1000-1400	1-12	Jones 2005b
Sand	M-PW	0.69-0.26	0.7	430-1490	1.5-9.9	Pan 2007
Sand	M-P			1670	12.1	Hunaiti 1997
<i>Fly ash (FA)</i>						
FA	C-Al			Moist-cured Autoclaved	5.5-7.5 7.9-9.3	Narayanan 2000a
FA	M-PD	0.4-0.1	0.4-0.6	650-1224	2-17.8	Nambiar 2006
Low lime FA	M-PD	0.18-0.07	1.1-1.5	1000-1400	3.9-7.3	Jones 2006b
<i>Others</i>						
Fine sand+FA (1:1)	M-PD	0.42-0.15	0.4-0.6	800-1250	2-14	Nambiar 2006a
Sand+FA(3:7)	C-Al+H	0.6-0.3	~0.7	1074-1141	~6	Keertana 2011
Sand+slag+SF <sup>c</sup> +FA	M-PW	0.63-0.30	0.3	710-1520	4.2-23.7	Pan 2007
EPS <sup>d</sup>	M-PD			275-1400	0.1-0.8	Laukaitis 2005
Expanded clay	M-P	0.3-0.1		700-1200	5-30	Weigler 1980
None	M-PD	0.5-0.2	0.3-0.4	787-1318	1.2-10.7	Nambiar 2006a
None	C-Al		0.4-0.6	450-1100	2-16	Just 2009

a: M-P = mechanical mixing of preformed foam (whether wet or dry is unknown); M-PD = mechanical mixing of preformed foam by dry method; M-PW = mechanical mixing of preformed foam by wet method; C-Al = chemical foaming by aluminium powder; C-Al+H = chemical foaming by aluminium powder and hydrogen peroxide

b: ranges of values are written in corresponding directions for each sample, so that the first and last values quoted for each property are each referring to the same mixes

c: SF = silica fume

d: EPS = expanded polystyrene particles

From Table 2-2, it is evident that regardless of the foaming method and the filler type, the compressive strength of foam concretes decreases with a reduction in density. This means that the density (or void volume) is critical to the strength of foam concrete, as is the case for any porous solid material (Mehta and

Monteiro 2006). Several model expressions have been developed for relating strength to density, gel-space ratio or porosity for foam concretes with different fillers, as summarised in Table 2-3.

**Table 2-3:** Summary of strength prediction models for foam concretes

Type	Models	Reference
Foam cement without filler	$\sigma_y = \sigma_0 \left( \frac{d_c}{1+k} \right)^b \left( \frac{1+0.20\rho_c}{\rho_c \gamma_w} \right)^b$ <p><math>\sigma_0</math>: theoretical paste strength at zero porosity; <math>d_c</math>: concrete density; <math>k</math>: water-cement ratio; <math>\rho_c</math>: specific gravity of cement; <math>\gamma_w</math>: unit weight of water, <math>b</math>: empirical constant</p>	Hoff 1972
Foam cement with sand	$S = K_p \left( \frac{\alpha c}{\alpha c + w + a} \right)^n$ <p><math>\alpha</math>: degree of hydration; <math>c</math>, <math>w</math> and <math>a</math>: absolute volume of cement, water and air of the initial composition; <math>n</math>: empirical constant</p>	Tam 1987
Foam concrete with fly ash	$f_c = A[B + C \ln t - D \cdot (W/C)]\alpha_b^E$ <p><math>t</math>: sample age; <math>W/C</math>: effective water-cement ratio; <math>\alpha_b</math>: binder ratio, i.e. the binder content (by volume) of the foamed concrete mixture as a fraction of the binder content of the paste; <math>A</math>, <math>B</math>, <math>C</math>, <math>D</math> and <math>E</math>: empirical constants</p>	Jones 2005a

#### 2.3.2.4 Shrinkage

Foam concrete exhibits much higher shrinkage than normal weight concrete. The measured drying shrinkage of foam concrete after 1 year ranges from 0.1 to 0.36% (Jones et al. 2003), which is 5 to 10 times higher than the typical shrinkage of dense mortar and concrete specimens with aggregate/cement ratios from 3 to 7 (Neville 2011).

The factors contributing to the high shrinkage include the use of little or no aggregate, and/or the microstructure of the hydration products, particularly the pore size and specific surface. According to Neville (2011), it is the aggregate that restrains shrinkage. When the sand to cement ratio increases from 1 to 3, the shrinkage of foam concrete decreases from 0.125% to 0.075% (Nambiar and Ramamurthy 2009). As fly ash or other supplementary cementitious materials are introduced, the hydration products will change in composition and structure. This is very important because the shrinkage properties of the hydrate phases will also be changed according to the gel chemistry, pore structure and specific surface area (Georgiades et al. 1991; Justnes et al. 1998). For example, in the case of replacing sand with fly ash, the shrinkage increases due to: 1) the reduced restraining capacity of fly ash compared to sand, 2) higher water requirement of mixes with fly ash to achieve a workable mix, and 3) probably the reduced foam volume requirement to achieve a given density (Nambiar and Ramamurthy 2009). To minimise shrinkage, it is suggested to keep the content of fillers such as lime and fly ash at a lower level; in comparison, the dosages of

superplasticiser, aerating agents and silica fume have been noted to have much smaller influence (Ramamurthy and Narayanan 2000).

## ***2.4 Development of geopolymer foam concrete***

In the following sections, only some basic mechanisms in aluminosilicate based geopolymer formation are reviewed; the primary focus is the development of geopolymer foam concrete derived from aluminosilicate precursors such as fly ash and metakaolin.

### **2.4.1 Geopolymerization**

Many chemical and physical analysis techniques, as well as computational modelling, have been applied in examining the geopolymerization mechanisms and the structure of the reaction products (Fernández-Jiménez et al. 2005; 2006a,b; Rees et al. 2007; 2008; Criado et al. 2007a; 2008; Yao et al. 2009; Provis et al. 2011; White et al. 2011). A generalized mechanism is that: (1) the aluminosilicate solids dissolve into the strongly alkaline aqueous phase; (2) the dissolved Al and Si species, and any silicate initially supplied by the activator, interact to form oligomers; (3) the supersaturated system begins precipitation to form gels; (4) geopolymer gel grows and bonds with the residual precursor particles to form a solidified binder; (5) gels continue the transformation to a more ordered state, usually towards zeolite-like phases. This reaction mechanism is now relatively well understood, and is controllable by manipulation of a number of different mix design and reaction condition parameters.

### **2.4.2 Important issues in geopolymer synthesis**

#### **2.4.2.1 Aluminosilicate precursors: metakaolin or fly ash**

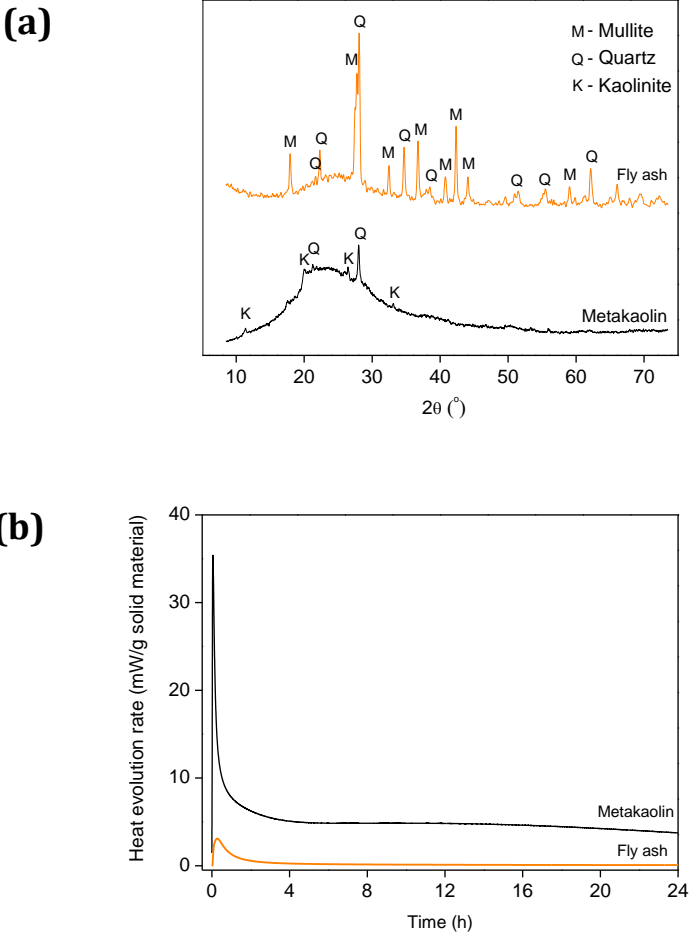
Apart from the alkali activators, which are the key components affecting the properties of geopolymers (Provis 2009a), selection of raw materials is the most critical issue in achieving desired performance. Two common raw materials used for geopolymer synthesis are metakaolin and fly ash, both of which contain considerable amounts of reactive amorphous Al and Si. Metakaolin was a typical raw material in early geopolymer synthesis studies (Davidovits 1982; 1991), while currently fly ash is becoming more popular as the applications focus has changed towards construction purposes.

Metakaolin is a dehydration product of kaolinite clay ( $\text{Al}_4[\text{Si}_4\text{O}_{10}](\text{OH})_8$ ) at 500-900°C (Zhang et al. 2009a). Metakaolin consists of plate-like particles, is c-axis disordered and contains 4-coordinated Si and a range of Al coordination environments (Singh et al. 2005; White et al. 2010a). It generally has a specific surface area of 9-20 m<sup>2</sup>/g as measured by N<sub>2</sub> sorption. In comparison, fly ash is comprised of fine, spherical, mostly glassy particles, and the surface area is only 0.6 to 4.2 m<sup>2</sup>/g, depending on the fly ash source (Ward and French 2003).

This morphological difference leads to a much higher liquid requirement in metakaolin-based geopolymer paste than in fly ash-based geopolymer paste (Provis et al. 2010). Metakaolin paste usually requires a liquid/metakaolin

ratio >0.6 by mass (Yao et al. 2009; Zhang et al. 2009b), and mortars need ~1.0 (Rovnaník 2010; Pacheco-Torgal et al. 2011). A lower liquid ratio can also be made to work, but needs a high pressure compaction process (Živica et al. 2011), which would not be suitable for normal concrete production. In comparison, fly ash geopolymer paste requires a liquid/ash ratio between 0.30 and 0.65 (Zhang et al. 2012a), and the concrete needs 0.40-0.96 (Diaz-Loya et al. 2011), depending on the fly ash properties and activator type. More liquid phase is required to wet the surface and inter-layer area of metakaolin particles to achieve a good workability, which can be quantified by the yield stress of the binder (Van Jaarsveld et al. 2002).

The second difference is the high reaction rate of metakaolin-based geopolymers and the faster strength development than fly ash-based geopolymer, particularly at low temperature. Figure 2-3 shows the results of X-ray diffraction (XRD) analysis of metakaolin and fly ash, and their reaction heat release at 20°C as measured by isothermal conduction calorimetry.



**Figure 2-3.** (a) XRD patterns of metakaolin and fly ash, and (b) their alkali activation heat evolution as measured by isothermal calorimetry. Activator has SiO<sub>2</sub>/Na<sub>2</sub>O ratio of 1.4, total dissolved solids concentration of 40%; the BET surface areas of metakaolin and fly ash are 14 and 0.9 m<sup>2</sup>/g, respectively (Zhang et al. 2013).

It should be noted here that for metakaolin, the secondary minerals present in



original kaolinite clay (Zhang et al. 2012b; Zibouche et al. 2009), the surface area of particles, and the reaction temperature (Rahierb et al. 2003; Zhang et al. 2012c) all have significant influences on the reaction rate and strength development. Similarly for fly ash-based geopolymers, the source of fly ash (Zhang et al. 2012a), surface area (Temuujin et al. 2009a; Kumar & Kumar 2011) and reaction temperature are all important. A general trend is that geopolymers derived from raw materials with higher surface area exhibit faster strength development. The effect of temperature is more complicated, and will be discussed later.

The third and most important difference is the structural stability of geopolymers, which will affect their potential applications. Geopolymers with Si/Al <3.8 derived from metakaolin can exhibit a trend of transformation from amorphous to zeolite-like crystalline structure under continuous curing conditions (moisture and warmth) (De Silva and Sagoe-Crentsil 2008). A systematic ageing study and an extensive review of accelerated ageing of geopolymers were presented by Lloyd (2009), who has concluded that amorphous geopolymer gels synthesised from metakaolin form crystalline zeolites upon hydrothermal ageing (95°C), accompanied by major restructuring of the gel and loss of compressive strength. In comparison, much less of the gel in a geopolymer derived from fly ash is converted to zeolite phases during ageing, corresponding with negligible strength loss. For these reasons, as Lloyd (2009) suggested, *'geopolymers based on metakaolin must be considered unsuitable for construction purposes'*.

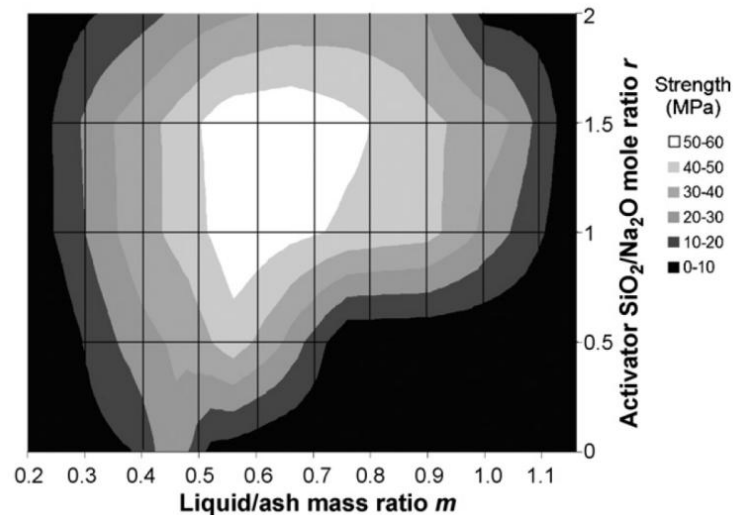
#### 2.4.2.2 Activator: MOH or $M_2O \cdot nSiO_2$ solution

Both alkali metal hydroxide (usually KOH and NaOH) and silicate solutions ( $K_2O \cdot nSiO_2$  and  $Na_2O \cdot nSiO_2$ ) can be used. The type of alkali metal cations plays an important role in determining the final structure of geopolymers and therefore their chemical and physical properties (Davidovits 1991; Van Jaarsveld & Van Deventer 1999; Phair & Van Deventer 2001; Lloyd et al. 2010). For example, introducing  $K^+$  cations into Na-based activators can prevent the quick (uncontrollable) setting of fly ash paste at room temperature (Keyte 2008). However, considering the cost for industrial production, sodium based activating solutions are more commonly used.

NaOH and KOH solutions are effective in the synthesis of metakaolin- and slag-based geopolymers. However, when fly ash is used as raw material, NaOH or KOH activation needs a high curing temperature. Hou et al. (2007) reported that fly ash-based geopolymers synthesized respectively by activation with 5-15M NaOH and KOH solutions exhibited very low compressive strength after 14 d curing at room temperature. Only a few cases demonstrate NaOH and KOH solutions are suitable at room temperature (Fu et al. 2007; Álvarez-Ayuso et al. 2008).

In most cases, the alkaline activation solutions are a mixture of alkali hydroxide and alkali silicate solution. Using soluble silicate containing activator is more favourable for achieving high strength geopolymers (Palomo et al. 1999). This is partially because of the more compact microstructure and higher volume of gels,

either for metakaolin based geopolymers (Duxson et al. 2005; White et al. 2012). The Si/Al and Na/Si ratio of the gel phases should be changed and will have effects on the macroscopic properties (Duchesne et al. 2010). When soluble silicate is used in activator, the modulus,  $\text{SiO}_2/\text{M}_2\text{O}$  molar ratio, usually written as  $M_s$ , is important (Provis et al. 2012), and its relative effects on the microstructure and macroscopic properties have been examined (Criado et al. 2007; Hou et al. 2007; Rattanasak and Chindaprasirt 2009). A general trend of the effects on fly ash geopolymer is shown in Figure 2-4.



**Figure 2-4.** Contour plot of compressive strength data for sodium silicate activated fly ash geopolymers (Provis et al. 2009b).

#### 2.4.2.3 Curing conditions: room temperature or hydrothermal

The curing conditions used in geopolymer synthesis include ambient conditions (20-25°C) and mildly elevated temperature conditions (30-150°C). High pressure (Živica et al. 2011) and high vacuum (Davidovits 1982) conditions have been introduced, but are not widely used.

A study on the effects of curing temperature (10-80°C) and time (1-4 h) shows that the treatment of fresh alkali-metakaolin mixture at elevated temperatures accelerates the strength development, but that the 28 day strengths of heat-treated binders are lower than in mixtures that are treated at ambient or slightly decreased temperature (Rovnaník 2010). This is probably because of the restrained reaction extent of metakaolin at high temperature. A recent study of the reaction kinetics and thermochemical show that elevating reaction temperature from 20°C to 40°C accelerates the reaction rate, however, the final reaction extent is higher at 20°C, particularly for low alkali system (Zhang et al. 2012a). On the other hand, elevated temperature curing is preferred for fly ash-based geopolymer due to the relatively lower reactivity of most fly ashes compared with metakaolin as discussed above. Table 2-4 lists some typical curing procedures used in laboratory preparation of fly ash-based geopolymers. It should be highlighted that curing under sealed and covered conditions

appears critical for high strength achievement.

**Table 2-4:** Typical curing procedures used in fly ash (FA) based-geopolymer preparation in the laboratory

Materials (mass %)	Curing procedures	Property description	Ref.
100% FA	85°C ×(5 h-7 d)	1) Prolonged curing time improves strength 2) Sealed curing prevents initial carbonation and is helpful for high strength	Criado 2005
100% FA	I: 25°C ×(16-676 h) II: 40°C ×(72-168 h) III: 60°C ×(16-120 h) IV: 85°C ×(1-6 h)	1) Reaction extent increases with curing time, and 85°C ×6 h reaches a extent similar to 25°C ×100 h 2) Strength of K-based geopolymer decreased as curing temperature increases	Andini 2008
100% FA	I: 20°C ×21 d; II: 70°C ×24 h+20°C ×7d	1) Using milled FA greatly improves strength 2) The strength of products by method I is lower than that by method II	Temuujin 2009a; 2009b
85 wt.% FA +15 wt.% Kaolin	(30/50/70°C)×(6-48 h)	1) Increasing temperature is helpful 2) Prolonging curing from 6 to 24 h gives strength increase 3) 48 h curing at elevated T is too long	Van Jaarsveld 2002
FA + Silica fume	I: 95°C covered×8h; II: 95°C×2h covered +150°C ×6h dry oven; III: 95°C×2h covered +95°C ×6h steam	1) I: 50-102 MPa; 2) II: 28-57 MPa; 3) III: 36-76 MPa	Kovalchuk 2007
FA + Ground slag	I: 27°C ×28d; II:27°C ×48h+60°C×4h	1) Increasing slag content from 0 to 50% results in higher strength 2) Strength of geopolymer containing 50% slag increases from 30 MPa (method I) to 45 MPa (method II)	Kumar 2010

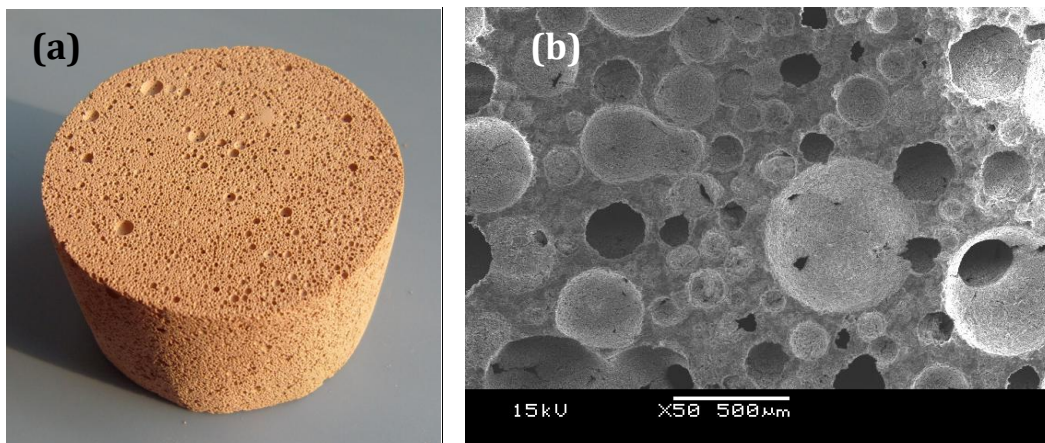
## 2.4.3 Geopolymer foam concrete technology

### 2.4.3.1 High temperature sintering method

Metakaolin-based geopolymer possesses high shrinkage when exposed to dry oven conditions (Zuhua et al. 2009b) or heating (Kong et al. 2007). To avoid microscopic and macroscopic cracks of geopolymers, so as to make geopolymer suitable for refractory applications, Bell and Kriven (2008) developed two geopolymer foams using H<sub>2</sub>O<sub>2</sub> and Al powder as foaming agents respectively.

The H<sub>2</sub>O<sub>2</sub> geopolymer foam was prepared by mixing 0 to 1.5% H<sub>2</sub>O<sub>2</sub> solution into a metakaolin-based mixture with composition of K<sub>2</sub>O·Al<sub>2</sub>O<sub>3</sub>·4SiO<sub>2</sub>·11H<sub>2</sub>O, which is known to convert to refractory leucite (KAlSi<sub>2</sub>O<sub>6</sub>) glass-ceramics on heating above 1000°C. The Al geopolymer foam was prepared by adding 3.0-5.0 μm sized spherical Al powder to the geopolymer paste. Both of these foams were cured at 200°C, starting from a moderate pressure (1.5-4 MPa) and ending at a high pressure (~12 MPa). The results showed that H<sub>2</sub>O<sub>2</sub> geopolymer foams had high compressive strength (44 - 77 MPa) but could not be converted to glass-ceramic since they cracked upon heating (1200°C for 3 h), while the Al geopolymer foams were successfully converted to crack-free ceramics on heating. One issue for the Al geopolymer foams was the high level of Al powder addition (60% by weight to geopolymer binder) and the difficulty in controlling its dissolution at high curing temperature.

Zhao et al. (2010) synthesised a geopolymer foam using fly ash and sheet glass powder as solid materials, and a compound of sodium dodecyl benzene sulfonate and gluten as foaming agent. The basic steps for making this geopolymer foam include preparing the foamed binder, shaping (with a short activation reaction to get initial strength) and drying at 105°C for 12 h, then sintering at 1050°C for 2 h. The appearance and pore structure of the sintered geopolymer foam are shown in Figure 2-5. The pore structure seems homogeneous in a millimetre range. In addition to quartz and mullite phases, anorthite (CaAl<sub>2</sub>Si<sub>2</sub>O<sub>8</sub>) was formed after sintering, which was thought to be the main reason for the high strength achieved. An example specimen was synthesised with 13 wt.% foam, and exhibited 6.76 MPa compressive strength and 0.414 g/cm<sup>3</sup> apparent density.



**Figure 2-5.** (a) Digital photograph of sintered geopolymer foam, and (b) an SEM image of the pore structure of sintered product. Original figures were provided by Zhao et al. (2010) and are acknowledged.

Several geopolymer foams have been shown in a report by Davidovits (2002) but without detailed foaming or synthetic information. According to the appearance (white and red colour) and application purposes (furnace insulation), those geopolymer foams may also be of the high temperature synthesised (sintered) type. Self-foamed or in situ foaming of high silica

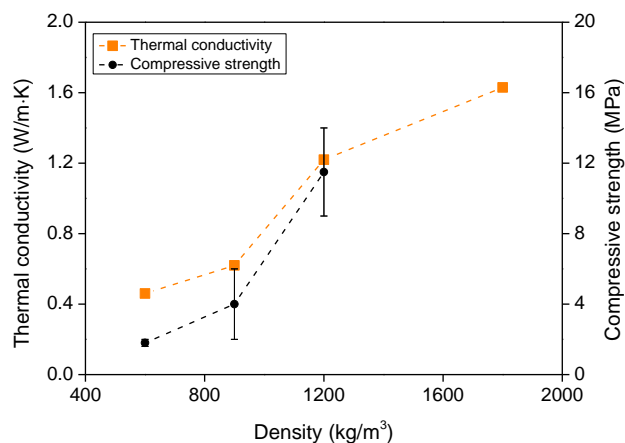
geopolymer systems ( $\text{Si}/\text{Al} > 24$ ) was reported due to the removal of the hydration water at temperatures of 100 - 300°C (Fletcher et al. 2005). Geopolymer foam gravels synthesised by the in-situ foaming method were found to possess much higher strength and water resistance than comparable silica gel foams (Buchwald et al. 2010).

#### 2.4.3.2 Low temperature mixing method

The high temperature (sintered) geopolymer foams have a relatively homogeneous void structure and high strength/density ratio, but it is more reasonable to describe them as porous ceramics rather than concrete. These products can feasibly be used as construction materials to replacing existing ceramic tiles, clay bricks and blocks, however, for very high-volume construction purposes, ambient temperature or slightly-elevated temperature synthesised products are more energy efficient and cost effective, and thus more attractive to industry.

- *Chemical foaming technique*

Arellano Aguilar et al. (2010) reported geopolymer foam concretes based on metakaolin binders and Al powder as gas-releasing agent. When blast furnace slag sand was required as aggregate, it was incorporated in a wet state, and added at the end of the mixing. Al powder was added at the end of mixing. Two curing conditions were used, 20°C×24 h and 75°C×24 h, followed by continued hardening at 20°C. The pores in the hardened products are in a millimetre scale. Figure 2-6 shows the thermal conductivity and the compressive strength as a function of density. The high measured thermal conductivity is because the measurement was conducted on as-cast samples, not oven-dried. The 28 d compressive strength varies from 1.3 to 14.5 MPa with mixture densities of 600-1200 kg/m<sup>3</sup>. Replacing metakaolin with 25 wt.% fly ash has some positive influence on strength, while using slag particle as aggregate seems negative in this respect.

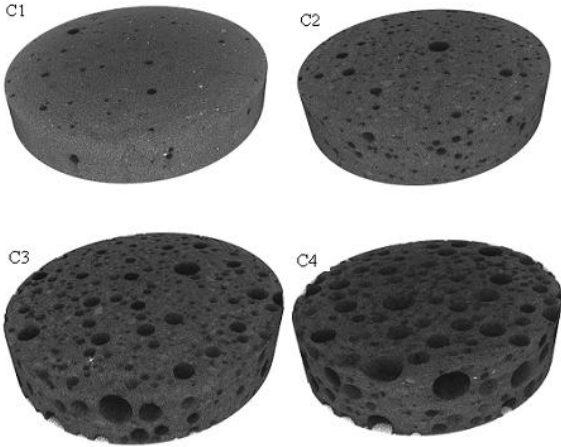
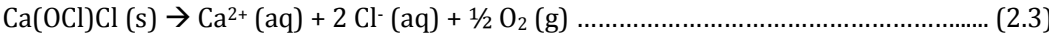


**Figure 2-6.** The thermal conductivity and compressive strength of metakaolin-based foam geopolymers (air dried). (Arellano Aguilar et al. 2010).

Kamseu et al. (2012) also developed metakaolin-based geopolymer foams with a

liquid/metakaolin ratio of 0.6, and the addition of Al powder foaming agent from 0 to 20 mg per 100 mL of activator, resulting in porosities from 30 to 70 vol.%. The appearance of metakaolin geopolymer foams and solid geopolymer are shown in Figure 2-7. An appropriately high Si/Al ratio, >1.79, was required to achieve a fine and homogeneous pore structure (Kamseu et al. 2012). The foams have much lower thermal conductivity (0.15-0.4 W/m·K) than the solid geopolymer (0.6 W/m·K). The thermal conductivity of solid binder was found to increase with increasing Si/Al ratio (Kamseu et al. 2011), which is consistent with previous research (Duxson et al. 2006a), and is related to increased connectivity, reduced porosity and finer pore size distribution as Si/Al ratio increases.

Using hypochlorites (NaOCl and Ca(OCl)Cl) as foaming agents were reported recently (Nyale et al. 2013; Birch 2012). The foamed geopolymer products were manufactured by adding a foaming agent in a ready-mixed geopolymer paste and setting at elevated temperatures (60-90°C) for hydrothermal curing and foaming. The foaming is based on the decomposition of the foaming agents:

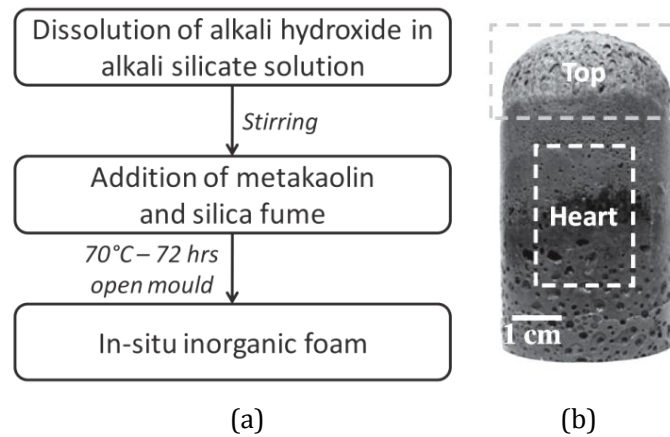


**Figure 2-7.** Geopolymers foamed with different Al powder contents: C1, C2, C3 and C4 contain 5, 10, 15 and 20 mg Al powder per 100 mL activator respectively; the binders contain Si/Al=2.0; C4 produces about 70 vol% porosity; the diameter of the cylinder is 18.85 mm. All specimens cured at room temperature. Original photographs were provided by Kamseu et al. (2012) and are acknowledged.

- *Silica fume in situ foaming technique*

Recently, Prud’homme et al. (2010) have proposed a low temperature in situ foaming method by adding silica fume into a geopolymer reactant mixture and cured at 70°C. The typical synthesis protocol of the in situ geopolymer foams includes alkali activator dissolution, stirring with metakaolin and silica fume and curing. In the sealed curing period, free silicon from the silica fume will be oxidized by water, releasing hydrogen gas, i.e.  $4\text{H}_2\text{O} + \text{Si}^0 \rightarrow 2\text{H}_2 + \text{Si(OH)}_4$ . During

the period when the geopolymer gels are growing and setting, the released gas is immobilised and thus high porosity is obtained. Figure 2-8 shows the synthesis procedures and a foam sample.



**Figure 2-8.** Synthesis protocol of in situ mineral foam (a) and photography of the synthesized foams (Delair et al. 2012).

The alkali activator solution type and concentration, clay type, silica fume and curing period will have effects on the foaming efficacy and also the properties of resultant geopolymer foams. For examples, increasing K/Al ratio from 0.65 to 1.73 by using more KOH, the foaming efficiency (final volume/initial volume) increases (Prud'homme et al. 2010); geopolymer foam derived from a  $K^+$  based activator is more easy to dissolve or degrade compared to that derived from  $Na^+$  based activator in contact with water (Delair et al. 2012).

By comparing the infrared spectra before and after reaction and the appearance of the four samples, metakaolin was seen to exhibit a higher reactivity and results in a more homogeneous sample than kaolin, illite or montmorillonite, which are also able to be used as precursors for in situ geopolymer foam synthesis (Prud'homme et al. 2011).

The curing temperature and time are both very important in pore size control, and thus determine the homogeneity of the structure as a whole. It was suggested that curing at  $70^\circ\text{C} \times (1-1.5) \text{ h}$  followed by  $23^\circ\text{C} \times 20 \text{ d}$ , or  $55^\circ\text{C} \times 9 \text{ d}$ , is helpful to control the pore size in a range around 1 mm (Henon et al. 2012). However, in comparison with OPC foam concrete and Al-foamed geopolymers, the pore size and distribution of this kind of foam is too large, and this could be one reason for the low strength ( $\sim 1 \text{ MPa}$ ) of these materials (Gouny et al. 2012). Given that the thermal conductivity is only 0.22-0.24 W/mK (estimated value, as the product was too heterogeneous to be measured directly), it is possible that it can be used as a non-structural insulation material (Prud'homme et al. 2010).

- *Mechanical pre-foaming technique*

In addition to the above cases based on metakaolin, fly ash has been used to make geopolymer foam concrete. Al Bakri Abdullah et al. (2012) reported their research on geopolymer foam concrete based on a Class C fly ash (CaO content

21.6 wt.%), synthesised by mixing pre-formed foam into the geopolymer mixture at a 2:1 volume ratio, and cured at two different conditions: room temperature and 60°C × 24 h + room temperature. The heat-cured products exhibited higher early strength as expected, but equal density (1650-1667 kg/m<sup>3</sup>), pore structure and 28 d strength (18 MPa) compared to those which were not heated.

Overall the development of geopolymer foam concrete is a relatively new field. Only limited information has been reported regarding the relationship between composition, structure and properties of such new materials.

#### **2.4.4 Perspectives for of geopolymer foam concrete**

##### **2.4.4.1 Environmental footprint of production and operation**

The environmental benefits of geopolymer foam concrete mainly lie in the sustainability of geopolymer production compared to OPC manufacturing, including lower resource and energy requirements and lower CO<sub>2</sub> emissions, as discussed in Section 2.2.2.

Apart from the sustainability aspects of the geopolymer binder, the synthesis conditions and foaming agents are also important factors affecting the environmental footprint of production. As discussed above, if geopolymer foam is synthesised by a sintering process (Bell and Kriven, 2009; Zhao et al. 2010), the environmental footprint of the product may be not comparable to OPC foam concrete, due to the high energy requirements associated with sintering. When aluminium powder and silica fume are used as foaming agents at high dosages (Bell and Kriven 2009; Prud'homme et al. 2011), much of the environmental benefit will be lost, and the material may become less 'green' than OPC foam concrete, due to the very high embodied energy of these materials. However, if a much lower dose of a metallic foaming agent is used, e.g. 0-20 mg Al powder per 100 mL activator (Kamseu et al. 2012), the foaming process will not have a severe impact on the environmental footprint of material production.

Finally, if the curing process takes place at room temperature or at a slightly elevated temperature (40 to 90°C) for a short time (<24 h), it does not require notably more energy in comparison with the curing of OPC foam concrete at room temperature, and potentially less than autoclaving conditions (usually ~180°C (Neville 2011)). Hence, it is suggested to use either a low dosage of foaming agents, or a preformed foam, to develop geopolymer foam concrete with optimised environmental advantages.

Moreover, using this new material will save operational energy due to its relatively lower thermal conductivity than normal weight concrete, as discussed in the preceding sections. Low thermal conductivity can reduce indoor temperature variations, thus reducing the energy requirements associated with heating and cooling. The exact reduction of operational energy is difficult to estimate within the scope of a review such as this because it depends on many other factors, for example climate, building design, mode of utilisation (residential, commercial or other), and building orientation. However, for

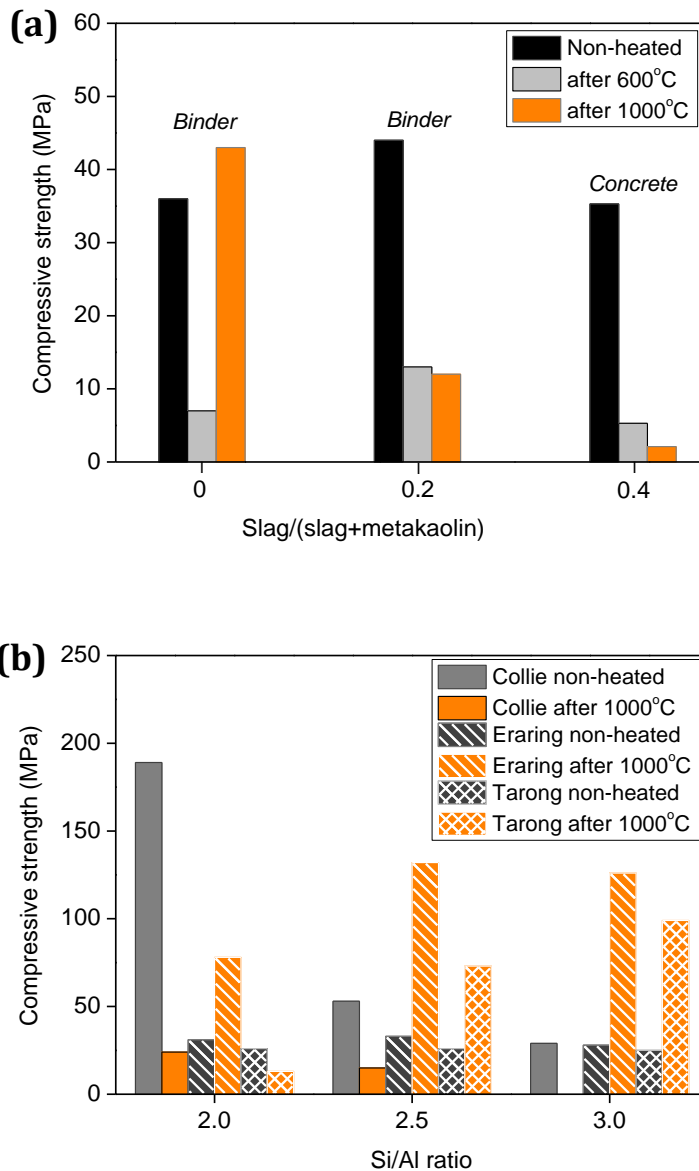


insulation or semi-structural applications, low thermal conductivity and low unit weight are generally considered beneficial.

#### 2.4.4.2 Strength after exposure to high temperature

An important aspect of the selection of construction materials for residential and commercial applications is the ability to retain structural integrity during and after fire exposure. OPC hydration products degrade irreversibly at temperatures higher than 200°C due to the loss of 'non-evaporable water' and the decomposition of  $\text{Ca(OH)}_2$  and other hydrate products, associated with an increase in overall porosity (Piasta et al. 1984). Therefore, upon exposure to high temperature or firing conditions (>600°C), most OPC products will lose strength dramatically. The residual strength depends on many factors, such as the mixture proportioning (Chan et al. 2000; Aydın and Baradan 2007).

Unlike OPC products, geopolymers have been widely demonstrated to show high temperature stability. This aspect has been well reviewed in the recent literature (Pacheco-Torgal et al. 2012). Metakaolin-based geopolymer binders tend to decrease in strength gradually up to 800°C, while increasing in strength after 1000°C exposure (Kovalchuk & Krivenko 2009; Bernal et al. 2011); conversely alkali activated slag/metakaolin blend mortar and concrete tend to lose strength consistently after heating from 200 to 1000°C (Bernal et al. 2012). Volcanic ash-based geopolymer mortars also show an increase in compressive strength after heating at 900°C compared to 750°C (Lemougna et al. 2011), and fly ash-based geopolymers exhibit good strength maintenance after fire temperature exposure (Kovalchuk and Krivenko 2009; Rickard et al. 2011). Figure 2-9 shows the variation of compressive strength in some typical metakaolin, metakaolin/slag blend and fly ash-based geopolymers after high temperature exposure. It is noted that these are all post-cooling strength tests; the actual strength of the material during high-temperature exposure is also critical, but much less widely studied for either Portland cement or geopolymer materials.



**Figure 2-9.** Compressive strength of different types of geopolymers before and after high temperature exposure: (a) metakaolin/slag blend-based binder and concrete, data from (Bernal et al. 2011a; 2012); (b) binders derived from different fly ashes, data from (Rickard et al. 2011).

The mechanisms governing the strength variation may be different for different types of geopolymers. Studies of metakaolin-based geopolymers by using conventional infrared spectroscopy and X-ray diffractometry (Duxson et al. 2006b), and more recently by the X-ray pair distribution function (PDF) method (Bell et al. 2008a; Bell et al. 2008b; White et al. 2010b), have revealed the transformation of reaction products from amorphous to crystalline (usually anhydrous members of the zeolite family) at high temperatures at an atomic scale. Briefly, amorphous aluminosilicate gels lose free water below 200-300°C with negligible change in the structural framework. After heating above 200-300°C gels release chemically bound T-OH groups and condense to form T-O-T linkages, along with relocation of alkali cations, resulting in increased overall

connectivity.

The condensed gels start to crystallise at a certain onset temperature, which is influenced greatly by the composition, in particular Si/Al ratio and alkali cation type. Na-aluminosilicate geopolymer gel with Si/Al=1.15 forms nepheline upon heating to 650°C, and at 800°C with Si/Al=2.15 (Duxson et al. 2006a); K-aluminosilicate geopolymer gels form tetragonal leucite at 1000°C with a composition of  $\text{KAlSi}_2\text{O}_6 \cdot 4.78\text{D}_2\text{O} \cdot 0.72\text{H}_2\text{O}$  (White et al. 2010b) or 1050°C with a composition of  $\text{KAlSi}_2\text{O}_6 \cdot 5.5\text{H}_2\text{O}$  (Bell et al. 2008a); Cs-aluminosilicate geopolymer gels with Si/Al = 2.0 form crystalline pollucite above 1000°C (Bell et al. 2008b). In combination with the findings from thermal shrinkage measurements (Duxson et al. 2006a; Duxson et al. 2007), it is proposed that: 1) the large shrinkage along with the loss of free water could be the main reason for the loss of strength; 2) the shrinkage due to the release of chemically bound -OH and gel condensation at high temperature does not affect the strength to a major extent, and 3) the condensation of the gels to form glass and ceramics after onset temperature is the main reason for the post-cooling strength increase.

However, this may be associated with volume variation, and could also result in softening during exposure to the high temperature which could compromise in situ (pre-cooling) strength retention properties. The zeolite crystalline phases present in structure, either before or after high temperature exposure, may contribute to the good post-exposure strength, or the formation of dense glassy binder regions may also be important (Kovalchuk and Krivenko 2009; Kong et al. 2008; Rahier et al. 2007).

Fly ash-based geopolymers also generally show good retention of strength after high temperature exposure. The microstructures of these materials consist of geopolymeric gels, some zeolitic phases, and a large volume fraction of residual fly ash particles (Criado et al. 2007b). The intrinsic shrinkage properties of the gels may be similar to those derived from metakaolin; however, the total shrinkage of the material is much less due to the lower gel fraction. The linear shrinkage is reported to be -6% to +15% (Rickard et al. 2010; Provis et al. 2012), which is much smaller than in metakaolin-based geopolymer, which may shrink as much as -20% (Duxson et al. 2006a; 2007).

The residual fly ash particles are high temperature products, which can remain stable under high temperature exposure. The presence of mullite and other thermally stable crystalline phases is believed to be important, as evidenced by the good thermal stability of a model geopolymer synthesised with an anorthite filler (Nair et al. 2007). The tendency towards being more ready to crystallize, or undergo ceramization, brings some beneficial effects related to residual strength, although the higher levels of iron in some fly ashes can also act as a flux.

Similar to metakaolin-based geopolymers, there are also many factors influencing the thermal stability of fly ash-based geopolymers, such as Si/Al ratio, alkali type and the nature of fly ash. A potential crystallisation-strengthening effect is observed (Rashad et al. 2011). Figure 2-9(b) shows that the fire resistance depends on the fly ash source. The Eraring and Tarong fly

ashes both contain higher mullite contents than Collie fly ash (Rickard et al. 2011). The strength loss of Collie geopolymer is probably due to the high content of iron oxides, which affect the thermal properties of the geopolymer by influencing thermal expansion, altering the phase composition, and changing the morphology after heating (Rickard et al. 2010).

The discussion above shows that geopolymers derived from fly ashes have particularly high temperature resistance. By selecting suitable fly ash and optimising the geopolymer gel Si/Al ratio and other parameters, it is practical to develop geopolymer foam concretes. They can be used in construction of buildings which require high temperature or fire resistance properties which organic foams or OPC foam concretes are not able to meet. The fact that some fly ash geopolymer concretes can even increase in strength following high-temperature exposure (Fernández-Jiménez et al. 2008) indicates that geopolymer foam concretes may have the potential of gaining structural value once exposed to fire. This unique property will potentially endow geopolymer foam concrete with applications in new markets.

## ***2.5 Challenges in developing geopolymer foam concrete***

Bringing geopolymer materials into the market is itself a process with many technical and industrial barriers, for example, the questions around durability and the lack of tailored standards (Van Deventer et al. 2012). Moreover, fabricating foam geopolymer concretes is not a simple copy of the existing OPC foam concrete production process. There are some existing and potential challenges, as detailed below.

### **2.5.1 Understanding of feedstock physics and chemistry**

Normal OPC foam concrete can be synthesised with Portland cements or blended cements, which are all standardised products. To synthesise geopolymer foam concrete, a reactive aluminosilicate material is required. There are many aluminosilicate containing minerals and industrial wastes which can be used as raw materials, but none of them is available in large quantities as a closely quality-controlled, consistent, standard product for geopolymer production. Clays and fly ashes appear to be two highly promising source materials. In comparison with clays, fly ash is probably more technologically suitable as it requires less alkaline activator while providing good workability.

However, fly ash particles are substantially heterogeneous in physical and chemical properties: inter-particle speciation (different particles in a sample) consists of glass-rich spherical particles, iron-rich particles and quartz particles in some cases, while intra-particle speciation (different parts within one fly ash particle) consists of aluminosilicate glass, mullite, quartz, magnetite and hematite (Ward and French 2003; Rickard et al. 2011; Keyte 2008). As shown in Figure 2-9(b), the composition and mineralogy of fly ash, for instance the content of iron oxides (Rickard et al. 2011), have marked effects on the high temperature performance of geopolymers. Additionally, fly ashes from different sources can lead to materials with quite different setting behaviour (Diaz-Loya et al. 2011). This will affect the pore structure, no matter whether the voids are

introduced by gas-releasing agent or pre-formed foam. Unfortunately, there is very limited specification regarding feedstock utilisation in geopolymer synthesis at present.

### **2.5.2 Differences between solid and foamed geopolymers**

From a chemical perspective, when gas-releasing agents and pre-foaming chemicals are introduced in the geopolymerization systems, their influences on the phase evolution of the binder are unknown. For example, Al powder is a commonly used gas-releasing agent in OPC foam concrete, and it has also been trialled in geopolymer foam concrete (Arellano Aguilar et al. 2010; Kamseu et al. 2012). The dosage and reactivity (fineness, surface treatment) of Al powder will influence on the geopolymer formation on atomic and nanostructural levels, as it releases soluble aluminates while evolving H<sub>2</sub> gas, and controlling the timed availability of aluminates is important in successful geopolymer synthesis (Hajimohammadi et al. 2010). However, the effects of Al powder and its hydrolysis products on geopolymerization kinetics, and the effect of high Al content on high temperature performance of geopolymers, remain to be further studied. It is noted that when prefoamed foams formed by an organic foaming agent are used in a geopolymer binder, a large volume of foam is required (Al Bakri Abdullah et al. 2012), as the air bubbles tends to collapse in mixing due to the high viscosity of the paste, which means the foaming efficiency is not high.

From a microstructural perspective, the difference between solid geopolymers and foamed geopolymers is also significant. Although a number of studies have examined the pore structure of OPC foam concrete as well as its influence on the mechanical and thermal insulation properties of the material, a good understanding of the effects of pore structure in geopolymer foam concretes has not yet been presented. Work aimed at revealing the phase and microstructural differences between solid and foamed geopolymers is still necessary.

## **2.6 Concluding remarks**

As a whole, the application of geopolymer materials in the construction industry is progressing relatively rapidly in some parts of the world, and more gradually in others. Development of geopolymer foam concrete may avert some considerations regarding durability aspects of geopolymer concretes, as such materials are usually used for non-structural purposes, and the introduction of this new construction material into market will also open new avenues for geopolymer use in niche applications.

The environmental advantages and high temperature strength of geopolymer foam concrete over OPC foam concrete have been discussed in detail in this review. The process of understanding feedstock mineralogy and chemistry, and thus building up a relevant database of specifications/standards, is an important step in enabling consistent formulation of optimal mixture compositions from locally-available materials, so as to control the consistency and properties of geopolymers. This is important in establishing a dedicated geopolymer feedstock supply chain, for dense as well as foam geopolymer concretes.

Considering the increasing demand for sustainable concrete in today's construction and housing industry, as well as the foreseeable advantages of geopolymer technology, future studies are necessary to understand the relationships between properties and structure of foam geopolymer concrete, and to clarify the most likely problems or issues involved in the manufacturing of these products, such as the selection of suitable fly ashes for different mixtures, and the durability of the products.

## Chapter 3: Research Plan and Methodology

### 3.1 Introduction

From the review in the last chapter, it is apparent that one of the challenges for GFC manufacture is the selection of suitable solid materials. This is particularly relevant for fly ashes which are extremely heterogeneous. A further issue is that the differences between solid geopolymer manufacture and geopolymer foam are unclear. Understanding feedstock mineralogy and chemistry, and building up a relevant database of specifications/standards, are important in enabling consistent formulation of optimal mixture compositions from locally-available materials, so as to control the consistency and properties of geopolymer products.

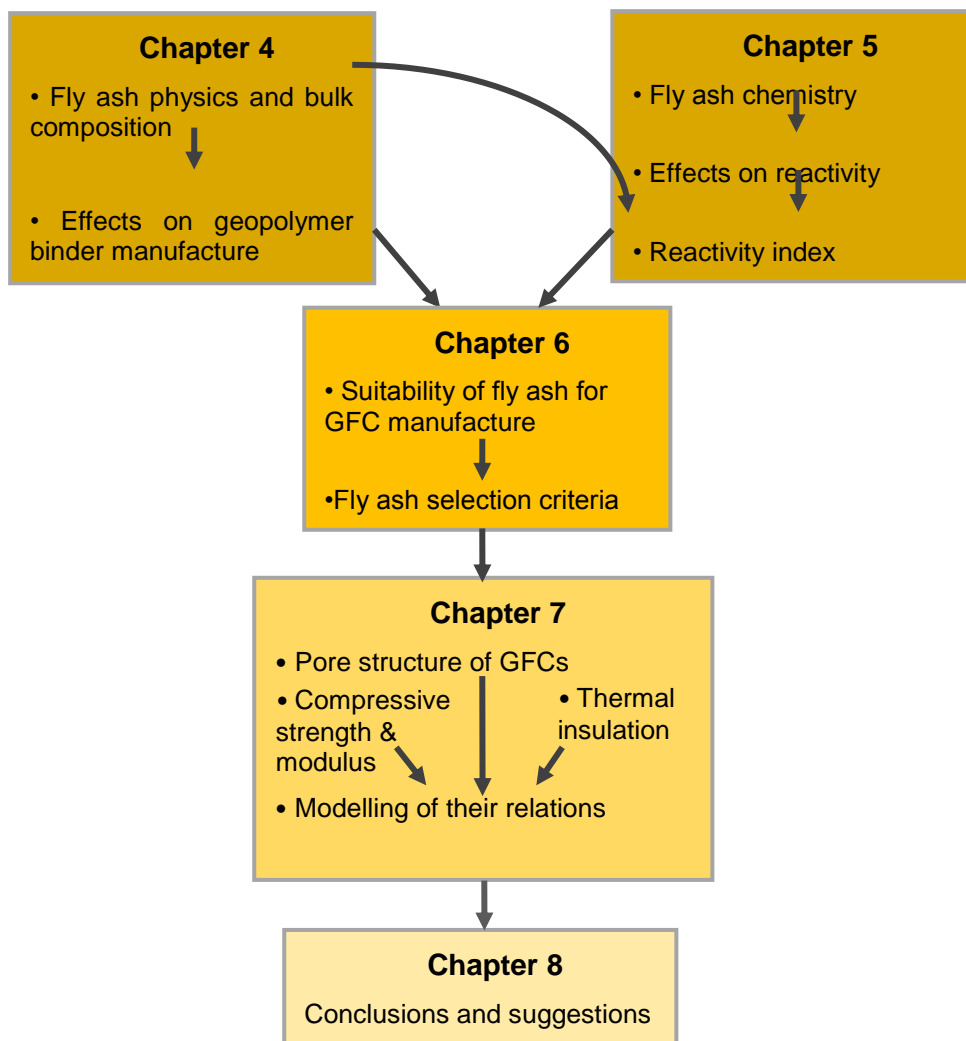
This chapter describes the research plan and methodology in this thesis. In the following sections, and the following chapters, the term *geopolymer* is used to describe any hardened binders manufactured under laboratory conditions by the alkali activation of *solid materials*. The *laboratory conditions* refer to 20-25°C (also called '*room temperature*'), RH=40-60% and normal pressure. The *alkali activating solutions* refer to the aqueous sodium hydroxide solutions and/or sodium silicate solutions. The *solid materials* refer to the solid, predominately amorphous materials that are generally in a powder form. In this research the solid materials includes coal fly ashes and ground granulated slag. It should be noted that no fine aggregates (such as river sand that are usually used in normal foam concretes) have been used in the manufacture of the GFCs in this project. The *GFC paste* is used to describe the foamed mixture before solidifying.

### 3.2 Research flow chart

This research is intended to answer some of the current challenges in GFC manufacture. The aims of this project include:

- (1) characterization of the physical properties of the selected fly ashes from different sources and to study their nature affecting the geopolymer properties;
- (2) investigation of the glass chemistry in the fly ashes and correlation with their reactivity;
- (3) investigation of the suitability of fly ashes for GFC manufacture and identification of the main factors that affect the quality of GFCs, in term of segregation and mechanical properties;
- (4) development of relevant models relating the properties of GFCs.

The flow chart in Figure 3-1 provides an overall schematic of the research.



**Figure 3-1.** Research flow chart of this thesis.

There is no doubt that the knowledge obtained in this study will form an important contribution to geopolymer science and technology. A better understanding of the relationships between the properties and structures of GFCs will fill a research gap between solid and foamed geopolymers. The following sections describe the materials and methods used in the research.

### **3.3 Materials**

#### **3.3.1 Alkali activating solutions**

Alkali activating solution is a key ingredient in geopolymer manufacture. This is not only because it provides a strong alkaline reaction medium for the solid materials, but also because it is the major cost. Different types of alkali activating solutions generate the geopolymers with different phases,



microstructures and mechanical properties (Fernández-Jiménez and Palomo, 2005). The economic and environmental costs are heavily dependent on the type and quantity of the activating solutions used in manufacture (McLellan et al. 2011).

It has been demonstrated in many studies that both sodium and potassium based alkali activators are effective in geopolymer synthesis (Duxson et al. 2005; MacKenzie et al. 2010; Somna et al. 2011; Pimraksa et al. 2011). The presence of potassium in activating solutions was reported to be able to increase the compressive strength of geopolymers, higher than those synthesized with single sodium based activating solution at the same concentration of alkali cations (Keyte, 2008). However, after consultant with industry and considering the cost for industrial production, sodium based activating solutions were selected for use in this research.

Granular sodium hydroxide with purity >99% was supplied by the Formosa Plastics Group (Taiwan). It was dissolved in water to make NaOH solutions with concentrations of 8, 10 and 14 mol/L and allowed to cool to room temperature (20-25°C). D-Grade™ liquid sodium silicate solution (LSS) was supplied by PQ Corporation (Australia), and the composition is provided in Table 3-1. To modify the SiO<sub>2</sub>/Na<sub>2</sub>O ratio of activator solution and also the concentration, the 12mol/L NaOH solution was mixed with the sodium silicate solution at a mass ratio of 0.646 to achieve a SiO<sub>2</sub>/Na<sub>2</sub>O = 1.0 and allowed to equilibrate at room temperature for at least 24 h prior to use.

**Table 3-1:** D-Grade™ sodium silicate specifications.

Liquid Sodium Silicate	D-Grade™
SiO <sub>2</sub> (wt.%)	29.4
Na <sub>2</sub> O (wt.%)	14.7
SiO <sub>2</sub> /Na <sub>2</sub> O mass ratio	2.00
SiO <sub>2</sub> /Na <sub>2</sub> O molar ratio	2.06

### 3.3.2 Solid materials

#### 3.3.2.1 Fly ash

One of the objectives of this project was to beneficially utilize fly ash as a solid material for GFC manufacture. Fly ash is a historical solid waste or a by-product of coal fired power stations, and has become a commercial product mainly for use in the cement and concrete industry throughout the world. Fly ash can also be used as secondary raw material in a variety of products, such as adsorbents for cleaning of flue gas and removing of toxic inorganic/organic compounds from wastewater (Ahmaruzzaman 2010). The largest consumer of fly ash is the cement and concrete industry, where fly ash is used as (1) replacement of cement in Portland cement concrete (2) pozzolanic material in the production of pozzolanic cements, and (3) set retardant ingredient with cement as a replacement of gypsum (Ahmaruzzaman 2010). The advent of cementitious,

high-lime fly ash has permitted cement replacements of 25–40% and up to 75% for parking lots, driveways and streets. High-volume fly ash concrete has long been recognized as a construction material (Haque et al. 1984). This type of concrete contains more than 50% of fly ash by mass of total cementitious materials. One of the benefits of replacement or addition of fly ash in cement and concrete is that it can reduce the hydration heat of cement, which is the main reason for shrinkage of large concrete structures such as dams and airport pavements.

Although fly ash is reported to have been 100% utilized in some countries, such as Denmark, Italy and the Netherlands, there still remains huge quantities of fly ash disposed of in ash ponds and landfills, particularly in developing countries. In China, it is reported that the annual production of coal ash (including bottom ash) is 200–300 million tonnes and the accumulated amount of fly ash exceeds 2500 million tonnes (Wang and Cui 2007). The utilization level is lower than 70% (Cao et al. 2008). In India, the total utilization of fly ash in 2011 was around 30 million tonnes (about 28%), of which the cement and concrete industry accounts for 50% (Alam and Akhtar 2011). There is a long history of fly ash use in Australia, however, the utilization rate is still very low: 9 percent of 8.1 million tonnes was used in 1991 and 32 percent of 12.5 million tonnes in 2002 (Heidrich 2003). The low utilization rate is mainly due to the low reactivity of the fly ash.

Table 3–2 presents the composition of 10 typical fly ashes generated in the power stations around Australia (Heidrich, 2003). The majority of fly ashes are categorised as Class F according to ASTM C618 – the sum of Al<sub>2</sub>O<sub>3</sub>, SiO<sub>2</sub> and Fe<sub>2</sub>O<sub>3</sub> is higher than 70 mol%. Class F fly ash contains much less calcium (usually < 10%) than Class C.

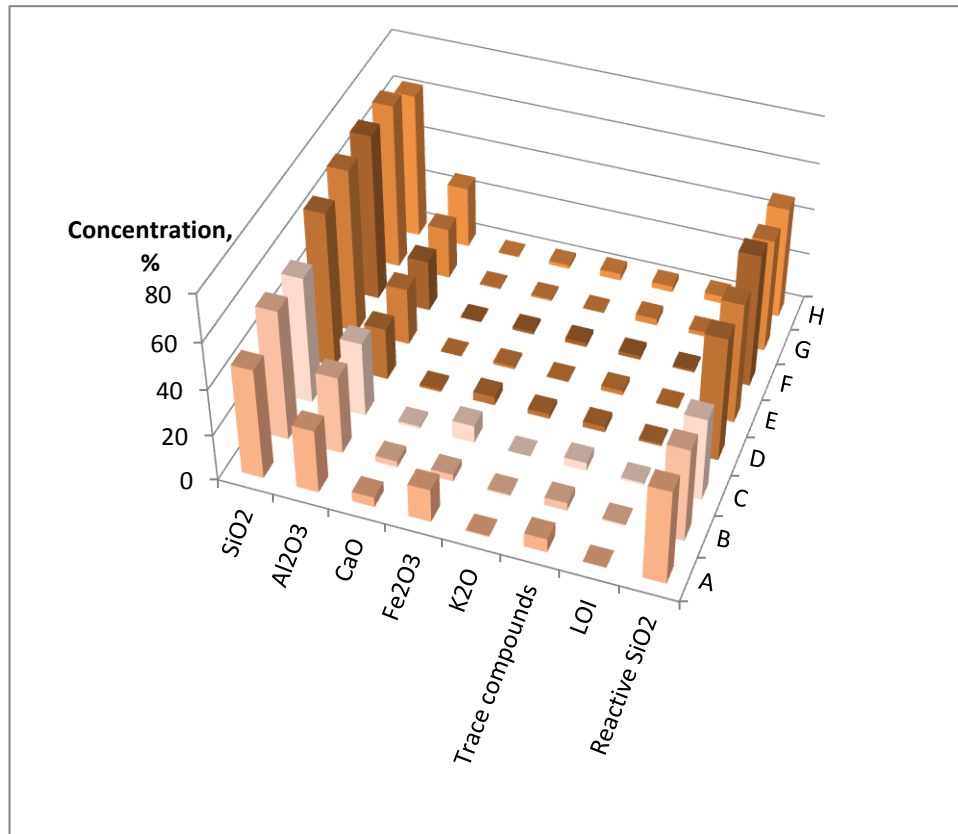
**Table 3–2:** Chemical compositions of 10 fly ashes generated in Australian power stations, wt.%. LOI is loss on ignition. Data from (Heidrich 2003).

Fly ash	SiO <sub>2</sub>	Al <sub>2</sub> O <sub>3</sub>	Fe <sub>2</sub> O <sub>3</sub>	CaO	MgO	Na <sub>2</sub> O	K <sub>2</sub> O	SO <sub>3</sub>	LOI
No.1	58.0	26.5	3.2	1.6	0.9	0.4	0.4	0.1	3.0
No.2	56.7	26.7	5.0	1.1	0.9	0.4	1.3	0.1	3.5
No.3	63.2	27.4	1.0	0.2	0.2	0.6	2.2	0.2	10.0
No.4	69.2	21.8	3.5	1.2	0.7	0.5	1.4	0.1	1.3
No.5	58.6	28.5	6.3	1.6	1.0	0.3	1.2	0.7	1.3
No.6	65.0	23.0	5.0	0.2	0.3	0.4	1.8	0.2	1.3
No.7	59.0	26.4	3.3	5.9	1.8	3.7	0.7	0.1	0.2
No.8	48.1	30.3	12.2	3.2	1.5	0.4	0.5	0.2	2.0
No.9	62.4	26.8	1.9	1.6	1.1	1.0	0.7	0.3	2.1
No.10	71.0	24.9	0.7	0.1	0.2	0.1	0.4	0.0	1.1
Mean	61.1	26.2	4.2	1.7	0.9	0.8	1.1	0.2	2.6
Std Dev	6.62	2.48	3.31	1.74	0.54	1.05	0.62	0.19	2.78

There is not a particular specification or standard that indicates which kind of fly ash is best suitable for geopolymer manufacture. This is because of the significant differences between these solid materials. Diaz–Loya et al. (2011)

studied the mechanical properties of geopolymer concretes made from 25 different fly ashes collected from different power stations located across the USA. The results showed that geopolymer concretes derived from Class F fly ashes had an average compressive strength of 36.2 MPa while a higher average strength of 50.3 MPa was obtained for concretes derived from Class C fly ashes. The average activator solution to fly ash ratio was also noticed a slightly higher for Class F fly ash. However, even with the lower strength, the utilization of Class F fly ash for geopolymer production brings the benefit of consumption of solid wastes.

In this research, 8 commercially available Australian Class F fly ashes were investigated to determine the oxide compositions, particle size and their reactivity in geopolymer manufacture. The individual names of the 8 fly ashes are not given in this thesis due to intellectual property issue. They are denoted as A, B, C... throughout the thesis. Figure 3-2 shows the chemical composition of the 8 fly ashes as determined by XRF and their reactive  $\text{SiO}_2$  contents as determined by wet chemical method. The relevant testing methods used in their determination will be described in the following sections.

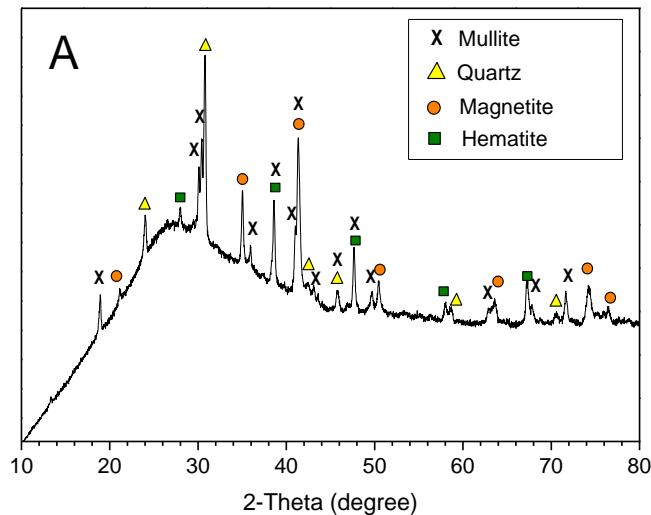


**Figure 3-2.** The chemical compositions and reactive  $\text{SiO}_2$  contents in the 8 collected fly ashes.

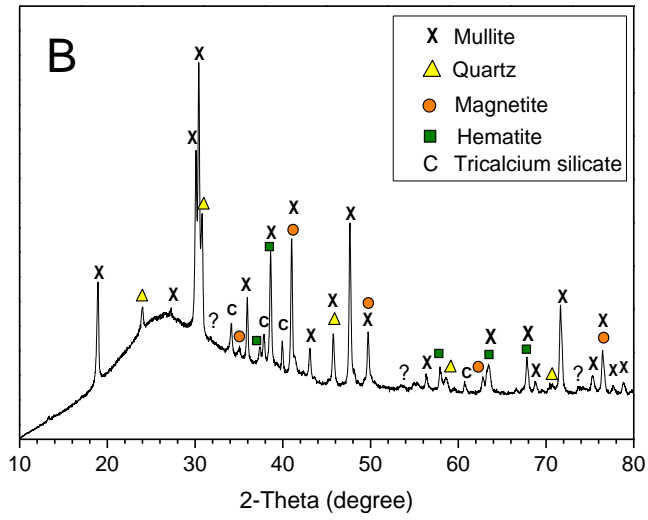
After a preliminary investigation of the compressive strength of the derived geopolymers (not reported here), five fly ashes (A, B, C, D, E) were then selected for further investigation as their derived geopolymers exhibited a good broad in compressive strength. The physical and chemical properties of the selected five fly ashes are expected to have significant effects on the final phases and structures of the geopolymer binders. A comprehensive understanding of the

factors determining the reactivity is fundamental for the valorisation of low calcium fly ash in geopolymer manufacture (Provis et al. 2009b).

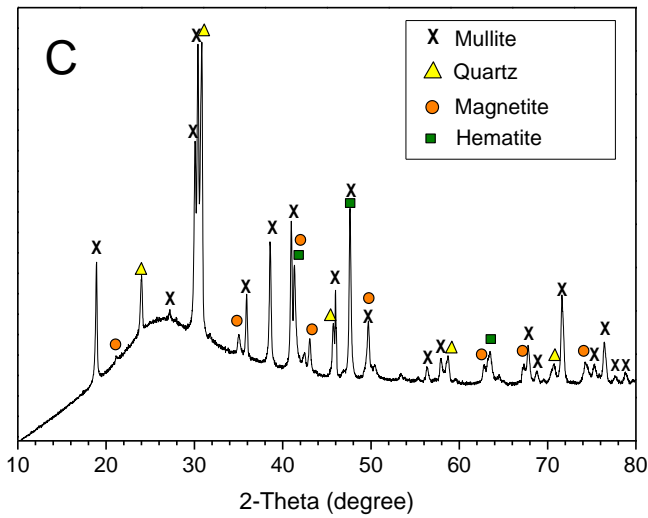
Figure 3–3 shows the Co K $\alpha$  radiation XRD patterns of the five selected fly ashes. The XRD patterns presented in this thesis all refer to Co K $\alpha$  radiation patterns. The XRD testing procedures will be described in Section 3.2.1. Beside the main amorphous content, the crystalline phases present in these fly ashes include mullite, quartz, magnetite and hematite. Different fly ashes from different source stations usually have mullite crystal with different composition, even for the fly ashes from the same station but different batches (time). An example is that the fly ash from Tarong power station (Queensland) contains a mullite of Al<sub>6</sub>Si<sub>2</sub>O<sub>13</sub> as characterized by Keyte (2008) and Al<sub>4.56</sub>Si<sub>1.44</sub>O<sub>9.72</sub> as characterized by Rickard et al. (2011). More physical and chemical properties of the five fly ashes, including the particle size, morphology and particle density will be shown and discussed in Chapter 4.



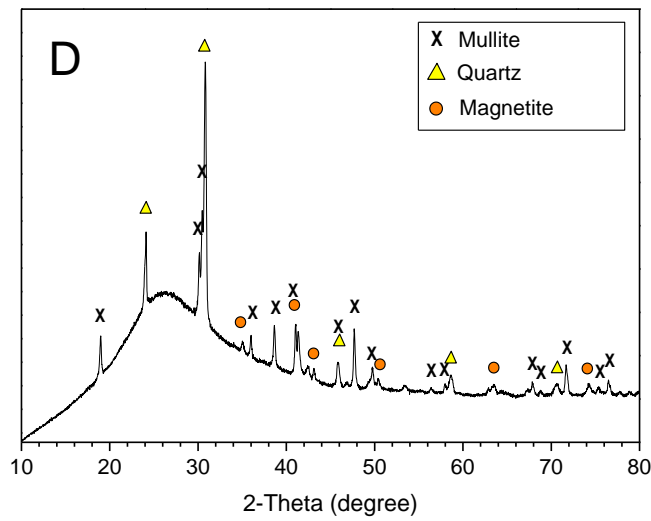
(a) Mullite, Al<sub>4.75</sub>Si<sub>1.25</sub>O<sub>9.63</sub> (ICSD# 66448); Quartz, SiO<sub>2</sub> (ICSD# 89280); Magnetite, Fe<sub>3</sub>O<sub>4</sub> (ICSD# 43001); Hematite, Fe<sub>2</sub>O<sub>3</sub> (ICSD# 15840).



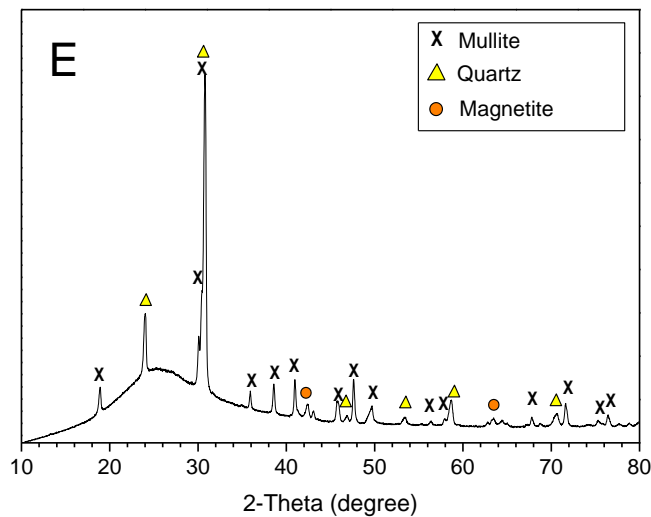
(b) Mullite,  $\text{Al}_{1.83}\text{Si}_{1.08}\text{O}_{4.85}$  (ICSD# 43298), Quartz,  $\text{SiO}_2$  (ICSD# 89280); Magnetite,  $\text{Fe}_3\text{O}_4$  (ICSD# 43001); Hematite,  $\text{Fe}_2\text{O}_3$  (ICSD# 15840); Tricalcium,  $\text{Ca}_3\text{SiO}_5$  (ICSD# 81100, could be a contamination by cement).



(c) Mullite,  $\text{Al}_{1.83}\text{Si}_{1.08}\text{O}_{4.85}$  (ICSD# 43298), Quartz,  $\text{SiO}_2$  (89280); Magnetite,  $\text{Fe}_3\text{O}_4$  (ICSD# 43001); Hematite,  $\text{Fe}_2\text{O}_3$  (ICSD# 15840).



(d) Mullite,  $\text{Al}_{4.75}\text{Si}_{1.25}\text{O}_{9.63}$  (ICSD# 66448), Quartz,  $\text{SiO}_2$  (89280); Magnetite,  $\text{Fe}_3\text{O}_4$  (ICSD# 43001); Hematite,  $\text{Fe}_2\text{O}_3$  (ICSD# 15840).



(e) Mullite,  $\text{Al}_{4.75}\text{Si}_{1.25}\text{O}_{9.63}$  (ICSD# 66448), Quartz,  $\text{SiO}_2$  (89280); Magnetite,  $\text{Fe}_3\text{O}_4$  (ICSD# 43001).

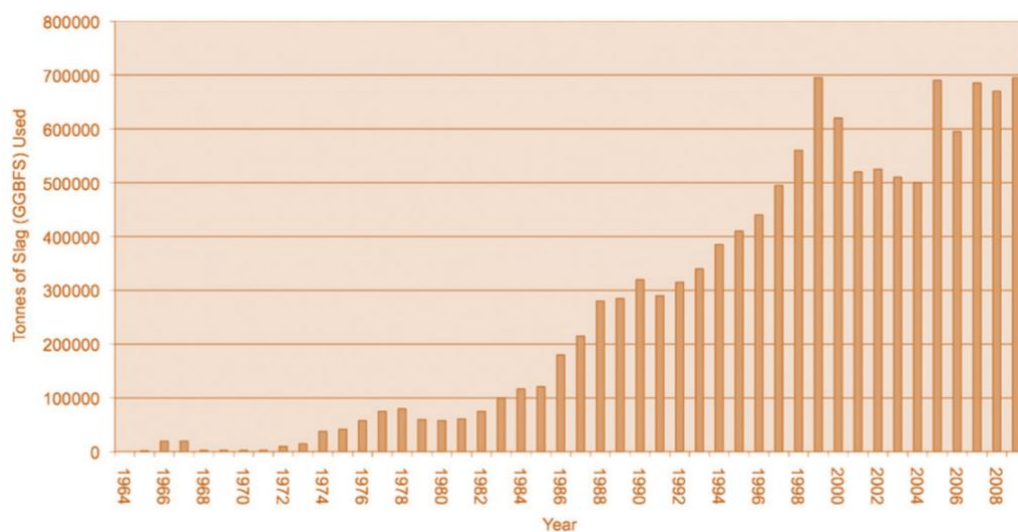
**Figure 3-3.** The XRD patterns showing the crystalline phases in the five selected fly ashes.

### 3.3.2.2 Slag

A ground granulated blast furnace slag (GGBFS, termed slag throughout this research) was used in the manufacture of GFCs for the purposes of shortening setting time and strengthening the binder phase as well. Slag is a by-product from iron production. According to the definition of Australasian (Iron & Steel) Slag Association (2011a), slag forms as the iron is reduced and the coke is consumed as energy. Slag being lighter floats on top of the molten iron "liquid". After separating from the heavier iron, the slag is typically tapped or quenched

rapidly by passing it through a trough of high pressure, high volume water sprays, the heat energy contained in the molten slag causes it to explode and instantly form granulated blast furnace slag (GBFS), GGBFS is formed when GBFS is further processed or ground using conventional cement clinker grinding technology.

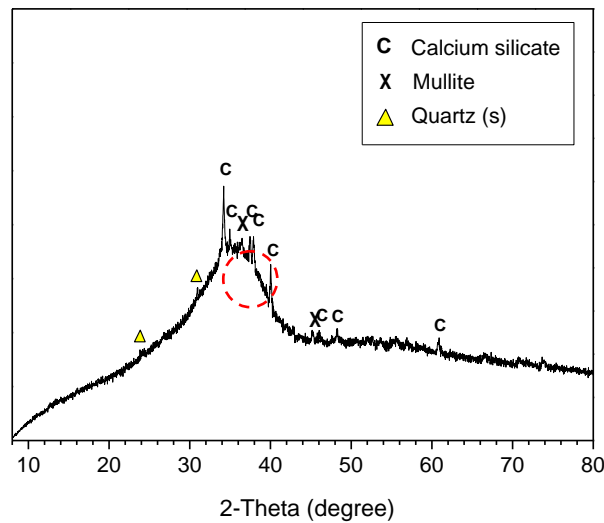
Slag is typically used in activation of granular pavement materials (such as steel slag) and as a cementitious material in the manufacture of concrete. Figure 3–4 shows the slag market statistics since 1964. Today Australia produces over 2 million tonnes of blast furnace slag annually, of which around 700 000 tonnes is used, that is 60% remains to be used (Australian Slag Association 2011b). With the cessation of iron and steel production in Australia, slag may become a versatile recoverable and renewable resource.



**Figure 3–4.** Sales of GGBFS in Australia. Figure cited from (Australasian (Iron & Steel) Slag Association (ASA), 2011a).

Alkali activation of slag results in a high strength and chemical resistant binder, which has been extensively studied and historically used in construction (Wang and Scrivener 1995; Shi et al, 2008; Puertas et al. 2006; Bernal et al. 2011b; 2011c).

In this research, a slag was used as a setting accelerator. The slag was a commercial product supplied by a Queensland concrete company. The main composition includes 33.3 wt.% of  $\text{SiO}_2$ , 14.6 wt.% of  $\text{Al}_2\text{O}_3$ , 41.7 wt.% of  $\text{CaO}$ , 6.1 wt.% of  $\text{MgO}$  and some other traces of metal oxides as determined by XRF. The XRD pattern showing the mineral components is presented in Figure 3–5. The slag consists mainly of amorphous phase and a minor quantity of tricalcium, mullite and quartz phases. The tricalcium is probably a contamination from the grinding and transportation using cement and concrete industry facilities, as that presents in fly ash B. The minor amount of mullite and quartz probably source from contamination of fly ash in packing, transportation and sampling. The broad diffraction hump indicates that the majority of the slag is amorphous.



**Figure 3-5.** XRD pattern of the slag used in this research. Calcium silicate,  $\text{Ca}_3\text{SiO}_5$  (ICSD# 81100); Mullite,  $\text{Al}_{4.75}\text{Si}_{1.25}\text{O}_{9.63}$  (ICSD# 66448); Quartz (s),  $\text{SiO}_2$  (ICSD# 71392 and 42498).

### 3.3.3 Foaming agent

Several foaming agents commonly used for making OPC foam concretes were considered for use in the research. The first and the most commonly used is metal powder, which has been used by industry for many years (more than 70 years) for autoclaved aerated concrete (AAC) or autoclaved cellular concrete (ACC), as discussed in Chapter 2. Al powder is commonly used and Fe powder is also popular. The foaming mechanism is that the metal powder reacts with  $\text{H}_2\text{O}$  to produce  $\text{H}_2$  gas, usually at elevated temperatures. The advantages of this type of foaming agents are the extremely fine voids and low dosage required (<1% of cement). The disadvantage is that the reaction time (that is foam development) is difficult to control. This is very important as the expansion of gas bubbles plays an important role in affecting the mechanical properties of products (Just and Middendorf 2009).

Geopolymerization systems are strongly alkaline and usually need elevated curing temperatures. These two factors may accelerate the foaming rate of metal powders and make control difficult. Additional consideration is the limited understanding of the influences of the introduction of out-sourced Al and Fe on geopolymer formation. For these reasons metal powders were not considered further.

The second candidates are hydrogen peroxide ( $\text{H}_2\text{O}_2$ ) and sodium peroxide ( $\text{Na}_2\text{O}_2$ ).  $\text{H}_2\text{O}_2$  has pungent odor, is corrosive to skin and eye and is very sensitive to the pH and temperature. An U.S. patent disclosed the utilization of  $\text{Na}_2\text{O}_2$  as foaming agent and alkali activation agent for slag (Bean and Malone, 1997). Due to its hygroscopic property,  $\text{Na}_2\text{O}_2$  is difficult to store. For these reasons the peroxides were not further considered. However,  $\text{Na}_2\text{O}_2$  is a potential candidate for GFC manufacture and is recommended to be investigated in the future.



The foaming agent selected for the research is a commercially foaming agent – a modified aqueous concentrate of surface active polypeptide-alkylene polyol condensate GEOFOAM™ SNP. It is a product of Cellular Concrete LLC (USA). This kind of foaming agent can either be pre-formed or formed by high speed mixing. As it is difficult to control the foam volume by the latter method, foam was produced by the pre-forming method and then quickly mixed into geopolymer paste.

### 3.3.4 Other materials and chemicals

#### 3.3.4.1 Mullite and quartz

In the FTIR analysis of reactivity of the fly ashes, mullite and quartz were used for comparison to the fly ashes. The mullite and quartz powder were supplied by Zhengzhou Xiangyu Foundry Materials Co. Ltd (Henan, China). The mullite is a product prepared by calcination of natural kaolin clay at 1100°C (as claimed by the supplier in the product specification). Their chemical composition as determined in this research by XRF analysis is given in Table 3-4.

**Table 3-3:** Composition of the mullite and quartz powder as determined by XRF, wt.%. (LOI is loss of ignition).

Composition	SiO <sub>2</sub>	Al <sub>2</sub> O <sub>3</sub>	TiO <sub>2</sub>	MgO	Fe <sub>2</sub> O <sub>3</sub>	CaO	K <sub>2</sub> O	SO <sub>3</sub>	LOI
Mullite	49.56	48.19	0.56	0.45	0.30	0.14	0.14	0.08	0.33
Quartz	99.60	0.19	-	-	0.05	0.03	-	-	0.08

Note: the mullite has some amorphous SiO<sub>2</sub> in it as well as the pure mullite phase - kaolinite is much more Si-rich than either of the two forms of mullite (2:1 or 3:2), they both have more Al than Si, so the extra Si in kaolin is converted into amorphous silica during calcination. In retrospect, this isn't a very good standard material because it has this unknown amorphous content. However, it is still useful for the comparison purpose.

For a fully dehydrated kaolinite, the SiO<sub>2</sub> and Al<sub>2</sub>O<sub>3</sub> can be expressed as 54.1 wt.% and 45.9 wt.% respectively. Table 3-4 shows that there are some Al rich impurity phases present in the original clay, which could be some secondary minerals present in the original clay, such as sillimanite (Al<sub>2</sub>O<sub>3</sub>·SiO<sub>2</sub>) and alunite (KAl<sub>3</sub>(SO<sub>4</sub>)<sub>2</sub>(OH)<sub>6</sub>). The elements Ti, Fe and Ca may come from other secondary minerals in the clay, such as limonite (Fe<sub>2</sub>O<sub>3</sub>·2H<sub>2</sub>O) and titanite (CaTiSiO<sub>5</sub>).

#### 3.3.4.2 Other chemicals

##### *Potassium hydroxide*

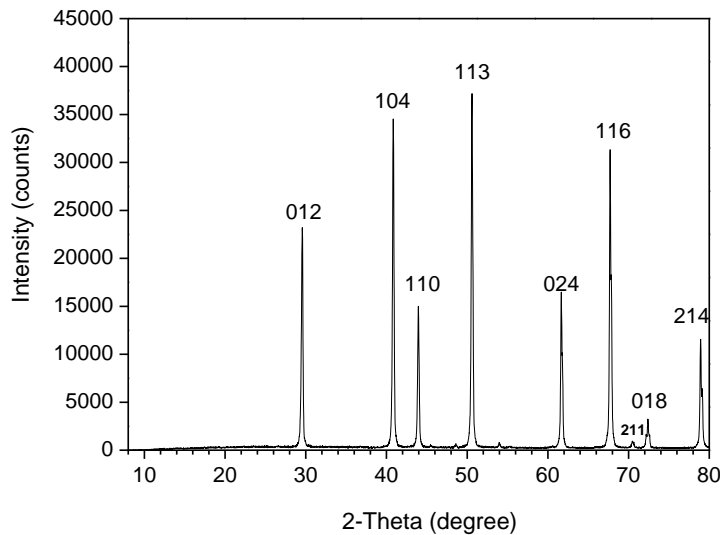
Analytical grade potassium hydroxide pellet supplied by Science Essentials (Brisbane, Australia) was dissolved to prepare KOH solution for examining the dissolution behaviour of fly ashes at high pH and liquid/solid ratio conditions.

##### *Hydrochloric acid*

A hydrochloric acid solution with concentration of 32 wt.% was supplied by Science Essentials (Brisbane, Australia). It was diluted to 4.76 wt.% (1:20) and used for the treatment of alkaline dissolved fly ashes and geopolymers.

##### *Corundum*

Corundum ( $\alpha\text{-Al}_2\text{O}_3$ ) was supplied by Aladdin (USA). As outlined in the product specification,  $\alpha\text{-Al}_2\text{O}_3$  phase is >99.99 % and the particle size  $D_{50}=0.2 \mu\text{m}$ . Figure 3-6 shows that the corundum is a perfect crystalline  $\alpha\text{-Al}_2\text{O}_3$ . It was used as the internal standard for quantitative X-ray diffraction (XRD) analysis of the fly ashes using the Rietveld refinement method.



**Figure 3-6.** XRD pattern of the corundum used as the internal standard for quantitative XRD analysis by Rietveld method. Corundum,  $\text{Al}_2\text{O}_3$  (ICSD# 60419).

### 3.4 Procedures

#### 3.4.1 Characterization of raw materials

##### 3.4.1.1 Measurement of the particle size distribution

The particle size distribution of the fly ashes was determined using a Malvern Mastersizer 2000 laser particle sizer. Particle sizes from  $0.02 \mu\text{m}$  to  $2000 \mu\text{m}$  can be measured with an accuracy of  $\pm 1\%$  at the  $D_{50}$ . Fly ash usually has a particle size range within  $1\text{-}100 \mu\text{m}$ , which is suitable to be tested using this equipment.

The specific surface area (SSA) can also be calculated from the results of the particle size distribution measurement using the following equation:

$$SSA = (6 \sum (V_i / d_i)) / (\rho \sum V_i) = 6 / (\rho D[3,2]) \dots \dots \dots (3.1)$$

in which:  $V_i$  is the relative volume in class  $i$  with a mean class diameter of  $d_i$ ,  $\rho$  is the density of the material, and  $D[3,2]$  is the surface area weighted mean diameter. This can be carried out automatically within the Malvern Mastersizer 2000 software, to rapidly estimate the particle surface area. In carrying out this calculation, it is assumed that the particles are perfectly solid spheres. This approximation may be particularly suitable for the fly ash measurement since fly ash particles are usually spheres. If the particles are porous, such as cenosphere or irregular such as milled ash, the result is not as accurate as gas absorption

approach, such as the Brunauer–Emmett–Teller (BET) method (Brunauer et al. 1938) may give a more accurate result. However, for a comparative purpose, the laser particle sizer is adequate.

#### 3.4.1.2 Determination of the particle density

The particle density of the fly ashes was calculated by measuring the displacement of fly ash in a fixed volume containing a liquid. Considering that fly ash may partially dissolve in water, acetone was used as the liquid. A sample of 10 ( $\pm 0.0002$ ) g of fly ash was placed in a 100 mL volumetric flask, which was filled with the acetone. The bottle was then weighed ( $M_e$ ) and the particle density of the fly ash  $D_{fa}$  was calculated using the following formula:

$$D_{fa} = 10 / (100 - (M_e - M_0 - 10) / \rho_e) \dots\dots\dots (3.2)$$

in which,  $M_e$  and  $M_0$  are the weight filled with fly ash and acetone, and the weight of neat flask, respectively;  $\rho_e$  is the density of acetone at 25°C.

The bulk density or unit weight of fly ash was also determined. Bulk density is the mass of sample for a given volume, including the volume of particles and inter-particle volume.

#### 3.4.1.3 BET surface area

A standard method for determining the surface area of a solid is by measuring the physical adsorption of gas molecules on its surface. This is commonly known as BET gas adsorption analysis named after Stephen Brunauer, Paul Emmett and Edward Teller (Brunauer *et al.* 1938). The BET adsorption isotherm is typically expressed as:

$$p / (v \cdot (p_0 - p)) = 1 / (v_m \cdot c) + (c - 1) \cdot p / (v_m \cdot c \cdot p_0) \dots\dots\dots (3.3)$$

in which  $p$  is the equilibrium pressure of adsorbate;  $p_0$  is the saturation pressure of adsorbate;  $v$  is the total volume of adsorbate gas;  $v_m$  is the monolayer adsorbed gas quantity and  $c$  is a BET constant.

When  $p / (v \cdot (p_0 - p))$  is plotted against  $p / p_0$  it will result in a straight line with the y-intercept ( $I$ ) being  $1 / v_m \cdot c$  and the slope ( $S$ ) being  $(c - 1) / (v_m \cdot c)$ . So  $v_m$  and  $c$  are determined by:

$$v_m = 1 / (S + I) \dots\dots\dots (3.4)$$

Surface area (SBET) can then be calculated using:

$$S_{BET} = v_m \cdot N \cdot s / (v \cdot a) \dots\dots\dots (3.5)$$

in which  $N$  is Avogadro's number;  $s$  is adsorption cross section of adsorbing species;  $v$  is molar volume of adsorbent gas;  $a$  is mass of adsorbent (g).

The BET analysis of the selected five fly ashes was conducted at the University of Queensland using Micromeritics Tristar 3000 with nitrogen as the adsorbate gas with the analysis bath temperature of 77.3 K.

#### 3.4.1.4 Dissolution behaviour

Dissolution experiments were performed in order to obtain a better understanding of the effects of alkaline activation medium and composition on their dissolution behaviour. Five batches of fly ash–liquid mixtures were prepared to examine the dissolution behaviour of fly ashes under different pH conditions. Table 3–5 lists the mixture composition, dissolution period and temperatures.

**Table 3–4:** Dissolution conditions of fly ash.

Dissolution medium	Liquid/ash mass ratio	Temperature / °C	Time / h
H <sub>2</sub> O	20	25	168
NaOH (1 M)	50	25	6
NaOH (4 M)	35	80	6
NaOH + LSS <sup>a</sup>	35	80	6
KOH (4 M)	35	80	6

a: the mixture gives a combination of 4 M NaOH + 1.3 M SiO<sub>2</sub>.

The fly ash–liquid mixtures were stirred to prevent sedimentation during the dissolving period. After the dissolution intervals, the fly ash–alkaline solution mixtures were repeatedly filtrated and washed 6 times with 1:20 HCl solution and water alternatively. The filtrated pastes were dried at 105°C for 48 h and retained for XRD, SEM and FTIR characterizations.

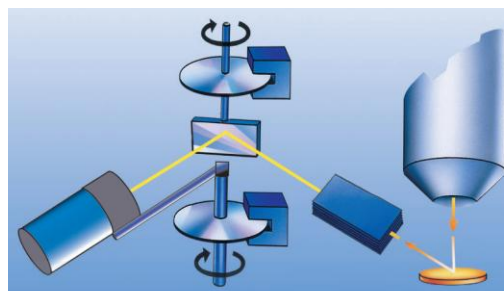
#### 3.4.1.5 XRD/XRF analysis for the phase determination

##### *ARL 9900 Series X-ray workstation*

The X-ray diffraction testing for original fly ashes, alkali–acid treated fly ashes and geopolymer samples were all performed on an ARL 9900 Series X-ray workstation (Thermo Fisher Scientific) at Nanjing University of Technology, as shown in Figure 3-7.



(a)



(b)

**Figure 3–7.** ARL 9900 Series X-ray workstation (a) and the operation principle (b).

For elemental composition and mineral component analysis, samples are usually studied using two separate X-ray instruments. The ARL 9900 Series X-ray workstation (Figure 3-7a) integrates a full X-ray diffraction facility for phase analysis in the X-ray fluorescence (XRF) analysis system through the high precision of its Moiré fringe positioning mechanisms (Figure 3-7b). Accurate sample positioning and the temperature stabilized environment of the ARL 9900 enabled excellent and stable analysis. Working under vacuum permits the use of a cobalt anode X-ray tube that prevents any fluorescence of iron which is common with copper anode tubes. Avoiding any iron fluorescence minimizes the spectral background and greatly improves the peak to background ratio, thus giving an accurate composition and mineral component analysis.

### *Sampling*

Two factors that may affect the diffraction precision have been considered: preferred orientation of powder and particle size of fly ash. It is well known that for powder samples, particularly those crystalline particles with tube, rod and sheet shape, the diffraction usually shows preferred orientation (unusually strong peak) if the samples are compressed. For the ARL 9900 workstation, the powder sample has to be compressed under high pressure to make a flat plate for both XRD and XRF testing. Fortunately, due to the fly ash sphere particle shape, the diffraction did not show evident preferred orientation. This was confirmed by comparing the diffraction patterns that obtained from ARL 9900 and that obtained from an ARL X'TRA X-ray diffractometer.

For normal qualitative XRD testing, 5 g sample was hand-milled in an agate mortar 0.2 mL methyl cellulose-based solution (1%) for 10 min to get a relatively homogeneous mixture. The mixture was then gently tied in a PP ring and pressed under a load of 5 tonnes. The pressed plate (diameter ~3 cm and thickness ~3 mm) was dried at 65°C in a vacuum oven for 6 h before being placed into the sample chamber. This drying procedure ensured no deformation on the surface of sample plates.

For quantitative XRD testing, 4 g sample was hand-milled in an agate mortar for 10 min and then hand-mixed with 1 g corundum (as a internal reference material) gently for another 15 min to obtain a homogeneous mixture, followed by pressing and drying. To obtain a possible error of the quantitative XRD analysis, sample plates with 10% and 15% corundum have also been prepared and tested.

### *XRD data collection and analysis*

XRD data were obtained on the ARL 9900 workstation using Co K $\alpha$  radiation ( $\lambda = 1.788996$  nm), tube power of 40 KV and  $i = 40$  mA. The 2-theta degree was recorded from 8 to 80° with a step size of 0.02° and count time of 4 s/step, thus needing 4 h to complete each sample.

Searching and matching of the phases present in the fly ashes were conducted using the software Crystallographica Search-Match (Version 2.1.1.0). To exclude the effects of the diffraction hump due to amorphous phase, an automatic background subtraction was done before peak matching. There were two mullite phases identified from the five studied fly ashes: Al<sub>4.75</sub>Si<sub>1.25</sub>O<sub>9.63</sub>

(ICSD# 66448) present in fly ashes A, D and E and  $\text{Al}_{2.83}\text{Si}_{1.08}\text{O}_{4.85}$  (ICSD# 43298) present in fly ashes B and C (Figure 3–2). The first mullite phase noted is more common (Rickard et al. 2011; Williams and van Riessen 2010) while the second type has also been found in some fly ashes (Keyte 2008).

The quantitative analysis was performed by the Reitveld refinement method. The XRD data and the corresponding crystallographic information files which include the crystal structure parameters ( $a$ ,  $b$ ,  $c$ ,  $\alpha$ ,  $\beta$  and  $\gamma$ ), space group, atomic position and temperature factor for each atom were introduced in GSAS–EXPGUI. The background was manually fitted and the Refine Zero function was used to correct the possible peak shift, in order to obtain a good fitting and accurate lattice parameters. Two fitting parameters,  $W_{\text{RP}}$  and reduced  $\text{CHI}^2$ , were used as the critical values to check the refinement efficiency.

#### 3.4.1.6 FTIR analysis

To get a better understanding of the reactivity of fly ash, Fourier transform infrared spectroscopy (FTIR) was used to analyse the Si(Al)–O vibration bonds in the fly ashes before and after alkali activation. FTIR spectra ( $4000\text{--}400\text{ cm}^{-1}$ ) were obtained by using a Thermo Nicolet Nexus FT–IR workstation and employing the conventional KBr disc method. Approximately 2 mg of fly ash was ground together with 200 mg of IR–grade KBr for 3 min. After drying at  $105^\circ\text{C}$  for 12 h, pellets were pressed and testing performed at a resolution of  $1\text{ cm}^{-1}$  with 192 scans referenced against a blank KBr pellet.

The relative absorbance spectra over the range of  $1400\text{--}400\text{ cm}^{-1}$  were subjected to a deconvolution analysis by using the Peakfit (Version 4.12) software with Gaussian peak shape and with variable peak width. The fitting process, including selecting the weighting function, setting the numbers and positions of component bands and adjusting the band shape, was performed according to the literature (Taylor 1990; Lee and Van Deventer 2003; Criado et al. 2007a) in combination with the self-fitting functions of the software. The nomination of band assignment will be discussed later in detail. The principle was to minimize the typical component band number to obtain regression coefficient  $r^2$  values above 0.999.

#### 3.4.1.7 SEM-EDS analysis

The morphology and local composition of the selected five fly ashes and their dissolved particles were analysed using an EVO MA18 scanning electron microscope (SEM) accompanied with an energy dispersive spectrometer (EDS). Samples were coated with gold, imaged and analyzed under high vacuum conditions with an accelerating voltage of 20 kV. For the EDS analysis, more than three points of the same morphology area were analysed. In Chapters 4&5 typical composition results are given.

### 3.4.2 Geopolymer manufacture

#### 3.4.2.1 Geopolymer pastes

Solid geopolymer specimens were manufactured at room temperature (20-25°C) by mixing the activation solution and fly ash at a given liquid to solid mass ratio in a laboratory cement mortar mixer. Two batches of specimens were prepared, one with additional water and the other with more activation solution, to compare the reactivity of fly ash under a high and a low concentration of alkali cations. The fresh pastes were poured into Ø53mm×108 mm moulds, sealed with plastic film wrap and allowed to cure at 40°C for 24 h and followed by 25°C cure to obtain 7 d and 28 d strengths.

#### 3.4.2.2 Geopolymer foam concrete (GFC)

GFCs were made from a geopolymer paste and prefoamed foam. Due to the lack of standards specified for geopolymer concrete, some Portland cement foam concrete specifications have been referenced. One principle in making all foamed pastes was that all the mixes were designed to have similar spreadability by flow test. The procedures are outlined in Figure 3-8.

A geopolymer paste was firstly mixed for 5–10 min; meanwhile, a diluted foaming agent was foamed using a foam generator. The aeration speed can be adjusted to make foams with different densities. The preformed foam was then quickly weighed, and mixed with geopolymer paste. The curing was an optimized procedure including 40°C curing immediately after cast and room temperature curing later.

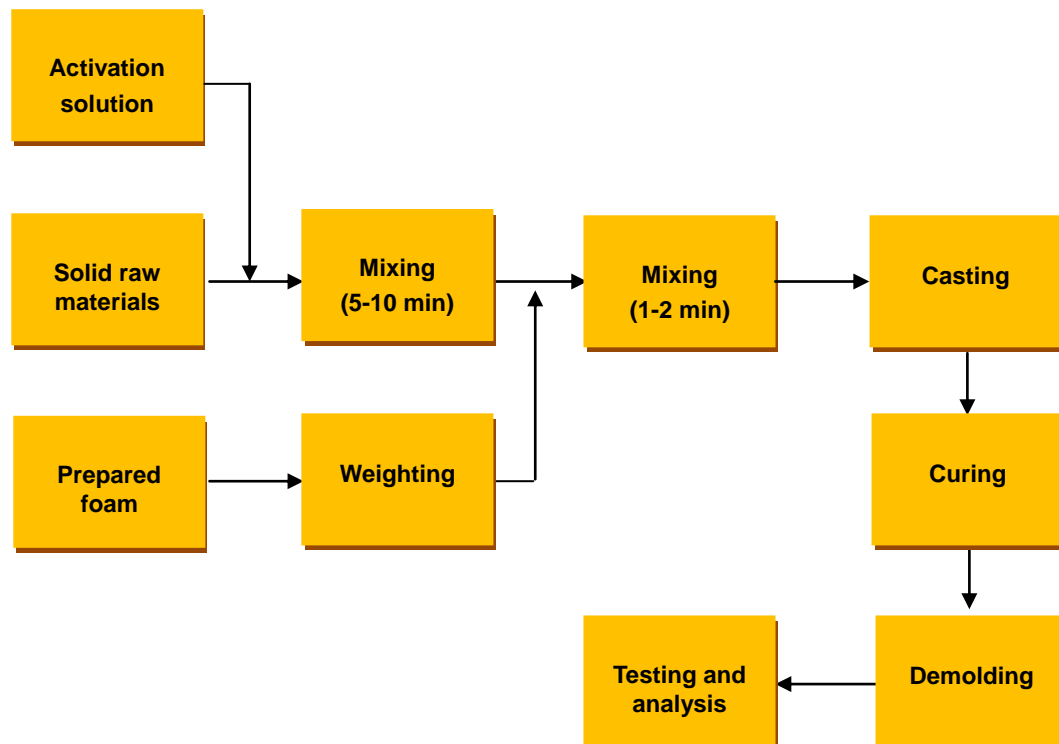


Figure 3-8. Sketch of foam geopolymer concrete preparation.

### 3.4.3 Characterization of geopolymers

#### 3.4.3.1 Procedures for mechanical testing

The testing of compressive strength and compression elastic modulus were carried out on a MTS universal mechanical testing machine. As there is no testing standard for lightweight geopolymer concretes, the commonly used standards ASTM C 495 (2007) and ASTM C 496/C 496M (2004) were referenced in this study, although the former indicated that the density of the sample should not exceed 800 kg/m<sup>3</sup>. The suggested mould in the standards for compressive strength testing should have a diameter of 75 mm ( $\pm 1.6$  mm) and a length of 150 mm ( $\pm 3$  mm). In this research, a polypropylene mould with diameter  $\varnothing=53$  mm ( $\pm 0.5$  mm) and length of 108 mm ( $\pm 0.5$  mm) was used throughout. To keep the diameter/length ratio to be 1/2, the demoulded samples were sanded on both top and bottom to reach a length of 106 mm ( $\pm 1$  mm). The loading rate was 0.5 mm/min. The strength was calculated according to the pressure (N) and the cross section (mm<sup>2</sup>) without any scaling factor. Both the compressive strength and splitting tensile strength were calculated in MPa and the strength stated is an average value of at least four samples manufactured from identical formulations and cured under the same conditions.

#### 3.4.3.2 Procedures for thermal conductivity measurement

In this project, one of the major aims is to develop a lightweight construction material with good thermal insulation property so as to reduce the heat transfer between indoor and outside environments, in order to decrease the energy consumption of buildings. Thermal conductivity is a typical parameter that is used for expressing the thermal insulation property. The lower the thermal conductivity, the better thermal insulation is.

The thermal conductivity measurement was made at ambient conditions using transient plane source (TPS) method on a Hot Disk 2500 system. This equipment can measure solids and liquids with thermal conductivities ranging from 0.001 to 1000 W/mK with reproducibility better than 1%. The experimental set-up is depicted in Figure 3-9. The TPS technique has been well discussed in the literature (Benazzouk et al. 2008). In comparison with stationary or steady state methods, the advantage of transient methods is that a full set of thermophysical parameters, including thermal conductivity, specific heat and thermal diffusivity, can be obtained within a single quick test.

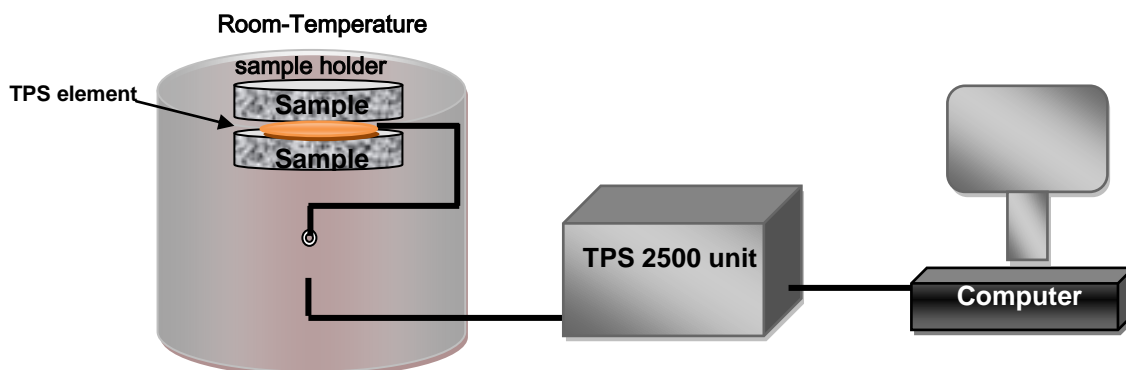


Figure 3-9. Sketch of the Hot Disk TSP 2500 system.



The measurement process can be briefly described as follows: a disk-shaped TPS element is placed between two disc samples. The TPS element is made out of a bifilar spiral, which provides the source of heat to the sample and also serves as a sensor of the temperature increase in the samples. Assuming that the conducting pattern is horizontally placed inside an infinite solid, the time dependent resistance of TPS element during the transient recording can be written as:

$$R(t) = R_0 (1 + \alpha \Delta T(\tau)) \dots\dots\dots(3.6)$$

where  $R(t)$  is the resistance of the TPS sensor at time  $t$ ,  $R_0$  is the resistance of the TPS sensor at time zero,  $\alpha$  is the temperature coefficient of resistivity,  $\Delta T(\tau)$  is the mean value of temperature rise in the TPS element.

Recording the change in potential difference  $\Delta E(t)$  across the TPS sensor, the thermal conductivity has been calculated with a developed Matlab program using the following relation:

$$\lambda = \gamma D(\tau_i) / \Delta E(t) \dots\dots\dots(3.7)$$

where  $\gamma$  is the constant depending on the different resistances in the Wheatstone bridge, which can be calculated with  $R(t)$ ;  $D(\tau_i)$  is the theoretical expression of time-dependent increase.

The samples were obtained from the geopolymers specimens of  $\varnothing 53 \times 108$  mm after ageing at ambient conditions for 28 d. The specimens were then cut into discs with thickness of 15 mm ( $\pm 2$  mm). In order to make sure a good contact between the sensor and the sample surface, all of the samples were polished. Figure 3-10 shows two pieces used for one sample. For each geopolymer mixture four testing values were available by placing the TPS element between A-a, A-b, B-a, and B-b. The four values were recorded to determine an average value.

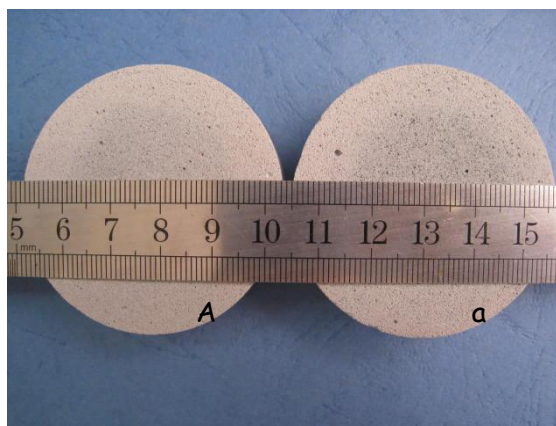


Figure 3-10. Two pieces of one geopolymer mixture for thermal conductivity testing.

The humidity of the sample has an important impact on the measured thermal conductivity (Narayanan and Ramamurthy 2000b; Duxson et al. 2006a). Because the drying process at high temperatures for long periods may change the phases of geopolymer, a moderate temperature 80°C and a short drying period 6 h was used in this research. It was noted that the weight loss did not exceed 1% if they were dried for 6 h longer. The porous microstructure and the small thickness enabled rapid drying of the samples at 80°C. The samples were quickly moved from drying condition to testing chamber, although which located at RH=40-60% room conditions.

3.4.3.3 Procedures for density measurement

Two densities of the GFCs were measured: the air dried density and the oven-dried density. The air dried density is useful in engineering applications; the oven dried density is particularly meaningful for foam concretes. The air dried density was measured after the specimens were demolded and aged under ambient conditions (23±5°C) for 27 and 59 d. The oven-dried density was measured after a >24 h oven-drying interval at 105 ± 5°C, as per ASTM C 495 (2007).

3.4.3.4 Procedures for porosity measurement by water saturation method

The porosity of the foam concrete was determined by a vacuum saturation method (Kearsley and Wainwright, 2002). Usually, the test sample should be a core taken from a large specimen, so as to avoid the possible effects of the surface on water absorption. In this research, the surfaces of geopolymer specimens were therefore carefully polished with sand paper. After measuring the sizes and oven-dried weight ( $m_{dry}$ ), specimens were evacuated under a vacuum of 80 to 100 kPa for 48 h and then boiled water was sucked in until all specimens were immersed. The immersed system was kept under the negative pressure for another 24 h. By this process it was believed that all of the air bubbles have been removed from the specimens as well as that in the boiled water. After the evaporation, specimens were removed from the water and weighed. Before weighing the water saturated weight ( $m_{sat}$ ), the excess water on the surface was blotted off with a wet towel. The water saturation porosity was calculated using the following formula, in which  $v$  is the volume of the polished specimen:

$$P=(m_{sat}-m_{dry})/v \dots\dots\dots(3.8)$$

It was noted that after sample immersion, the water became slippery, which was thought to be due to the dissolution of alkali in geopolymer into water. This may affect the accuracy of measurement. A correction method was to measure the density of water after immersing and calculate how much mass was dissolved from each specimen. The mass of Na<sub>2</sub>O in activator solution was only 5-8% of the dry fly ash. After geopolymerization, the dissolved mass should be less and the error caused by this problem should be very limited. Therefore, the error due to dissolution was ignored in this research.

#### 3.4.3.5 Procedures for pore structure analysis

In autoclaved aerated concrete, the pores can be classified in many ways as summarized by Nambiar and Ramamurthy (2007): (i) artificial air pores, intercluster and interparticle pores; or (ii) macropores formed due to the expansion of the mass caused by aeration and micropores which appear in the walls between the macropores; or (iii) micro capillaries (<50 nm) and macro capillaries (>50 nm to 50  $\mu\text{m}$ ) and artificial air pores (>50  $\mu\text{m}$ ). Visagie & Kearsely (2002) classified the pores into gel pores, capillary pores and air voids.

In this research, two types of pore were evaluated: the pores present in the solid geopolymer binders and the pores introduced in the foam geopolymer concretes. The first have influences on the mechanical properties of solid geopolymers while the second is one of the main factors that contribute to the properties of GFCs.

##### *Mercury intrusion porosimetry (MIP) analysis*

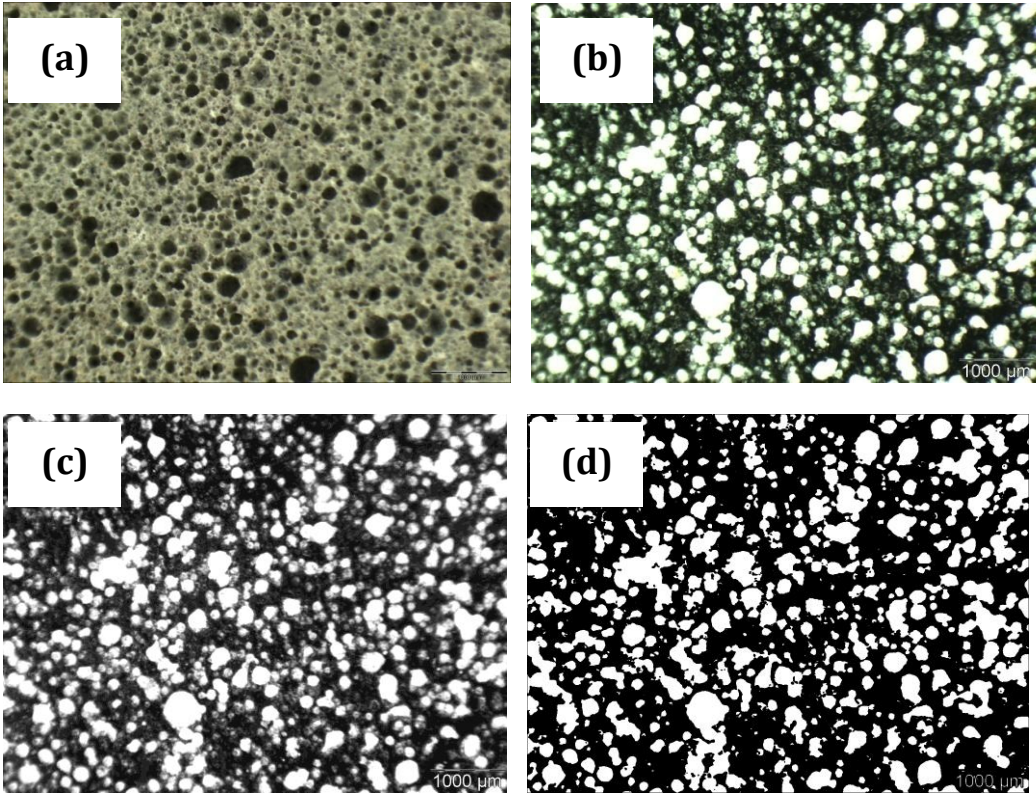
The pore size and distribution of geopolymer binders was analyzed by mercury intrusion porosimetry (MIP). MIP has been very widely used in pore structure characterization for cement based materials (Gallé 2001; Yang 2006; Pipilikaki and Beazi-Katsioti 2009) and geopolymers (Bakharev 2006; Okada et al. 2009; Rovnaník 2010). MIP has been criticized regarding the assumption that all pores are considered cylindrical and that the contact angle is fixed (Taylor 1997). It should be noted that the mercury porosity method may give high pore volumes because mercury intrusion under high pressure may breakdown the microstructure of the geopolymer (Hewlett 2004). Nevertheless, MIP is an appropriate method for comparative purposes.

Since the sampling procedures, particularly the drying process, may affect the MIP testing result to a large extent (Gallé 2001), a careful sampling was performed. The specimens were firstly crushed into small pieces with size around 3×3×3 mm and then the selected small samples were stored in acetone (or ethanol) for at least 24 h to remove the pore water. After being dried at 65  $\pm$  2°C for at least 6 h, the samples were transferred into a desiccator until testing. The testing was performed on a Poremaste GT-60 MIP (Quantachrome) with the surface tension of mercury set as 0.48 N/m and contact angle of 140°. This contact angle value is typical in blended cement MIP analysis (Kroehong et al. 2011) and was adopted in this project.

##### *Optical image analysis (IA)*

Pore (or air voids) characterization was also carried out with an image analysis (IA) system consisting of an Olympus optical microscopy and the Analysis-FIVE software (Olympus Product 2013). The sample preparation was referenced the method proposed by Nambiar and Ramamurthy (2007). Specifically, the oven-dried specimens were first polished on a machine, cleaned with compressed air (to blow away the fine particles in the open air voids), coated with black ink and allowed to dry for several hours. White talc powder was then spread on the black surface and slowly filled into the air voids by vibrating the specimens and pressing with a flat glass slide. The excess powder was wiped away with the edge of a razor blade and then with normal office adhesive tape, which can remove the powder lying on the binder while retain the powder in voids

unaffected. This method attained a surface with sharp and easily distinguishable boundaries of the air voids and matrix by their high colour contrast under optical microscopy. As the objective was to observe the air voids of foam geopolymer, a low magnification of 20× was selected.



**Figure 3-11.** The optical microscopy images of the polished surface of foamed geopolymer (a); surface coated with black ink (b); grayed photo (c) and converted into the binary format (d).

Figure 3-11 shows a set of optical images including sampling and image processing. 10-30 images were captured from each specimen. All of the pores identified from the images were listed together for further analysis. Parameters of interests include pore size (equivalent diameter) distribution and shape factor. The shape factor, given by Eq. 3.9, is an index reflecting the pore roundness. It equals unity for a perfect circle and is less for irregular shape pores.

$$\text{Shape factor (SF)} = (\text{perimeter})^2 / 4\pi(\text{area}) \dots\dots\dots (3.9)$$

3.4.3.6 Procedures for XRD/FTIR/SEM-EDS/TGA analysis

Both solid and foamed geopolymers were studied by XRD, FTIR and scanning electron microscopy (SEM) analysis to understand their phases, microstructure and micro morphology.

For the XRD and FTIR analysis, powder samples were prepared by grinding the oven-dried specimens, which had been fractured and stored in acetone (or

ethanol) for at least 24 h before. The drying procedure, 65°C for at least 6 h, was the same as described in the MIP testing procedure. The data collection and analysis as those described above for fly ash analysis.

For the SEM analysis, selected fractured samples (without polishing) were also dried at 65°C for 6 h and sprayed with a thin Au coating to enhance conductivity. Both solid and foamed geopolymer samples were tested on a scanning electron microscope (SEM) accompanied with energy dispersive spectrometer (EDS) and at an accelerating voltage of 20 kV.

Thermogravimetric analysis (TGA) was performed using a TGA Q500 instrument at a heating rate of 10°C/min from 25 to 890°C under air conditions.

### ***3.5 Concluding remarks***

The chapter provides details of the materials and testing methods employed in the research. Subsequent chapters will reference the materials and methods when appropriate.

## **Chapter 4: Physical Properties of Fly Ashes and Their Effects on the Liquid Requirement and Microstructure of Geopolymer Binders**

### ***4.1 Introduction***

This chapter investigates the particle size distribution, surface area, density and bulk composition of five selected fly ashes (termed A, B, C, D and E throughout the thesis) from the power stations around Australia. The effects of these physical characteristics on the liquid requirement of paste, the microstructure and strength of hardened binders have been studied.

To produce geopolymer foam concretes for non-structural to semi-structural applications, synthesis of a binder with appreciative mechanical properties is the first step. As there are many fly ashes commercially available, understanding the relationship between physical and chemical properties of fly ash and the properties/performance of geopolymer binders is critical for establishing a database of fly ash utilization. Such a database will provide guidance for both solid and GFC manufacture.

As discussed in Section 3.1.2, the utilization of fly ash for profitable-purpose is still a small fraction of global production although it has been widely used as a supplementary cementitious material in conventional concrete. Using fly ash to produce geopolymer binders may bring about a real 'valorisation' of fly ash (Provis et al. 2009c). However, it does not mean that fly ashes from different sources are all suitable for use. Diaz-Loya et al. (2011) studied the mechanical properties of geopolymer concretes made from 25 different fly ashes collected from power stations across the U.S. The resultant concretes from 11 Class F fly ashes had an average compressive strength of 36 MPa while it was 50 MPa for concretes made from 11 Class C fly ashes. However, the strength range was wide with one concrete sample from Class C fly ash only achieving a compressive strength of 2.7 MPa while some Class F fly ash concretes exhibited strength around 12 MPa. Three fly ashes were excluded for they are neither Class F nor Class C according to their  $SO_3$  content and particle size distribution. Other researchers also found a similar problem when Australian fly ashes from different sources were used in geopolymer mortars. Some fly ashes generate geopolymers with high compressive strength while some remain poorly reacted, and thus are unsuccessful for making geopolymer mortars (Keyte 2008; Provis et al. 2009c).

The reason for the large variation in the properties of geopolymer products, even though they are prepared at similar activation conditions, is the highly heterogeneous nature of fly ash. As the minerals in coal vary from one source to another, and even from time to time at the same plant, the milled coal has different particle sizes and the temperature inside of boiler may vary from 800 to 1400°C, the collected fly ash therefore varies significantly in particle size, shape and composition.

## 4.2 Particle characteristics of the selected fly ashes

The important chemical and physical properties of fly ashes include their composition, particle size distribution, particle density, and specific surface area. Milling fly ash particles was found to improve the final compressive strength of hardened binders (Kumar and Kumar 2011), which could be related to the enhanced reaction rate and extent since the particles are smaller and the content of amorphous phases is increased (Rao et al. 2010). There are very few reports of the effects of particle size or surface area for fly ash from different sources. Particle density was found to be closely related to composition, particularly with the Si, Al, Fe and Ca content (Furuya et al. 1987; Ghosal and Self 1995; Rickard et al. 2011; Shirai et al. 2011); however, its effects on geopolymer synthesis have received limited concern. In this section, these properties are to be characterised, so as to gain knowledge before understanding the properties of hardened binders.

### 4.2.1 Chemical composition

The chemical composition of fly ash was determined by XRF, as discussed earlier in Section 3.1.2, and the results are given in Table 4-1. The determination of reactive silicate in fly ashes was undertaken by Spectrometer Services Pty. Ltd. (Australia) by a wet chemical method through acidification.

It is clear that fly ash A has the smallest amount of SiO<sub>2</sub> and Al<sub>2</sub>O<sub>3</sub>, totalling 74.8 wt.%. B and C have similar amounts of SiO<sub>2</sub> and Al<sub>2</sub>O<sub>3</sub>, at around 85 wt.%. D and E have highest contents of SiO<sub>2</sub> and Al<sub>2</sub>O<sub>3</sub>, up to 90 and 96 wt.%, and their reactive SiO<sub>2</sub> contents are much higher than the three others.

**Table 4-1:** Chemical compositions (wt.%) of fly ash as measured by XRF. LOI is loss on ignition at 1000°C. \*SiO<sub>2</sub> is the reactive silica determined by wet chemical method.

Ash	SiO <sub>2</sub>	Al <sub>2</sub> O <sub>3</sub>	CaO	MgO	K <sub>2</sub> O	Na <sub>2</sub> O	Fe <sub>2</sub> O <sub>3</sub>	P <sub>2</sub> O <sub>5</sub>	SO <sub>3</sub>	TiO <sub>2</sub>	LOI	*SiO <sub>2</sub>
A	47.5	27.3	4.25	1.48	0.54	0.74	14.3	0.91	0.29	1.47	0.53	40.4
B	53.3	32.5	6.90	0.90	0.59	0.27	3.10	0.10	0.30	1.60	0.50	40.0
C	54.4	32.1	1.06	0.75	0.22	0.14	7.49	0.09	0.04	2.14	0.85	35.5
D	67.3	22.5	1.00	0.53	2.11	0.50	3.74	0.09	0.07	0.90	0.90	53.3
E	71.2	24.7	0.08	0.12	0.53	0.01	1.16	0.04	0.02	1.42	0.43	52.0

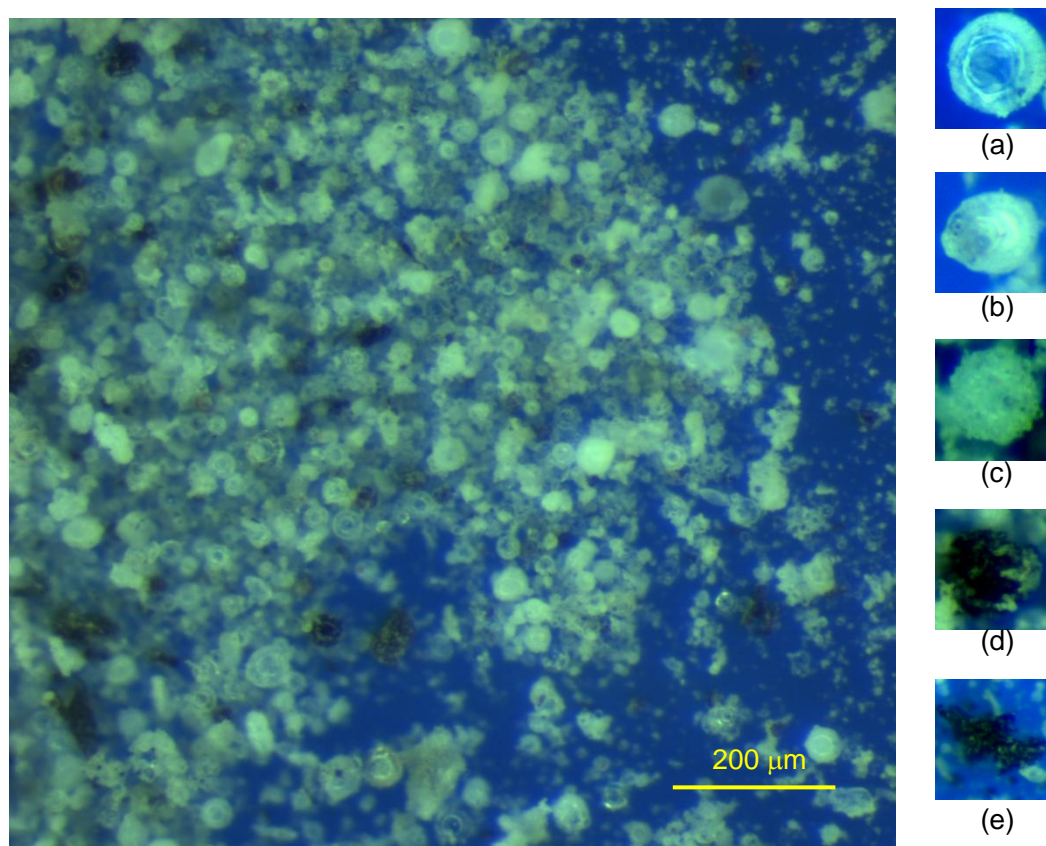
Another notable difference lies in the iron content. Iron usually presents as maghemite or hematite phases. Fly ash A has quite a high content of Fe<sub>2</sub>O<sub>3</sub> (14.3 wt.%). Fly ash C also has a considerable amount of iron, which could be one of the reasons that A and C are yellow. More physical properties are given in the following section. According to ASTM C 618, these fly ashes can all be classified as Class F in terms of their total mass fraction of SiO<sub>2</sub>, Al<sub>2</sub>O<sub>3</sub> and Fe<sub>2</sub>O<sub>3</sub>.

### 4.2.2 Morphology and particle size

The five selected fly ashes were observed with optical microscopy to identify their morphology characteristics. Figure 4-1 shows a typical optical micrograph



of fly ash (sample D) and more pictures are attached in Appendix A1. Many of the visually distinguishable particles ( $>30\ \mu\text{m}$ ) have a shell structure (Figure 4-1a), that is they are cenospheres (Fisher et al. 1978; Diamond 1986). These cenosphere particles are formed due to the molten drops being bloated by gases released by the combusting gas. The average wall thickness increases with increasing particle size, while the  $\text{SiO}_2/\text{Al}_2\text{O}_3$  ratio decreases with the particles size increasing (Ngu et al. 2007). Solid ash particles were also observed (Figure 4-1b). The potential influences of the wall thickness and composition on reactivity under geopolymerization conditions are discussed later. There are many coarse particles that appear to consist of a cluster of fine particles (Figure 4-1c). These particles are possibly formed by the aggregation of molten aluminosilicate droplets during cooling, in which way the finer droplets can minimize surface free energy. Black and brown iron-rich particles (Figure 4-2d) are also observed; particularly in sample A. Irregular black particles are unburned carbon (Figure 4-2e) and some white to yellow angular amorphous are quartz, which come from the original coal.



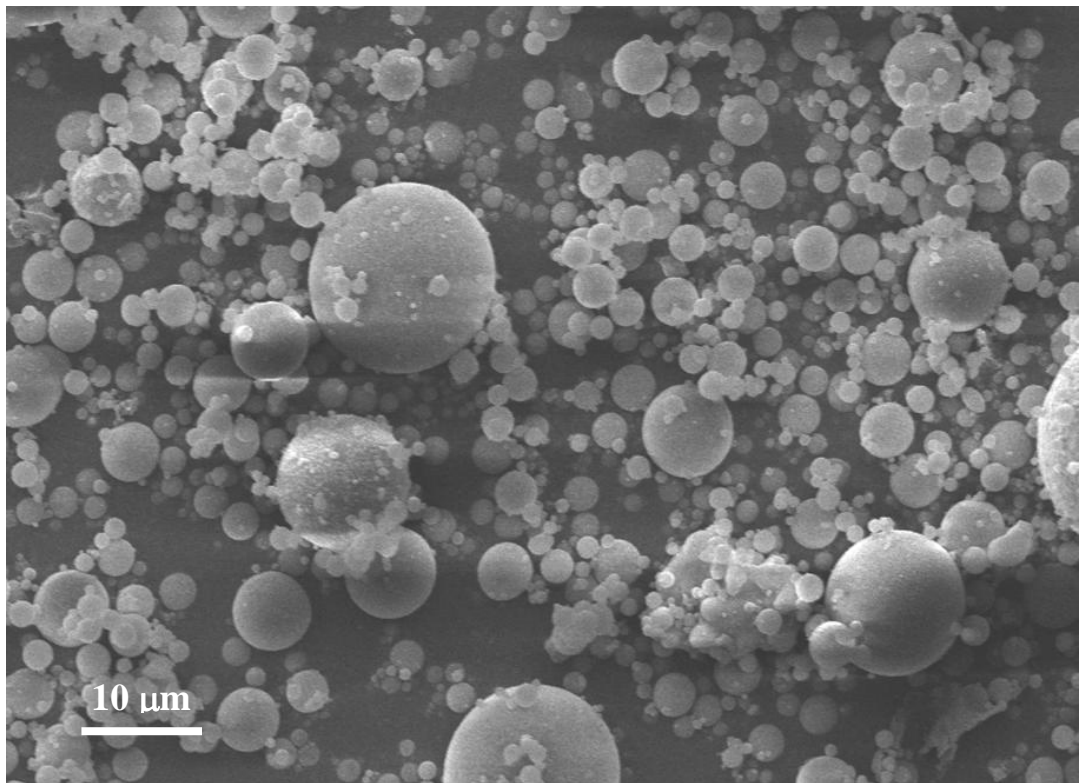
**Figure 4-1.** Optical images of fly ash particles (sample D). The small images on the right side emphasize specific particles: cenosphere particle (a), solid particle (b), particle formed by aggregation of finer ones (c), iron-rich particle (d) and carbon particles (e).

To obtain the surface and morphology details of particles, the five selected fly ash samples were studied by SEM. Figure 4-2 shows typical SEM images at different magnifications for the five fly ashes. As is widely appreciated, most fly ash particles are spherical and with a diameter from 1 to  $100\ \mu\text{m}$ . It is observed that the particles of fly ash A are much finer than the other four samples, and

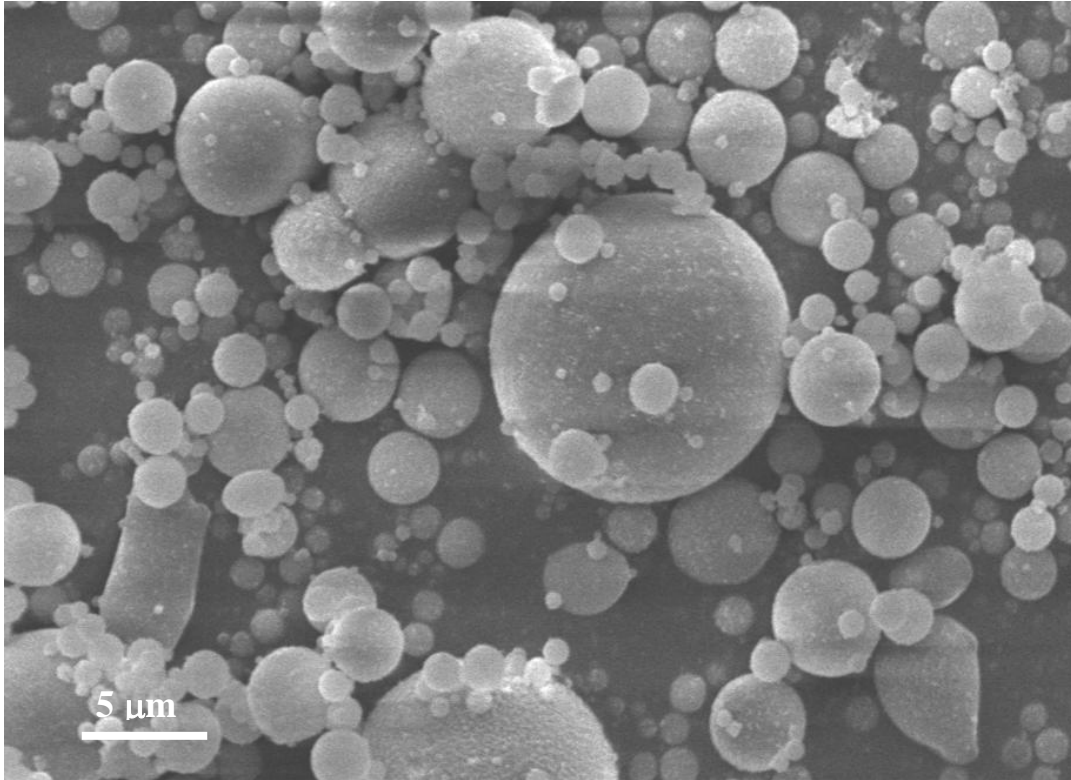


most of the particles are  $<5\ \mu\text{m}$ . The other four fly ashes have many irregular particles, as indicated by the arrows in the figures. These irregular particles mostly have a rounded vesicular shape (non-rigid), and probably are derived from the original minerals in coal, which have not been sufficiently fired (Fisher et al. 1978). Although most of the particles show a very smooth surface, very fine crystalline particles are embedded in the glass phases. In fly ash B and E, some broken shells were observed. These morphological features of fly ash particles will be discussed in more detail in the following sections.

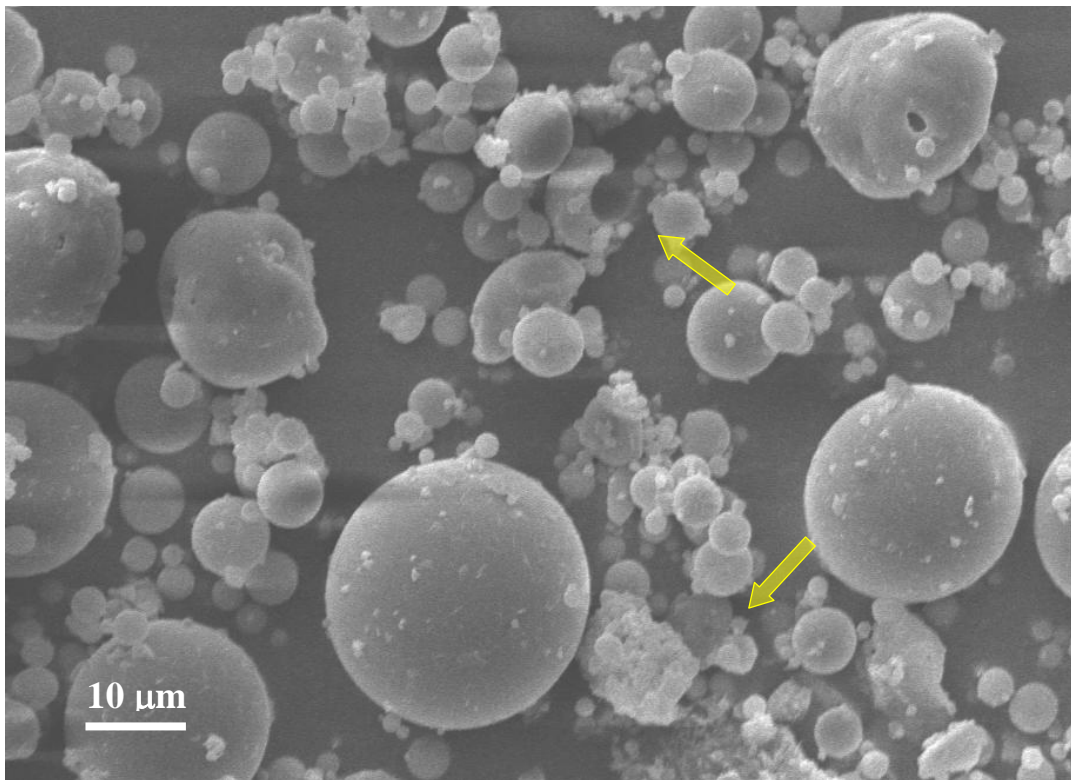
The particle size distributions of the fly ash samples were analysed by a laser particle size analyser. Figure 4-3 presents the cumulative particle size distributions of the fly ash samples. The characteristic particle diameters for different samples are given in Table 4-2.



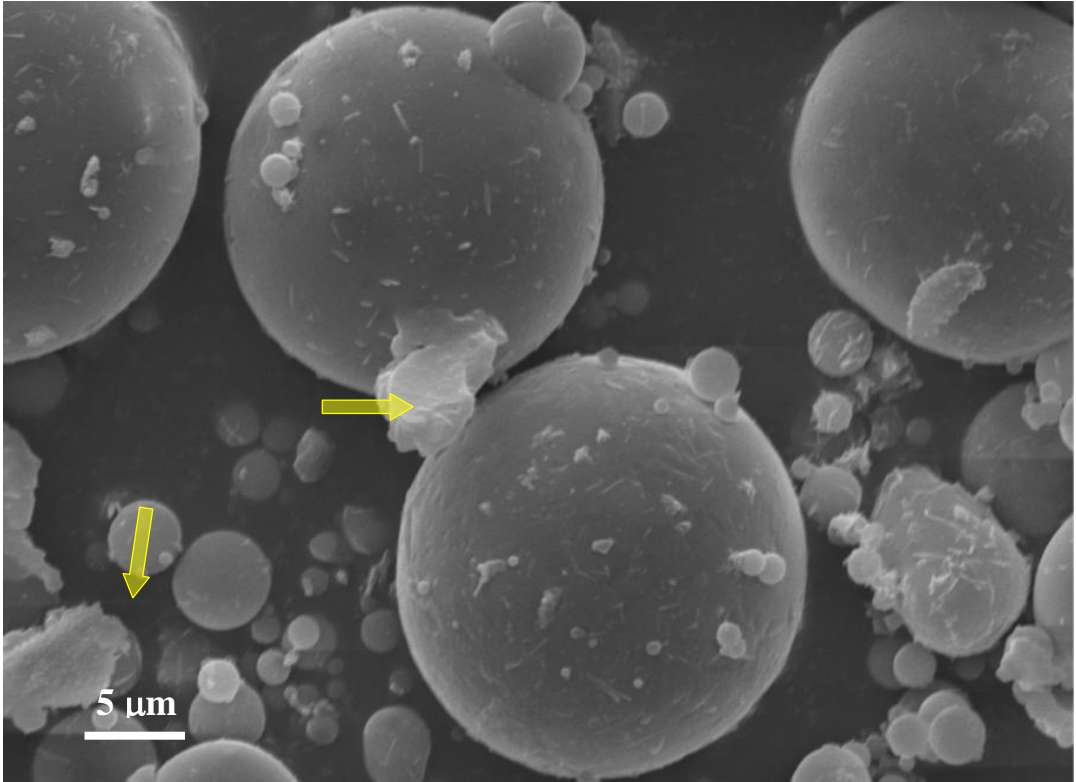
(a) Fly ash A



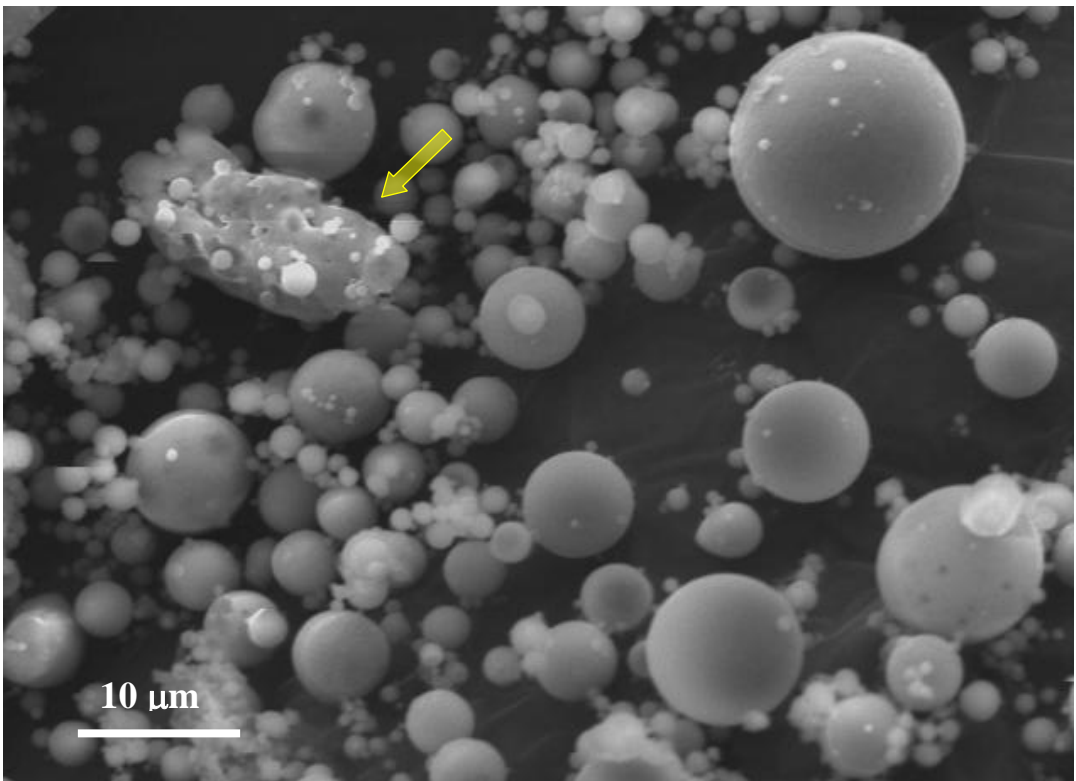
(b) Fly ash A



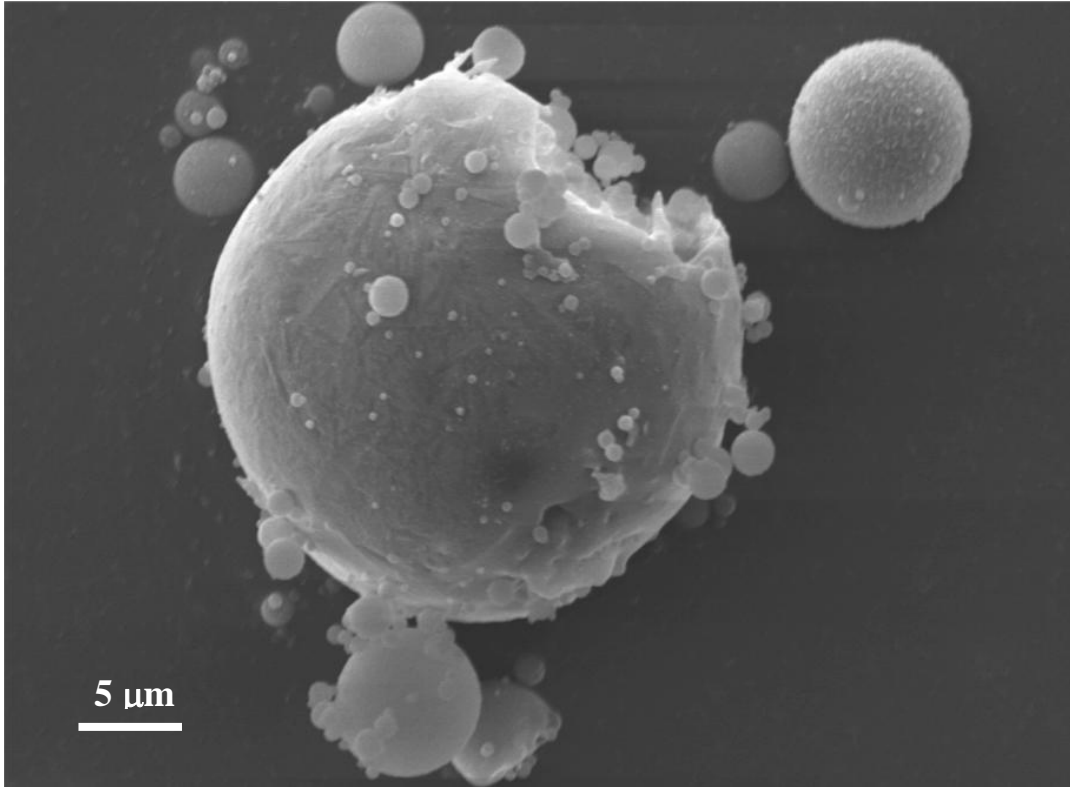
(c) Fly ash B



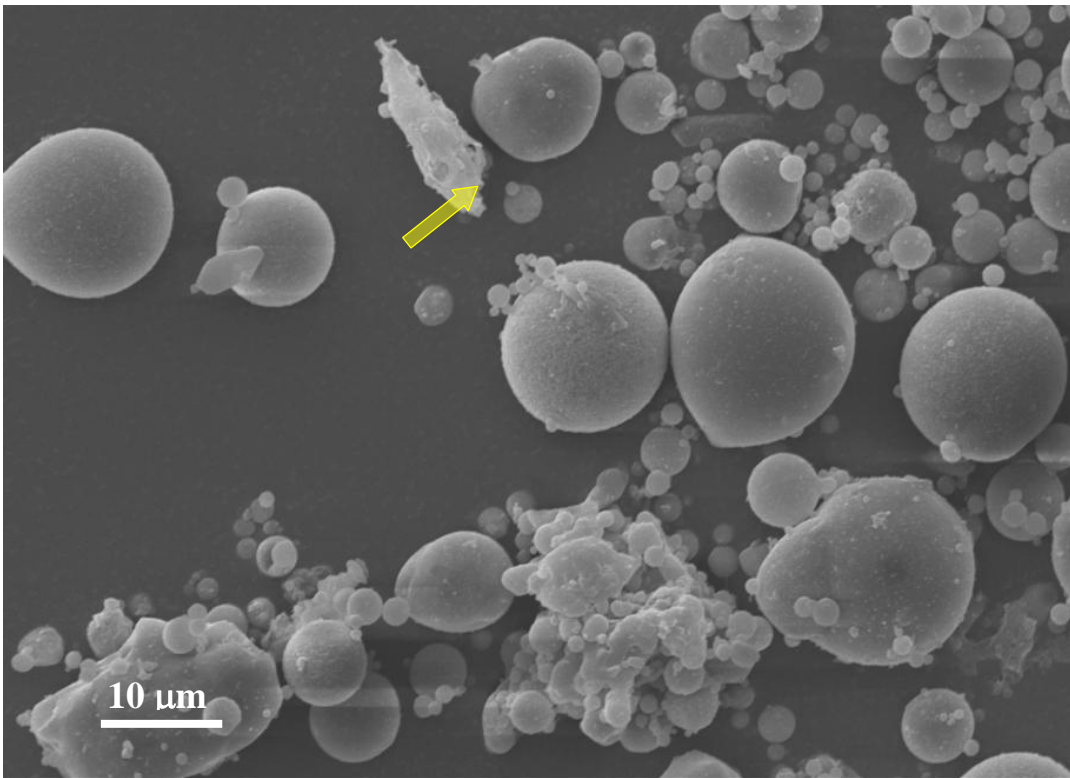
(d) Fly ash B



(e) Fly ash C

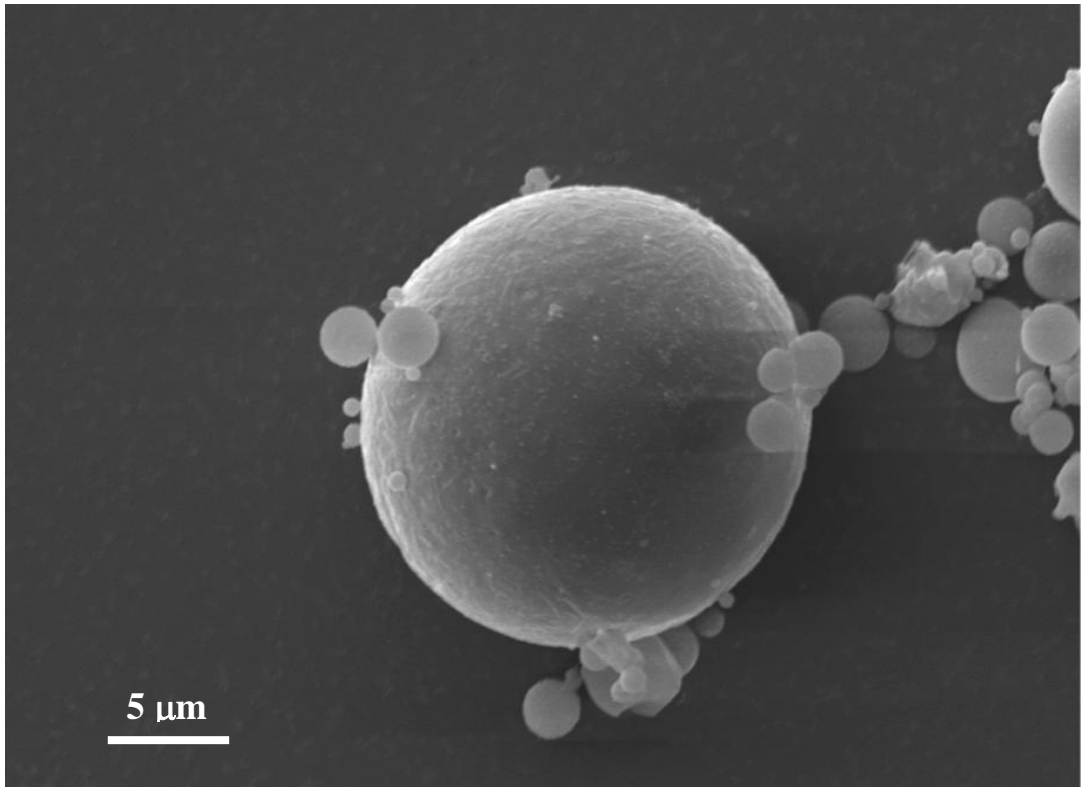


(f) Fly ash C

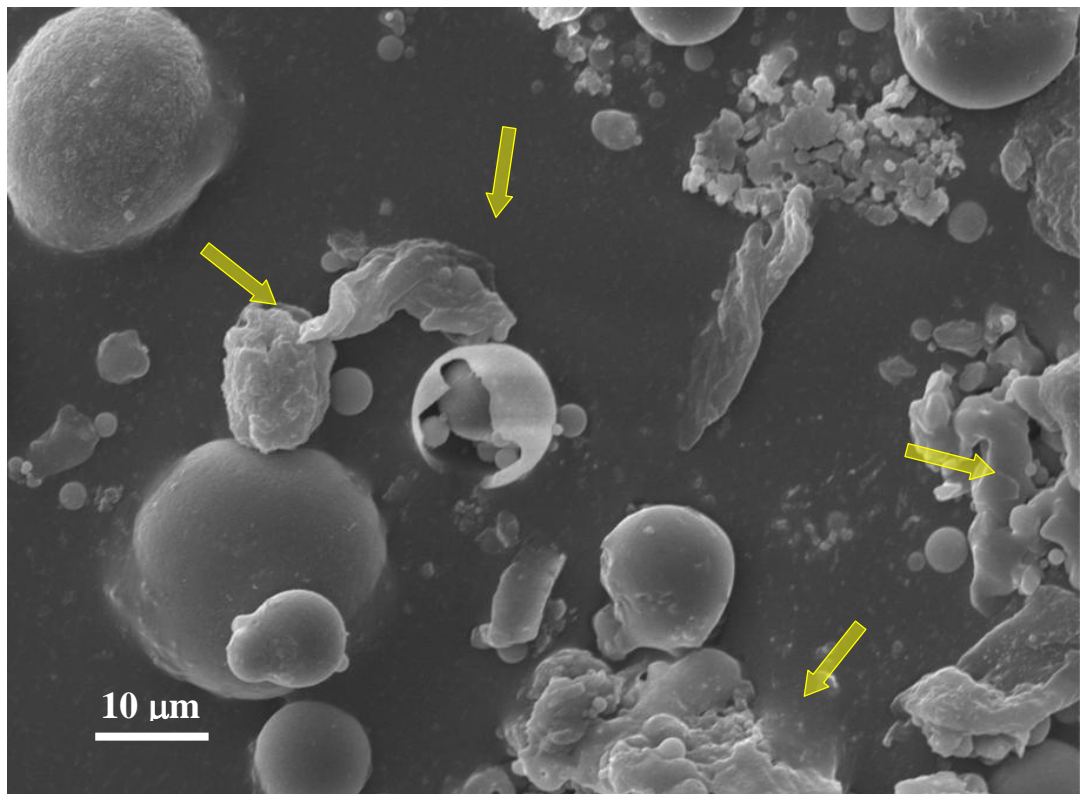


(g) Fly ash D

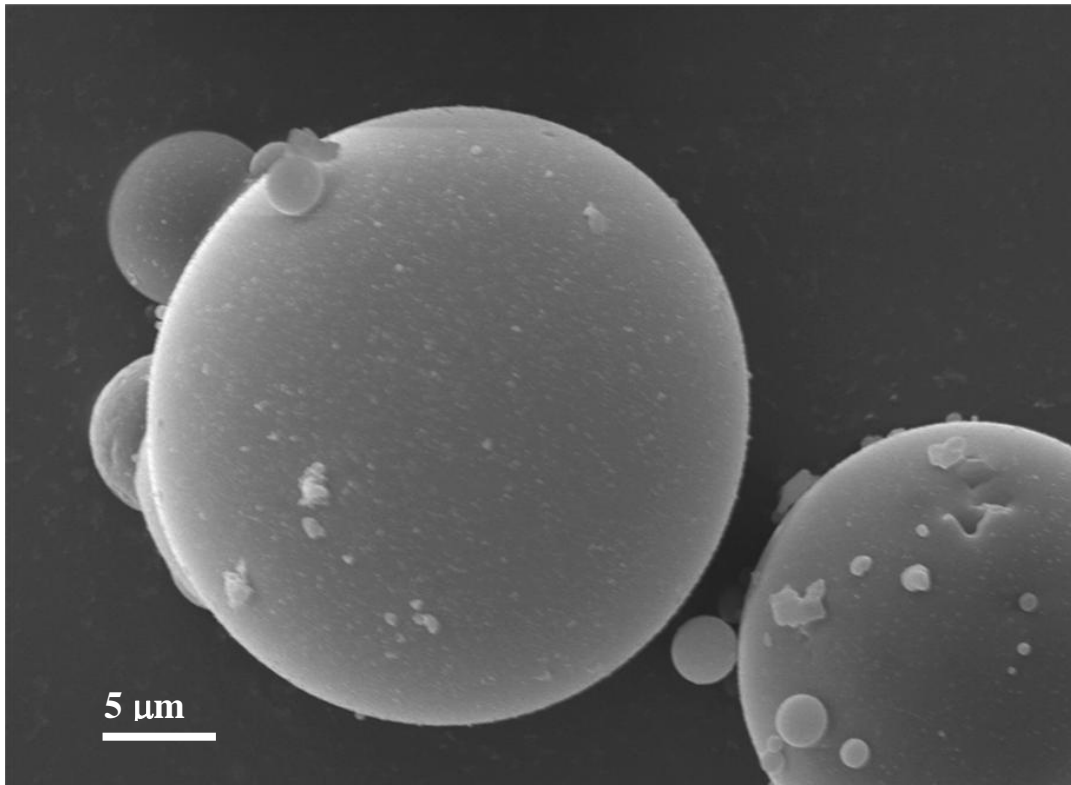




(h) Fly ash D



(i) Fly ash E



(j) Fly ash E

Figure 4-2. SEM images of the five selected fly ashes.

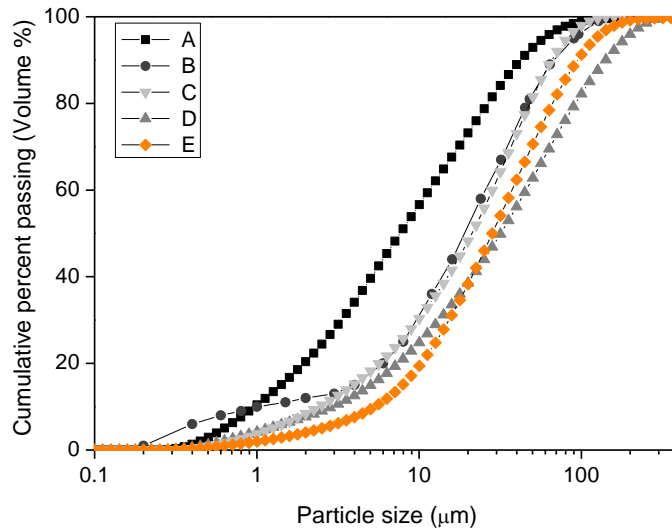


Figure 4-3. Cumulative particle size distributions (volume %) of fly ash samples.

Fly ash A is much finer than the other four samples. Particle size at the D<sub>50</sub> level is in the order A << B < D < E < C, and the volume fraction of particles < 10 μm is in the order A >> B ≈ D > C > E. Regardless of the influence of composition, the particle size could be one of the factors that affect the reactivity of fly ash, albeit it has been reported to have very limited affect (Keyte 2008). This aspect will be further examined in Chapter 5.

**Table 4-2:** Particle characteristic parameters of fly ashes.

Parameters	A	B	C	D	E
D <sub>10</sub> / $\mu\text{m}$	1.0	1.0	2.9	2.1	5.3
D <sub>50</sub> / $\mu\text{m}$	7.6	18.0	31.9	21.2	28.2
D <sub>90</sub> / $\mu\text{m}$	42.1	64.5	141.0	65.6	66.3

### 4.2.3 Surface area

The surface area was determined by measuring the physical adsorption of N<sub>2</sub> molecules on its surface according to the Brunauer-Emmett-Teller (BET) method (Brunauer et al. 1938). The particle size analyser also gives the approximated surface area of each fly ash by assuming that all particles are perfect spherical. The result is given in comparison with the analysis by the BET method. The testing results are listed in Table 4-3.

**Table 4-3:** Surface area of the five fly ashes as determined by the BET method and the laser particle size analyser.

Method	A	B	C	D	E
BET / m <sup>2</sup> /g	1.9	2.5	1.2	1.1	0.8
Particle size analyser / m <sup>2</sup> /g	2.1	2.4	0.9	1.0	0.6

Fly ashes A and B have more than double the surface area of C and D, and more than 3.5 times more than E. Comparing the BET surface area with the values estimated from the laser particle sizer fly ash A exhibits a 10% lower surface area while the other three exhibit higher surface area. Many factors may cause the different results obtained using these two testing methods. First, the estimation method for the laser particle sizer is based on the assumption that all particles are perfectly spherical. Using the volume and equivalent diameter, it then calculates the equivalent surface area, and the influence of non-spherical shapes has not been taken into consideration. As shown in Figure 4-2, fly ash B, C, D and E do have irregular particles, which have a higher real surface area compared to the assumed 'perfect spherical' particles. For fly ash E, beside the influences of shape factor, residual carbon may also play a significant role in affecting its surface area, as it has been noted that there were visible carbon particles which were separated from the rest of the ash when this ash was mixed with acetone for density measurement.

### 4.2.4 Particle density

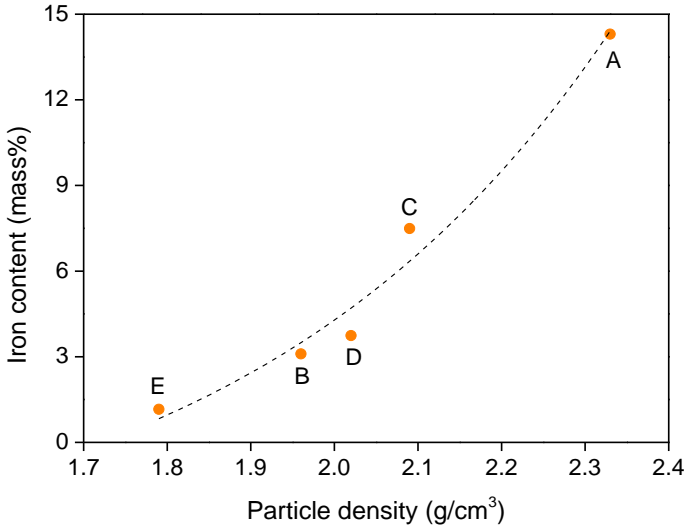
The particle density of fly ash was calculated by measuring the displacement of fly ash in a 100 ml volumetric flask containing acetone at 20°C. In this method, the measured density includes the effect of closed voids in the hollow particles, meaning that the measured should be theoretically lower than the true density (Shirai et al. 2011). In practice the particle density is actually more important than the true density, for example, it can be used to determine the inter-particle voids (Section 4.3) and the volume of solid materials, either in geopolymer

synthesis or Portland cement/concrete. Table 4-4 lists the particle density of fly ash samples. The data are the mean of three repeated testing values.

**Table 4-4:** Particle density of fly ashes as determined by Archimedes method.

Fly ash	A	B	C	D	E
Density / g/cm <sup>3</sup>	2.33	1.96	2.09	2.02	1.79

Figure 4-4 plots the relationship between the particle density and iron content for the five fly ashes. It can be seen that the particle density has a quadratic function of iron content in the studied range. This trend was also observed in the data reported by Furuya et al. (1987). The iron present in fly ash not only affects the density but also affects the thermal stability of geopolymer products (Rickard et al. 2011). The iron content may not be an essential factor for blended Portland cement concrete production. In this project, however, as the density and high temperature resistance are two key properties of foamed geopolymer concretes, the influence of iron will be studied in more detail. In particular, the role of iron content in affecting the reactivity of fly ash will be investigated.

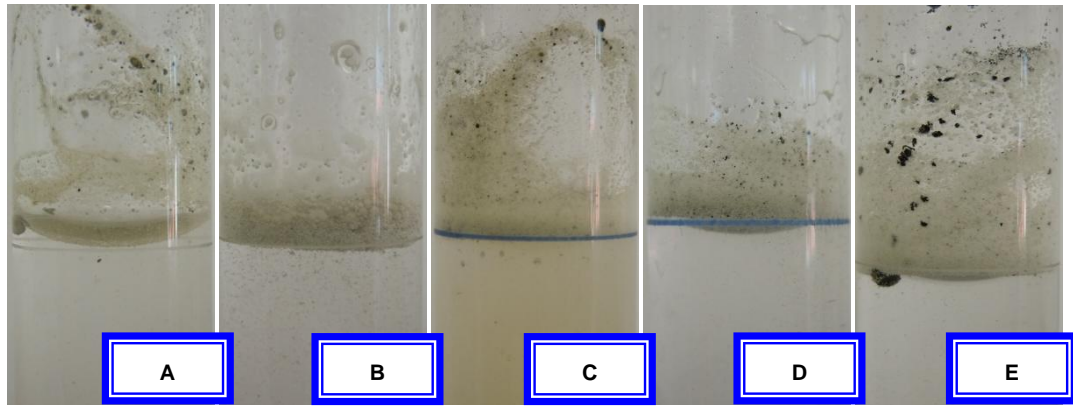


**Figure 4-4.** Relationship between iron content and fly ash density.

**4.2.5 Residual carbon in the fly ashes**

Figure 4-5 gives an illustration of the residual carbon particles in fly ashes when they were mixed in acetone for the particle density determination. There are no naked eye-observable residual carbon particles floating on the liquid top or on wall of the tube for fly ash B. By contrast, the other four fly ashes all have some carbon particles. By inspection it seems that B is the ‘cleanest’ while E appears to have the highest amount of carbon.



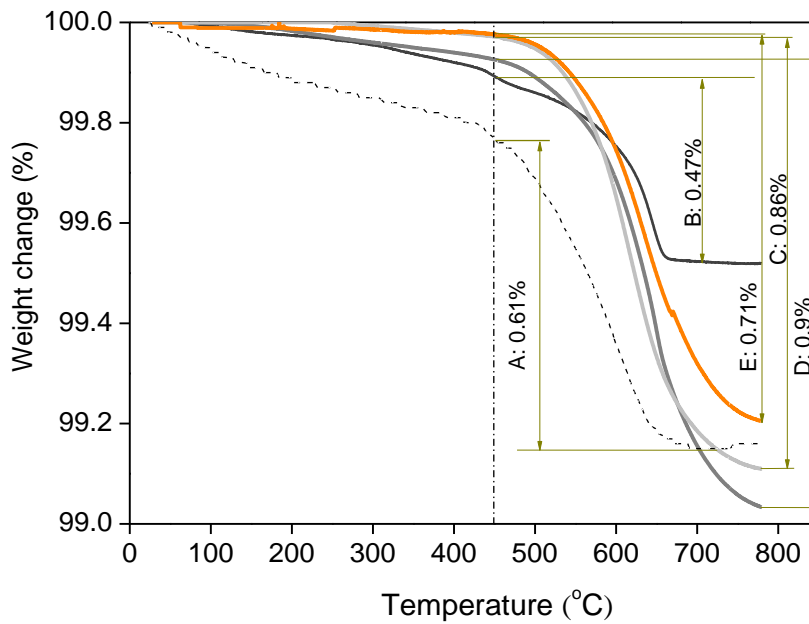


**Figure 4-5.** Fly ashes mixed with acetone in tubes (most of the black dots are carbon particles).

Residual carbon particles have a porous structure and much higher specific surface area than fly ash particles (Hwang et al. 2002). There are limitations placed on the carbon content for fly ash to be used in cement and concrete industry because the carbon particles can affect air entrainment, water-cement ratio, setting behaviour, and colour of the concrete. In particular, the carbon particles are found to absorb the air-entraining surfactants, thus reduce the air content and the foam stability in the paste (Jolicoeur et al. 2009). This could be a problematic issue for the manufacture of geopolymer foam concrete. One of the criteria is that the LOI (loss-on-ignition), representing mainly carbon content, must be lower than 6 wt.% according to ASTM C 618. The measured LOI of any fly ash studied in this project is lower than 1 wt.% (Table 4-1), which is much lower than the required level. It should be noted that LOI is not only due to carbon residual but also consists of the burning of some carbonate and sulfates and bio-contamination as well.

For geopolymer synthesis, since a higher surface area needs more liquid to saturate, the presence of carbon particles will increase the liquid requirement for a given mass of fly ash. For the fly ashes studied in this project, all were collected through electrostatic separation process to remove unburned carbon. Most fly ashes collected from power stations in Australia are very 'clean' in this aspect. The residual carbon, if measured by LOI, is usually <3 wt.% (Heidrich 2003), but it is still thought to have some influence on geopolymer production.

To further compare the content of residual carbon, oven-dried (105°C) fly ash samples were analysed by thermogravimetric analysis (TGA) in air conditions (Figure 4-6). The mass loss during heating between 450 to 800°C was regarded as residual carbon content.



**Figure 4-6.** Thermogravimetric analysis (TGA) of fly ashes up to 800°C.

Figure 4-6 shows the mass of residual carbon in all the five fly ashes is less than 1 wt.%. In comparison with the data in Table 4-1, it is surprisingly noted that the fly ash E has 0.71% weight loss by TGA while it has LOI of 0.43%. This unusual difference, carbon residual by TGA is supposed to be lower than LOI, is probably due to sampling error, such as drying. Other fly ashes have very consistent carbon residual values as LOI measured.

It is reported that the surface area of unburned carbon is 10 to 100 times over the specific surface area of fly ash (Hwang et al. 2002). The BET surface areas of fly ash C and E are 1.16 and 1.07 m<sup>2</sup>/g; whereas when determined by laser particle sizer, these values are 0.939 and 0.643 m<sup>2</sup>/g, respectively. Regardless of the influence of particle shape, the residual carbon particles in fly ash C and E possess surface areas which can be calculated to be 25.8 and 60.1 m<sup>2</sup>/g, which are consistent with the reported range of 24-58 m<sup>2</sup>/g (Hwang et al. 2002).

### ***4.3 Liquid requirements of the selected fly ashes and the compressive strengths of the derived geopolymer binders***

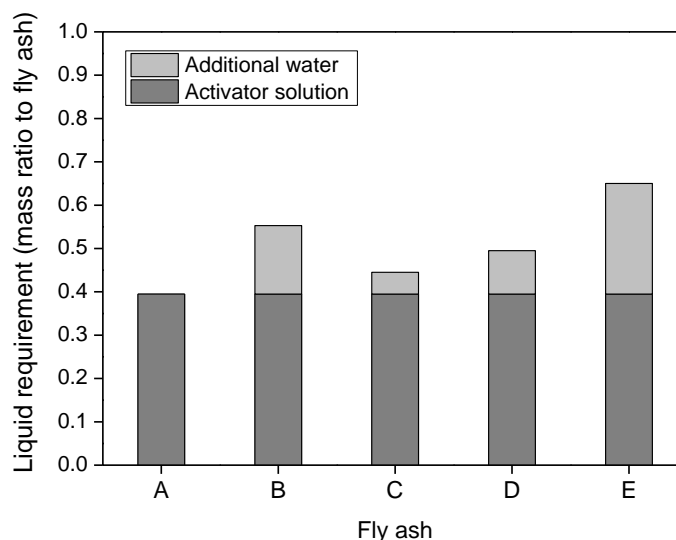
The five selected fly ashes show significantly different particle characteristics that are expected to cause varied liquid requirements (Keyte 2008). It is well known that the water/cement ratio is one of the most important factors that affect the mechanical properties of the binders and concretes (Neville 2011). The mechanical properties of fly ash-based geopolymer concretes, as well as their setting behaviour and thermal stability can vary substantially as the fly ash source varies (Van Jaarsveld and Van Deventer 1999; Diaz-Loya et al. 2011, Provis et al. 2012). The compressive strengths of geopolymer binders are a critical property that must be assessed to evaluate their potential to be a replacement for Portland cement in foamed concretes. Determining the

compressive strength of hardened binders also provides an assessment of the reactivity of the selected fly ashes. In this section, the effects of particle characteristics, in particular density and shape, on the liquid requirement of geopolymer pastes and the compressive strength of resultant binders were investigated.

### 4.3.1 Effects of particle characteristics on the liquid requirement of geopolymer pastes

It has been found that the type and concentration of activator solution are important factors affecting the compressive strength of resultant geopolymers (Keyte 2008). To minimize the variables in geopolymer synthesis in this study, fly ash was activated at a constant activator/ash mass ratio of 0.395. Workability was assessed by the flowability, which was tested by a polypropylene cone with top and bottom diameters of 65 mm and 80 mm respectively, and a height of 40 mm. This is a self-made mould used for testing the flowability of geopolymer paste. The sizes are modified according to the standard size of cone recommended by American Petroleum Institute for testing the flowability of neat cement paste (API 10B-2, 2005).

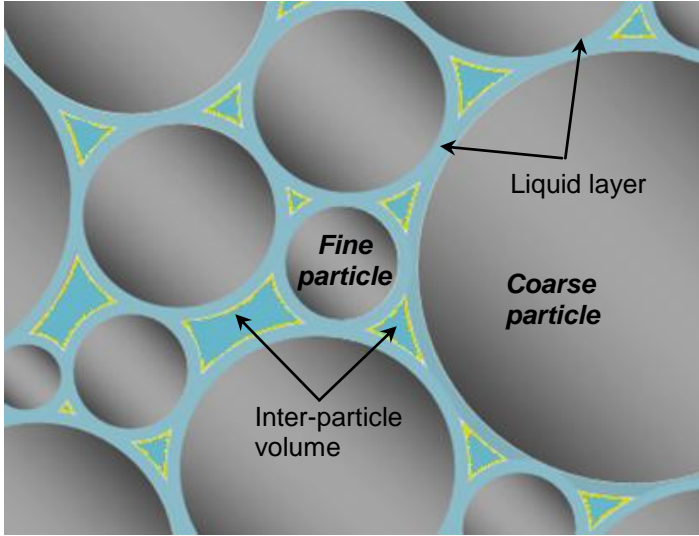
The liquid requirements for the five fly ashes are presented in Figure 4-7. It was found that at this activator/ash ratio, fly ash A generated a paste with very good workability. The flowability of paste A reached up to 160 mm in diameter, suggesting that it is a material that can be poured into molds and vibrated easily. For the other four pastes to achieve a very similar workability as the geopolymer paste A, fly ashes B, C, D and E need 0.158, 0.05, 0.1 and 0.255 (mass ratio to fly ash) additional water, respectively. It is interesting to note that fly ash A has the finest particle and also relatively higher surface area but it requires much less liquid. By a first glance, the liquid requirement of fly ash has no evident relationship with its specific surface area (Table 4-3).



**Figure 4-7.** Liquid requirement of fly ash to achieve a paste with good workability (flowability between 140 to 170 mm as measured using a cone with top and bottom diameters of 65 mm and 80 mm and height of 40 mm).

When liquid is mixed with solid powder to make a homogeneous paste, it needs to wet the surface of the particles. However, the lack of a direct relationship between the liquid requirement of fly ash and its specific surface area suggests that there are some more factors affecting the liquid requirement.

Figure 4-8 sketches the fly ash particles in a paste, with reference to the aggregate packing model of concrete mixture (Midorikawa et al. 2009). Beside the requirement for surface wetting, liquid is also needed to fill up the inter-particle volume. The packing state of particles may change the 'compact liquid' requirement.



**Figure 4-8.** Sketch of the fly ash particles in a paste. Inter-particle volume refers to the space between packed particles, including the volume occupied by liquid layer.

For a given volume of fly ash, if there are more fine particles, the compact liquid requirement should be less as the fine particles can partially fill up the inter-particle volume between coarse particles. Under these conditions, particle size and its distribution will play the most important factors in determining the liquid requirement because the liquid layer depends mainly on the surface area.

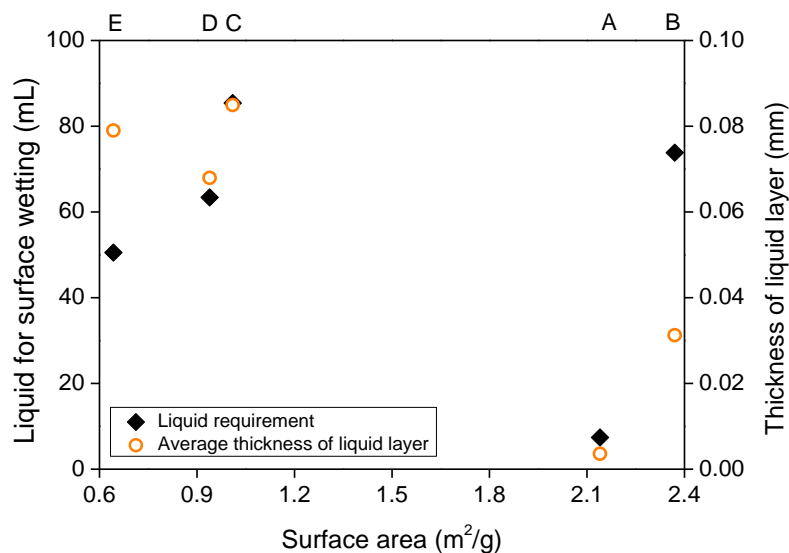
However, for a given mass of fly ash, as is the situation in this investigation, the density of fly ash becomes important because it determines the total volume (packing volume). There are two different densities should be considered: one is the particle density, and the other is the packing density, which refers to the mass of unit volume fly ash at naturally packing condition. The inter-particle volume can be simply estimated by subtracting the particle volume from the total volume.

Table 4-5 lists the particle density and the packing density of each of the five fly ashes. A general trend can be found that the liquid requirement depends largely on the inter-particle volume. The inter-particle volumes of fly ash B and E are much larger than the other three and the respective liquid requirements are also much higher.

**Table 4-5:** Particle density and calculated packing density of the five fly ashes, with the inter-particle volume as estimated by subtracting the particle volume from the total volume, and the liquid required to achieve sufficient flowability of the pastes made from each ash.

Fly ash	Particle density/ g/cm <sup>3</sup>	Packing density/ g/cm <sup>3</sup>	1000 g of fly ash		
			Inter-particle volume / cm <sup>3</sup>	Liquid requirement / cm <sup>3</sup>	Liquid layer/ cm <sup>3</sup>
A	2.33	1.44	264.3	272	7.7
B	1.96	1.16	355.9	430	74.1
C	2.09	1.38	258.2	322	63.8
D	2.02	1.28	286.2	372	85.8
E	1.79	0.94	501.2	552	50.8

It is easy to calculate out the volume of liquid layer for the surface wetting by subtracting the inter-particle volume from the total liquid requirement. Figure 4-9 plots the liquid requirement for surface wetting and the average thickness of liquid layer as a function of specific surface area.



**Figure 4-9.** Liquid requirement for surface wetting and the average thickness of liquid layer as a function of specific surface area.

It is immediately noted that there is no clear trend or a direct relation between the surface area and liquid requirement for surface wetting, neither with the average thickness of liquid layer. There must be other factors affecting the liquid requirement for surface wetting or the thickness of liquid layer. One possible factor is the viscosity of the activator. As the liquid requirement is determined by measuring the flowability of paste, the viscosity of activator may also have some influence. For sodium silicate solutions at a constant modulus (SiO<sub>2</sub>/Na<sub>2</sub>O molar ratio), both static and dynamic viscosity decrease as concentration decreases (Yang et al. 2008). Considering that the amount of activator used in this investigation was kept constant in the different fly ash systems, and the additional water reduced the viscosity, it would be predicted

that pastes B and E should exhibit much higher flowability. Instead, these two pastes were noted to exhibit much lower flowability (~140 mm).

The shape of fly ash particles is then an important factor that should be considered. As shown in Figure 4-2 most of the particles in sample A are very smooth. In samples B and E, many particles are of angular shape and some cenosphere structures are broken. These two shape factors will cause the sliding between particles to be difficult, yielding a low flowability of paste, unless the liquid layer on the surface is thick enough to enable easy movement. An increased liquid requirement is also noted when making geopolymer pastes with fluidized bed combustion fly ash, which is much more irregular compared to pulverized coal combustion fly ash (Chindaprasirt et al. 2011). This result indicates that shape factors have marked influences on the liquid requirement when it is measured by flowability.

The carbon particle present in fly ash seems also important. In samples A and B, the residual carbon is 0.64 wt.% and 0.47 wt.%, while in samples C, D and E it is 0.86 wt.%, 0.9 wt.% and 0.71 wt.%, respectively. Except for fly ash B, the general trend is that the higher carbon content and the higher the liquid requirement for surface wetting. The thickness of liquid phase on the fly ash particle surface could be equivalent. However, because of the absorbance of porous carbon particles, the average or 'apparent' thicknesses in fly ash C, D, E need to be much higher.

From the above analysis, it can be concluded that the inter-particle volume is the most important factor determining the liquid requirement. When using mass fraction as the basis of the formulation, the inter-particle volume is influenced by two particle characteristics: the density and particle size distribution. The shape of the fly ash particle also has a considerable influence, particularly when the liquid requirement is assessed by flowability. In comparison, the specific surface area is less important. The initial dissolution of fly ash may also have some influence, but any detailed comment in this regard needs further examination of the reactivity of the fly ashes.

#### **4.3.2 Compressive strengths of hardened binders synthesized from the fly ashes**

There is no doubt that a thorough understanding of the reactivity of fly ash is very useful for geopolymer proportioning. However, one challenge raised is how to define or measure the reactivity. In the cement and concrete field, there are many approaches to measure the reactivity of fly ash, such as dissolved silica (reactive silica), conductivity, heat of hydration, calcium consumption, hydration layer depth, gel surface area and volume, which have been well reviewed by Bumrongjaroen et al. (2007). However, most are not directly appropriate for assessing the reactivity of fly ash in geopolymer production due to the fact that they are developed based on the reaction between cement or calcium hydroxide and fly ash.

An indirect evaluation method for reactivity is to measure the macroscopic properties, such as compressive strength, of geopolymer mortars or concretes (Keyte 2008; Diaz-Loya et al. 2011). However, this method introduces many variables such as the properties of the aggregate and the interaction between

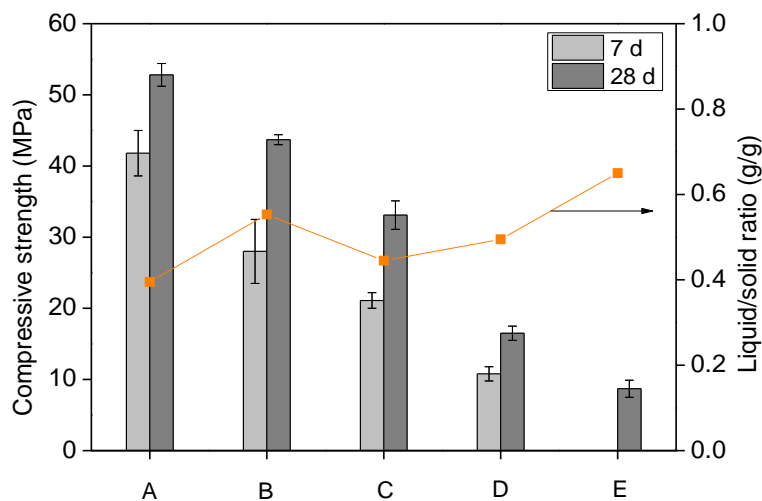
geopolymer binder and aggregate. Testing the compressive strength of geopolymer binders synthesized without aggregate (assuming similar mixture design and curing conditions) is more 'direct', but the brittle fracture of paste specimens can sometimes lead to statistical errors. Nonetheless, this is the method selected here due to its relevance.

Table 4-6 gives the composition of the binder mix and also indicates the adjusted concentrations of dissolved Si, Na<sup>+</sup> and OH<sup>-</sup> because of the utilization of additional water. The activator solution was mixed with fly ash for 5 min and then additional water was added as required and mixed for 2-3 min until a uniform paste was observed. The additional water was added to ensure easy moulding and is expected to influence hardened strength to a certain extent. The curing was conducted at 40°C for 24 h, then at ambient conditions until testing.

**Table 4-6:** Compositions of geopolymer mixtures and concentration of Si, Na<sup>+</sup> and OH<sup>-</sup>.

Mixture	Fly ash / g	Activator / g	H <sub>2</sub> O / g	Liquid/ash / g / g	[Si]/ mol/L	[Na <sup>+</sup> ]/ mol/L	[OH <sup>-</sup> ]/ mol/L
A	1000	395	0	0.395	4.3	8.8	4.6
B	1000	395	158	0.553	3.1	6.6	3.4
C	1000	395	50	0.445	3.4	7.0	3.7
D	1000	395	100	0.495	3.0	6.7	3.5
E	1000	395	255	0.650	2.5	5.1	2.7

The compressive strengths of hardened geopolymer pastes at 7 d and 28 d are presented in Figure 4-10. The geopolymer specimens synthesised with fly ash A exhibited the highest compressive strength. For the geopolymer synthesised from fly ash E, however, the compressive strength was too low to be tested at 7 d. After curing for 28 d, it only achieved 8.7 MPa.



**Figure 4-10.** Compressive strengths of geopolymer binders at 7 d and 28 d.

The specimens were made with the same quantity of activator solution (the mixture of LSS and NaOH solution), which means that the total solid composition of the geopolymer mixtures is equivalent. It is believed that it is the difference of reactivity of fly ash that leads to variation of compressive strength.

However, one argument is that the additional water used in mixtures B, C, D and E has changed the activation conditions. It is indeed a variable that can affect the geopolymerization rate at the early age. Calorimetry testing of the NaOH activation of metakaolin shows that at the same NaOH content, systems that activated with higher concentrations of NaOH (meaning lower liquid/ash ratio) generate higher reaction rates at the dissolution and early polymerization stages while the total heat released are equivalent to that activated with lower concentration NaOH solutions (Yao et al. 2009). Although the reaction mechanisms of alkali activation of mekaolin and alkali activation of fly ash are substantially different, from a long term of view, this variable (NaOH concentration) may not be a major issue, particularly given the small varied range (all of the solutions give a high pH that theoretically higher than 14).

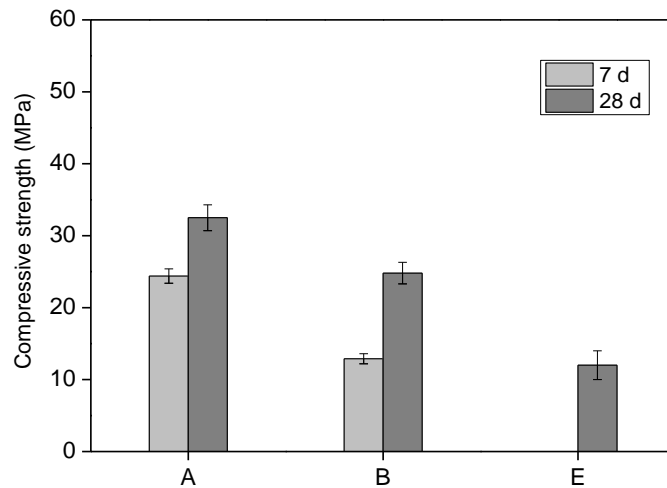
To avoid this, a second set of specimens was prepared by activation of selected fly ashes (A, B and E) with an activator of lower concentration. Table 4–7 lists the composition of these geopolymer mixtures. The water was premixed with the activator instead of being directly added to the pastes. The low concentration activator was prepared and cooled down to room temperature at least 24 h prior to use. This enables the design of a mix with good workability but introduces another viable: the total solids content.

**Table 4–7:** Composition of geopolymer mixtures activated with lower concentration solution.

Mixture	Fly ash / g	Activator / g	H <sub>2</sub> O / g	Liquid/ash / g / g	[Si]/ mol/L	[Na <sup>+</sup> ]/ mol/L	[OH <sup>-</sup> ]/ mol/L
A <sub>L</sub>	1000	280	70	0.350	3.4	7.0	3.7
B <sub>L</sub>	1000	359	91	0.450	3.4	7.0	3.7
E <sub>L</sub>	1000	479	121	0.600	3.4	7.0	3.7

The compressive strength of hardened geopolymers was tested after the same curing and aging procedure as the first set, and the results are shown in Figure 4–11.





**Figure 4-11.** Compressive strength of geopolymers synthesized with low concentration activator solution at 7 and 28 d.

As expected, the resultant geopolymer specimens exhibited the following order of compressive strength:  $A_L > B_L > E_L$ . Comparing the strengths in Figure 4-10 and 4-11 and the adjusted Si,  $\text{Na}^+$  and  $\text{OH}^-$  concentrations, some other variables related to the activator solution must be considered, such as the mixing procedure of paste. Mixing the activator solutions (NaOH and sodium silicate) separately will lead to different activation processes, from the perspective of chemical reaction. It has been argued that when NaOH is separately mixed with fly ash first and then liquid sodium silicate solution is added, the resultant geopolymers possess higher strength due to the high initial dissolution of the ash, particularly at relatively low LSS/NaOH ratios (Rattanasak and Chindaprasirt 2009). From this point of view, the order of addition of the extra water here may also influence the activation of fly ash. In the first set of experiments, the addition of water after the concentrated activator solutions (NaOH first, sodium silicate second) was mixed with the ash may make a significant contribution to the much higher strength of specimen B. However, in the second set, this possible influence was avoided.

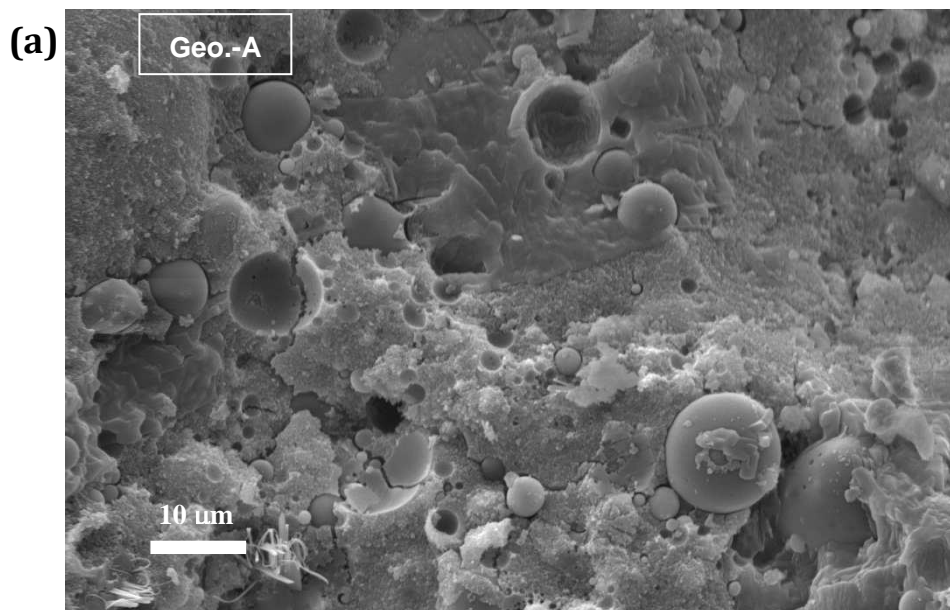
By combining the testing results in current study and those in the reported research (Bakharev 2006; Keyte 2008; Rickard et al. 2011), it is reasonable to make a conclusion that the reactivity of fly ashes under geopolymerization conditions is in the order  $A > B > C > D > E$  if it is assumed that the fly ash from each power station will not change dramatically with time. This conclusion has some value for the selection of fly ash for geopolymer production. However, mechanical testing is only a macro-level observation of the reactivity of fly ash. The inherent factors influencing the reactivity of fly ash should be addressed and evaluated before more practical implications can be drawn and widely applied for geopolymer production.

#### ***4.4 Factors affecting the mechanical properties of hardened binders***

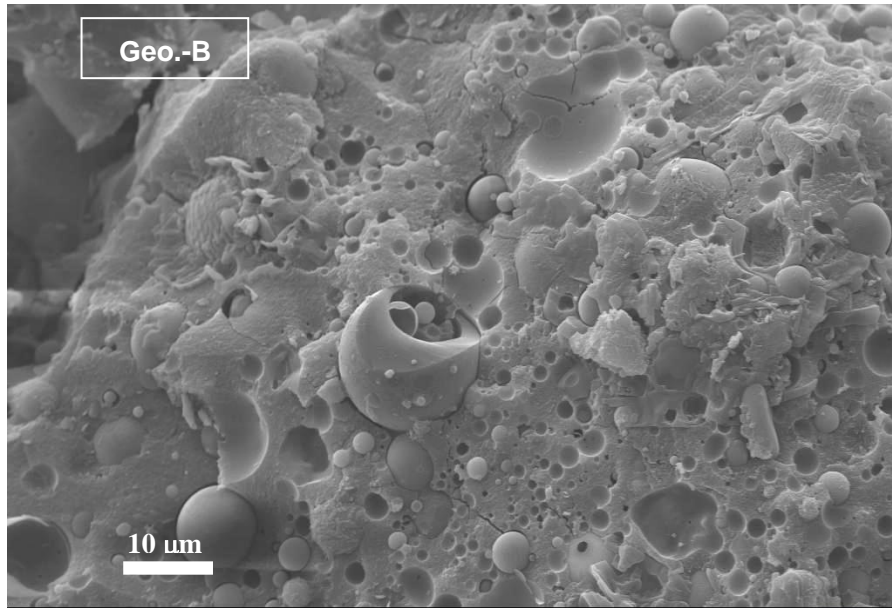
The discussion presented above demonstrates that the compressive strength of binders synthesized from different fly ashes can vary substantially. The varied mechanical properties of geopolymer binders could be due to their different micro-scale properties, which are inherently affected by the raw materials and activation conditions. In this investigation, as the activator solution was kept constant and the curing and aging conditions were the same for all mixes, the most likely factors are: (1) the varied amounts of additional water, which usually result in different microstructures of hardened binders; and (2) the dissolution of fly ash, which determines the composition of binder gels.

##### **4.4.1 Microstructures of hardened products**

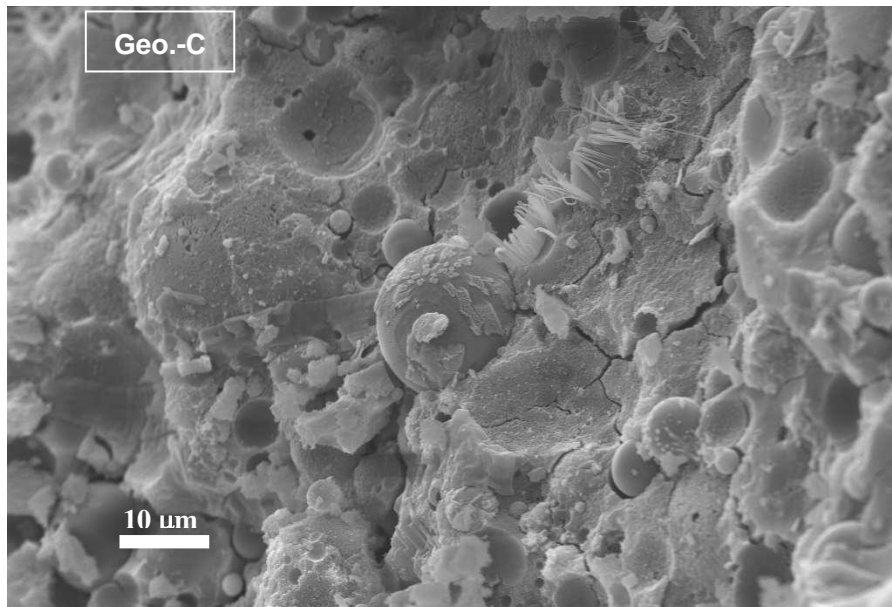
The fracture surfaces (without polishing) of the hardened binders were observed by SEM, while the mineral components were tested by XRD, which are respectively shown in Figure 4-12 and 4-13.



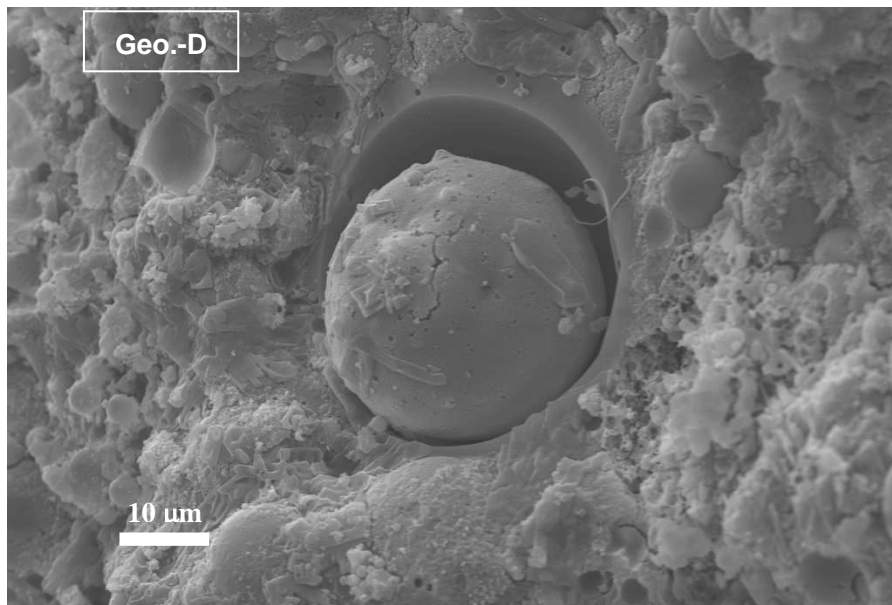
(b)

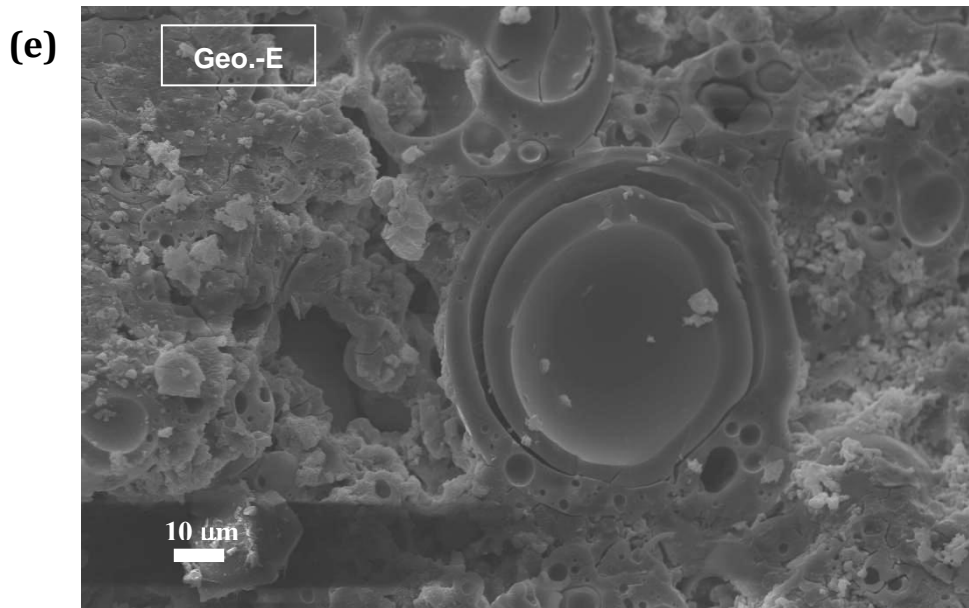


(c)

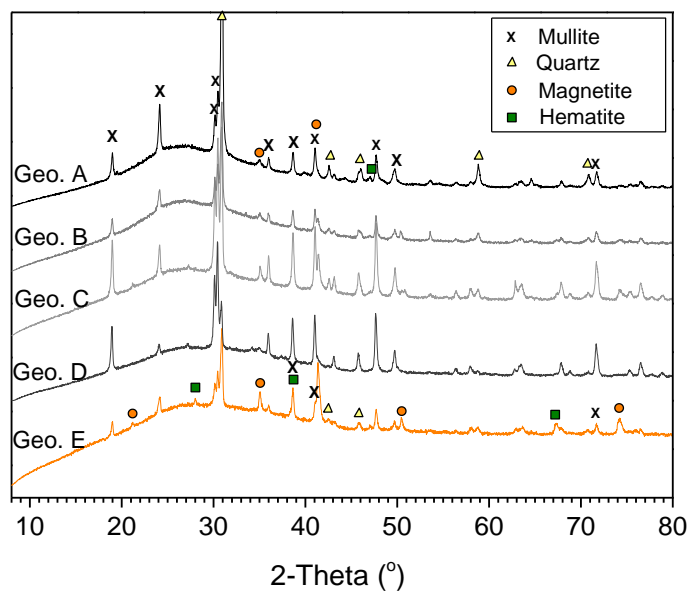


(d)





**Figure 4-12.** Representative SEM images of geopolymer binders (after 28 d) made by activation of fly ashes with a constant activator/ash ratio.



**Figure 4-13.** XRD diffraction patterns of geopolymer binders (after 28 d) made by activation of fly ashes with a constant activator/ash ratio.

From the SEM images and XRD data, the geopolymerization products consist of amorphous geopolymeric gels, a large number of residual fly ash particles, and pores in various scales, consistent with the widespread understanding of this material. Most residual particles embedded in gels have apparently smooth surfaces while only a few particles show the extraction of glass phases from surface, leaving mullite particles more conspicuous, as observed in other studies (Lloyd et al. 2009a; 2009b; Wang et al. 2011; Chindaprasirt et al. 2011). From XRD analysis, all of the resulting geopolymers consist of amorphous gels with

remnant fly ash crystalline phases. The crystalline phases are the same as those detected in the original fly ashes (Figure 3-2). In these products, no detectable zeolite phases or alkali carbonation products have been identified. This is thought to be due to the low temperature curing schedule and relatively mild activation conditions, unlike in those systems with longer-term hydrothermal curing (Criado et al. 2007a).

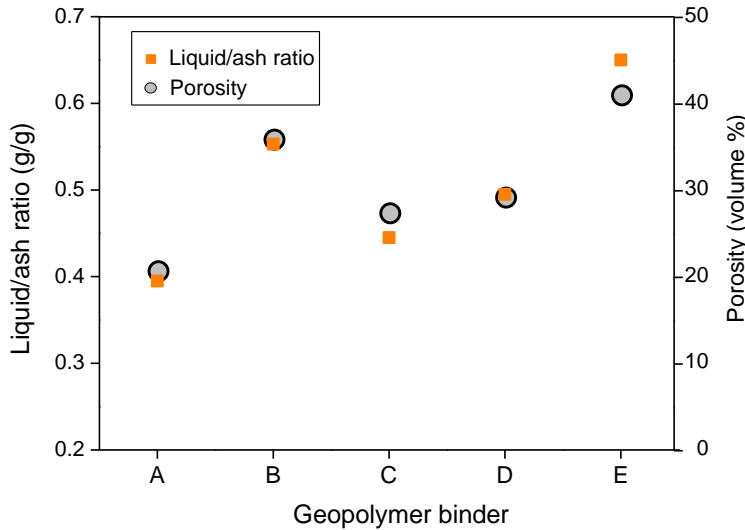
Given the fact that most fly ash particles have a multi-phase surface, which consists of mullite, quartz or magnetite and glass (Laperche and Bigham 2002), it seems more realistic that the smooth surfaces of most particles contribute to their very limited dissolution. This is not surprising when considering that the dissolution extent of Class F fly ash is only 10-20 wt.% in strong alkaline solution at a liquid/solid ratio of 40-1000, at 40°C for 24 h (Chen et al. 2011; Pietersen et al. 1990), while in this investigation, fly ashes were reacted with the activator at a liquid/solid ratio of 0.395-0.650 at 40°C for 24 h. This low liquid content and highly concentrated condition should be expected to yield a lower extent of dissolution of fly ash, and the further time of reaction at room temperature will not enhance the dissolution of fly ash too much. It is reported at a liquid/solid ratio of 1000 and pH=13.7, the 28 d dissolution extent of fly ash is only about 15 wt.% (Ben Haha et al. 2010). A recent study indicates that Class C fly ash with a high content of calcium only proceeds to 15-18 wt.% reaction extent after being activated at a liquid/solid ratio of 0.67-1.0, heated to 65°C for 48 h and cured at 25°C for 7 d (Chindaprasirt et al. 2011). It is reasonable to believe that the Class F fly ash should show a low reaction extent in geopolymerization systems after 28 d.

Since the reaction extent of fly ash is limited, the condensation of dissolved silica in the activator solution becomes even more important, somewhat similar to the role of sodium silicate in agglomeration of sand (Kouassi et al. 2011). A study observing a fly ash geopolymer paste mixture with environmental scanning electron microscopy (ESEM) has shown that the presence of a higher concentration of silicate in the activator results in a more compact binder structure (Lloyd et al. 2009b; Duchesne et al. 2010).

This means that if the concentration of dissolved silica species in the activator is not high enough and the dissolution of fly ash is very limited, the inter-particle volume cannot be fully filled by the precipitated gels. The major part of the water can evaporate out from an un-sealed sample during polymerization, while some of the water may remain in the aluminosilicate gels after condensation, mainly in physically bound water and some surface hydroxyl groups, that is in forms of  $\text{Si-OH}\cdots\text{H}_2\text{O}$  and  $\text{Al-OH}\cdots\text{H}_2\text{O}$  (Kirschner and Harmuth 2004; Dimas et al. 2009; Zhang et al. 2012). If this mechanism is true, geopolymer binders E and B should have higher porosity due to their higher inter-particle volumes.

An analysis of the porosity as measured by MIP for 28-day hardened binders is presented in Figure 4-14. Generally, the porosity increases with the increasing liquid requirement. During solidification of the paste, the inter-particle volume will be filled by the precipitation products derived from dissolved Si, Al, Na and Ca. As the dissolved Si and Na contents supplied by the activator in the five geopolymer mixes were constant, the porosity of the hardened binder should be mainly affected by the inter-particle volume ratio, the dissolution extent of fly ash and the amount of water added. A smaller inter-particle volume and higher

dissolution extent will result in a lower porosity. The less water used, the lower is the porosity.



**Figure 4-14.** Porosity of geopolymer binders as determined by MIP.

It has been reported that geopolymers by activation of 100% fly ash exhibit very stable porosity evolution during the first 28 days as determined by nitrogen absorption method (Sindhunata et al. 2008) and X-ray micro tomography (Provis et al. 2012). It means that the porosity is mainly depending on the initial dissolution of solid materials and solidification of all dissolved materials in the very early age. If it is assumed that: 1) the total volume of the mix, the sum of fly ash packing volume and excess liquid volume, does not change after the mix hardens; and 2) the volume of precipitated sodium silicates from the activator can be calculated from the mass and density, and it will take a part volume of the total liquid volume, then the influences of particle dissolution on the porosity can be assessed between the fly ashes.

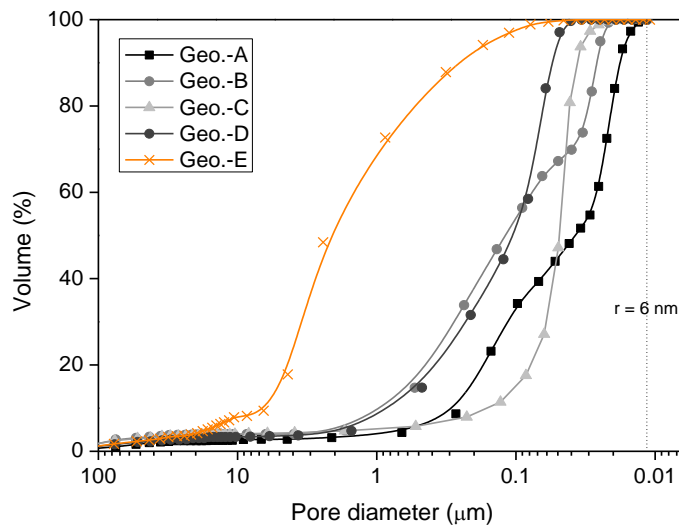
The calculated volume fractions of the different components for each mix are shown in Table 4-8, where  $R_{IP}$  is the volume fraction of inter-particle in the total volume of mix;  $R_{SA}$  is the volume fraction of sodium silicate supplied by the activator and incorporated into aluminosilicate gel, with a density taken to be the mean of two zeolites commonly noted in geopolymer products: analcime ( $2.27 \text{ g/cm}^3$ ) and faujasite ( $2.09 \text{ g/cm}^3$ );  $R_L$  is the total liquid volume fraction; and  $R_L - R_{SA}$  is the remaining volume fraction after part of the total liquid volume is filled by the generation of aluminosilicate gel from the sodium silicates supplied by the activator.



**Table 4-8:** The relationship between the volume fraction of liquid in fresh mix and the porosity of hardened binders.

Mix	$R_{IP}$	$R_{SA}$	$R_L$	$R_L - R_{SA}$	Porosity
A	0.376	0.095	0.387	0.293	0.217
B	0.380	0.071	0.459	0.388	0.359
C	0.328	0.084	0.408	0.324	0.274
D	0.330	0.077	0.429	0.352	0.292
E	0.450	0.060	0.495	0.436	0.416

The remaining volume fraction ( $R_L - R_{SA}$ ) is 0.02-0.076 higher than the measured porosity by MIP. This remaining volume fraction fraction can be regarded as the theoretical total porosity, including the finer pores that cannot be filled by the liquid mercury. This is a well-known drawback of MIP measurement. Geopolymer binder A has the lowest remaining volume fraction and this is consistent with the highest strength. This rule seems however not suitable for binder B. In addition to porosity, it is well known that for cementitious materials, their strength is also affected the pore size and shape distribution. As reviewed by Taylor (1997) from Odler and Rössler’s work, “the main factor influencing strength was porosity, pores with a radius below 10 nm were of negligible importance”. It is suggested that the total porosity should not be used and that the capillary or free water porosity or the volume of pores above a certain size being more appropriate. Figure 4-15 presents the pore size distribution of the geopolymer binders as measured by MIP.



**Figure 4-15.** Cumulative pore size distributions of geopolymer binders as measured by MIP.

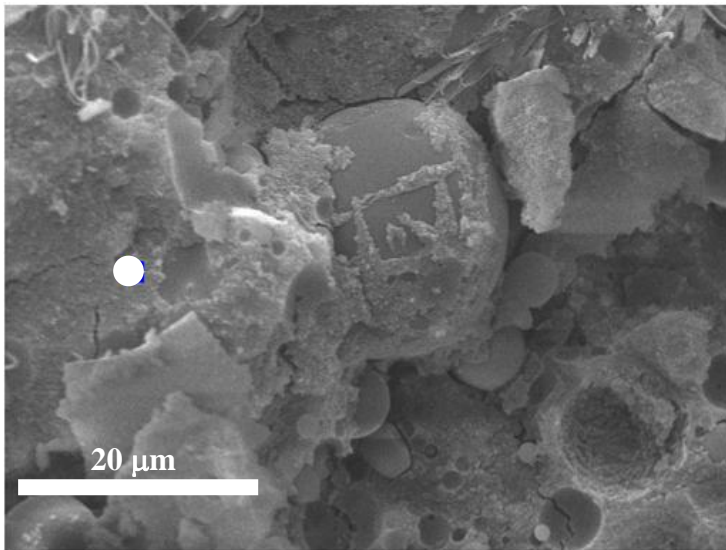
The pore size distribution changed significantly as a function of the liquid requirement of the ash. The large pores (>50 nm) present in the binders comprise 44% of total pore volume for binders A and C, 67% for geopolymer B, and more than 95% for geopolymers D and E. Particularly for geopolymer E, most pores are larger than 100 nm. The large pores may have a negative effect

on the strength.

However, as a whole, almost all of the detected pores are  $>6$  nm in radius, the size that could be filled by the mercury by the MIP pressure in this investigation. It means that the porosity in this pore size range should be the most important factor if it is assumed that the material matrixes are equivalent in mechanical properties. This cannot explain the relatively high strength of binder B, which has a high level of 'harmful' pores. Hence, the fact that geopolymer binders A, B and C have higher compressive strength is more likely to be related to changes in the geopolymeric gels in terms of composition and quantity rather than the formation of an 'optimal' microstructure in terms of porosity and pore size distribution.

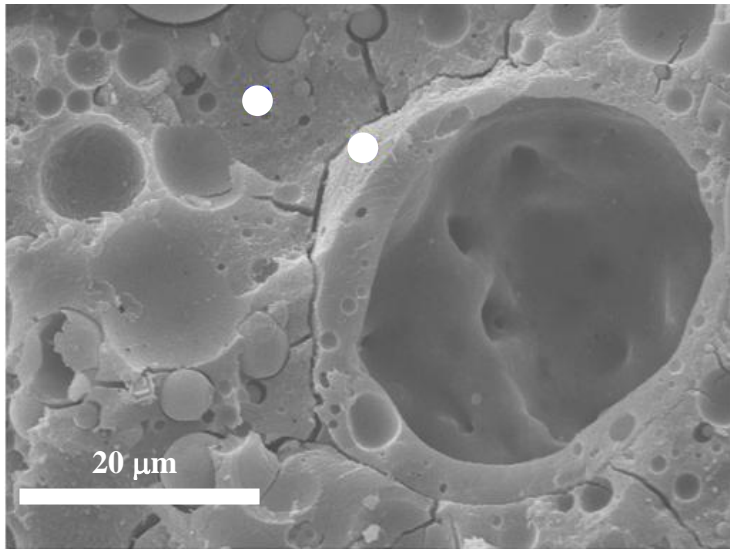
#### 4.4.2 Composition and quantity of geopolymeric gels

SEM-EDS analysis was used to study the composition of the geopolymeric gels in each binder. It is important to note that at a high accelerating voltage ( $>15$  keV), high resolution SEM images can be achieved easily, however, the EDS analysis may provide composition information of a deeper layer rather than at the surface due to the penetration of the electron beam (Lloyd et al. 2009a). Additionally, the geopolymeric gels in the binders are substantially heterogeneous (Wang et al. 2011), unless the binder is synthesized from a clear solution (Dimas et al. 2009). Therefore, the EDS analysis in this study was conducted on more than 5 points for each sample to give an average value, although this number may be still too low to get a really average value. Figure 4-16 shows representative SEM images with marked points and their EDS spectra.

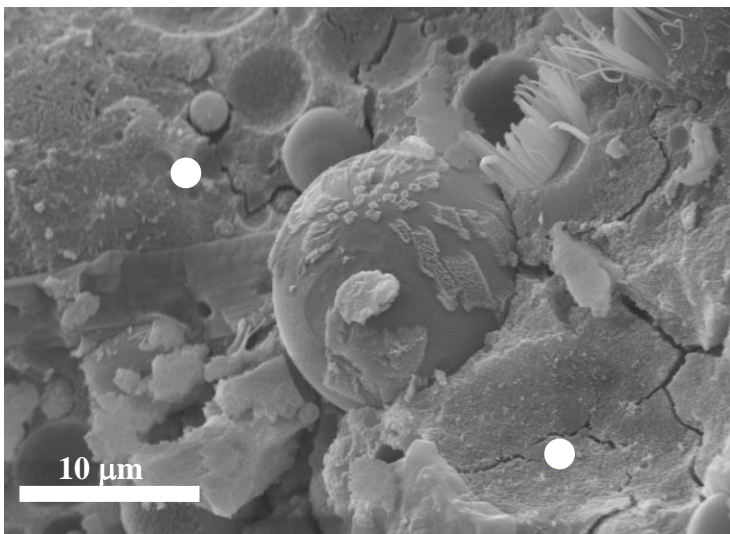


(a)

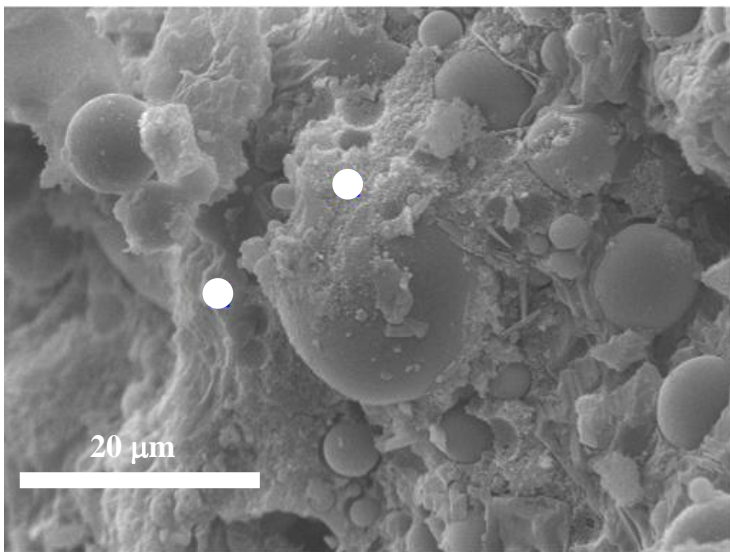




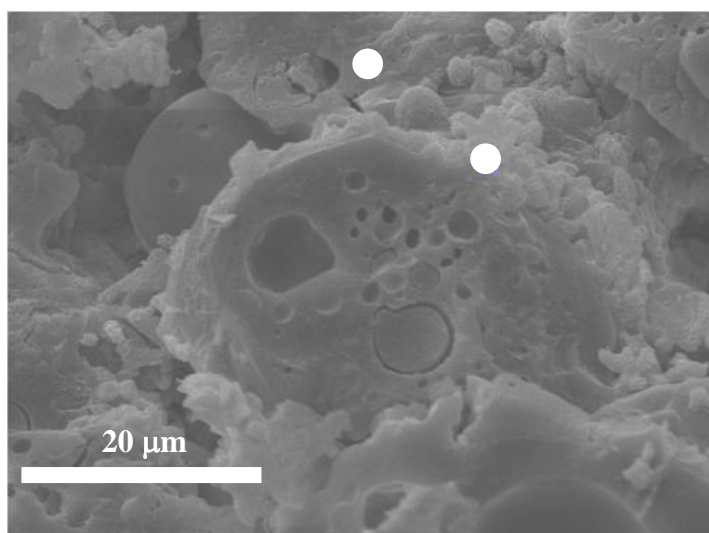
(b)



(c)



(d)



(e)

**Figure 4-16.** Representative SEM-EDS analysis area of fracture surface of hardened binders: (a) binder A; (b) binder B; (c) binder C; (d) binder D; (e) binder E.

**Table 4-9:** Composition of amorphous gels in hardened binders as determined by EDS analysis, atom %. Others are atoms of O, C and Au.

Binder	Na	K	Mg	Ca	Al	Fe	Si	Ti	(Si+Al)/(M+2Me)
A	8.3	-	-	-	7.6	10.6	13.4	-	2.53
B	8.1	0.4	0.6	1.6	7.9	2.3	17.8	-	1.99
C	6.3	-	-	0.9	7.6	0.4	12.2	0.2	2.44
D	15.3	0.3	-	-	4.3	0.3	9.8	-	0.92
E	15.6	-	-	-	5.1	-	10.9	-	1.02

It can be seen that in binders D and E, there are much higher concentrations of Na atoms than in the other three. The products around fly ash A contain lower concentration of Fe than the other binders. This is in disagreement with the previous findings that Fe is retained mainly in residual fly ash (Lloyd et al. 2009a). The unusual high Fe concentration in binder A is probably due to the iron bearing fly ash particles in deeper layer. The role of Fe is still elusive because geopolymers usually contain a relatively low concentration of Fe, and the amorphous nature of products also makes the characterization of Fe-containing products difficult by normal methods, such as XRD and FTIR. By comparing the reaction products on the fly ash surface and in the bulk binder matrix, it is noted that the concentration of Na atoms is related to the concentration of Al rather than the concentration of Fe. This finding may suggest that Fe atoms are present in forms of ferric hydroxides, such as  $\text{Fe}(\text{OH})_3 \cdot n\text{H}_2\text{O}$ , instead of acting as a network former in the geopolymer framework. This can be partially confirmed by the association of arsenic with the iron hydroxide or oxyhydroxide species in iron-rich fly ash rather than geopolymers with addition of iron in form of  $\text{Fe}_2\text{O}_3$  (Van Deventer et al. 2007).

If it is assumed that Al and Si are network formers, while Na, K, Mg and Ca are network modifiers, and the polymerization degree of network can be defined by the molar ratio of  $(\text{Si}+\text{Al})/(\text{M}+2\text{Me})$  where M is an alkali metal and Me is an alkali earth metal, it can be seen that for binders A, B and C, the ratio is around

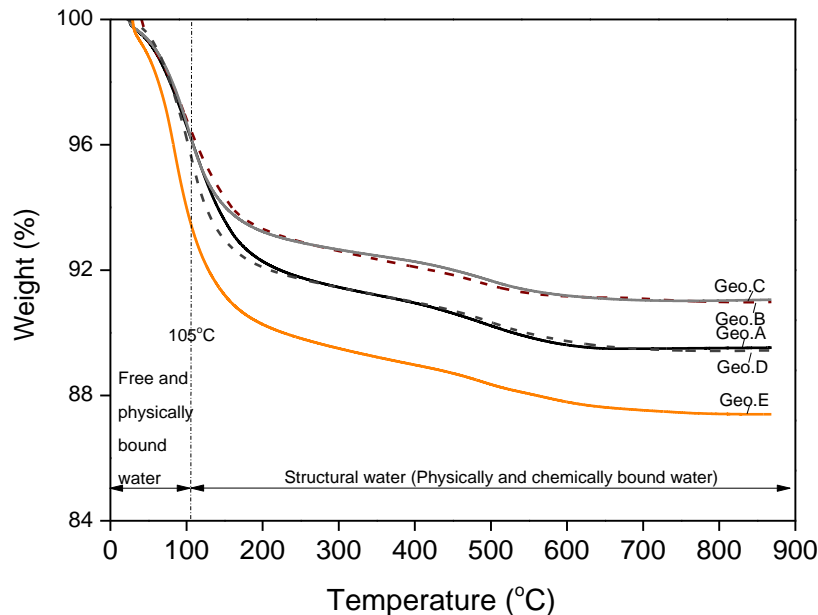
2.0, while for geopolymers D and E, it is 0.92 and 1.02 respectively. The higher polymerization degree in A, B and C could account to some extent for the high specific strength of the former three binders.

On the other hand, if regardless of the effects of composition of gels, the quantities of gels in the hardened binders are supposed to have a more significant contribution to the strength, as it is the gel which binds the residual particles together. The quantity of gels formed can be determined by weighing the residual fly ash after dissolution of the 100°C × 24 h dried binder powders in HCl solution, if it is assumed that the residual fly ash cannot be dissolved at room temperature (Fernández-Jiménez et al. 2006a). Table 4-10 shows the quantities of gels in hardened binders as determined by the acid dissolution method.

**Table 4-10:** Gel phase of hardened geopolymer binders (28 d) as determined by dissolution of the geopolymers in 1:15 HCl solution at 25°C.

Mass %	Binder A	Binder B	Binder C	Binder D	Binder E
Gel quantity	50.0	32.8	22.6	17.4	20.0

The quantities of gels in the hardened binders vary in the order of A > B > C > E > D. A general trend can be seen that higher quantity of gel phases results in higher mechanical strength. Given that the activator used for preparing this batch of specimens was held constant, the variation in the quantity of gel should result from the varied reaction extent of different fly ashes.



**Figure 4-17.** TGA data for the geopolymer binders (28 d).

To quantify the reaction extent of fly ash, the geopolymer binders were further investigated by Thermogravimetry analysis (TGA), with the results shown in

Figure 4-17. As the sample pieces were stored in acetone (this storage actually provides a drying condition to remove free water) and dried at room temperature for 24 h before testing, the free water may not be fully removed. Therefore, the weight loss before 105°C is assumed mostly due to the evaporation of free water, and maybe a part of physically bound water (Bazant and Kaplan 1996). Based on the quantity of the structural water (strongly physically and chemically bound water and perhaps the water held in small pores), the extents of reaction of the fly ashes are calculated (Table 4-11). The mass ratio of solid content ( $\text{SiO}_2+\text{Na}_2\text{O}$ ) supplied by the activator to the total solid materials is 12.5% for all mixes.

**Table 4-11:** Structural water in hardened geopolymer binders (28 d) as determined by TGA and the reaction extent of the corresponding fly ash.

	Binder A	Binder B	Binder C	Binder D	Binder E
Structural water (wt.%)	6.8	5.5	5.3	6.3	6.2
Reaction extent (wt.%)	40.8	18.7	10.2	4.3	6.4

The structural water in binders is in a range of 5.28 to 6.77 wt.%. The fly ash reaction extent is in the order of A> B> C> E> D, which is consistent with the quantity of geopolymeric gels. The reaction extent of fly ash may be over-estimated due to the dissolution of iron bearing glassy and mineral phases in HCl solution (Choo et al. 2013). The result of gel analysis suggests that both the composition and quantity of gels play important roles affecting the compressive strength of binders. In particular, all these variations are related to the reactivity nature of the fly ash, which not only lies on particle physics but more likely lies on the chemistry of fly ash and will be explored further in the following chapters of this thesis.

#### **4.5 Concluding remarks**

Five fly ash samples sourced from different power plants around Australia were used to manufacture geopolymer binders in laboratory conditions, enabling investigation of the relationship between the physical and chemical properties of fly ash and the mechanical properties of geopolymer products.

The results indicate that fly ashes from different sources may result in geopolymers with strength varying remarkably. In particular, fly ash A exhibited the highest reactivity. The resulting geopolymer paste reached 41.8 MPa at 7 d and 52.8 MPa at 28 d, while for fly ash E, the paste was < 1 MPa at 7 d and only 8.7 MPa at 28 d.

The possible factors that may affect the mechanical strengths of binders were analysed. The firstly studied factor is the microstructure of hardened binders. By analysing the porosity and pore size distribution, it is found that the high strength of binder A is related to its much lower porosity and smaller pore structures. The extremely low strength of geopolymer E could potentially result from the higher porosity as well as the relatively higher volume of large pores.

The secondly studied factor is the composition and quantity of gels in the binders. It is observed that the  $(\text{Si}+\text{Al})/(\text{M}+2\text{Me})$  ratio varies around 2.0 in the

gel binders for geopolymers of higher strength, while it is 0.9-1.0 for geopolymers of lower strength. Moreover, the quantity of gel phases varies substantially, from 50 wt.% for binder A to 17.4 wt.% for binder D. The general trend is that a higher  $(\text{Si}+\text{Al})/(\text{M}+2\text{Me})$  ratio (within the range studied) and more gel phase will result in a binder of higher strength.

This chapter has demonstrated that fly ashes from different sources exhibit substantially different physical properties. One important property is the inter-particle volume of fly ash, the space between pecked particles, which largely determines the liquid requirement. The liquid requirement furthermore affects the porosity of hardened binders and their production costs. Another factor is the reaction extent of fly ash, which determines the quantity and composition of gel phases. Fly ashes D and E, containing higher quantities of Si and Al, do not exhibit higher reactivity, even from the perspective of reactive  $\text{SiO}_2$ . Instead, the one which contains more 'impure' elements seemingly has a higher reactivity. A general trend obtained is that fly ash with higher network-modifying cations seems to possess higher reactivity. This aspect needs to be further studied to gain a fundamental understanding of the nature of fly ash reactivity. It is not only important for understanding the reaction mechanisms of geopolymerization, but also useful for guiding the selection of fly ash for its manufacture.

# Chapter 5: Glass Chemistry of Fly Ash, and Its Effects on Geopolymerization Reactivity

## 5.1 Introduction

The previous chapter highlighted the importance of particle physics of fly ash in affecting the liquid requirement and consequently the porosity and pore size of geopolymer binders. However, the principle of porosity cannot explain the high strength of geopolymer binder B. The results of gel phase analysis strongly suggest that the reaction extent of fly ash is critically important. An evident relationship is that a higher reaction extent of fly ash gives a higher quantity of gel phases (associated with variation in composition), and generally a higher compressive strength of the binder. Therefore, a thorough understanding of the reactivity of fly ash is very necessary for proportioning geopolymer mixes.

Comparing the SEM images of the surfaces of original fly ash particles and those embedded in geopolymer binders, dissolution seems only to happen to the glassy part. This means that the reactive components are the glassy or amorphous parts present in fly ash. This mechanism has been assumed and also demonstrated by some researchers (Fernández-Jiménez et al. 2006a; Lloyd et al. 2009a; Williams and Van Riessen 2010). However, very limited attention has been paid to the glass chemistry of fly ashes, and the effects on their reactivity under geopolymerization conditions (Duxson and Provis 2008; Keyte 2008; Diaz and Allouche 2010; Rickard et al. 2011). The lack of attention to the importance of glass chemistry of fly ash may be due to the fact that most previous studies used a single-sourced fly ash. The aim of this chapter is to investigate the concentration and nature of glass phases in the five selected fly ashes, so as to develop a comprehensive index for quantifying the reactivity of fly ash under geopolymerization conditions.

In this chapter, the glass phases in as-received and alkali-leached fly ashes will be investigated using XRF and Rietveld quantitative XRD (RQXRD). The compositional properties of glass phases are discussed in relation with the reactivity of the five fly ashes, as reflected by the compressive strength of hardened binders. In addition, based on the understanding of glass chemistry, the possibility of using FTIR as a quick indicative test of the reactivity of fly ash is demonstrated.

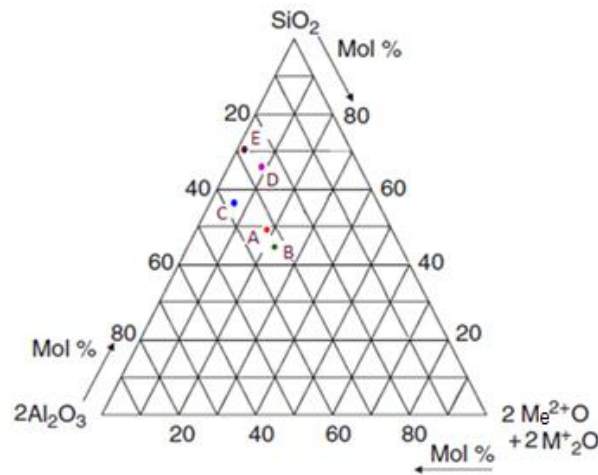
## 5.2 The importance of glass composition of fly ash

### 5.2.1 Examination of bulk composition and reactivity of fly ash

From bulk compositions of fly ashes as determined by XRF (Table 4-1), fly ash A has the smallest total content of  $\text{SiO}_2$  and  $\text{Al}_2\text{O}_3$ , 74.8 wt.%. D and E have highest contents of  $\text{SiO}_2$  and  $\text{Al}_2\text{O}_3$ , up to 90 and 96 wt.%, and their reactive  $\text{SiO}_2$  contents are much higher than the three others. As Si and Al are the backbone in the geopolymeric gels, it would be reasonable to expect that fly ashes D and E would have the highest potential to generate geopolymers of highest strength. However, the compressive strength testing results indicate that fly ashes D and

E are 'inactive', and their reaction extents are much lower than that of fly ash A. Therefore, a bulk composition analysis simply reporting total Si and Al content in fly ash is not of value in the analysis of ash reactivity. Several studies (Fernández-Jiménez et al. 2006b; Rickard et al. 2011) have been reported the role of amorphous (glassy) aluminosilicate phases and the availability of Si and Al in geopolymerization which should be considered.

Duxson and Provis (2008) proposed a pseudo-ternary composition diagram in attempt to indicate the relationship between quantity of alkali and alkali earth oxides, alumina content, silica content and the reactivity of fly ash. Figure 5-1 shows the diagram, which has been reorganized according to the bulk composition of the five fly ashes in this study. Table 5-1 gives the normalized molar fraction Si, Al, M and Me (M=Na, K; Me=Ca, Mg) based on their molecular of oxides. The molar ratios of (M+2Me) to Si and Al are also calculated. It should be noted that the iron, titanium and other elements present are excluded from these calculations.



**Figure 5-1.** Pseudo-ternary composition diagram (Duxson & Provis 2008) for the five selected fly ashes, of which the compressive strength development is in the order A> B> C> D> E. Alkali and alkali earth oxides are summed, and represented as the total molar number of charges on the respective cations.

**Table 5-1:** Normalized chemical compositions of fly ash in molar ratio terms. Only Si, Al, Ca, Mg, K and Na oxides are considered.

Fly Ash	SiO <sub>2</sub>	2 Al <sub>2</sub> O <sub>3</sub>	2 CaO	2 MgO	2 K <sub>2</sub> O	2 Na <sub>2</sub> O	(M+2Me)/Si	(M+2Me)/Al
A	0.480	0.324	0.129	0.046	0.007	0.014	0.409	0.605
B	0.458	0.329	0.178	0.024	0.006	0.004	0.464	0.648
C	0.554	0.384	0.032	0.023	0.003	0.003	0.111	0.156
D	0.659	0.259	0.029	0.016	0.026	0.009	0.123	0.314
E	0.701	0.286	0.002	0.004	0.007	0.0002	0.018	0.045

A general trend for the relationship between composition and reactivity can be observed: fly ash which contains more alumina and higher (M+2Me)/Al possesses higher reactivity, and in comparison, the latter seems more important.

In silica glasses, alkali and alkali earth metal cations are classified as network modifiers and affect the decomposition (or leaching) of glasses to a significant extent. An early study by Douglas and El-Shamy (1967) showed that the apparent reaction constants of aqueous-leaching of alkali (Li, Na and K) and of silica from alkali oxide-silica glasses both increase with increasing alkali content in glasses at 30 to 70°C. This is because that the network-modifying cations present in glasses cause the presence of non-bridging oxygen (NBO) sites, which are more readily active in ion exchange, hydrolysis and detaching of Si sites. In addition, alkali cations brought into solution as a result of the ion exchange promote the breakdown of the silica structure. This is because of the fast equilibrium of surface sites (Douglas and El-Shamy 1967). Indirect evidences for this mechanism are the higher concentrations of dissolved silica in solutions with higher Na/Si ratios (Hasegawa et al. 1987; Thornton and Radke 1988).

Fly ash particles are highly heterogeneous and consist of several crystalline phases, such as mullite and quartz, embedded in a glass phase. In Figure 4-16c, an SEM image shows the residual fly ash particle with well crystalline particles raised after the reaction of the glassy part. If these crystalline phases are supposed to be non-active in geopolymerization, the reactivity then will be closely related to the composition and chemistry of glass phases. This point has been stressed in some other research studies (Lloyd et al. 2009a; Williams and Van Riessen 2010). Due to the presence of crystalline phases, the composition of amorphous (glassy) phases will be significantly different from the bulk composition of the ash, and there may also be compositional heterogeneity within the glassy component itself. Therefore, simple consideration of the bulk composition is unable to satisfactorily answer the question of why fly ash A is very active while E is much less reactive than the others.

Another notable difference between the selected ashes is the iron content. Fly ash A has quite a high iron content (14.3 wt.% as  $\text{Fe}_2\text{O}_3$ ) and fly ash C also has a considerable amount of iron. Iron phases usually present in crystalline phases, such as maghemite and hematite (Font et al. 2010). However, Fe atoms can also be present in 'impure' mullite as a substitution for Al (Williams and Van Riessen, 2010) and may also be present in silica glass as compositional defects (Dove et al. 2008). Such a high concentration of iron should not be ignored, unfortunately there has been very limited attention paid to this aspect. Lloyd et al. (2009a) studied the microstructure of iron containing fly ash particles and found that some particles contains almost pure iron oxide, while some contain a mixture of iron-rich and silica-rich phases. Substitution of magnesium and aluminum into the iron-rich spinel phase was also confirmed by BSE and EDS analysis. In combination with studies by Bayukov et al. (2005), Hinckley et al. (1980), Dudas and Warren (1987) and Vereshchagina et al. (2004) as well as by Xu et al. (2004), it suggests that only a small quantity of the iron in fly ash is in a form that could participate in IPC formation. For those magnetic fly ash particles the outer coating of aluminosilicate glass rich in Fe, Ca, Na, K, and Mg are much reactive, while the interstitial glassy phase that is relative low in Fe is less active.

From the bulk chemical composition analysis, a general trend obtained is that fly ash with higher network-modifying cations possesses higher reactivity.

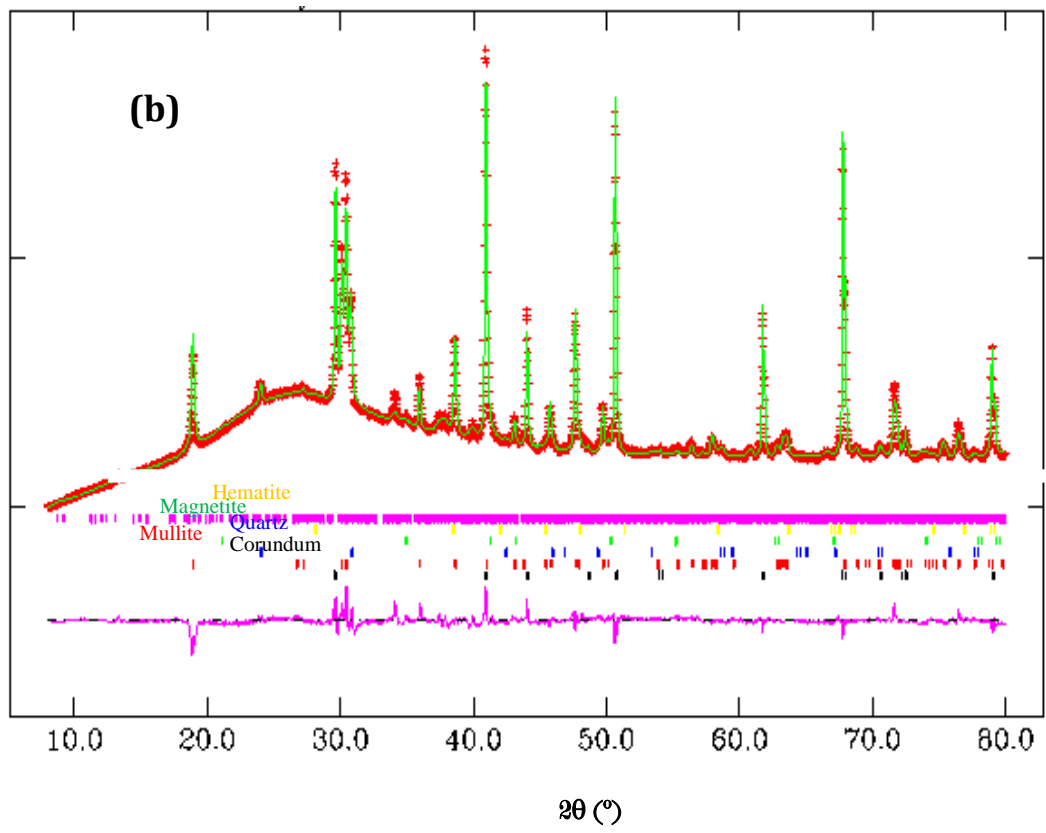
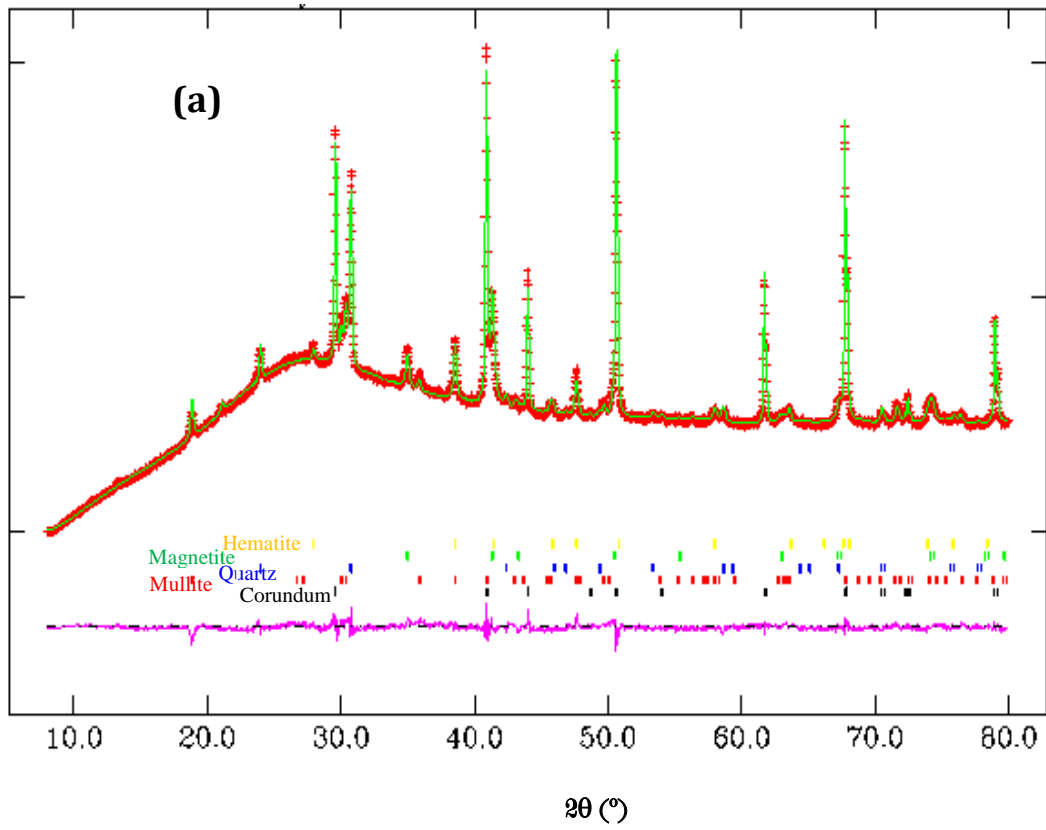


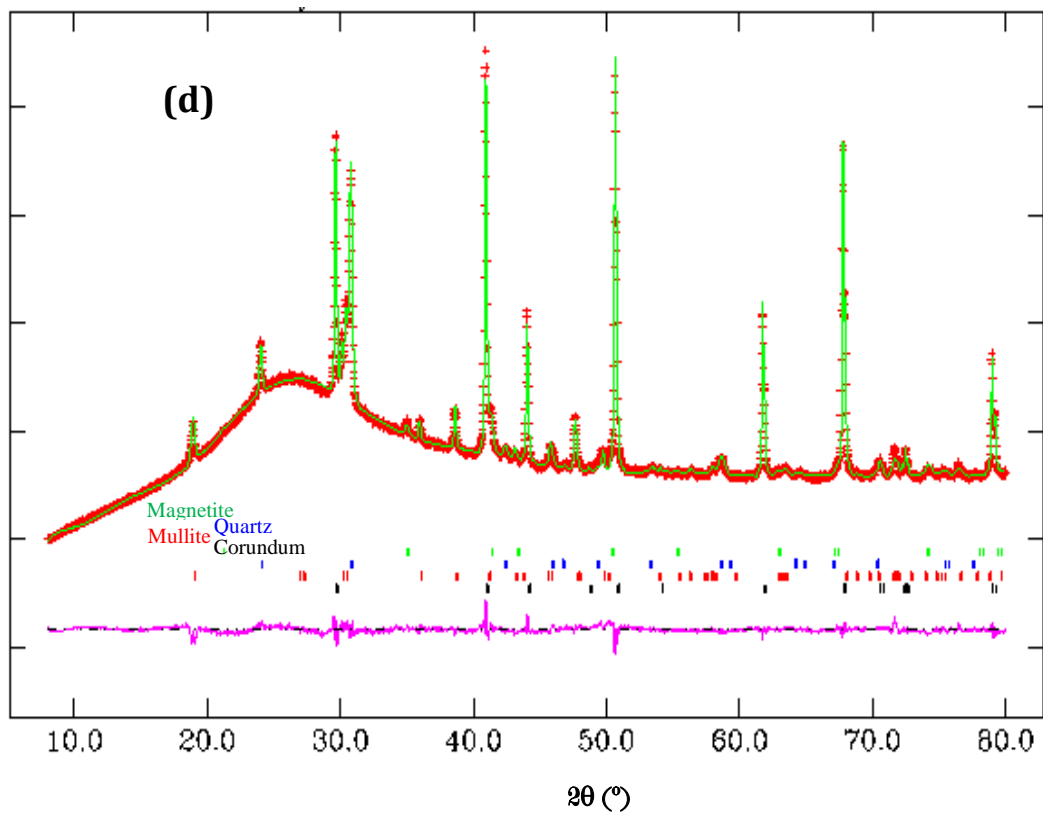
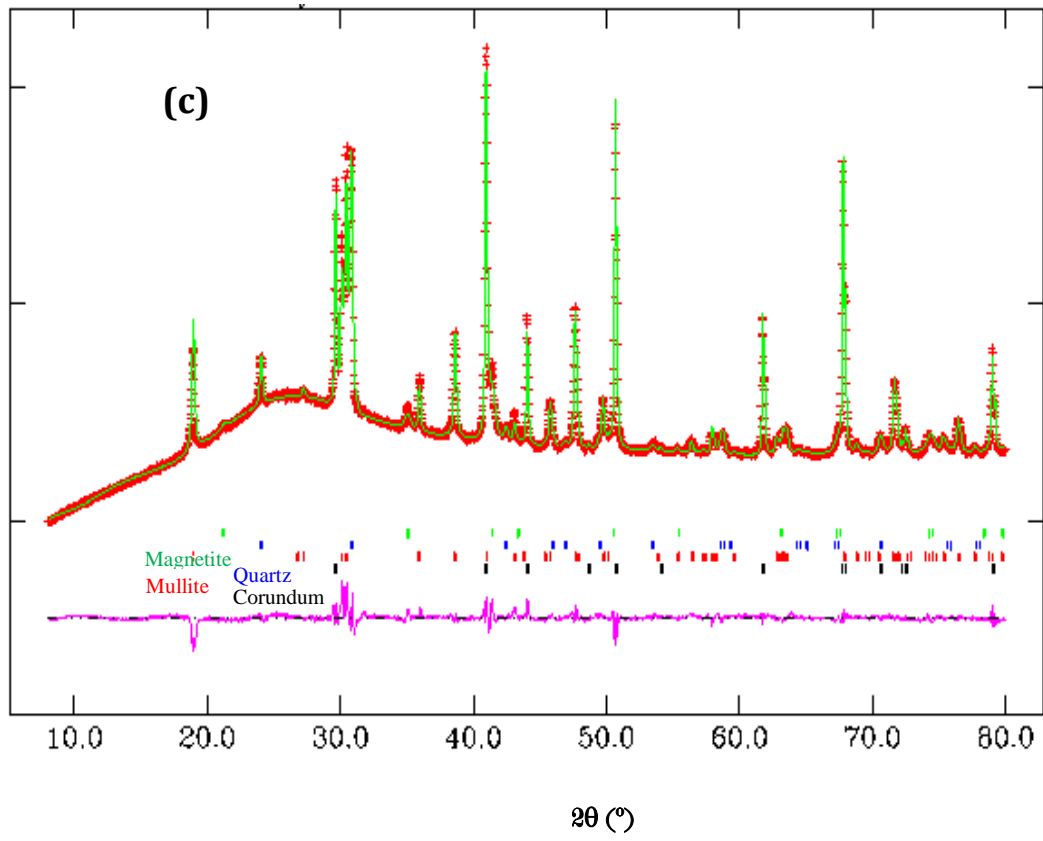
However, given the heterogeneous nature of fly ash, a further analysis of the crystalline and amorphous components in the five fly ashes is necessary. It is expected will to disclose more information from a view of glass chemistry to answer the question that why fly ash A is very active while E is much less reactive.

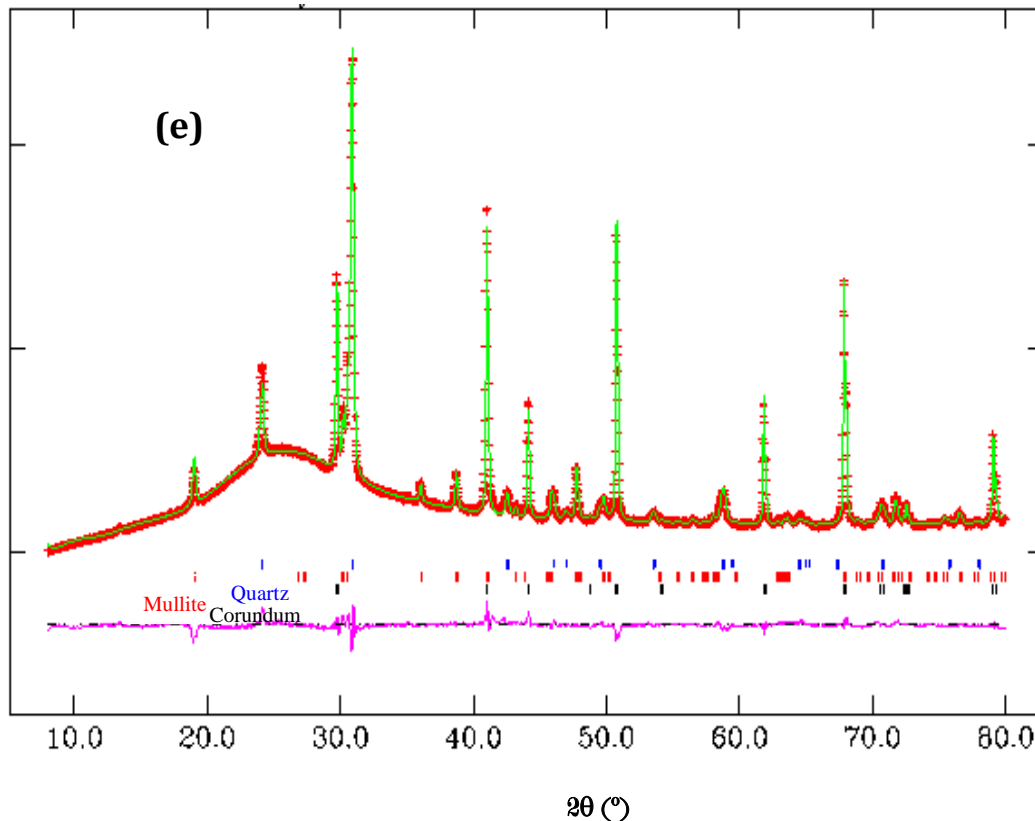
### **5.2.2 Determination of crystalline and amorphous components in fly ash**

While there are many available methods that are able to semi-quantify the crystalline and amorphous components in fly ash (Fernández-Jiménez et al. 2006a; 2006b), this project focuses on using Rietveld quantitative XRD (RQXRD) method (Rietveld 1969), which has been proven widely in studying the mineral and glassy components in fly ash (Ward and French, 2006; Williams and Van Riessen 2010). RQXRD is better suited for quantitative analysis of fly ash as a complex material than other methods of analysis of XRD data, such as the reference intensity ratio method (Font et al. 2010), because it uses the full profile of the diffraction patterns. The utilization of the full profile minimises the inaccuracies in the raw data raised from systematic errors, such as peak overlap, preferred orientation, sample broadening and the lack of a pure standard (De La Torre et al. 2001).

In this study XRD data were collected from the five fly ash samples without particle classification. This process will avoid the possible compositional preference due to particle size classification (Brouwers and Van Eijk 2002); however, the direct utilization of fly ash particles in sampling may cause some extent of preferred orientation of peaks due to the presence of some coarse particles. It is understood that grinding the fly ash can reduce the particle size, but it may also cause phase changes due to the mechano-chemical effects (Boldyrev 2006). The detected concentration of mineral phases could be reduced due to the broadening of their characteristic peaks, although may be slight (Kumar and Kumar 2011). Using RQXRD with corundum as spike material (internal standard) can minimise the negative effects of these particle-classifying and grinding sampling methods. The diffraction patterns and the analysis results are plotted in Figure 5-2.







**Figure 5-2.** Rietveld refinement XRD plots showing the observed (red crosses) and calculated (red solid) patterns, and the difference between them (bottom pink line) for fly ash A (a), B (b), C (c), D (d) and E (e) mixed with 20 wt. % corundum as internal standard.

The Rietveld method enables a good quantification result, as indicated by the difference pattern shown as the bottom line in each figure. The names of crystalline phases corresponding to diffraction Bragg peaks are also given.

To examine the accuracy of this method, parallel mixtures for fly ash A and E with 10 wt.% and 15 wt.% of standard were also analysed (figures are shown in Appendix A2). Compared to other two standard levels, the utilization of 20 wt.% standard overestimates the amount of amorphous phases for fly ash E while underestimates that for fly ash A. The error of each phase is different: it is within 8.6% for each phase in fly ash A while a bit large in fly ash E, 16% for mullite, 6.9% and 7.1% for quartz and amorphous phase. The error arises from many sources: sample quality, sampling method and data collection. The Rietveld quantification fitting itself has an error, as indicated by  $W_{RP}$ . In overall, the average error of this method is within 10%. Thus the results that summarized in Table 5-2 is thought to be acceptable, particularly given the fact that crystalline phases are not 'pure' (i.e. there is a significant degree of substitutionally disorder component in the mullite and iron oxide phases in fly ash (Gomes et al. 1999; Gomes and Francois 2000)) and some phases, such as magnetite and hematite, are low in concentration (< 5 wt.%).

**Table 5-2:** Crystalline and amorphous phases of the five selected fly ashes as determined by Rietveld quantitative XRD method, mass %.

Components (ICSD)	A	B	C	D	E
Mullite, Al <sub>4.75</sub> Si <sub>1.25</sub> O <sub>9.63</sub> (66448)	18.7±1.1			15.7	24.1±3.8
Mullite, Al <sub>1.83</sub> Si <sub>1.08</sub> O <sub>4.85</sub> (43289)		13.6	15.3		
Quartz, SiO <sub>2</sub> (89280)	3.1±0.3	2.6	6.5	5.0	13.1±1.5
Magnetite, Fe <sub>3</sub> O <sub>4</sub> (43001)	2.5±0.1	1.3	2.4	0.9	-
Hematite, Fe <sub>2</sub> O <sub>3</sub> (15840)	1.5±0.1	0.8	-	-	-
Amorphous	74.2±1.5	81.7	75.8	78.4	62.8±5.3
W <sub>RP</sub> , %	3.02	6.05	3.89	3.32	5.03

Note: composition of A and E is given as the mean obtained with three standard addition levels.

The amorphous content given in Table 5-2 should possibly be considered an upper bound. The amorphous content of each fly ash is based on a simple mass balance by assuming all of the remaining components except for the crystalline phases detected by XRD are all amorphous. Actually, there may be some other minor crystalline phases such as calcium silicates, anhydrite, gypsum and some other minor alkali-containing sulfates or carbonates, such as the unknown phase in fly ash B (Figure 3-2b). These minor phases were considered negligible in the calculations. From the literatures, it is reported that fly ash A contains 70-80 wt.% of amorphous phase (Lee and Van Deventer 2003); fly ashes C and E contains 76 and 68 wt.%, respectively (Keyte 2008). It has been also reported that fly ashes D and E contains 62.7 and 50.8 wt.%, respectively (Rickard et al. 2011). The current quantified results are between those reported values, and seem reasonable.

By a first glance, fly ashes A, B, C and D have equivalent quantities of amorphous phases but fly ashes A and B exhibited much higher reactivity. It can be proposed that the composition and chemistry of glassy phases play more important roles than their quantity in controlling the reactivity. The composition of the amorphous fraction is estimated in Table 5-3, by simply subtracting the determined crystalline components from the bulk composition.

**Table 5-3:** Chemical composition (wt.%) in the amorphous part of fly ash as calculated from the bulk composition and crystalline composition. 'Others' includes P<sub>2</sub>O<sub>5</sub>, SO<sub>3</sub>, trace components, and LOI.

Fly ash	SiO <sub>2</sub>	Al <sub>2</sub> O <sub>3</sub>	CaO	MgO	K <sub>2</sub> O	Na <sub>2</sub> O	Fe <sub>2</sub> O <sub>3</sub>	TiO <sub>2</sub>	Others
A	39.98	13.02	4.25	1.48	0.54	0.74	10.2	1.47	2.52
B	46.16	23.54	6.90	0.90	0.59	0.27	0.95	1.60	0.79
C	41.66	23.14	1.06	0.75	0.22	0.14	4.99	2.14	1.70
D	58.59	10.51	1.00	0.53	2.11	0.50	2.74	0.90	1.52
E	52.40	6.30	0.08	0.12	0.53	0.01	1.16	1.42	0.88

By comparing the reactive silica (\*SiO<sub>2</sub>) given in Table 4-1 and the SiO<sub>2</sub> fraction in amorphous phase, it is found that fly ashes A and E show similar quantities while fly ashes B, C and D have ~5% higher SiO<sub>2</sub> in the amorphous phase. If

RQXRD is assumed to be accurate, it seems that in the amorphous phases, not all of the silica is able to be dissolved in the reactive silica determination test (where the ash is dissolved in HCl solution under high temperature and high pressure conditions and measured with ICP-OES). This could be due to the presence of imperfectly crystallized quartz and/or mullite, which are difficult to dissolve but ascribed as amorphous phases by RQXRD.

The major elements in the amorphous phases are Si and Al. A high concentration of Al in the glass does not necessarily endow fly ash with high reactivity, unless there are enough charge compensators for Al present in 4-coordination ( $\text{AlO}_4$  tetrahedra). If this is not the case, the excessive Al atoms may rearrange with Si to form locally mullite-like structures. Besides, the Fe in silicate glasses may form stable local phases due to the lack of charge balancers (Lloyd et al. 2009a), and this issue is discussed in more detail below. These mechanisms possibly explain why the reactive silicate as determined by acid dissolution method is relatively less than the quantity of amorphous Si in fly ashes B and C.

The concentrations of Ca in the aluminosilicate glass in fly ash A and B are relatively higher than in other fly ashes. The concentration of other network-modifying cations Mg, K and Na are very low. The influences of network-modifying cations in the structure of glass and the leaching mechanisms in solution have been discussed briefly in the above section. Beside Si, Al, Ca, Mg, K, and Na, the concentrations of Fe and Ti in the amorphous part are also relatively high. It is necessary to understand the roles of Fe and Ti in glasses before giving a quantitative evaluation of the contribution of amorphous composition on the reactivity of fly ash. With a full understanding of the roles of these elements in glass, in combination with the particle physical properties, it is possible to develop a comprehensive index to quantify the reactivity of fly ash under geopolymerization conditions.

### ***5.3 Reactivity index of fly ash for geopolymer manufacture***

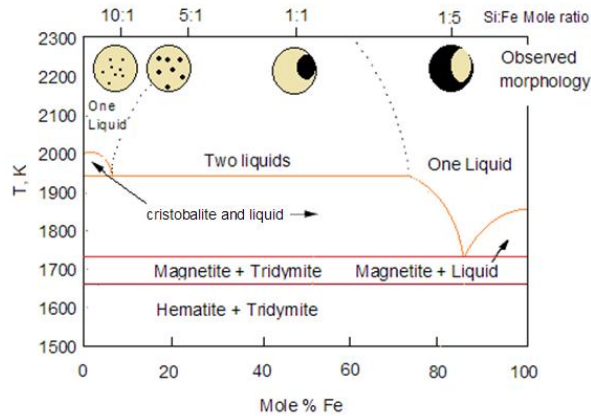
This section describes the state-of-art understanding of the roles Fe and Ti in silica and aluminosilicate glasses, particularly in presence of alkali and alkali earth cations. Based on the understandings, an index for quantifying the reactivity of fly ash is developed, with consideration of surface area of particles. Dissolution experiments at different liquid/solid ratios are performed to examine the validations of the reactivity index.

#### **5.3.1 The development of reactivity index for fly ash**

##### **5.3.1.1 The roles of Fe**

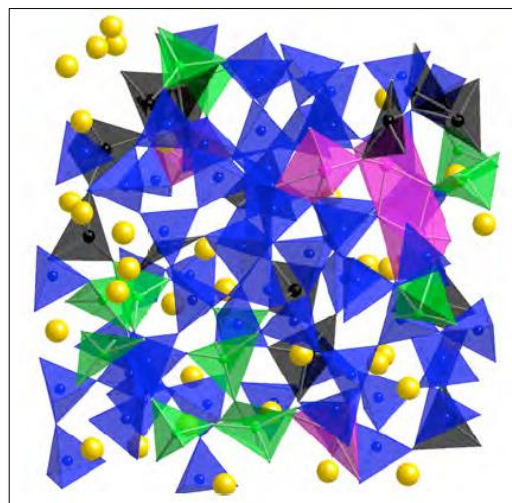
In  $\text{Fe}_2\text{O}_3\text{-SiO}_2$  glasses, the state of iron depends on both temperature and its concentration. A binary phase diagram shown in Figure 5-3 indicates that under 2000K (1727°C) Si and Fe tend to form cristobalite and a liquid phase while under 1730K (1457°C), Si and Fe tend to form separate phases, such as magnetite and tridymite or hematite and tridymite at lower temperature. It means that  $\text{Fe}^{2+}$  and  $\text{Fe}^{3+}$ , regardless of their content, are 6-coordinated and have limited capability to substitute for Si in the glass network (Ehrman et al.

1999). During cooling, they favor of phase segregation as Fe-enriched phases, not able to contribute significantly to the network structure.



**Figure 5-3.** Phase diagram of the SiO<sub>2</sub>/FeO-Fe<sub>2</sub>O<sub>3</sub> system. Reorganized from reference (Ehrman et al. 1999).

However, the glassy phase of fly ash contains a certain quantity of aluminum and alkali/alkali earth ions. When aluminum, alkali and alkali earth ions are incorporated in silica glass, the state of iron will be changed due to the charge balance capability of alkali and alkali earth cations (Weigel et al. 2008; Cormier et al. 2010). In the silica glasses with composition of NaFe<sub>x</sub>Al<sub>1-x</sub>Si<sub>2</sub>O<sub>6</sub> it is reported that the majority of Fe<sup>3+</sup> is 4-coordinated and plays a network forming role, like most of the Al<sup>3+</sup>, according to the model shown in Figure 5-4. Both FeO<sub>4</sub> and AlO<sub>4</sub> are randomly distributed and connected with SiO<sub>4</sub> tetrahedra by sharing corners. Only a small fraction of Fe<sup>3+</sup> and Fe<sup>2+</sup> in 5-coordinated states (FeO<sub>5</sub>) will tend to form clusters and to share edges with each other (Weigel et al. 2008). With the concentration of Fe in glass decreasing, more Fe tends to be in a 4-coordinated state. For instance, in glass NaFe<sub>0.5</sub>Al<sub>0.5</sub>Si<sub>2</sub>O<sub>6</sub>, 66 mol% of Fe is 4-coordinated, 32 mol% of Fe is 5-coordinated and 2 mol% in other states (Weigel et al. 2008).



**Figure 5-4.** Structure model of glass with composition of NaFe<sub>0.5</sub>Al<sub>0.5</sub>Si<sub>2</sub>O<sub>6</sub>. SiO<sub>4</sub>, AlO<sub>4</sub> and FeO<sub>4</sub> tetrahedra are represented in blue, green and black respectively. FeO<sub>5</sub> polyhedra and Na atoms are represented in pink and yellow respectively (Weigel et al. 2008).

To evaluate the effect of the amorphous composition on the reactivity of fly ash, a molar percentage basis is used, as shown in Table 5-4. Other oxides have been ignored due to their low concentrations.

**Table 5-4:** The molar fraction in the amorphous part of the fly ashes.

Fly ash	SiO <sub>2</sub>	Al <sub>2</sub> O <sub>3</sub>	CaO	MgO	K <sub>2</sub> O	Na <sub>2</sub> O	Fe <sub>2</sub> O <sub>3</sub>	TiO <sub>2</sub>
A	0.662	0.127	0.075	0.037	0.006	0.012	0.063	0.018
B	0.651	0.195	0.104	0.019	0.005	0.004	0.005	0.017
C	0.680	0.222	0.019	0.018	0.002	0.002	0.031	0.026
D	0.835	0.088	0.015	0.011	0.019	0.007	0.015	0.010
E	0.900	0.064	0.001	0.003	0.006	0.000	0.007	0.018

The molar fraction of Al is higher than the total molar fraction of charge of alkali and alkali earth metals, which means there are not enough charge balancers in any of the selected fly ash samples. At this condition, Al and Fe take the roles of both network former and modifier. In addition, as discussed earlier, Fe<sup>3+</sup> can also substitute for Al<sup>3+</sup> in mullite-like glasses (Gomes et al. 1999; Gomes and Francois 2000), which will cause a lower concentration of network modifiers, but their contribution is difficult to determine here. Fe may tend to be in role of network former while the remaining fraction, both Fe<sup>3+</sup> and Fe<sup>2+</sup> in 5-coordinated act as network modifiers (Guillot and Sator 2007; Weigel et al. 2008).

### 5.3.1.2 The roles of Ti

Titanium in silica glasses also plays a very complicated role. In TiO<sub>2</sub>-SiO<sub>2</sub> systems, homogeneous glasses can only form when TiO<sub>2</sub> content is low (usually < 10 mol%, depends on the preparation method), while high concentration of titanium tend to form clusters and phase separation (Henderson and Fleet 1997; Ehrman et al. 1999). Within homogeneous region, Ti<sup>4+</sup> acts as a network former, substituting for Si<sup>4+</sup> in 4-coordination. Outside the homogeneous region, 6-coordinated Ti<sup>4+</sup> may occur due to the formation of cryptocrystalline anatase. However, in glasses, Ti<sup>4+</sup> is also in 5-coordination, particularly dominant at low TiO<sub>2</sub> concentration (<3.6 wt.%) (Henderson et al. 2002).

In alkali and alkali earth cation-containing glasses, the structural role of Ti becomes more complicated. According to Henderson et al. (2002), in alkali metal bearing glasses, Ti<sup>4+</sup> presents in 4-coordinated state at low TiO<sub>2</sub> concentration but is predominantly in 5-coordinated at higher TiO<sub>2</sub> concentration. The levels of 'low' and 'high' here vary according to the alkali metal. For instance, Ti<sup>4+</sup> is present exclusively in 4-coordination in TiO<sub>2</sub>-Na<sub>2</sub>SiO<sub>3</sub> only when TiO<sub>2</sub> <1.0 wt.% but in TiO<sub>2</sub>-K<sub>2</sub>SiO<sub>3</sub> when TiO<sub>2</sub> <12.9 wt.%. In alkali earth metal containing glasses, Ti<sup>4+</sup> tend to be present in 5-coordinated state and will partially transform to 4-coordinated as TiO<sub>2</sub> content increases.

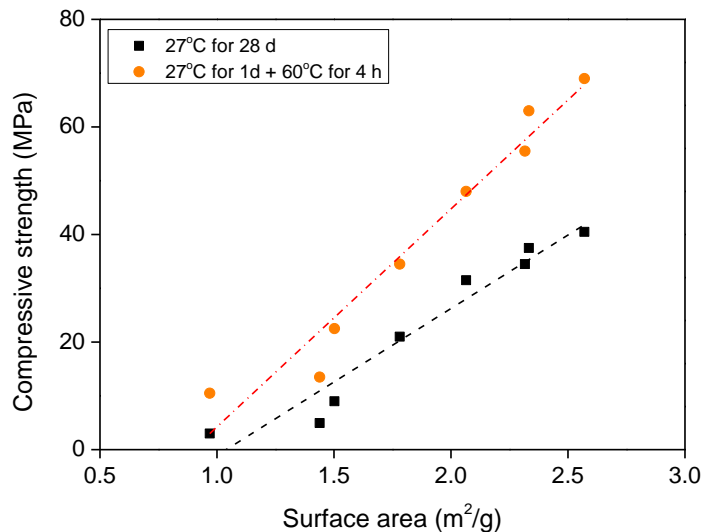
In fly ash, the glassy phase involves Al and some Fe, making the structural role of Ti yet more complex. However, as the TiO<sub>2</sub> content is relatively low in fly ash (usually <2 wt.%), Ti<sup>4+</sup> will tend to be 4-coordinated if it is assumed that the



whole amorphous part is homogeneous glass, particularly given that the alkali and alkali earth metal cations tend to be charge compensators for Al and Fe tetrahedra.

### 5.3.1.3 The effects of particle surface area

The surface area (SA) also affects the dissolution rate and final reaction extent of fly ash particles. Geopolymerization is not a simple solution reaction at high liquid/solid ratio; it should be a complicated combination of solution reaction, solid dissolution reaction and solid reaction. So it is not simple to provide an exact description of the influence of the particle geometry. However, if considering compressive strength as an effective index indicating fly ash reactivity, the SA has a linear relationship with its reactivity, as shown in Figure 5-5. It should be noted that the SA is measured by a particle size analyser, as discussed in Section 4.1.3, the measured values may be a slightly lower than the real values due to the effects of the particle shaper factor. The increase of SA of fly ash is able to be induced by vibratory milling, with little change in mineral properties (Kumar and Kumar 2011).



**Figure 5-5.** The relationship between surface area of fly ash and the compressive strength of derived geopolymer binders at two curing conditions. Data are from reference (Kumar and Kumar 2011).

### 5.3.1.4 Reactivity index for fly ash

Based on the above understanding of the roles of Fe and Ti and the effects of surface area of particles, a comprehensive index can be proposed, if it is assumed that:

- (1) the crystalline phases in fly ash are relatively pure and unreactive;
- (2) only the amorphous phase components undergo dissolution under the geopolymerization conditions;
- (3) the Si-O, Al-O, Fe-O and Ti-O bonds linked with network modifiers are much weaker (i.e. more reactive) than Si-O-Si and Si-O-Al;

- (4) in the amorphous (glass) phase: both Si<sup>4+</sup> and Ti<sup>4+</sup> are 4-coordinated, playing the role of network former; Ca<sup>2+</sup>, Mg<sup>2+</sup>, Na<sup>+</sup> and K<sup>+</sup> preferably play the role of network modifier; and
- (5) in the amorphous (glass) phase Fe may be a network former or a network modifier (in particular some Fe<sup>3+</sup> cations act as network formers, and some are network modifiers),

then the reactivity index (RI) for fly ash is able to be defined as:

$$RI = (2(CaO\% + MgO\% + Na_2O\% + K_2O\%) + 2 [^5]FeO\% + 6 [^5]Fe_2O_3\%) \times NSA \dots\dots\dots (5.1)$$

wherein CaO, MgO, Na<sub>2</sub>O, K<sub>2</sub>O, <sup>5</sup>FeO and <sup>5</sup>Fe<sub>2</sub>O<sub>3</sub> (5-coordinated FeO and 5-coordinated Fe<sub>2</sub>O<sub>3</sub>) is provided as molar percentages in the glass phase in fly ash. NSA is a normalised SA, that is NSA=SA/(1 m<sup>2</sup>/g). The unit of this reactivity index is 1.

The total Fe content can be determined by XRF in the form of Fe<sub>2</sub>O<sub>3</sub>. The concentration of network modifier 5-coordinated Fe and its charge (both Fe<sup>2+</sup> and Fe<sup>3+</sup> are present in aluminosilicate glasses) change according to the concentration of Fe and other elements in the glassy phase (Mysen and Virgo 1985). The concentrations may be quantified using neutron diffraction and Empirical Potential Structure Refinement (EPSR) modeling methods (Weigel et al. 2008) or other methods. As the concentration of Ti is very low and the network modifier Ti is only probably several percentages of total Ti, so the network modifier Ti cations are ignored here.

In this study, the concentration of Fe<sup>3+</sup> and Fe<sup>2+</sup> in 5-coordination are approximated by linearly fitting the results of Weigel et al. (2008). Table 5-5 lists the compositions of their iron bearing aluminosilicate glasses, and the distribution of Fe<sup>3+</sup> and <sup>5</sup>Fe (including <sup>5</sup>FeO and <sup>5</sup>Fe<sub>2</sub>O<sub>3</sub>).

**Table 5-5:** Composition of the iron bearing aluminosilicate glasses and the distribution of Fe<sup>3+</sup> and <sup>5</sup>Fe. Data from (Weigel et al. 2008).

System	Fe (atom%)	Al (atom%)	2Ca+2Mg+Na+K (atom%)	Fe <sup>3+</sup> /Fe (%)	<sup>5</sup> Fe/Fe (%)
NaFeSi <sub>2</sub> O <sub>6</sub>	10.3	0	9.7	88	36
NaFe <sub>0.8</sub> Al <sub>0.2</sub> Si <sub>2</sub> O <sub>6</sub>	8.2	2	10.1	87	33
NaFe <sub>0.5</sub> Al <sub>0.5</sub> Si <sub>2</sub> O <sub>6</sub>	5	5	10.1	86	32

If it is assumed that Na is equivalent to all other network modifiers, which is also a hypothesis for above RI assumption, two linear fitting equations based on the understanding of effects of alkali and alkali earth on the roles of Fe cations and their coordination states are developed:

$$Fe^{3+}/Fe (\%) = 89.42 - 1.73 (2Ca + 2Mg + Na + K) / Fe \dots\dots\dots (5.2)$$

$$^{55}\text{Fe}/\text{Fe} (\%) = 91.75 - 59.23 (2\text{Ca} + 2\text{Mg} + \text{Na} + \text{K}) / (\text{Fe} + \text{Al}) \dots\dots\dots (5.3)$$

The concentration of Fe<sup>3+</sup> and Fe<sup>2+</sup> in 5-coordinated state in the five fly ashes are approximated using the above two equations and the reactivity index then can be easily calculated, as shown in Table 5-6. It is better to use the SA measured by the particle size analyser because this method avoids the effects of the highly porous carbon particles in fly ash.

**Table 5-6:** The concentration of modifiers, normalised surface area (NSA) and the calculated the reactivity index (RI).

Ash	Si+Ti	Al	Fe	2Ca+2Mg+Na +K	2 <sup>55</sup> Fe <sup>2+</sup> +3 <sup>55</sup> Fe <sup>3+</sup>	Modifier	NSA	RI
A	0.684	0.256	0.128	0.260	0.188	0.449	2.140	0.961
B	0.770	0.479	0.012	0.312	0.016	0.328	2.360	0.774
C	0.719	0.452	0.063	0.084	0.148	0.232	0.939	0.218
D	0.986	0.206	0.035	0.123	0.061	0.184	1.010	0.186
E	0.890	0.124	0.015	0.020	0.035	0.055	0.643	0.035

The order of reactivity indexes for the five fly ashes fits exactly the same order of the measured reactivity by compression testing of the hardened binders. The reactivity index explains satisfactorily the question why fly ash A is very active and why fly ash E is so inactive. This index gives a direct insight into the nature of fly ash (potentially also suitable for other aluminosilicate glassy feedstocks), based on fundamental physical and chemical properties. It can potentially be used for feedstock selection, comparison and can also be used for predicting the strength of geopolymers, if the activation conditions are identical.

The following dissolution experiments on the selected fly ashes under different liquid/solid ratios are performed with the aim of examining the validation of the reactivity index. The investigation on the dissolved particles may also provide information to support or disprove the above assumptions and to gain a better understanding of the roles of Fe and Ti in fly ash. One expected finding is that, for instance, fly ash A will exhibit much higher dissolution rate and extent than the others in a given period.

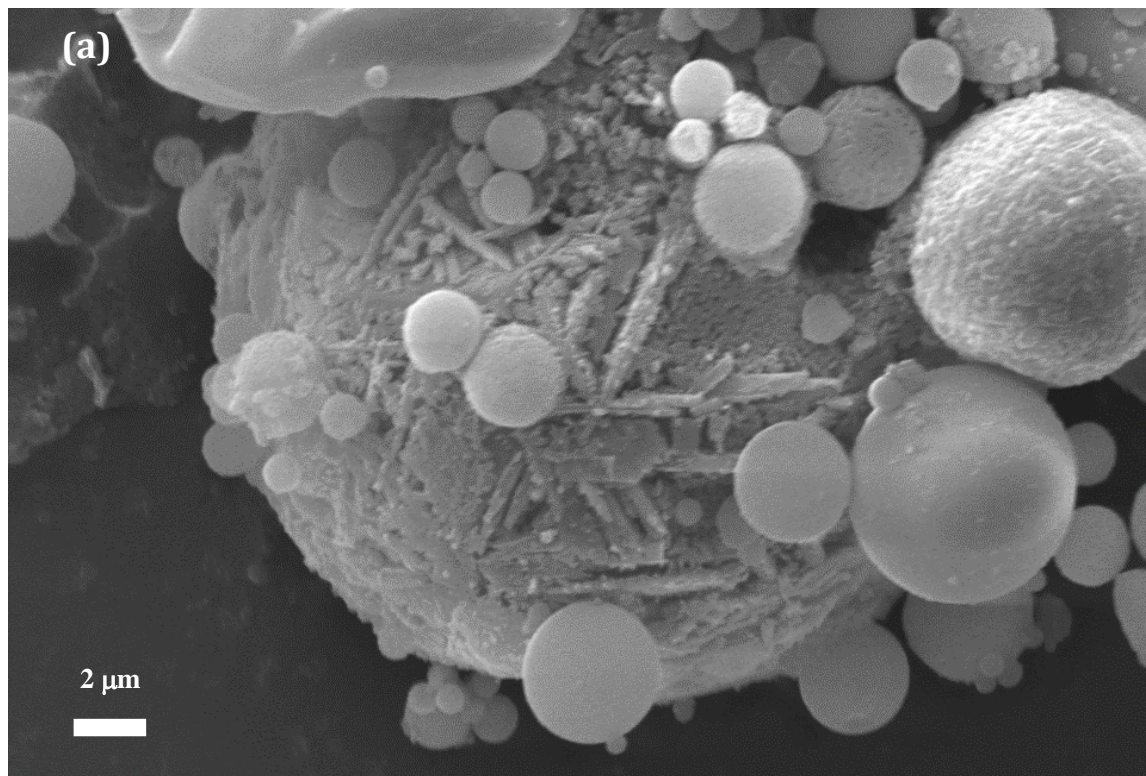
**5.3.2 Dissolution of fly ashes A, B and E at high liquid/solid ratio conditions**

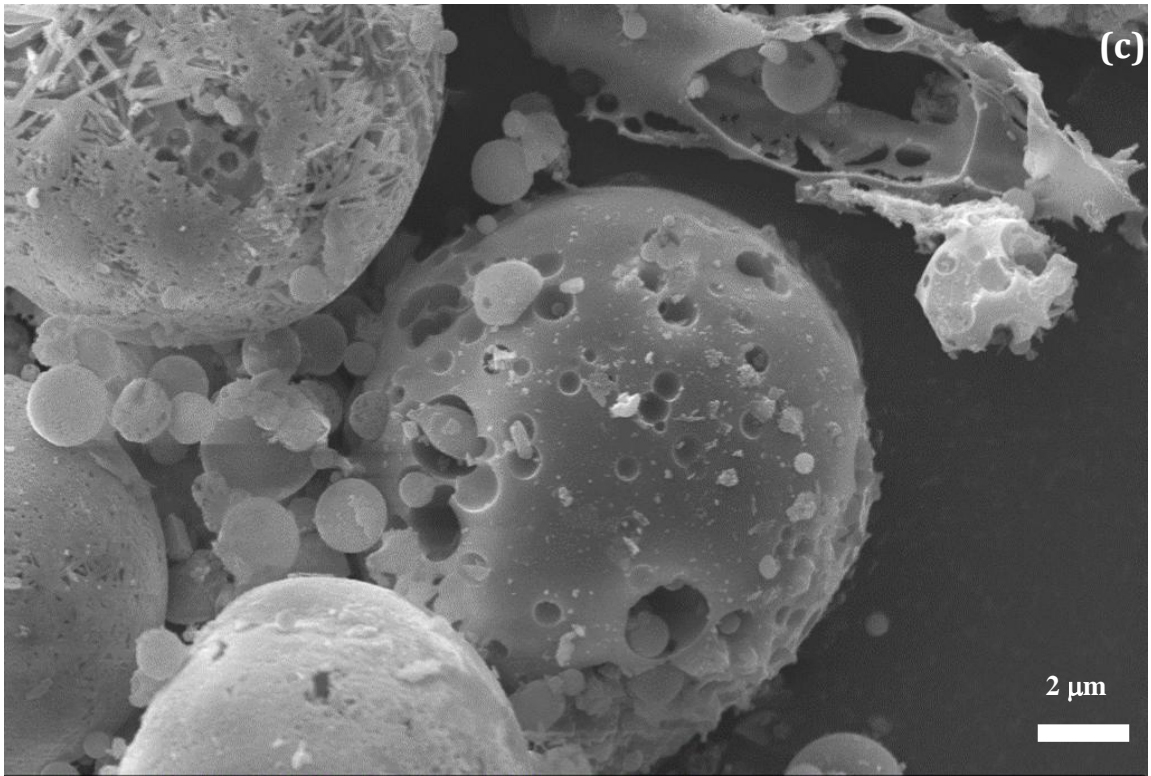
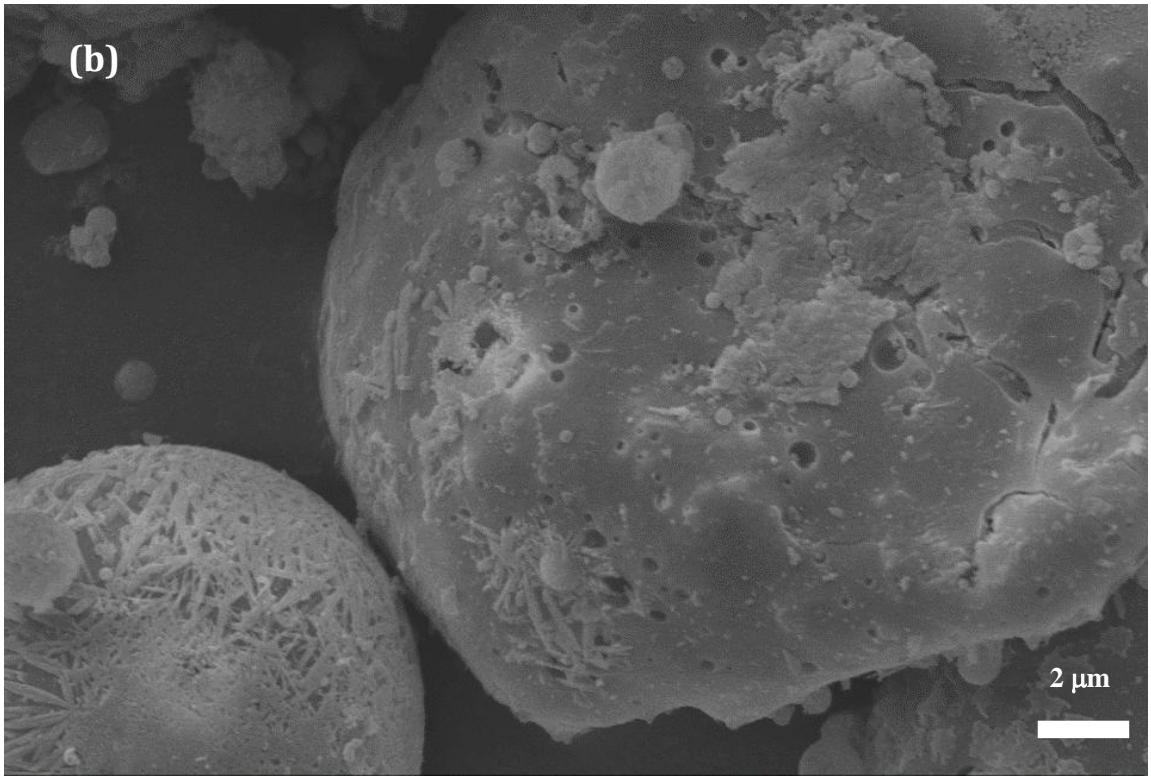
For fly ash dissolution, it was reported that NaOH is somewhat more aggressive than KOH probably due to the higher activity coefficient for Na<sup>+</sup> compared to K<sup>+</sup> (Pietersen et al. 1990). In geopolymer manufacture, however, K<sup>+</sup> seems more positive for achieving high strength products (Andini et al. 2008; Keyte 2008). In addition, a higher dosage of soluble silicate (>200 mM) in solutions was reported to be able to enhance the dissolution of fly ash (Lee and Van Deventer 2002). To find the mechanisms behind these issues, three solutions were used in this project: 4 M KOH solution, 4 M NaOH solution and sodium silicate solution of (4 M NaOH+1.3 M SiO<sub>2</sub>). The fly ash sample was mixed with alkaline solutions at a liquid/solid ratio of 35 g/g. Using such high concentration of

alkaline solutions is to maintain the high pH (>14) during dissolution. The experiments were conducted in a water bath at 80°C equipped with a stirring system, which helped prevent fly ash particles from agglomerating. The samples after dissolution have been washed with a 1:20 HCl solution at room temperature for 5 minutes to neutralize and dissolve possible precipitation products. The phases in fly ashes A, B and E samples before and after alkaline dissolution were also investigated by RQXRD and SEM-EDS.

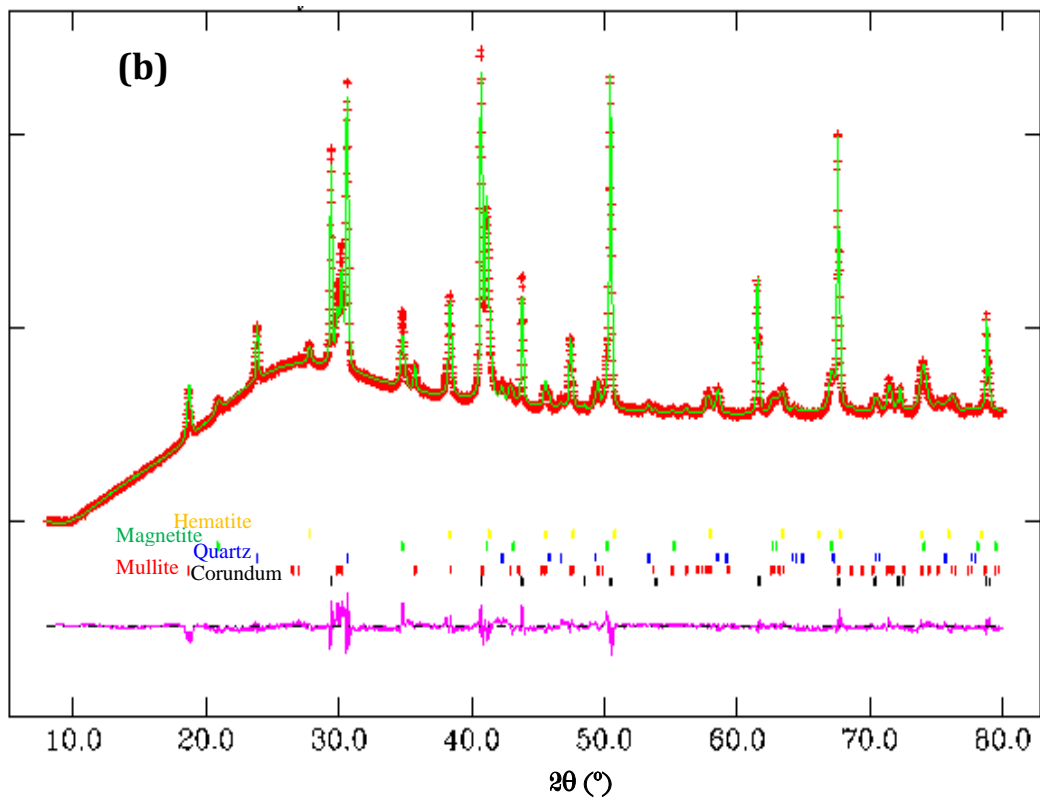
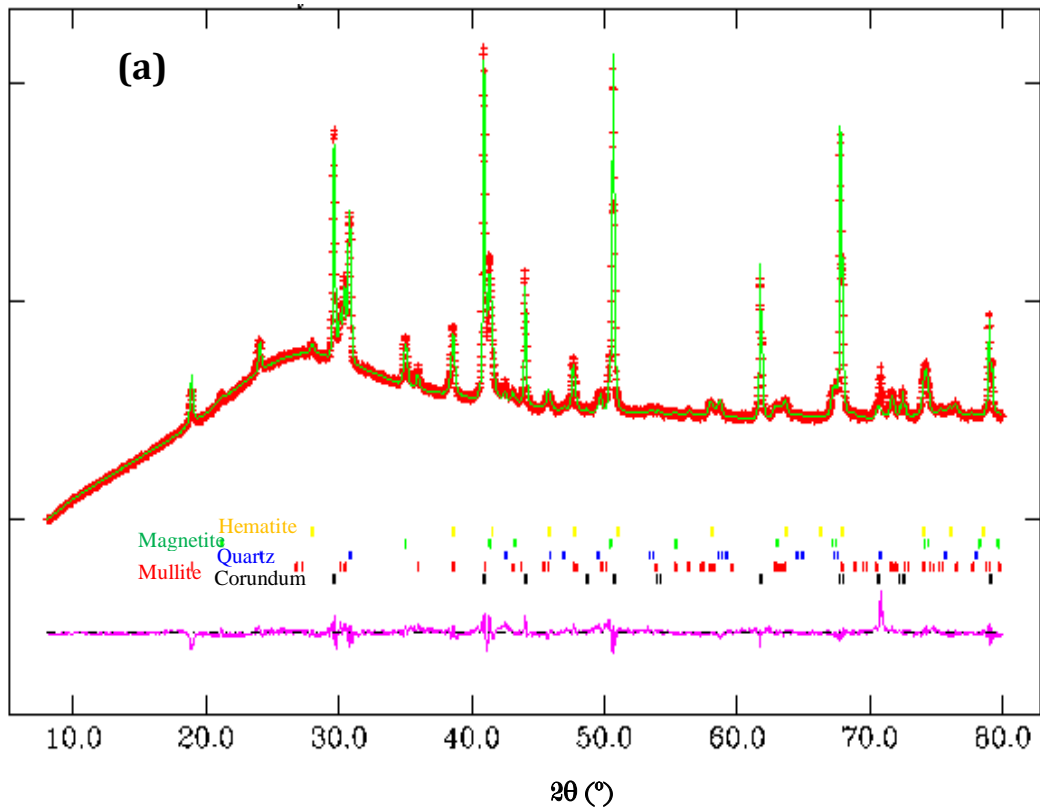
#### 5.3.2.1 Dissolution of fly ash A

Figure 5-6 shows the SEM images of typical morphology of particles of fly ash A after alkaline dissolution. The RQXRD phase analysis is shown in Figure 5-7.

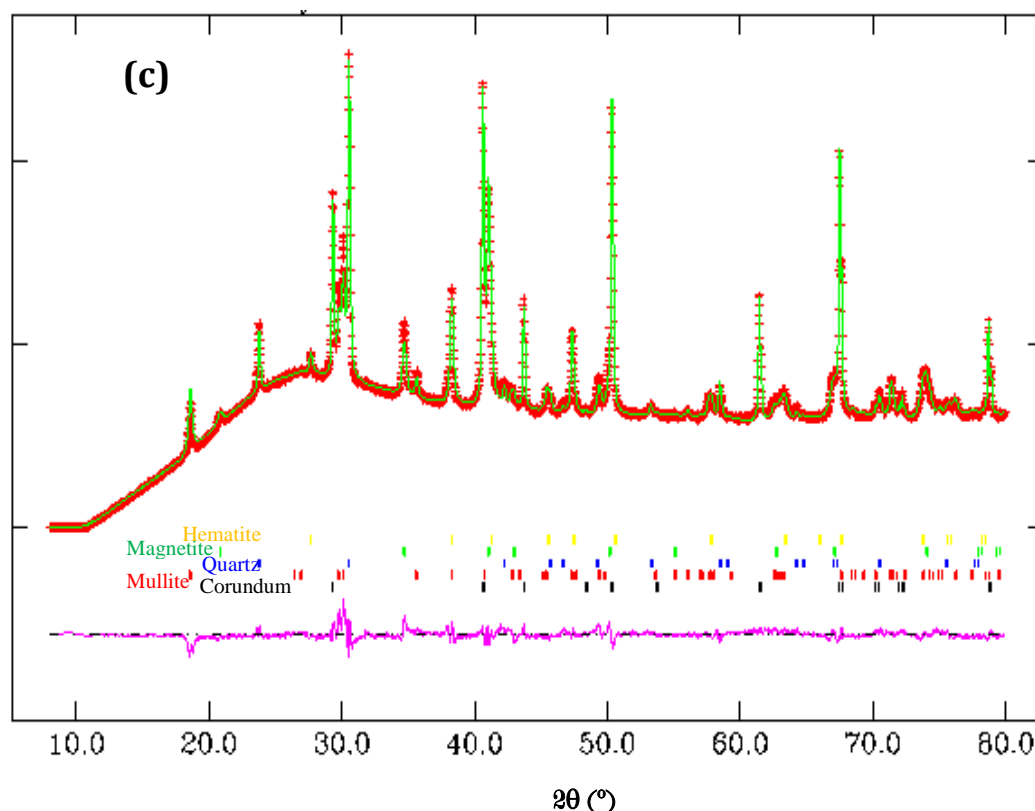




**Figure 5-6.** Typical SEM images of fly ash A particles after dissolution at 80°C for 6 h in (a) 4 M KOH , (b) 4 M NaOH and (c) sodium silicate solutions.







**Figure 5-7.** Rietveld refinement XRD plots showing the observed (red crosses) and calculated (green solid) patterns of fly ash A after dissolution by (a) 4 M KOH, (b) 4 M NaOH and (c) sodium silicate solutions.

Comparing the XRD patterns between the original fly ash A in Figure 5-2(a) and the dissolved ones in Figure 5-7, one notable change is the relative intensity of mullite and quartz. The sample dissolved by KOH solution shows higher mullite characteristic peaks ( $d=5.3975 \text{ \AA}$  {110},  $3.4279 \text{ \AA}$  {120} and  $3.399 \text{ \AA}$  {120}), but less increase in the main quartz peak ( $d=3.3428 \text{ \AA}$  {110}). However, samples dissolved by NaOH and sodium silicate solutions both show higher mullite and quartz characteristic peaks. This indicates a selective dissolution of crystalline phases (not only glass phases), although it is recognized that the intensity of peaks may not be a very accurate index due to possible preferred orientation.

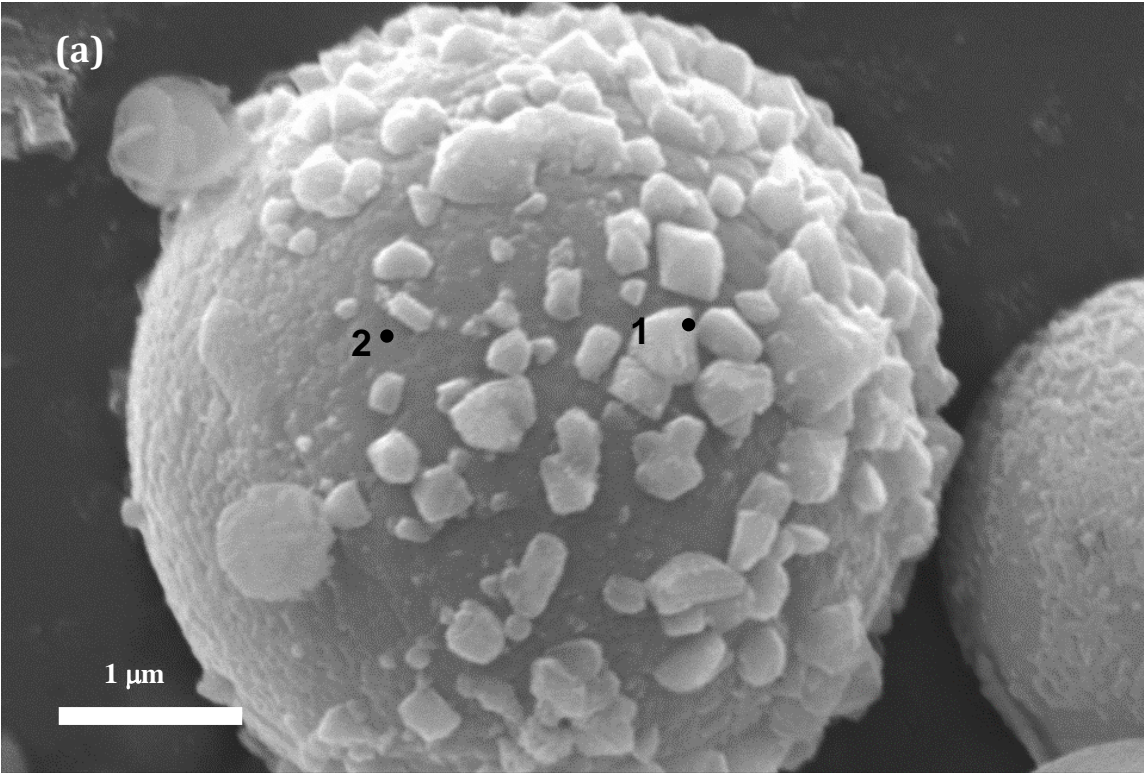
The RQXRD analysis of the phases present in dissolved fly ash A are summarised in Table 5-7. The components of original fly ash are also presented for comparison. After leaching in KOH solution at  $80^\circ\text{C}$  for 6 h, the components in the rest do not change too much compared to the original ash. This is consistent with the SEM observations, as shown in Figure 5-6(a). Many of the small particles still have smooth surface, and only a thin layer of glass dissolves.

**Table 5-7:** Composition (wt.%) of dissolved fly ash A by alkaline solutions at  $80^\circ\text{C}$  for 6 h.

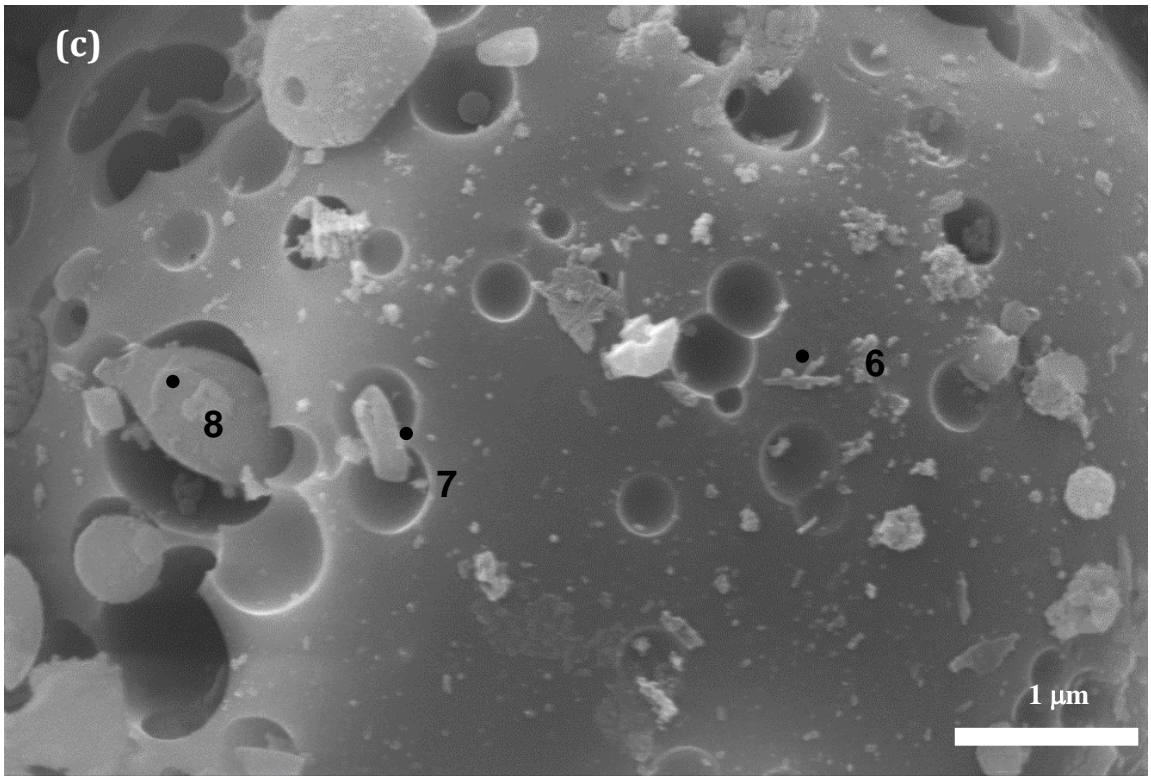
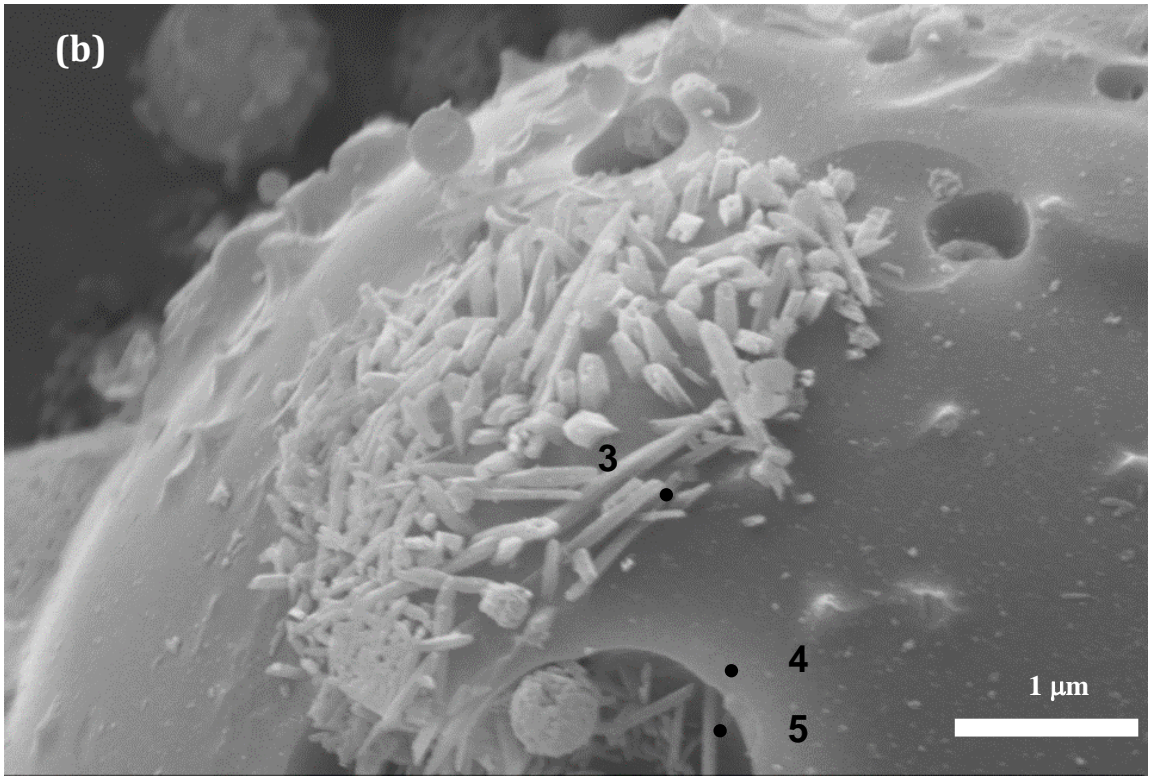
Solution	Mullite	Quartz	Magnetite	Hematite	Amorphous
<i>Original</i>	18.7	3.1	2.5	1.5	74.2
4 M KOH	19.0	3.4	3.0	1.5	73.1
4 M NaOH	24.6	5.4	4.8	2.1	63.1
4 M NaOH+1.3 M SiO <sub>2</sub>	34.7	7.6	6.1	2.6	49.0

The diffraction intensities of crystalline phases increase significantly in the remnant fly ash after sodium based dissolution. This is consistent with the findings that  $\text{Na}^+$  is more aggressive than  $\text{K}^+$  for fly ash dissolution (Pietersen et al. 1990). This is attributed to the higher concentration of  $\text{Na}^+$  in the leached layer because of its smaller ionic radius, and  $\text{Na}^+$  ions are known to promote the breakdown of silica structure (Douglas and El-Shamy 1967). The presence of soluble silica in alkaline solution ( $\sim 1.3 \text{ mol/L}$ ) indeed improves the dissolution of fly ash, comparing the residual amorphous phases in Table 5-7.

Figure 5-8 shows the SEM-EDS images used for local composition analysis of some ash particles with exposed crystals after dissolution. The compositions measured at the marked points are given in Table 5-8.







**Figure 5-8.** SEM-EDS analysis of fly ash A: (a) iron-rich particle dissolved by the KOH solution; (b) mullite-rich particle dissolved by the NaOH solution; (c) glass-rich particle dissolved by the sodium silicate solutions.

**Table 5-8:** Local compositions in the residual particles after dissolution, as determined by EDS analysis, atom %.

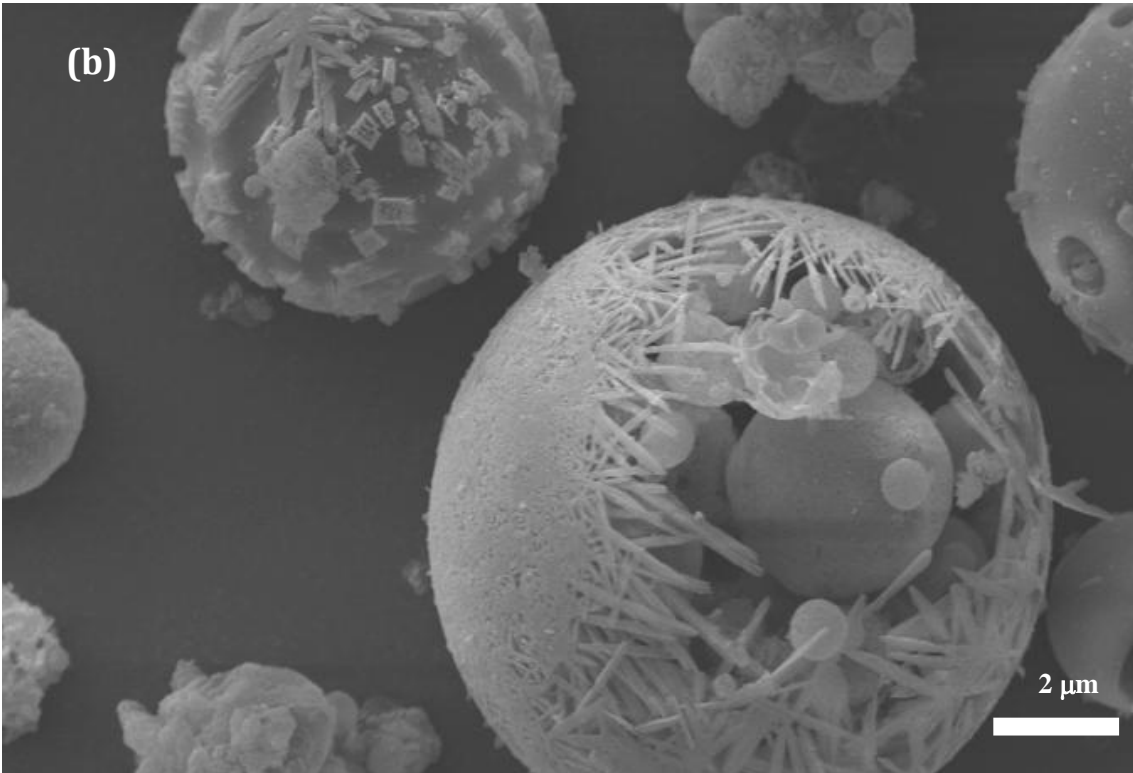
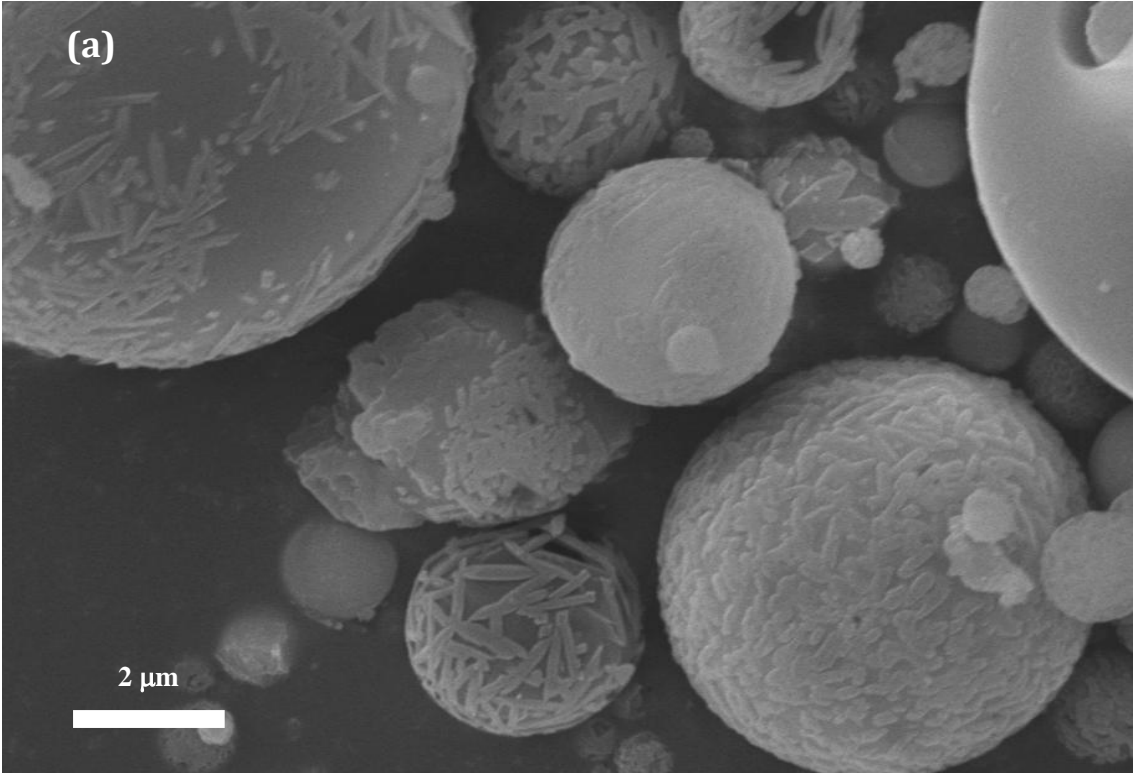
Spots	C	O	Na	Mg	Al	Si	K	Ca	Mn	Fe	Si/Al	Feature
1	7.9	60.5	-	1.4	2.0	2.2	-	0.3	1.3	24.5	1.1	Magnetite
2	1.3	64.5	0.9	-	7.9	22.0	2.6	-	-	0.7	2.8	Glass
3	5.7	68.8	-	-	13.8	11.7	-	-	-	-	0.8	Mullite
4	9.1	67.3	-	-	7.7	12.9	-	1.7	-	1.3	1.7	Glass
5	5.7	65.1	-	-	11.3	14.2	-	2.3	-	1.4	1.2	Glass
6	3.3	59.6	2.7		9.2	21.8	1.69	1.1	-	0.6	2.4	Glass
7	3.9	68.8	2.6		10.4	13.2	0.44	0.3	-	0.4	1.3	Mullite?
8	1.5	73.0	1.7		5.2	17.3	0.35	0.4	-	0.6	3.3	Glass?

From the SEM-EDS analysis results, it can be seen that in the iron-rich particle, there are magnetite crystals formed with Mg, Ca and Mn substitution for Fe and embedded in the glass. Similar findings were reported by Gomes et al. (1999) and Lloyd et al. (2009a). The glass surrounding the magnetite crystals contains a much higher concentration of Na and K than the average value in the whole glass phase. It suggests that the formation of magnetite may preferentially happen in particular particles with relatively higher concentrations of alkali and alkali earth cations, rather than happening in all particles, although the average Si/Fe ratio is lower than 10 (Ehrman et al. 1999). The detected Si/Al ratio on mullite crystals is 0.85, much higher than in the XRD detected crystal (0.26). This is believed due to the deep electron trajectories and large interaction volume (Lloyd et al. 2009a). As the EDS analysis is conducted at a voltage of 20 kV, it is also measuring the Si in the glass underneath the mullite crystallites.

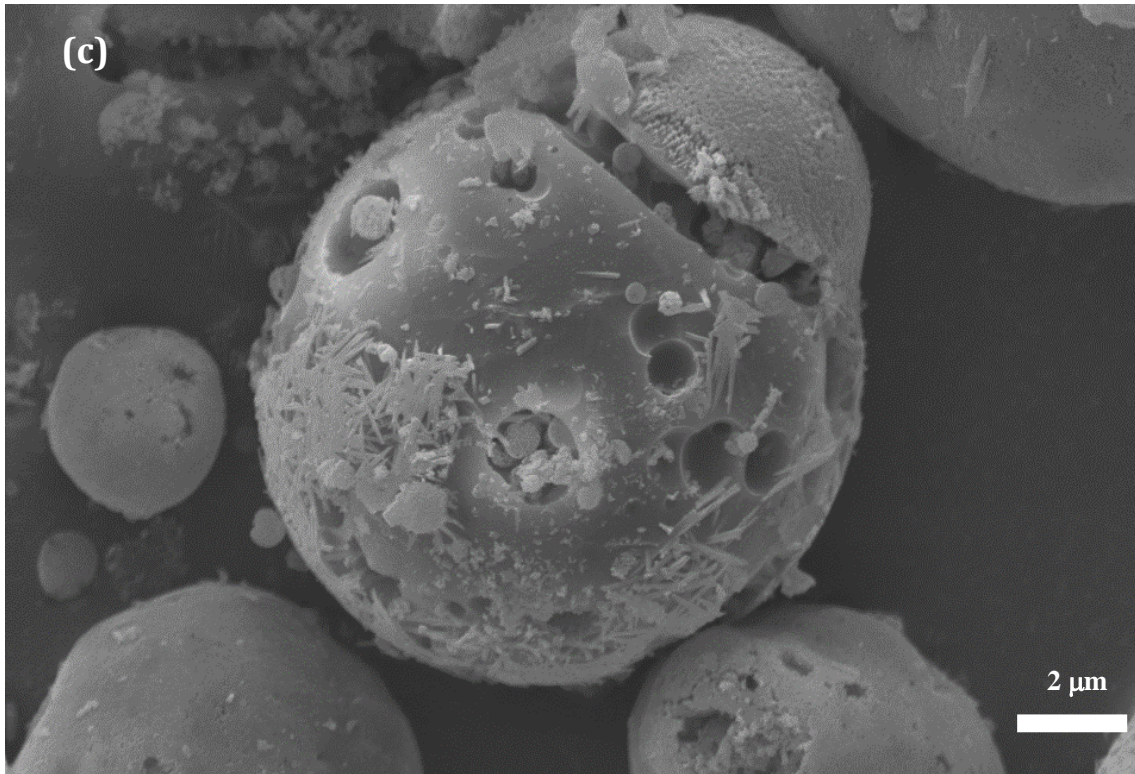
After dissolution, the Si/Al ratios in the glass phases are from 1.25 to 2.76. It is noted that the Si/Al ratios around the erosion holes (spots 4 and 5 and maybe 7) are lower than in the glass bulk (spots 2 and 6), and also lower than the average value in the glass as a whole (Table 5-4). This result provides some hints that the dissolution may preferentially start from the high Al local regions. Another finding is that around the erosion holes, the Fe and Ca concentrations are relatively higher than in the bulk glass. These findings support the above assumption that the bonds of Si-O, Al-O, Fe-O and Ti-O linked with network modifiers are much weaker than in Si-O-Si and Si-O-Al.

### 5.3.2.2 Dissolution of fly ash B

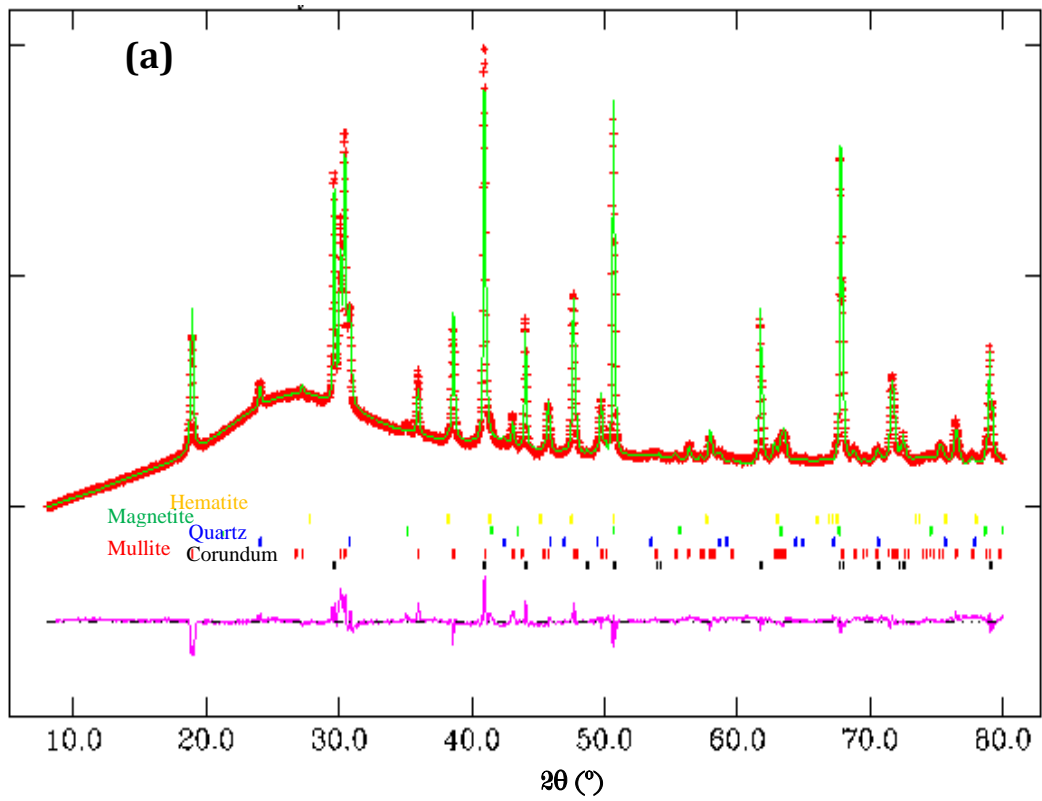
Figure 5-9 shows the SEM images of typical morphology of particles of fly ash B after alkaline dissolution. The RQXRD phase analysis is shown in Figure 5-10.

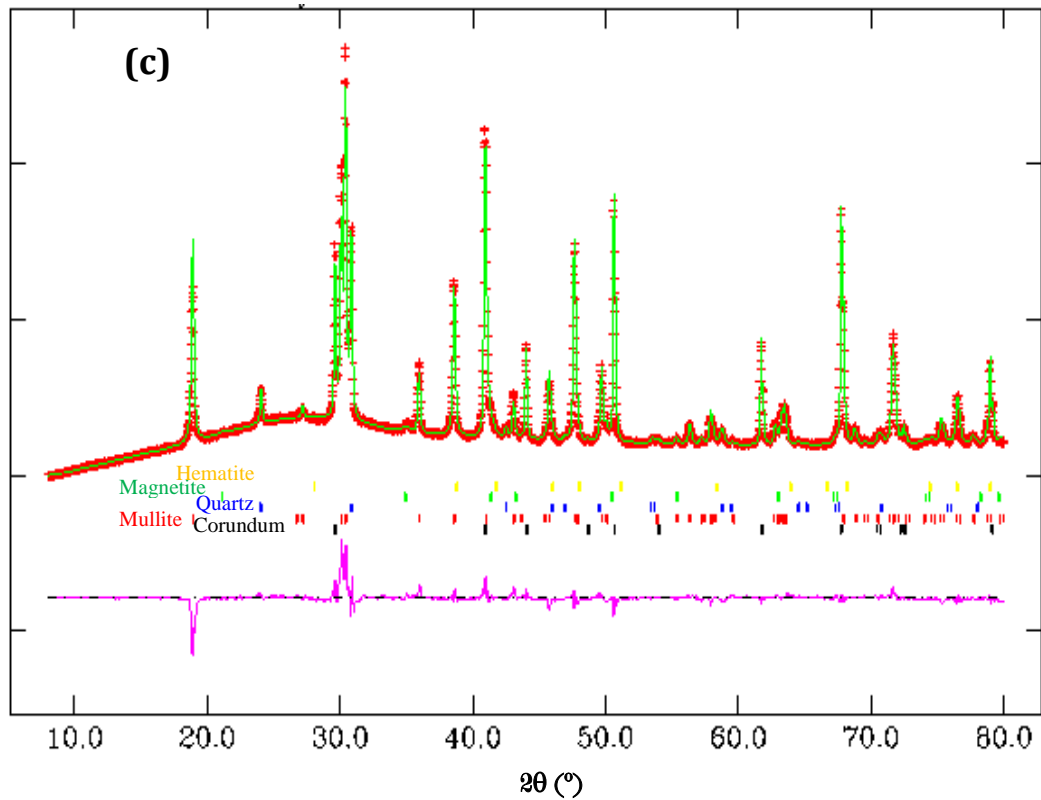
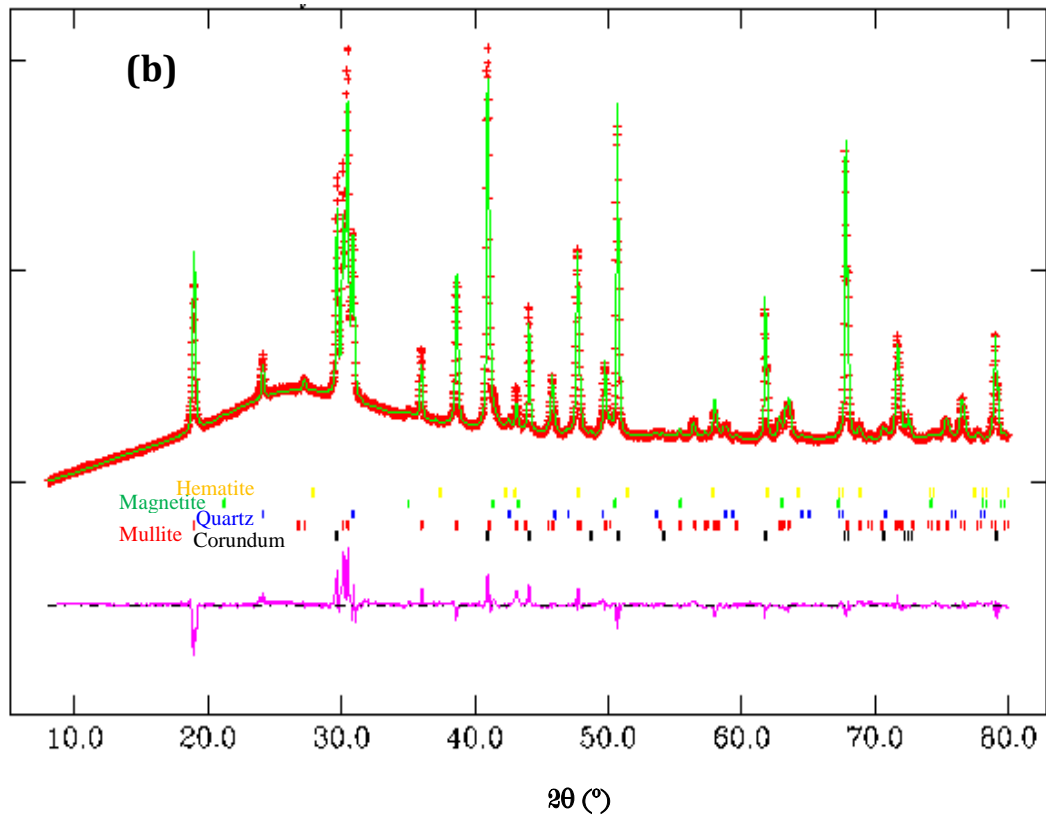






**Figure 5-9.** Typical SEM images of fly ash B particles after dissolution at 80°C for 6 h in (a) 4 M KOH , (b) 4 M NaOH and (c) sodium silicate solutions.





**Figure 5-10.** Rietveld refinement XRD plots showing the observed (red crosses) and calculated (green solid) patterns of fly ash B after dissolution by (a) 4 M KOH, (b) 4 M NaOH and (c) sodium silicate solutions.

A common feature found in Figure 5-7 for fly ash A and Figure 5-10 here is that the patterns of the samples that dissolved by KOH solution are nearly the same

as those of the original fly ashes shown in Figure 5-2. In combination with direct observations in the SEM images, it is reasonable to conclude that the dissolution of fly ash in the KOH solution is slower than in the NaOH and sodium silicate solutions under the conditions of this study. The RQXRD analysis results listed in Table 5-9 confirm this trend.

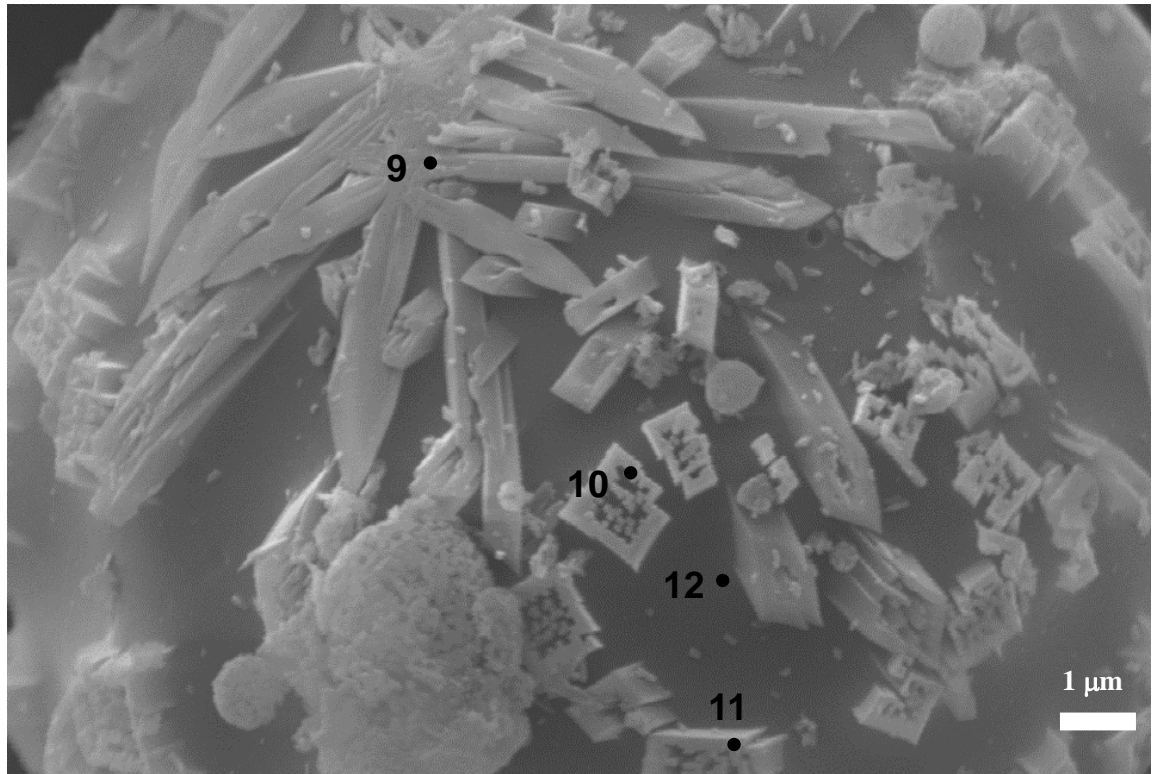
**Table 5-9:** Composition (wt.%) of dissolved fly ash B by alkaline solutions at 80°C for 6 h.

Solution	Mullite	Quartz	Magnetite	Hematite	Amorphous
<i>Original</i>	13.6	2.6	1.3	0.8	81.7
4 M KOH	15.3	2.8	0.9	0.5	80.5
4 M NaOH	20.6	4.0	1.0	0.1	74.3
4 M NaOH+1.3 M SiO <sub>2</sub>	27.5	5.2	1.0	0.3	66.0

In addition, the positive effect of a high concentration of soluble silicate in alkaline solution on the dissolution of aluminosilicate is again confirmed for fly ash B. This effect in geopolymerization was first reported by Lee and Van Deventer (2002a), where the mechanism was explained by the effect of precipitation on fly ash particles and in solution. It was stated that the polysilicates or colloidal silicates that formed in the solutions with high soluble silicate dosage can absorb the dissolved Ca and Al, and in effect, stabilise the Ca and Al in the solution phase and prevent Ca(OH)<sub>2</sub> precipitation in highly alkaline conditions.

However, another important factor that should be considered is the dissolution mode of fly ash. If the colloidal silicates are formed on the particle surface, their precipitation will hinder the travelling of dissolved Si and Al and other cations from the surface into in aqueous solution when the thickness and density of the silicates reach to certain levels. The dissolution may change from a liquid-controlled diffusion step to a solid reaction model (Rees et al. 2008; Lloyd et al. 2009a). Therefore, at a high liquid/solid ratio, the presence of soluble silicate can increase the dissolution rate of fly ash, but it is noted under some circumstances it may also hinder the dissolution under very low liquid/solid ratio conditions, such as the cases of geopolymerization. This aspect will be further discussed by comparing with the dissolution results with the reaction extents in geopolymers in Section 5.3.3.

Figure 5-11 shows an image for SEM-EDS analysis of fly ash B dissolved by the NaOH solution.



**Figure 5-11.** SEM-EDS analysis of a mullite-rich particle of fly ash B that dissolved by the NaOH solution .

The compositions measured at the marked spots are listed in Table 5-10. The well-crystallised mullite particles again show an Si/Al ratio of 0.8 to 0.9, between the ratio in the mullite as detected by XRD (0.59) and the average value in the glass part (1.67). This again suggests that is not suitable to use the EDS analysis at high voltages, for instance, 20 kV used in this study, for the composition analysis if the particle is smaller than the electron penetration depth. Nevertheless, SEM-EDS analysis is still useful for the composition analysis of the bulk glass. The spot 12 has an Si/Al ratio of 1.8, which is very close to the average value in the glass part.

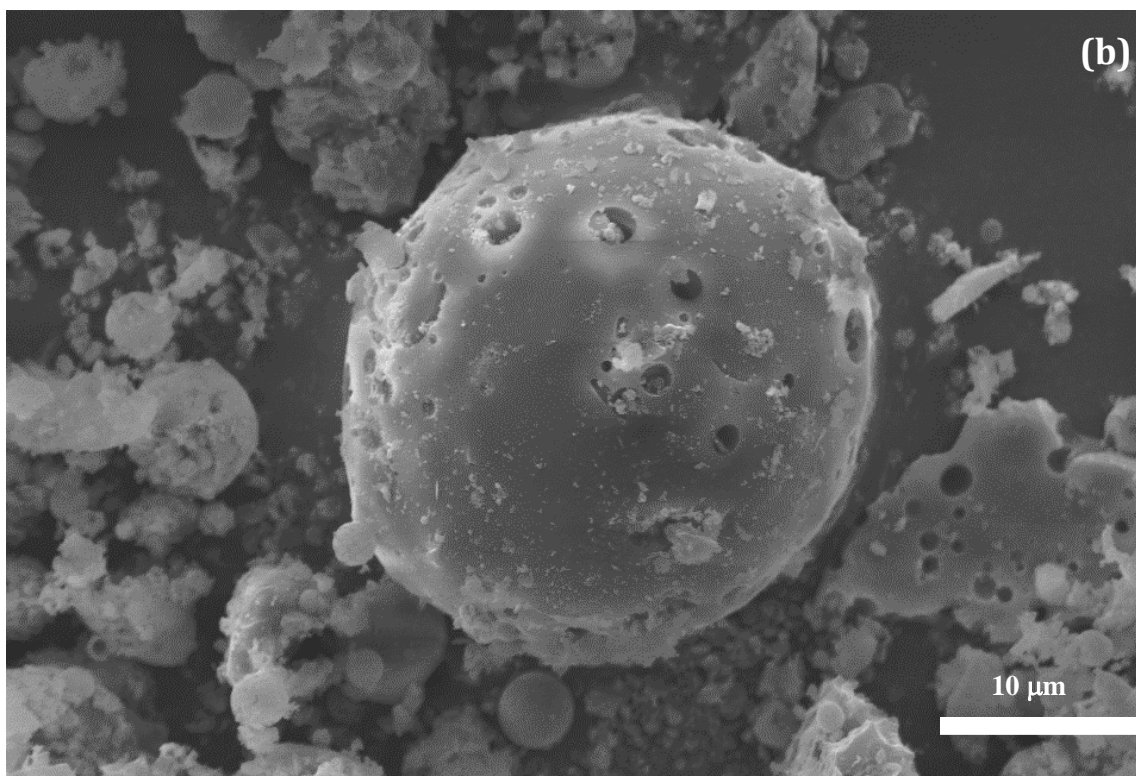
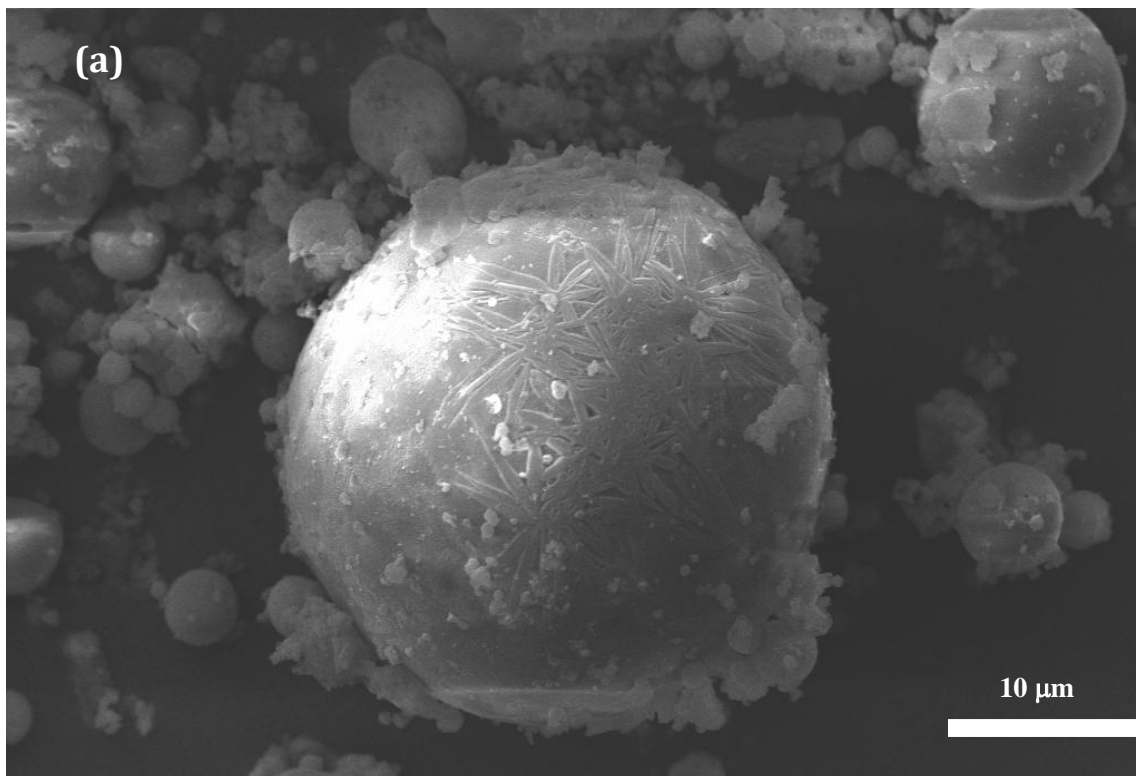
**Table 5-10:** Local compositions in the residual particles after dissolution, as determined by EDS analysis, atom %.

Dots	C	O	Na	Mg	Al	Si	K	Ca	Ti	Fe	Si/Al	Feature
9	6.2	65.4	-	-	14.9	13.6	-	-	-	-	0.9	Mullite
10	3.6	68.5	-	-	15.8	12.2	-	-	-	-	0.8	Mullite
11	9.0	55.3	-	-	20.4	15.3	-	-	-	-	0.8	Mullite
12	8.7	64.4	-	-	9.3	16.4	0.6	-	0.3	0.3	1.8	Glass

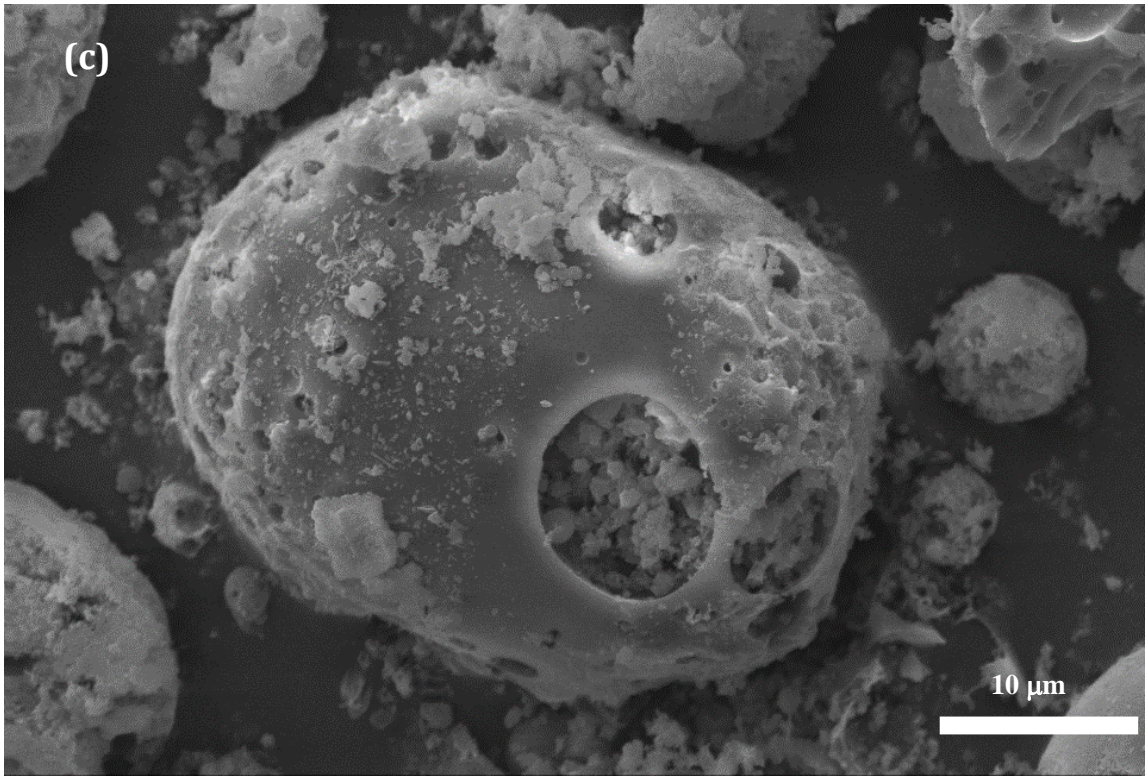
### 5.3.2.3 Dissolution of fly ash E

Figure 5-12 shows the SEM images of typical morphology of particles of fly ash E after alkaline dissolution. The RQXRD phase analysis is shown in Figure 5-13.

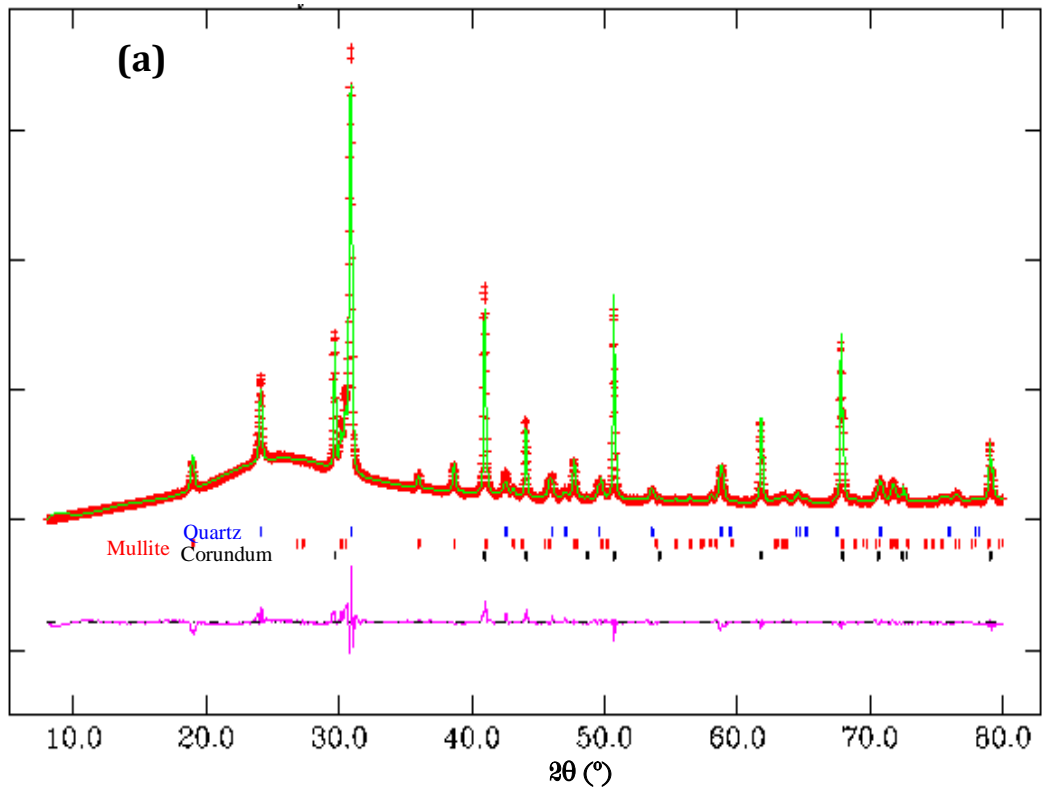


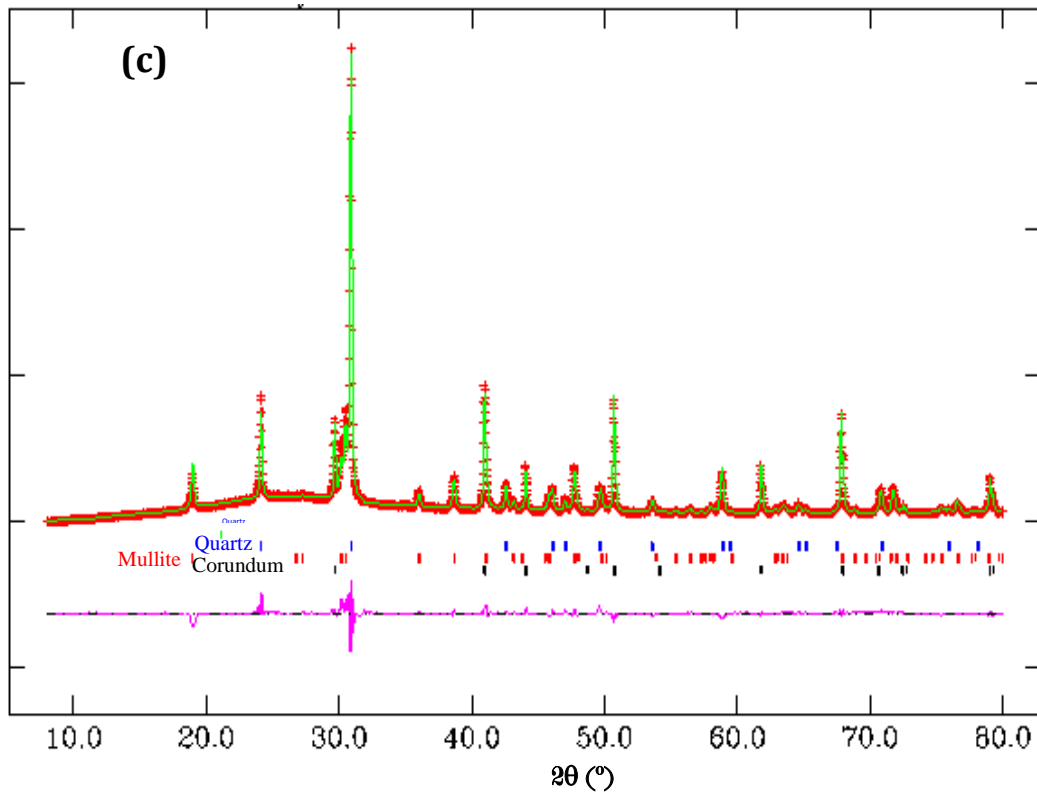
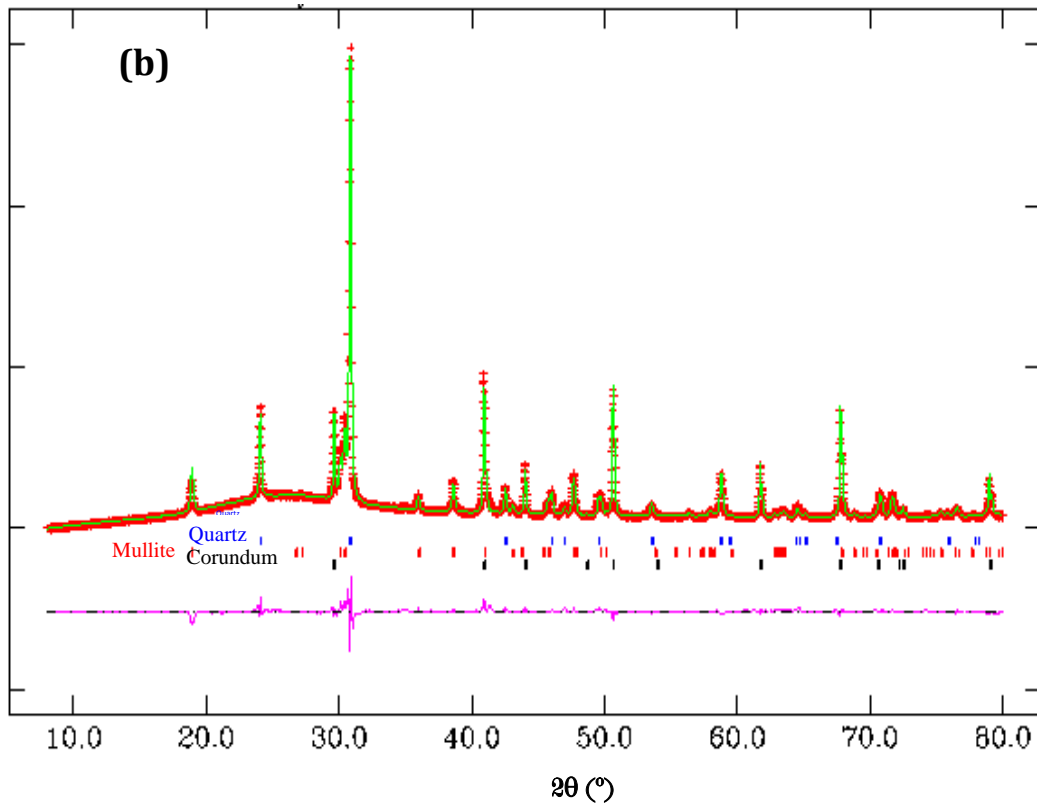






**Figure 5-12.** Typical SEM images of fly ash E particles after dissolution at 80°C for 6 h in (a) 4M KOH , (b) 4M NaOH and (c) sodium silicate solutions.





**Figure 5-13.** Rietveld refinement XRD plots showing the observed (red crosses) and calculated (green solid) patterns of fly ash E after dissolution by (a) 4 M KOH, (b) 4 M NaOH and (c) sodium silicate solutions.

From the SEM images, it is observed that the residual fly ashes are more rigid, porous and fragmented comparing with the dissolved particles of fly ash A and

B. The RQXRD analysis shows that the diffraction intensity of the broad hump from 20° to 30° attributed to the glass phase becomes very flat in the sample leached by sodium silicate solution (Figure 5-13c). The composition in the dissolved fly ash is summarized in Table 5-11.

**Table 5-11:** Composition (wt.%) of dissolved fly ash E by alkaline solutions at 80°C for 6 h.

Solution	Mullite	Quartz	Amorphous
<i>Original</i>	24.1	13.1	62.8
4 M KOH	27.6	16.3	56.1
4 M NaOH	42.7	22.6	34.7
4 M NaOH + 1.3 M SiO <sub>2</sub>	52.5	25.1	22.1

Fly ash E also dissolves less amorphous phases in KOH solution than in the two sodium-based solutions and the presence of high concentration of soluble silicate did again enhanced the dissolution of amorphous phases.

#### 5.3.2.4 Dissolution rate controlling factors

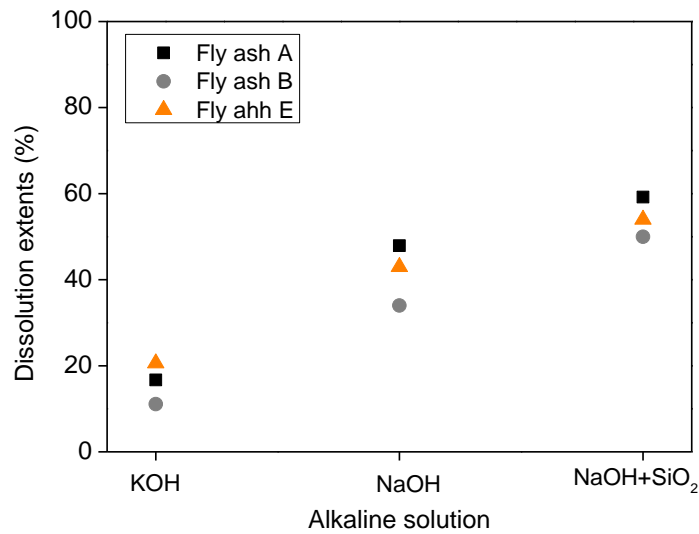
From the SEM and SEM-EDS images, it is evident that the crystals in fly ash particles remain well after the dissolving process at the three alkaline conditions. It is difficult to confirm the exact dissolution extent of the crystals in fly ash in the absence of supporting information from situ direct observations; however, by using the obtained data, it is possible to estimate the dissolution extent of the crystalline phases and amorphous phase in each fly ash. The calculations are based on the assumption that the most retained phase in the dissolved fly ash, either mullite or quartz or magnetite, is supposed to be unreactive. That is, for example, in 100 g of fly ash E, there was 24.1 g of mullite, as shown in Table 5-8. After dissolution by the KOH solution, if mullite was unreactive and the mass was 27.6% of the sample, the remained mass of the dissolved fly ash E should be 87.3 g. On the other hand, if quartz was unreactive and the mass was 16.3% of the sample, the remaining mass of the dissolved fly ash E should be 80.4 g. This mass is lower than the case of assuming that mullite was unreactive, which suggests that some mullite had dissolved. Using the second assumption that quartz is supposed to be unreactive, it is possible to calculate that the remaining mullite was 22.2 g and glass was 45.1 g. From these calculations and analysis, the selectiveness and extents of each phase in the studied fly ashes in different solutions can be assessed. The calculation results are summarized in Table 5-12.

**Table 5-12:** Reaction extents of each phase in the dissolved fly ashes (wt.%).

Fly ash	Solution	Mullite	Quartz	Magnetite	Hematite	Glass
A	4 M KOH	15.3	8.6	0	16.7	17.9
	4 M NaOH	31.5	9.3	0	27.1	55.7
	4 M NaOH + 1.3 M SiO <sub>2</sub>	24.0	0	0	29.0	72.9
B	4 M KOH	0	4.3	38.5	44.4	12.4
	4 M NaOH	1.5	0	50	91.9	40.9
	4 M NaOH + 1.3 M SiO <sub>2</sub>	0	1.1	62.0	81.4	60.0
E	4 M KOH	8.0	0	-	-	28.2
	4 M NaOH	0	2.6	-	-	68.8
	4 M NaOH + 1.3 M SiO <sub>2</sub>	0	12.0	-	-	83.8

It can be seen that the dissolution behaviour of mullite and quartz in fly ash A is different from those in fly ashes B and E. Due to the high concentration of Fe and maybe a significant substitution of Al in the mullite, the dissolution extents of this 'impure' mullite are 15.3 and 31.5 wt.% in the 4 M NaOH and KOH solutions, respectively. Although the dissolution extent is lower in the 4 M NaOH + 1.3 M SiO<sub>2</sub> solution, the glass dissolves much more. For fly ash B, the calculated dissolution extents of magnetite and hematite are too high. This is probably not accurate because the concentrations of these two phases in fly ash B are very low and it is difficult for the RQXRD analysis to obtain accurate values after dissolution. However, it is clear that the dissolution of mullite and quartz in fly ash B is very limited. This means the mullite and quartz in fly ash B are much less reactive than those in fly ash A. The selective dissolution of the mullite and quartz in fly ash E is more evident. This is probably because of the different structures, and particularly the purity, of crystals.

The total dissolution extents for each fly ash sample are shown in Figure 5-14. The value presents a dissolution extent of the bulk particle. Fly ash A exhibits a much higher dissolution extent than fly ashes B and E in the two sodium-based media. However, fly ash E exhibits even a higher dissolution extent than fly ashes A and B in KOH solution and it also dissolves more than fly ash B in the two sodium-based media. This is contrary to the expectation, as discussed above, that fly ash A and B will exhibit much higher dissolution rate and extent than E in a given period. This then raise the question: is the reactivity index wrong?



**Figure 5-14.** Dissolution extents of fly ashes in alkaline solutions at 80°C for 6 h.

Chen et al. (2011) proposed that the dissolution of fly ash in KOH solutions can be divided into three stages at a liquid to solid ratio of 40 g/g. In stage one, only a thin film or gel (alteration) layer scattered on fly ash particles, and the reaction progress is controlled by the rate of glass network dissolution. At this stage, the glass chemistry of fly ash plays a determining role. With the dissolution continuing, the Al and Si reach a critical concentration, commence gelation to form a thicker layer covering the residual particles, and may also be scattered in solution. The critical values for Si and Al may be different, depending on the dissolution medium (Park and Englezos, 1999). At this stage, the dissolution rate-controlling factor becomes the diffusion of both activating ions and dissolved ions through the gel layer. The third stage starts from crystallization of zeolite on top of the gel layer. At this stage the dissolution rate is also controlled by diffusion.

In this study, the liquid to solid ratio used was 35 g/g, between the values of 10 g/g used by Lee and Van Deventer (2002a) and 40 g/g used by Chen et al. (2011). The dissolution temperature 80°C in this study is higher than the temperature used by Lee and Van Deventer (2002a), which was 20°C and also higher than the temperature used by Chen et al. (2011) which was 20-70°C. In their research, they both reported the presence of gels covered on the residual fly ash particles. Therefore, a gel layer is believed also to form on the residual particles in this study, but has been removed by the HCl solution. For fly ashes A and B in the KOH solution, the dissolved Al is supposed to form aluminosilicate gels with the Si species due to the high activity of  $[Al(OH)_4]^-$  (Weng and Sagoe-Crentsil 2007) and this may bring forward the commencement of the diffusion-controlled stage. In addition, the presence of higher concentrations of calcium and magnesium in the glass phases of fly ash A and B will modify the equilibrium of dissolved solution in order to induce condensation of polysilicates (Niето and Zanni 1997). For this reason, the dissolution of fly ashes A and B may be slower than in fly ash E-liquid systems in the KOH solution. The lower solution extents of fly ash B in the sodium-based media

under the dissolution conditions do not mean its reactivity is lower compared to fly ash E.

The above dissolution results and discussion indicate that it is difficult to compare the reactivity of fly ashes by comparing their dissolution extent, unless the dissolution is still in the first stage. A high liquid to solid ratio may help to prevent the precipitation of gel layers on fly ash particles and keep the dissolution in the first stage.

Pietersen et al. (1990) investigated the dissolution of Class F fly ashes in NaOH solution at a liquid to solid ratio of 1000 mL/g. In Table 5-13 their experimental results are reorganized and presented. The fly ashes used for dissolution have been classified by sieving (only 35-50  $\mu\text{m}$  particles are used) followed by density separation.

**Table 5-13:** Fly ash dissolution by NaOH (pH=13.7) at a liquid to solid ratio of 1000 mL/g at 40°C. Data from (Pietersen et al. 1990).

Sample <sup>a</sup>	EFA-B	EFA-E	LB-B	KEMA1-B	KEMA1-E	LM-B	LM-E
Glass (wt.%) <sup>b</sup>	0.95	0.92	0.74	0.73	0.86	0.67	0.62
Si/Al in glass	1.69	1.45	1.85	1.66	1.61	1.72	1.89
Active bonds <sup>c</sup> (mol%/g)	0.43	0.35	0.26	0.40	0.31	0.23	0.15
120 h dissolution of Si (wt.%)	20	24	25	24	20	25	20
Bulk dissolution extent <sup>d</sup> (wt.%)	19.00	22.08	18.5 0	17.52	17.20	16.7 5	12.4 0

a: A sample denoted with "-B" mean its density is 2.6-2.3 g/cm<sup>3</sup>, with "-E" means its density is <1.4 g/cm<sup>3</sup>. The surface area between the samples is very similar (maximum difference is about 20%).

b: The small amount of crystalline iron was not excluded from the glass phase in analysis. From the bulk analysis, magnetite contents in fly ashes EFA, LB, KEMA1 and LM are 0.7 wt.%, 0.5 wt.%, 0.7 wt.% and 1.4 wt.% respectively. The glass content given here is therefore slightly higher than the real value.

c: 'Active bonds' is the molar concentration of 2(CaO% + MgO% + Na<sub>2</sub>O% + K<sub>2</sub>O%) + 2 [5]FeO% + 6 [5]Fe<sub>2</sub>O<sub>3</sub>%, as used in calculation of the reactivity index (RI). Using the concentration of active bonds here instead of RI is because the specific surface areas of the fly ashes should be very close as they were classified in the same particle size range.

d: Corrected based on amorphous phase.

The dissolution extent listed in Table 5-10 is achieved after 120 h at 40°C. The high liquid/solid ratio ensured that in this period, the dissolution extent seems only time-dependent. It means the effects of gel precipitation are very limited. At this high liquid/solid ratio, the bulk dissolution extent is found to have a close relationship not only with glass content but also the chemistry. A general trend is that fly ash that contains higher reactive bonds exhibits higher dissolution extent. The exception for fly ash EFA-B and EFA-E is possibly due to the inaccurate characterisation of mineral components. The general trend confirms that the proposed mechanism for the reactivity index is reasonable, if it is assumed that the effect of small variation in surface does not make large contribution to the dissolution extent.

### 5.3.3 Dissolution of fly ash under geopolymerization conditions

At geopolymerization conditions the liquid to solid ratio is usually between 0.3 and 0.8, depending on the workability of the paste. At such low liquid conditions, the influence of precipitation should be more critical.

In Table 4-11, the fly ash reaction extent under geopolymerization conditions with the same quantity of activator has been measured by the HCl dissolution method, which was proven to remove all of gels as observed in the SEM images of dissolved fly ash particles. The dissolution extent is 18.7 to 6.4 wt.% for the fly ashes B to E, while it is very high for fly ash A, which achieved 40.8 wt.% reaction. This very high dissolution extent may consist some dissolved iron-bearing phases under HCl conditions. However, a general trend is that the fly ash with higher reactivity index exhibits higher reaction extent under geopolymerization conditions.

In addition, the reaction extent of fly ash under the conditions with the same alkalinity of activator (see Table 4-7) has been measured by the HCl dissolution method in this section. Table 5-14 presents the dissolution extent of the selected fly ashes.

**Table 5-14:** Dissolution extents (wt.%) of fly ashes A, B and E under geopolymerization conditions with the same alkalinity of activator (40°C × 24 h+ 25°C × 27 d).

	A	B	E
Bulk dissolution	21.0	18.8	6.6
Glass dissolution <sup>a</sup>	28.3	23.1	10.5

a: It is an estimated value based on the assumption that only glassy phase dissolves.

The dissolution range of the bulk fly ash is consistent with the range determined by other researchers (Rattanasak et al. 2011; Chindaprasirt et al. 2011). However, it is much lower than the reported reaction degree of fly ashes by Fernández-Jiménez et al. (2006b), who obtained a reaction degree ~60 % of high Al fly ash and ~40% for low Al fly ash. This could be because their fly ashes are much more reactive. This result shows that the slow initial dissolution and fast precipitation in reaction system E hinders the transformation of glass phases to geopolymer gels, and this limited reaction extent is partially accounting for the low strength of binder E.

Rickard et al. (2011) investigated the mineral and glass composition of three Class F fly ashes that collected from three different power stations in Australia. Their results are represented in Table 5-15. Although a direct measurement of dissolution extent was not performed by those authors, the compressive strength of geopolymer binders suggests that in the geopolymers Tarong fly ash may have lower reaction extent than the other two. The order of reactivity index of the three fly ashes fits well with their strength of the geopolymers.

**Table 5-15:** The relationship between the reactivity indexes of the three typical Australian fly ashes and the compressive strength of their geopolymers. Data from (Richard et al. 2011).

		Collie	Eraring	Tarong
Glass (wt.%)		54.00	62.74	50.82
Active bonds (mol% per gram)		0.36	0.24	0.04
Surface area in volume (m <sup>2</sup> /cm <sup>3</sup> )		1.59	0.92	0.99
Density (g/cm <sup>3</sup> )		2.4	2.02	2.0
Specific surface area (m <sup>2</sup> /g)		0.66	0.46	0.50
Reactivity index (mol%·m <sup>2</sup> /g)		0.24	0.11	0.02
Compressive strength	Si:Al=2.0	128	31	26
of geopolymer binders (MPa)	Si:Al=2.5	53	33	26
	Si:Al=3.0	29	28	25

The above dissolution experiments suggest that only a small fraction of fly ash is dissolved under geopolymerization conditions, particularly when specimens set and harden fast at elevated temperature. Therefore the initial dissolution controlled by the glass chemistry is very critical to obtain a high reaction extent. In addition, the activator is also important because the initial dissolution and the consequent condensation depend on its composition, and this aspect has been extensively studied recently (Duxson et al. 2005; Rattanasak and Chindaprasirt 2009; Silva de Vargas et al. 2011; Bondar et al. 2011; Somna et al. 2011 ).

To summarise, the dissolution experiment reveals that mullite and quartz phases present in 'impure' fly ash are much more reactive than those in fly ash with low concentrations of modifiers. In general, the amorphous phases are much more reactive and suffered more attack by alkaline solutions. The early dissolution at the stage when the rate was controlled by the glass network dissolution is very important for the total reaction extent of fly ash, particularly under geopolymerization conditions. A certain concentration of soluble silicate in the alkaline solution improves the dissolution rate, which means that it is probably beneficial to use a silica containing activator for geopolymer manufacture. Finally, the dissolution results confirm that the proposed reactivity index does give an inherent description of the nature of glass phase in fly ash, and is useful in predicting the reactivity of fly ash.

#### ***5.4 FTIR analysis: a quick indicator test for reactivity of fly ash***

Rietveld quantitative XRD (RQXRD) in combination with XRF analysis provide the most internally valid method of evaluating the glass chemistry and appropriately provides the core evidence for quantifying the reactivity of fly ash. However, there are also shortcomings of RQXRD. Before performing Rietveld quantitative analysis, it is necessary to obtain accurate lattice parameters for each phase present in fly ash. However, as the crystalline phases present in fly ash are usually not well crystallized, and usually contain various impurities, their lattice parameters are consequently not the same as those used for pure, single crystalline materials. Besides, RQXRD analysis is a time-consuming process. To obtain high quality X-ray data that are suitable for performing RQXRD analysis, data collection usually takes a long period (several hours to



several days, depending on the instrument used). The analysis of the collected data is also not a trivial task. These two shortcomings not only limit the precision and accuracy of the results, but also hinder the translation of results to engineering applications, where quick and effective tests are more welcomed.

Most recently, Valcke et al. (2013) proposed a new method to quantitatively measure the reactivity of fly ash that was feature sizing and chemical typing (FS&CT). This method used an electron microscope to capture the particle size and elemental composition of fly ash particles simultaneously. However, the shortcoming is that it only gives bulk composition, and particularly in the surface layer of particles, which is apparently not enough for understanding of the reactivity of fly ash, as discussed above.

The importance of glass chemistry in determining the reactivity of fly ash has been demonstrated in the above two sections. In specification, in glassy phases, the alkali and alkali earth metal cations present as charge balancing cations associating with alumina tetrahedra Si-O-Al(IV), and also in NBO sites Si(Al)-O-M( $\frac{1}{2}$ Me) as well. The iron tends to be both network former as Si-O-Fe(IV) and network modifier Si(Al)-O-Fe. The T-O bonds linked with M<sup>+</sup>, Me<sup>2+</sup>, <sup>[5]</sup>Fe<sup>2+</sup> or <sup>[5]</sup>Fe<sup>3+</sup> are much more active and act as defects for glass dissolution. The higher concentration of these reactive bonds, the higher reactivity of fly ash is.

From this perspective, FTIR spectroscopy could be an appropriate technique to get a quick and qualitative understanding of the reactivity of fly ash. IR techniques have been shown to be powerful in revealing information about the Al-O and Si-O bonds in aluminosilicate glasses at a molecular level (Taylor 1990; Gervais et al. 1987). The variation of the main vibration band around 1000 cm<sup>-1</sup>, assigned to the (Si, Al)-O-Si structures, can reflect the incorporation of alkali and alkali earth metals (Taylor 1990; Merzbacher and White 1988) and iron and titanium cations (Scarano et al. 1993; Ehrman et al. 1999), which play very important roles in determining the dissolution of glassy phases in fly ash as discussed above. Several studies have used IR techniques in characterizing the geopolymerization process and products (Lee and Van Deventer 2003; Rees et al. 2007a; 2007b; Criado et al. 2007), however, only limited attention has been paid to the use of this technology to aid in understanding of the reactivity of fly ashes from different sources (Fernández-Jiménez & Palomo, 2005).

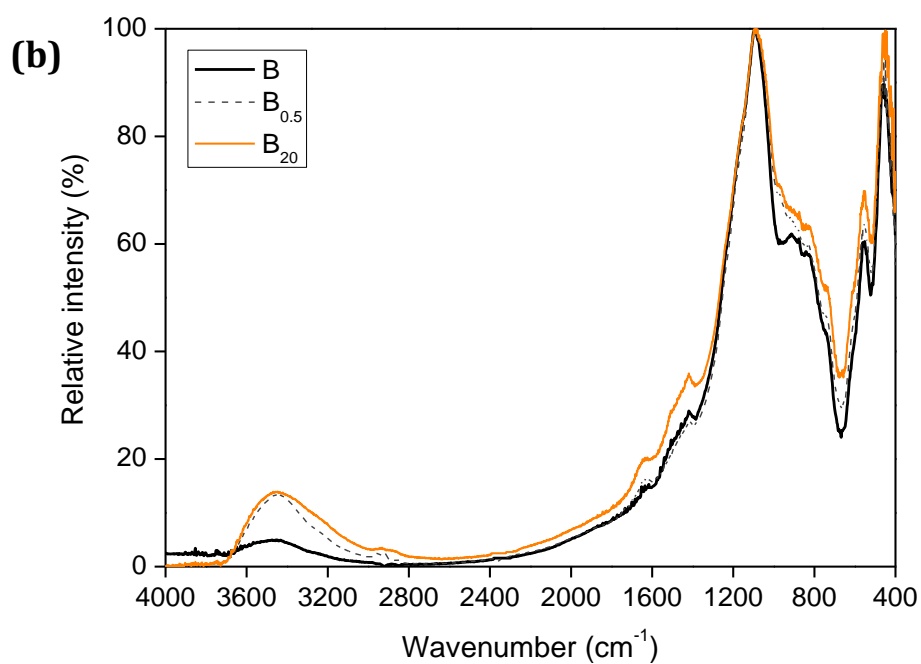
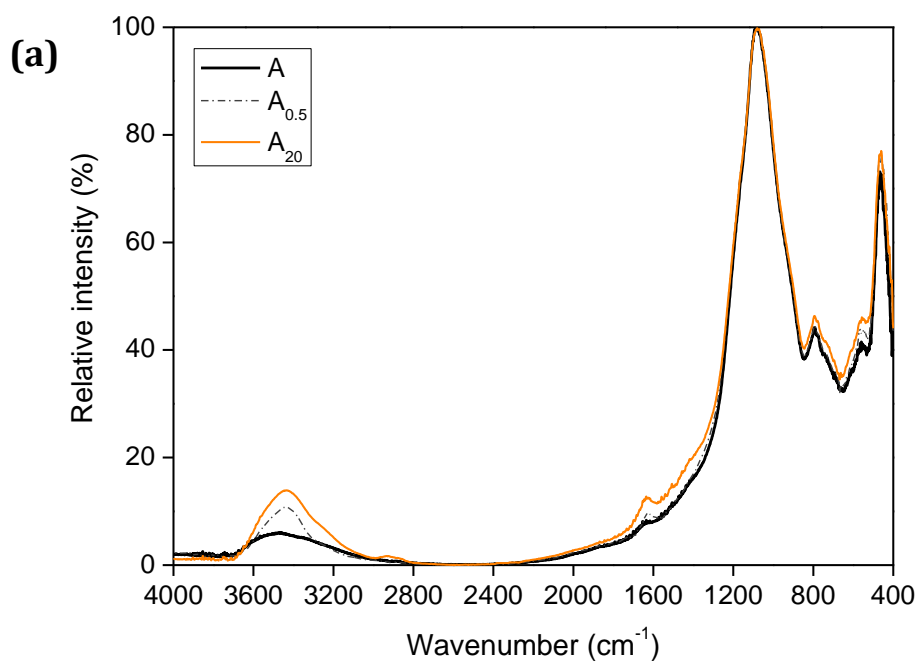
The primary aim of this section is to use FTIR spectroscopy to examine the Si and Al environments in the five well-understood fly ashes. The reactive Si and Al will be identified and correlated with the strength of geopolymers, with a view towards obtaining insights into the nature of each fly ash. In addition, the geopolymers derived from the five fly ashes were also analyzed to examine the environment changes of Si and Al.

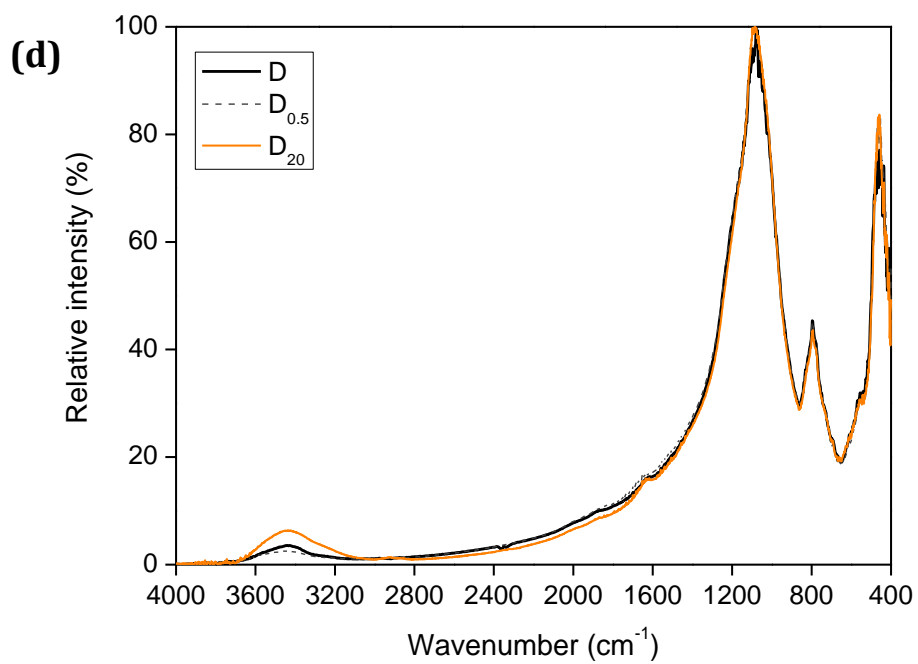
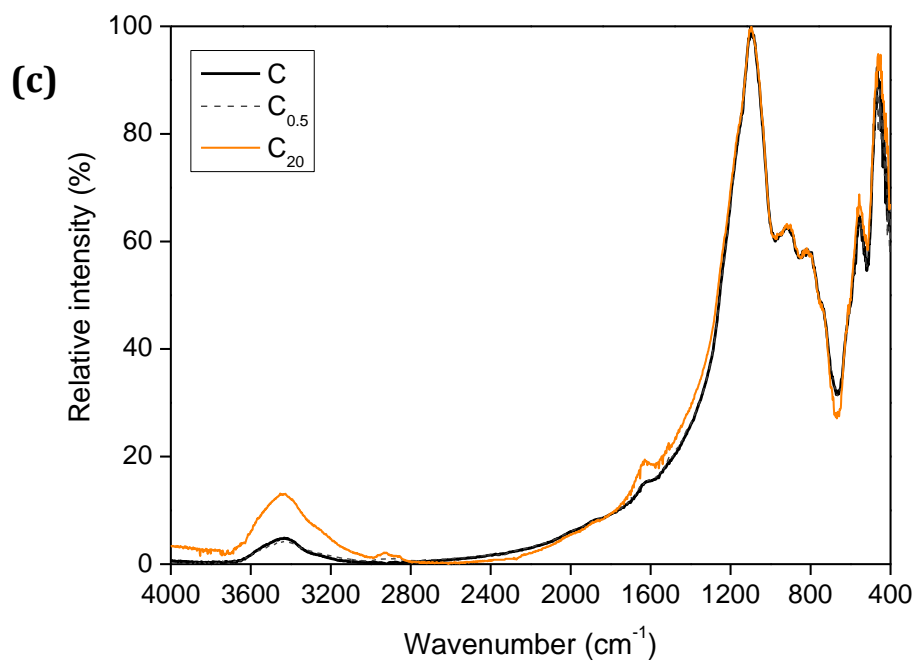
#### **5.4.1 FTIR analysis of fly ash**

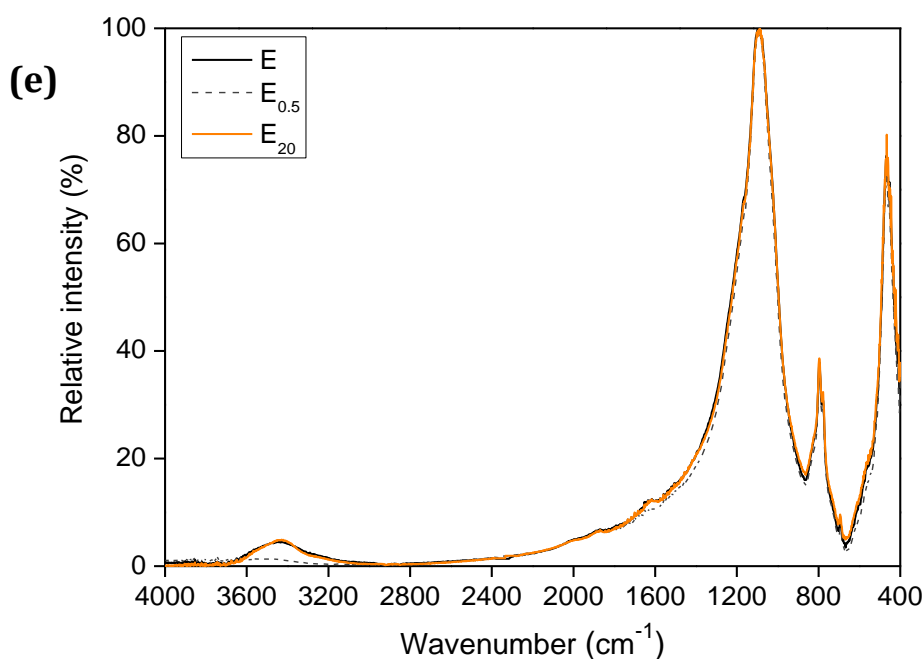
##### **5.4.1.1 FTIR analysis of the original fly ashes and those mixed with water**

To examine the reactivity in water, although fly ash is usually non-hydraulic, the five fly ashes were mixed with water at liquid/ash ratios of 0.5 and 20, at 25°C

for 7 d. The dried powders (105°C for 48 h) were also analyzed. Figure 5-15 shows the FTIR spectra of the five fly ashes before and after contact with water.







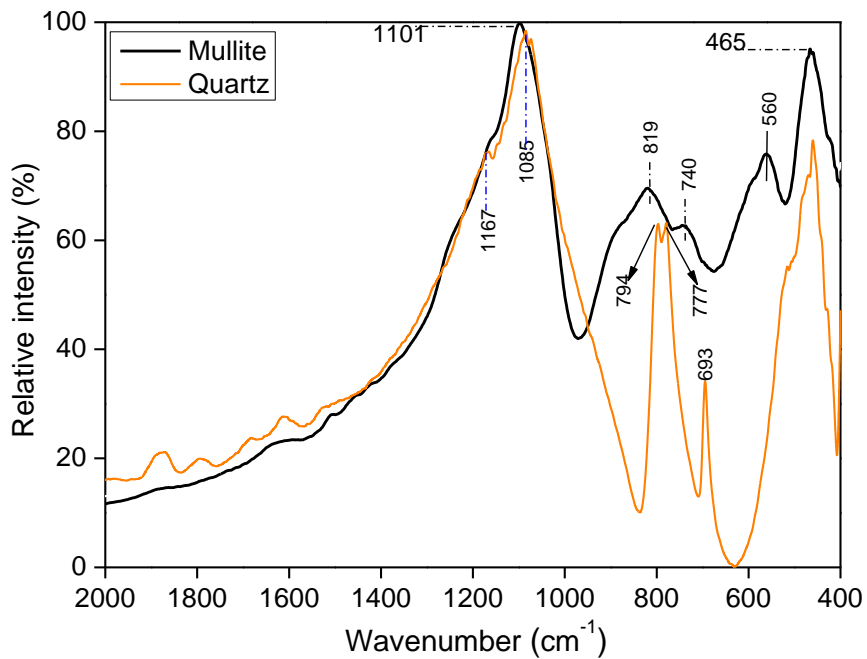
**Figure 5-15.** FTIR spectra of fly ashes A (a), B (b), C (c), D (d) and E (e) before and after contacting with water for 7 days at water/ash ratios of 0.5 and 20 g/g (as indicated by subscripts) at  $25\pm 2^\circ\text{C}$ . The fly ashes were dried at  $105^\circ\text{C}$  for 48 h before testing.

In general, the spectra of the fly ashes do not change significantly after contact with water, meaning that the fly ashes are stable in neutral aqueous conditions. Only very small changes in the bands around  $3450$  and  $1630\text{ cm}^{-1}$ , due to vibrations of hydroxyl groups, are observed.

Comparing the FTIR spectra of the five fly ashes, the bands observed in the region  $1400\text{--}400\text{ cm}^{-1}$  are substantially different. In the high-frequency ( $1200\text{--}650\text{ cm}^{-1}$ ) region, the main band centered at  $\sim 1080\text{ cm}^{-1}$  is assigned to the Si(Al)-O-Si asymmetric stretch. This band is typical of the spectra of silicate glasses, and its frequency depends slightly on the state of hydration, NBO concentration and Al content (Taylor 1990; Gervais et al. 1987). A distinguishable broad vibration hump from  $900$  to  $800\text{ cm}^{-1}$  appears in the curves of fly ashes A, B and C. In contrast, there is only a sharp band centered at  $800\text{ cm}^{-1}$  for fly ashes D and E. In the low frequency ( $650\text{--}400\text{ cm}^{-1}$ ) region, a band appears at  $540\text{ cm}^{-1}$  in the curves of fly ash A, B and C but disappears for fly ash D and E. A reasonable deconvolution of the spectra, together with a clear assignment of resolved bands, should be more helpful in understanding the information provided by the spectra.

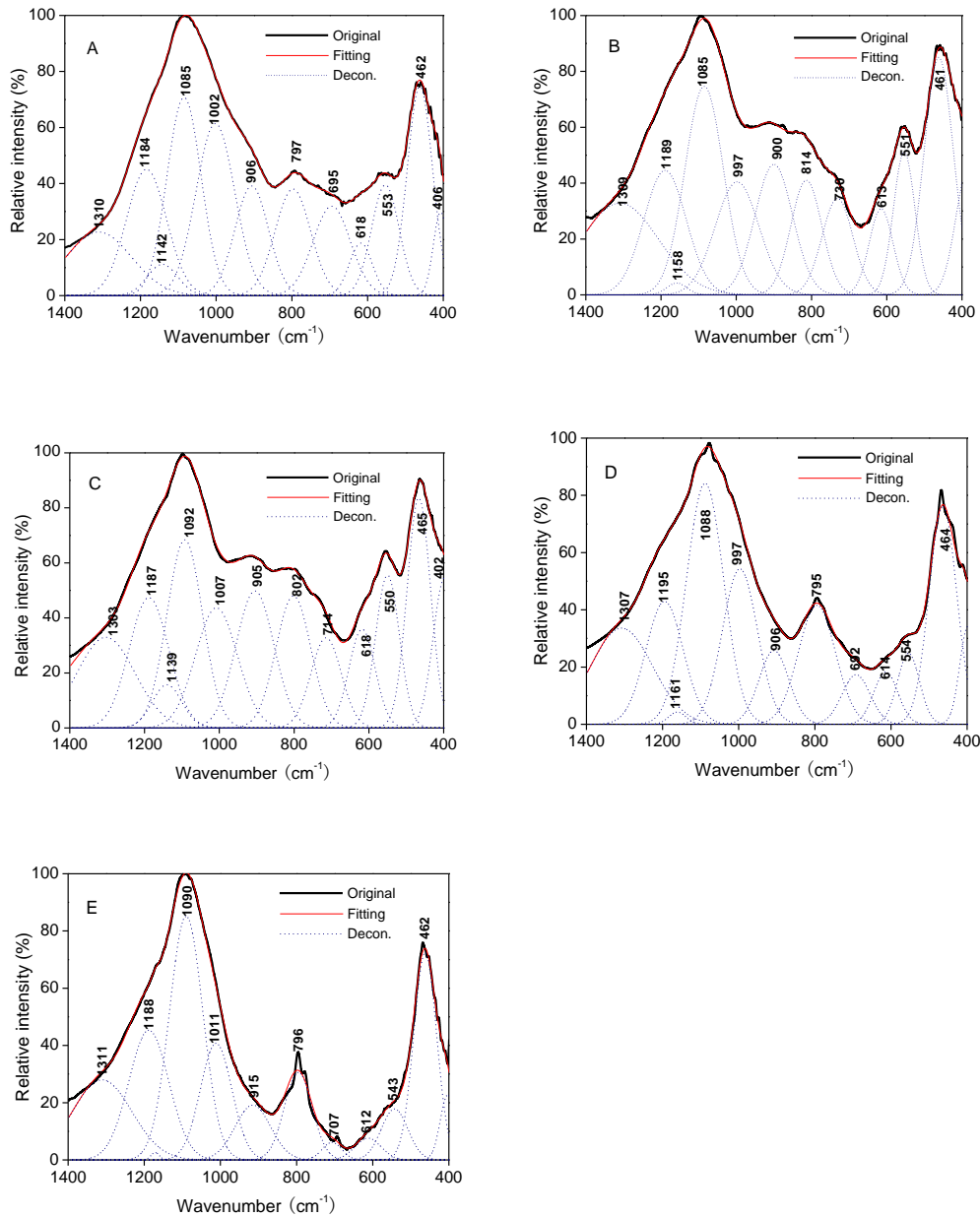
#### 5.4.1.2 The relationship between band concentration and the reactivity of fly ash

Before performing the band assignment and deconvolution, it is desirable to also compare the spectra of mullite and quartz, which are often regarded as non-reactive components present in fly ash, as discussed above. Figure 5-16 shows the FTIR spectra of the mullite and quartz.



**Figure 5-16.** FTIR spectra of mullite and quartz. The mullite may contain some quartz as it is calcination products of kaolinite.

From the shape of the main band at  $1101\text{ cm}^{-1}$  of the spectrum of mullite, it is also possible to distinguish bands located at  $\sim 1200$  and  $\sim 1165\text{ cm}^{-1}$ . For the spectrum of quartz, the main Si-O stretching band is located at  $1085\text{ cm}^{-1}$ , with three relatively symmetric bands in the lower frequency region:  $777\text{-}794$ ,  $693$  and  $465\text{ cm}^{-1}$ . Comparing the spectra in Figure 5-15, the intensity of the band near  $800\text{ cm}^{-1}$  in mullite is much higher than in fly ash. In the spectra of fly ashes, it is identified that the vibration bands of Al-Si glasses overlap with those of mullite in the higher frequency ( $\sim 1000$  and  $\sim 900\text{ cm}^{-1}$ ) and lower frequency ( $\sim 700$  and  $\sim 465\text{ cm}^{-1}$ ) regions.



**Figure 5-17.** Deconvolution spectra of Si-O-T bands of fly ashes over 400-1400  $\text{cm}^{-1}$ .

Figure 5-17 shows the result of deconvolution of the main band over the range 1400-400  $\text{cm}^{-1}$ . The principle applied in the deconvolution procedure is to minimize the number of vibration bands, with consideration of typical position for both of Si-O and Al-O vibrations in Al-Si glass, 3:2 mullite and quartz. The band assignments are given in Table 5-16.

Based on the fundamental work that has been done on the IR spectroscopy, a classification for the resolved bands to be 'active' or 'inactive' can be assigned. When a band is defined as active, this means the linked Si and Al atoms are more easily available to be dissolved under geopolymerization. These bonds are

mostly those with one to four NBO atoms, known as Q<sup>3</sup>, Q<sup>2</sup>, Q<sup>1</sup> and Q<sup>0</sup>, respectively. The study by Taylor (1990) shows that when the concentration of network depolymerizing cations increases, the vibrations attributed to stretching of Si-O<sup>-</sup> and Al-O<sup>-</sup> systematically shift toward lower frequencies.

**Table 5-16:** Assignment of the resolved bands in Figure 5-17.

Position/ cm <sup>-1</sup>	Assignment	Classification of bonds	Reference
>1184	Asymmetric stretching of Si-O-Si in silicate framework structures, Q <sup>4</sup>	inactive	Yang 2000
1139-1161	Asymmetric stretching of (Si,Al <sup>IV</sup> )-O-Si in mullite or mullite-like structures	inactive	Voll 2001 Fernández-Jiménez 2006
1085-1092	Asymmetric stretching of (Si,Al <sup>IV</sup> )-O-Si in glass (may partially overlap with mullite and quartz), Q <sup>3</sup>	active	Voll 2001 Taylor 1990
997-1011	Asymmetric stretching of (Si,Al <sup>IV</sup> )-O-Si in amorphous glasses, could be composed of higher Al concentration	active	Taylor 1990
900-915	Stretching of Si-O-(M, Me, Fe) where M is an alkali metal or Me is an alkali-earth metal, or Si-OH	active	Taylor 1990
795-814	Symmetric stretching of Si-O-Si in quartz, and stretching Al <sup>VI</sup> -O in mullite-like structures	inactive	Voll 2001 Tuchman 1992
692-730	Symmetric stretching of Al-O in Si(Al <sup>IV</sup> )-O-Al <sup>IV</sup> linkages	active	Taylor 1990
612-618	Bending of O-Al <sup>IV</sup> -O in mullite or mullite-like structure	inactive	Voll et al. 2001
543-554	Symmetric stretching of Al-O-Si in mullite or mullite-like structures	inactive	Taylor 1990 Voll 2001
<461-465	Bending of Si-O-Si and O-Si-O in Si-rich glass or quartz	inactive	Voll 2001 Tuchman 1992

To quantify the effects of active bonds, it is assumed that the relative areas of the resolved bands are proportional to their concentration in fly ash. However, it does not mean the activity of those reactive bonds is equal. Considering the fact that bands appearing in the lower region represent the vibrations of weaker bonds in glasses, and also the contribution of NBO atoms, it should need a reactivity coefficient to multiply to the area. This reactivity coefficient may be related to atom radius and the site energy (or bond strength), which further depends on the coordination number (CN) and other parameters. For example, the Al-O bond has site energy of -2666, -2569 and -2526 kJ/mol for Al atoms which are 6-coordinated in pyrope, 5-coordinated in Addalusite Al<sub>2</sub> and 4-coordinated in sillimanite Al<sub>2</sub>, respectively (Velbel 1999). The site energy difference will definitely affect the dissolution behaviour. However, it is not possible to give a coefficient without a rigorous experimental examination.

In this study, in order to simplify, the reactive bonds from high to low region are assumed to be equivalent. The active bond concentrations in fly ashes A, B, C, D

and E are thus 58.2%, 55.0%, 53.9%, 52.2% and 39.1%, respectively. The concentration order of active bonds indicates a general trend that fly ash A is the most active but not much different from fly ashes B, C and D. If the particle size of fly ash is considered in combination with these data, similar as the calculation of RI that is to multiply the unified specific surface area to the concentrations of active bonds, new indexes obtained are 1.2, 1.3, 0.5, 0.5 and 0.25 for fly ashes A, B, C, D and E, respectively. This index can be called 'specific reactive bond index'.

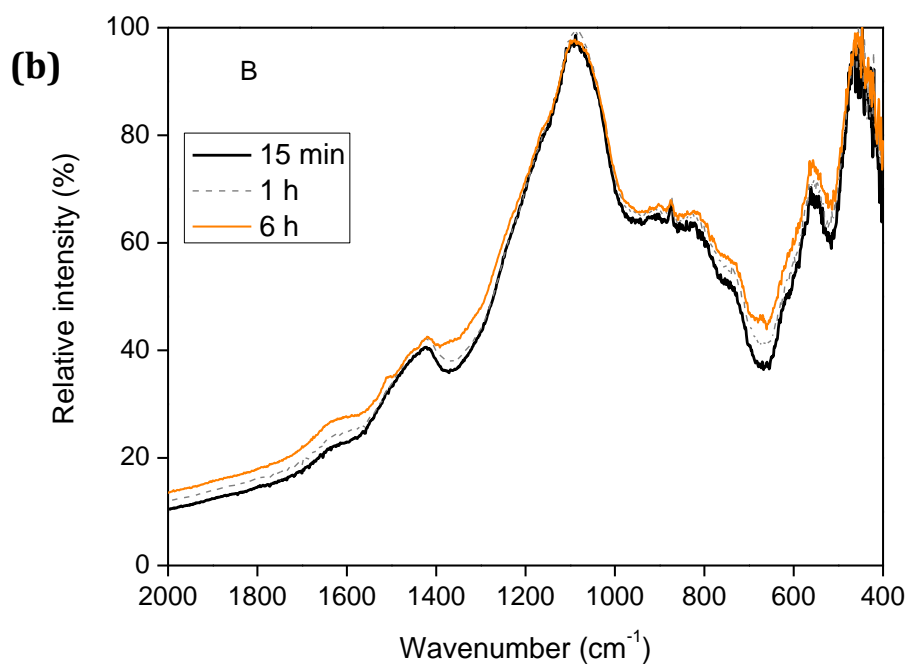
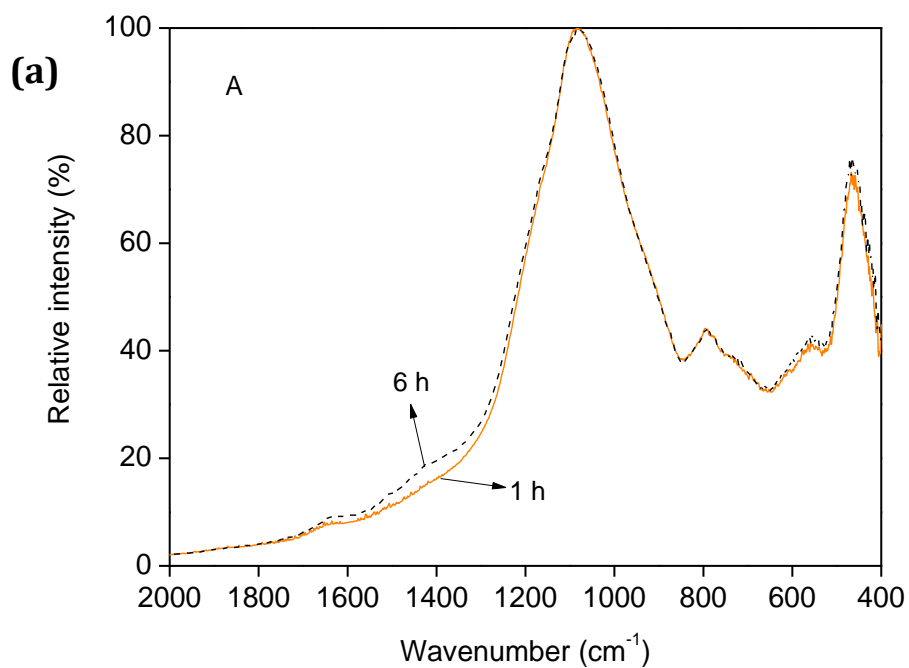
While it is obviously a simplification, because fly ash particles are highly heterogeneous, it does provide an initial indication of the likely performance of the materials. The advantage of this index compared to RI is that it considers the reactive bonds, regardless of whether the bonds are in glass or in imperfect crystals. The order of 'specific reactive bond index' is generally consistent with the RI ranking of the fly ashes, as determined by RQXRD and XRF, and the trend measured by the compressive strength development of the geopolymers formed from each ash. When considering the mechanical activation of fly ash, the improved surface that is composed of broken Si-O and Al-O bonds is entirely reactive surface; therefore, milling fly ash into finer particles is an effective way to improve reactivity.

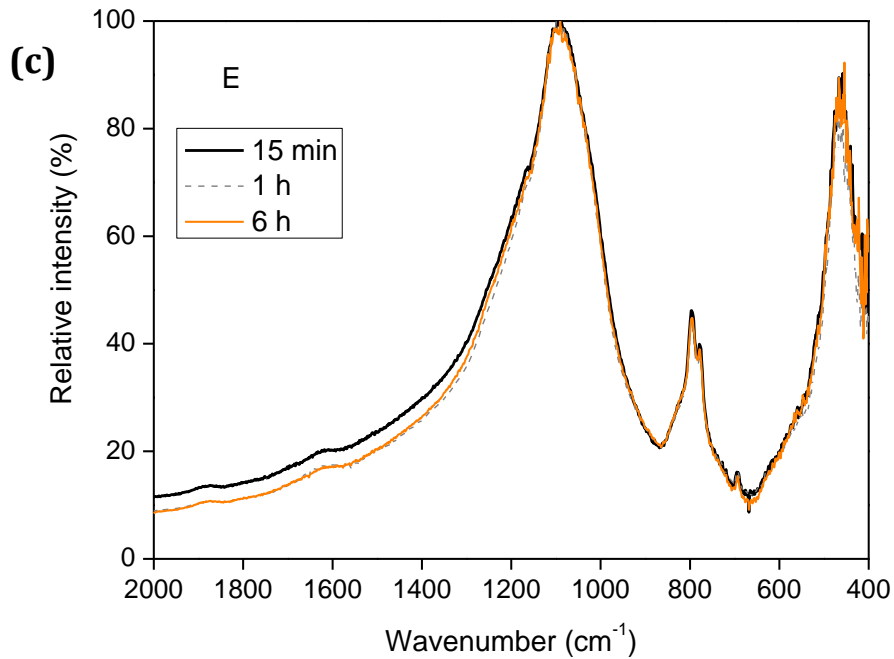
#### 5.4.1.2 FTIR analysis of dissolved fly ashes by alkaline solutions

A simple way to verify the classification of bonds is to compare the FTIR spectra for fly ashes before and after dissolution in alkaline solution, and observe the difference after the glass phase has been selectively leached or dissolved. Here two batches of fly ashes were analyzed. The first batch includes the fly ashes that were leached 1 M NaOH at room temperature for different periods. The second batch is mixed in 4 M NaOH, KOH and the sodium silicate solution at 80°C, the same as analyzed by the RQXRD method in Section 5.3.2.1 to 5.3.2.3. The liquid/solid ratio for alkaline dissolution was kept at 35 g/g.

Figure 5-18 shows the FTIR spectra of fly ashes after leaching in 1 M NaOH for different periods at 25°C. Compared with the as-received fly ash, there is no evident change in the FTIR spectra, except for the slight increase in absorbance intensity at 1640  $\text{cm}^{-1}$ , indicating the stretching of Si(Al)-OH bonds or chemically bonded water molecules. This implies that the dissolution at room temperature is slow. This result is consistent with the results of Pietersen et al. (1990), who reported that the dissolution extent of several Class F fly ashes, either for separated solid samples or cenosphere samples, is less than 5% after 100 h dissolution in NaOH solution at pH=13.7.

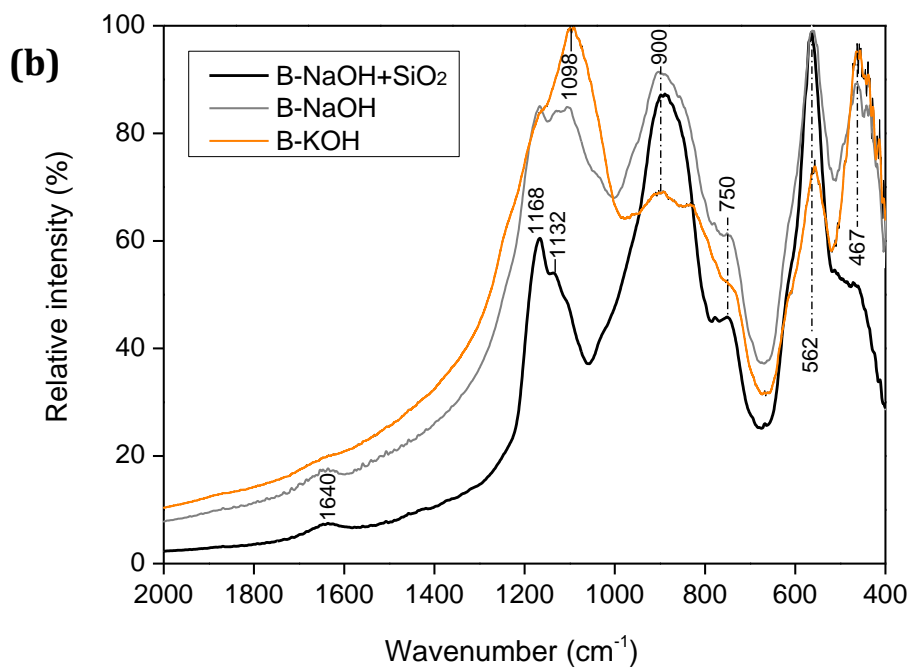
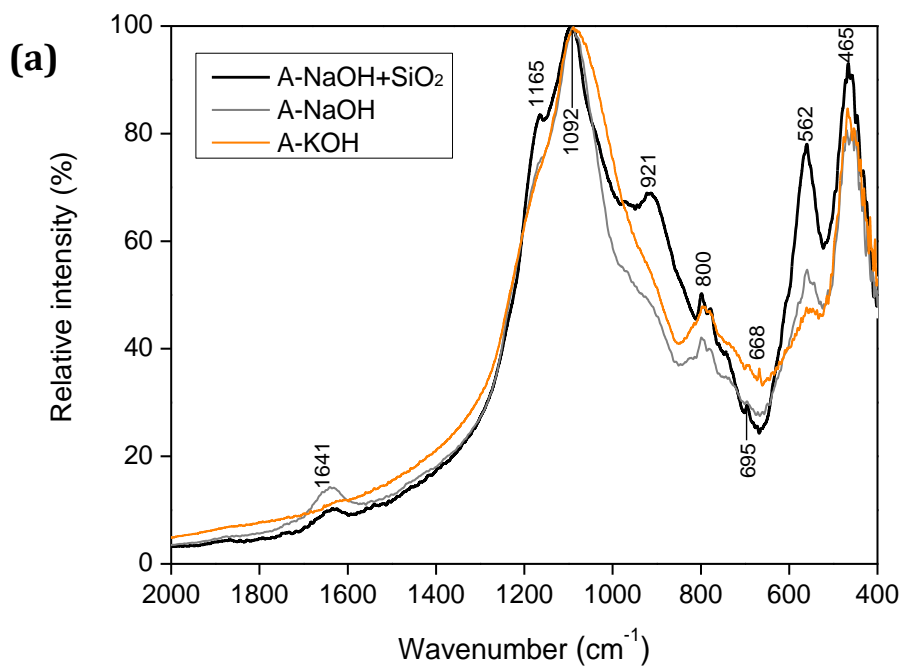


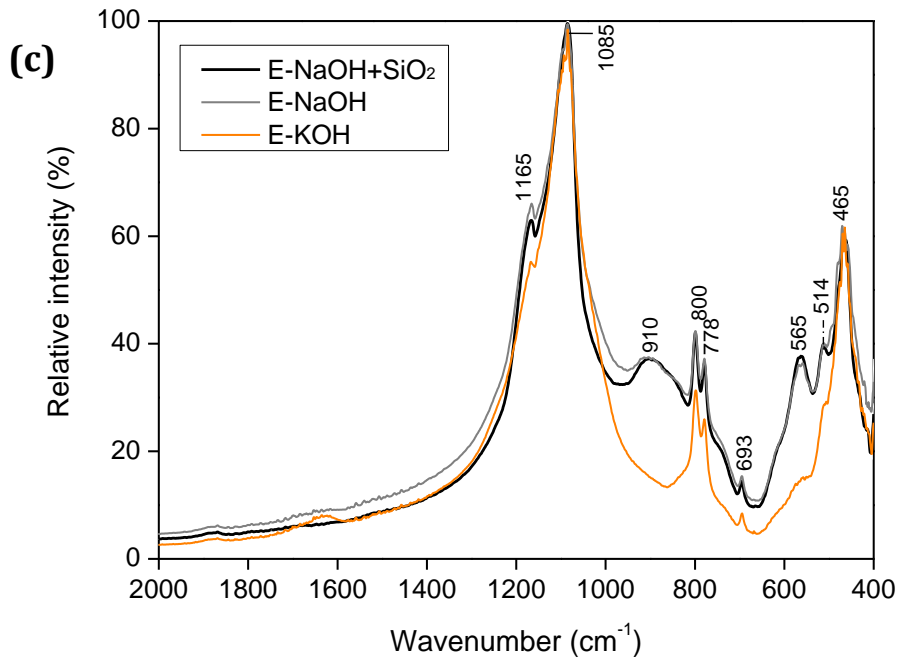




**Figure 5-18.** FTIR spectra of fly ash A (a), B (b) and E (c) dissolved in 1 M NaOH for different periods at 25°C.

Figure 5-19 shows the spectra of dissolved fly ash in 4M NaOH, 4M KOH and sodium silicate solutions at 80°C. The spectra of samples after KOH dissolution do not change very much, meaning that fly ash also did not dissolve in KOH solution. This result is consistent with RQXRD analysis. After NaOH and NS dissolution, the bands in the high frequency region (>1100 cm<sup>-1</sup>) and middle region (~900 cm<sup>-1</sup>) both become more prominent, and the relative intensity of bands at ~562 cm<sup>-1</sup> becomes much higher after dissolution. This indicates that the concentration of bonds with vibration next to these three regions become less. This result supports the classification of bands in Table 5-13.



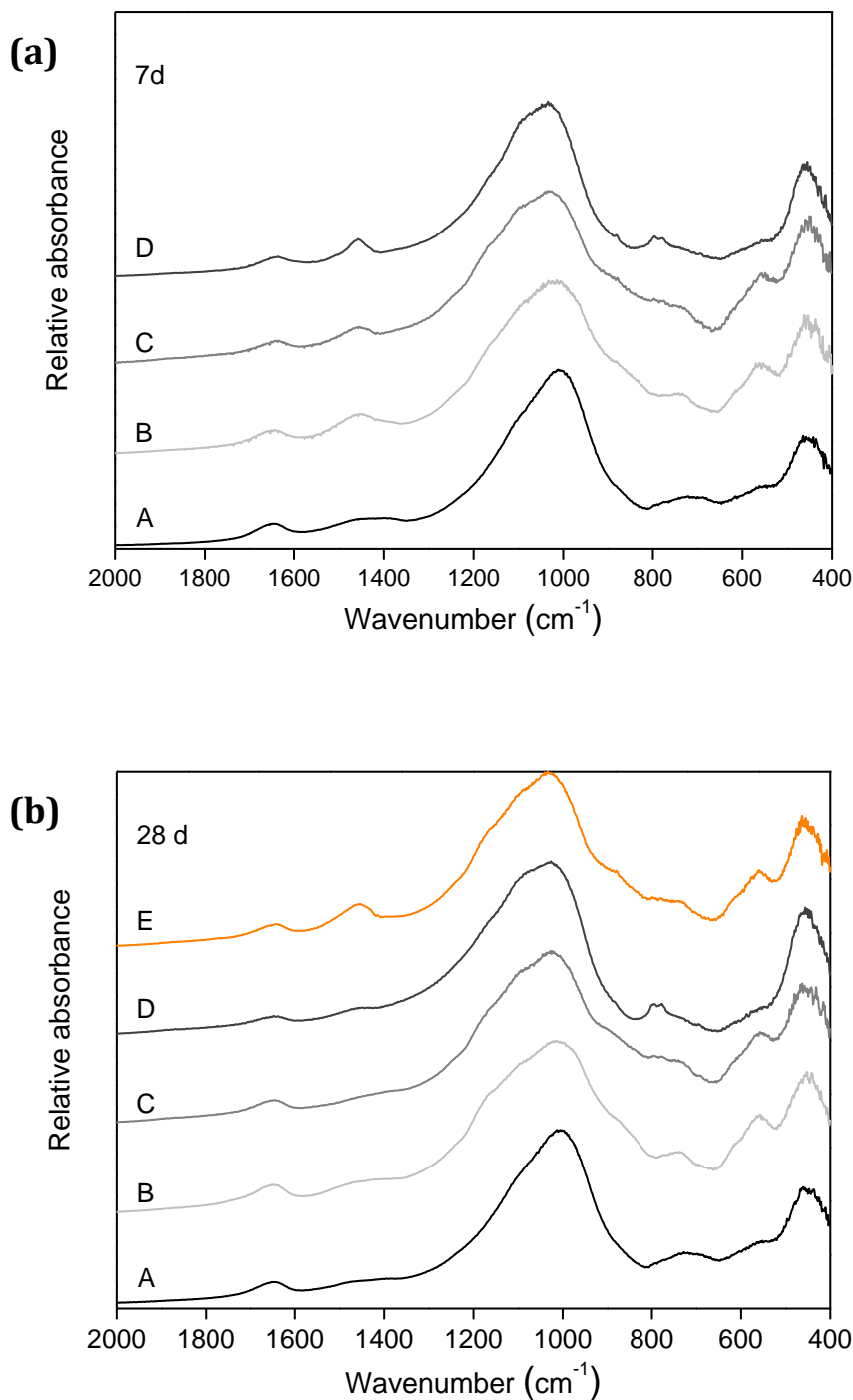


**Figure 5-19.** FTIR spectra of fly ash A (a), B (b) and E (c) dissolved in 4 M KOH, 4 M NaOH and 4 M NaOH + 1.3 M SiO<sub>2</sub> solutions at 80°C for 6 h.

#### 5.4.2 FTIR analysis of resultant geopolymer binders

Figure 5-20 shows the FTIR spectra of the geopolymer binders synthesized with the same quantity of activation solution (Table 4-6). Sample E was not able to be collected and tested at 7 d due to the slow compressive strength development.

After reaction with sodium silicate solutions, all samples show a band shift from 1080 cm<sup>-1</sup> towards 1000 cm<sup>-1</sup>. This is usually ascribed to the formation of geopolymeric gels. The main spectral region centered at 1000 cm<sup>-1</sup> is symmetric in geopolymer sample A. For the other four samples, there is a composed shoulder band near 1090 cm<sup>-1</sup>, although the spectra have not been deconvoluted. This suggests that geopolymers B, C, D and E should contain a considerable amount of unreacted fly ash. The lower reaction extent may explain the lower strength of the other four samples.



**Figure 5-20.** FTIR spectra of geopolymer samples at 7 d (a) and 28 d (b).

Another notable change in the 28 d spectra is the decreased intensity of bands at  $\sim 1440\text{ cm}^{-1}$  which are assigned to the vibration of  $\text{CO}_3^{2-}$  groups. Only sample E shows a relatively high intensity at this position. The higher intensity at this position in the spectra after 7 d is thought to be caused by the carbonation of the alkaline activator, which remains in the pores because of the limited reaction. At early age, there remains a large quantity of activator in the samples.

Once the samples are subjected to compression testing, crushed and ground into powder, the remains alkali in the pore network reacts with CO<sub>2</sub> in ambient conditions. At ages beyond 28 d, most of the alkali content is consumed, thus less remained to carbonate. This can explain the ongoing strength improvement after 7 d. However, due to the much lower reactivity of fly ash E, there is still much activator remaining after 28 d, and thus the higher carbonation is observed.

### ***5.5 Concluding remarks***

Glassy (amorphous) phases are usually regarded as active components of fly ash in geopolymerization. By Rietveld quantitative XRD and XRF analysis, it is found that the composition and chemistry of glassy phases play an equally important role as the quantity of these phases in affecting the reactivity of fly ash. In glassy phases, both FeO<sub>4</sub> and AlO<sub>4</sub> tend to randomly distribute and connect with SiO<sub>4</sub> tetrahedra by sharing corners and this is due to the alkali/alkali earth cations, which act as charge compensators. If O-Al(IV) and O-Fe are regarded as active bonds, it is found that their quantity order in the five ashes studied matches well with the reactivity order, implying that the quantities of O-Al(IV) and O-Fe are important in affecting the reactivity of fly ash. Dissolution analysis confirms this mechanism. Besides, dissolution analysis also shows that the crystals such as mullite and quartz are also suffered dissolution, particularly in the 'impure' fly ashes, which have relatively higher concentration of network modification. Fly ash A shows a higher dissolution extent than fly ashes B and E; however, fly ash E reaches an even higher extent of dissolution than fly ash B in sodium alkaline solutions. The differences in dissolution behaviour are explained by the rate-controlling mechanisms during dissolution at different stages.

Based on the understanding of glass chemistry, FTIR can be adopted as a rapid indicator test for the reactivity of fly ash. FTIR testing provides a qualitative to semi-quantitative method for examining the reactivity of fly ash. The absorbance bands at 1085-1092, 997-1011, 900-915 and 692-730 cm<sup>-1</sup> can be recognized as signs of reactivity. Deconvolution can provide a quantitative insight into reactivity, particularly in combination with the effects of particle size or surface area on dissolution.

With the understanding of the fly ash physics and chemistry and the reactivity under geopolymerization conditions, it reasonable to expect that the geopolymer foam concretes with fly ashes A, B and C used for the geopolymer binder should have higher strength than those produced from fly ashes D and E if it is assumed that the activation, foaming and curing conditions are the same. The question will thus be asked in the following chapter: is this true?

## **Chapter 6: Development and Investigation of Trial Manufacture of GFCs**

### **6.1 Introduction**

This chapter follows on the selection of suitable fly ashes for GFC manufacture as outlined in Section 3.1. A wide range of trial mixtures were investigated to obtain a better understanding of the influences of fly ash physics and chemistry on the properties of GFCs. The study in this chapter commences with the foam and paste stability, followed by hardened foam strength measurement and continues with a detailed investigation of the microstructure of the hardened foam concretes.

As a key component, foam plays an important role in affecting the structure and thus the strength of the hardened foam concretes. The stability of the foam should be a critical factor as it may have different setting behaviour at a higher pH (of the geopolymer binder) compared to OPC systems. The effect of foam addition on the geopolymerization of fly ash is unknown. Examination of the stability of foam will be the first research priority in this chapter because such stability determines the development of a stable paste for the manufacture of GFCs.

The previous two chapters have examined the reactivity of the five selected fly ashes through evaluating the compressive strength of the hardened solid geopolymers and their dissolution behaviour in different alkaline environments. Fly ashes A, B and C exhibited higher reactivity, while fly ashes D and E exhibited particularly low reactivity. This indicates that fly ashes A, B and C are more suitable to be used for the manufacture of strong and solid geopolymers. However, it remains unclear whether they are suitable for the manufacture of GFCs.

Beside the source of the fly ash, the alkali concentration and soluble silicate are both important factors that affect the properties of the geopolymer binder. Many researchers have noticed that for a particular fly ash there is normally an optimal alkali concentration. For example, within an optimal alkali concentration range between 6.39 and 7.54 M, the optimal modulus of the alkaline aqueous phase was around 0.63 (Panias et al. 2007). However, for Gladstone fly ash, it was found that an alkali activator with a modulus between 0.7 and 1.7 usually results in the strongest geopolymer binders (Provis et al. 2009b). Thus further investigation of the effects of composition of alkali activators is needed.

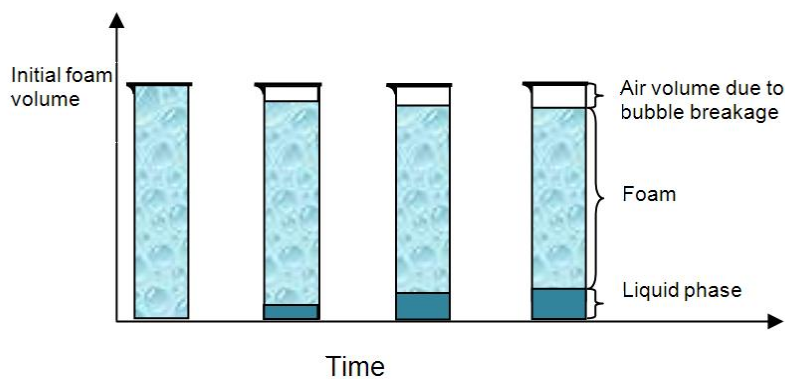
### **6.2 Foam stability**

The foam used to introduce bubbles into geopolymer binders is pre-foamed using a surface active polypeptide-alkylene polyol condensate solution. The pre-foamed foam should be stable during mixing and before initial setting, to enable the foamed paste to form a porous structure with well distributed fine bubbles. If the foam decays quickly, the structure of foamed geopolymer will

collapse or large bubbles will form due to the coalescence of the fine bubbles. Foam stability is a critical factor affecting the final structure of foam geopolymers.

In the early stage of foam formation, the Gibbs and Marangoni non-equilibrium effects are responsible for the accumulation of bubbles (Tan 2005). There is a period of rest during which there is no apparent change before the onset of the decaying process, which is indicated by phenomenon such such as volume variation, bubble collapse, or changes in the bubble size or the general aspect of the foam. After these two short stages, the foam begins to decay slowly as time elapses (Iglesias et al. 1995). Measuring the volume change after a specific time can help to quantify the foam stability.

The simplest method for estimating the stability of foam is to follow its change in volume with time. In this project, the volume change is of particular interest. The volume loss as time elapses or while under shear stress, i.e. during mixing, will cause a change of the volume of the foamed paste. The bubble size change with time is also important; however, considering that the bubbles are difficult to change once they are successfully mixed into the stiff paste, the foam stability in terms of bubble size has not been evaluated in this research. The foam stability was measured by monitoring the foam column height after the pre-foaming and pouring the mix into a graduated cylinder. A sketch of a typical foam volume observation is shown in Figure 6-1.



**Figure 6-1.** Sketch of foam stability recording.

Unlike the dynamic equilibrium used in the Bikerman's classical method (Iglesias et al. 1995), in this study, foam is in a static state after being poured into the graduated cylinders. This situation is more like the case once the bubbles are introduced into geopolymer binders. The stiffness of binder may have certain influences on foam stability but in not within the scope of this research.

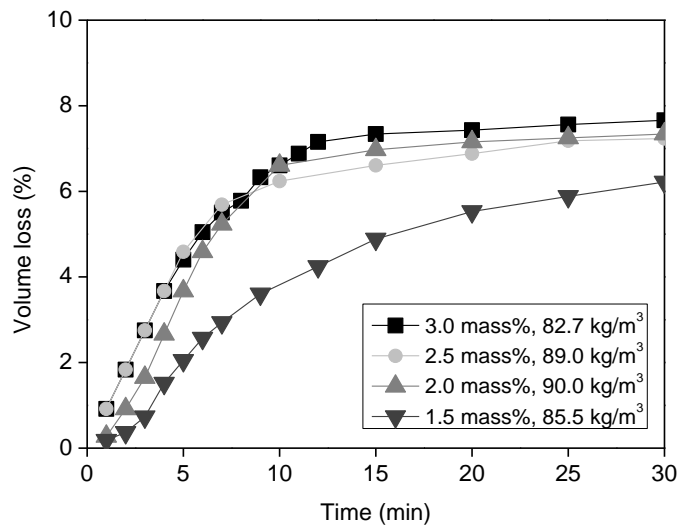
The liquid phase of the foam drains downwards so that the quality of the foam varies with height; the top foam contains the lesser amount of liquid and most of the bubble size in the top was much larger than at the bottom. Both the top air volume and bottom liquid phases were recorded as volume loss. To exclude the possible effect of the column dimensions, three graduated cylinders with size of



1000 mL (diameter=60.5 mm), 500 mL (diameter=47.5 mm) and 250 mL (diameter=31.5 mm) were used to give an average value.

### 6.2.1 Effect of foaming agent concentration on the foam stability

The foaming agent is a commercially available product (active surface polypeptide-alkylene polyol) and its foaming capacity at different concentrations should be examined before use. Figure 6-2 shows the effect of the concentration of this foaming agent on foam stability as tested by the method described above. The density of the resulting foam is in the range of 80-90 kg/m<sup>3</sup>.



**Figure 6-2.** Effect of the concentration of the foaming agent (active surface polypeptide-alkylene polyol) on the stability of foam.

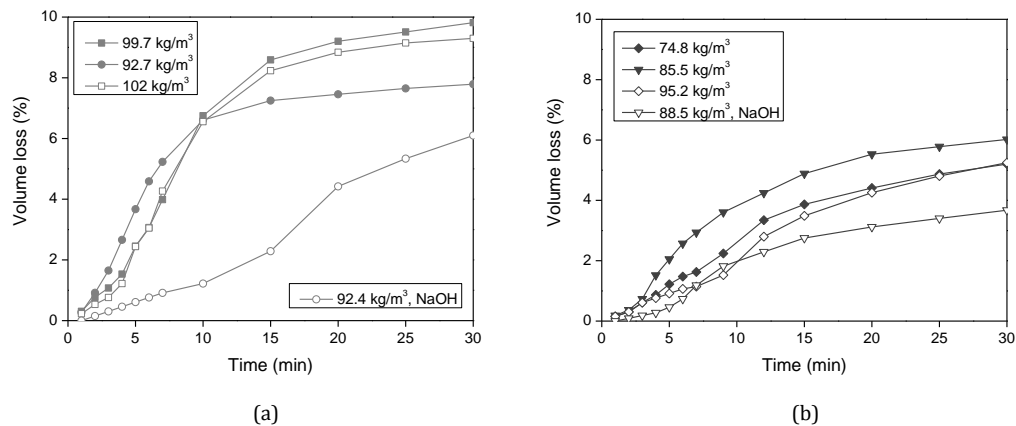
The effect of the concentration of foaming agent on the foam stability is not very evident in the studied range. In the first 7 min, it seems that foam synthesized from a higher concentration solution is less stable. However, when concentration is higher than 2.0 wt.%, the difference is not evident, particularly after 10 min. The experimental results suggest that using 1.5 wt.% foaming agent is adequate to make stable foam.

The stability of foam depends on many factors, such as surface tension of the liquid phase, film thickness and viscosity and environment temperature. However, there is usually a threshold concentration for the foamability and stability for a particular foaming agent. Higher concentrations than the threshold level will decrease the stability due to reduced Marangoni effect (Wan et al. 2003). In this study, the concentration of 1.5 wt.% was selected as an optimal value. Lower concentrations than this level generate lower foamability, while higher concentrations cause slight instability.

### 6.2.2 Effect of foam density and pH on the foam stability

By changing the foaming solution flow rate, it is possible to change the foam density. Figure 6-3 shows the effect of foam density on the stability, as

measured by volume variation versus time for a foam that was mixed with 12 mol/L NaOH solution at a volume ratio 250, that is foam in the 250, 500 and 1000 mL graduated cylinders was mixed with 1, 2 and 4 mL NaOH solution, respectively. Values presented in Figure 6-3 are mean of three records in the three different graduated cylinders. The errors (not shown) were relatively large ( $\pm 30\%$ ) which may be due to the differences of wall effects.



**Figure 6-3.** Effect of foam density on the stability: (a) foaming agent=2.0 wt.%; and (b) 1.5 wt.%.

The data indicate that the foam density has little effect on its stability. It was expected that higher foam density would have resulted in higher stability, as the thickness of bubble wall will be increased. However, the results indicate that the foam volume only changes by  $\pm 2\%$  when the density changes.

An interesting finding is that in both the 2.0 wt.% and 1.5 wt.% systems, the foam mixed with NaOH solution exhibited higher stability than those without addition of the NaOH solution, especially in the first 10 min after being generated. Similar phenomena have been reported by other researchers (Zhang et al. 2006; Sun and Qiao 2012), who used oleic acids and protein based foaming agents, which are the same type as used in this project. One well known mechanism is that the adsorption of the ionic species by the surfactant molecules at the surface of foam films establishes an electric double-layer which makes the foam stable (Zhang et al. 2006). This property is important because fresh geopolymer binders are usually of high pH ( $>12$ ). The foaming agent selected in this study seems particularly suitable for geopolymer manufacture. This is not a lucky choice. The investigator discussed with the foaming agent suppliers and required an agent which is stable under high pH conditions.

### 6.3 Evaluation of the fly ashes for GFC manufacture

The introduction of foam into freshly mixed geopolymer binders is a simple and practicable method to synthesize foam geopolymer concretes. However, as demonstrated in the previous two chapters, fly ashes from different power stations will generate different binders, as evaluated in terms of liquid requirement, compressive strength of the hardened paste and microstructure properties. The suitability of the studied fly ashes for foamed geopolymer could

be different to their suitability in dense geopolymers. The following sections details the laboratory evaluation of several important aspects that are usually regarded as acceptance criteria for foam concretes.

### 6.3.1 Workability of fresh foamed pastes

Because foam concrete paste must not be vibrated during casting in order to avoid bubble breaking and segregation, it requires a high workability after mixing. The workability of a fresh foamed geopolymer paste depends on many factors, such as quantity of activator, fly ash properties and the foam content.

Table 4-6 has shown that fly ashes from different power stations require different amounts of liquid phase to achieve a practicable workability of paste. Considering that the introduction of foam into the freshly mixed paste will increase the 'real' liquid phase in foamed paste, a reduced amount of activator was used for foam geopolymer. Table 6-1 lists the composition of the binder. For fly ash E, considering the very low compressive strength (<1 MPa), more alkaline activator was used instead of additional water. The additional water was mixed separately after mixing of activator solutions. The binders mixed with a low quantity of activator were too viscous to generate good workability, except for binder A.

**Table 6-1:** Composition of geopolymer binders for foam concrete synthesis.

Binder	Fly ash / g	Activator / g	H <sub>2</sub> O / g	Comments
A	1000	350	0	Workable
B	1000	400	100	Very low workability
C	1000	350	50	Low workability
D	1000	350	50	Low workability
E	1000	500	100	Very low workability

The foam was generated, weighed and immediately added to the binder within a range of 0-15% by mass of dry fly ash. The mixing of foam and binder was at a high speed (360r/min) for <1 min. The spreadability of each foam geopolymer paste was measured by the steel cone method (recommended by Brady et al. (2001)), and the results are shown in Figure 6-4.

Figure 6-4 shows that the workability of the foam geopolymer pastes manufactured by the method in this research mainly depends on the source of the fly ash. Foam pastes manufactured with fly ash A exhibited the best workability, although with the lowest liquid phase. This is closely related to the good workability of solid binder A, which is flowable on a glass spreadability testing table. On the other hand, pastes manufactured with fly ash B or E do not show high workability, although the liquid phase was the highest quantity compared to the others. It is specified that for the normal foam concrete, the spreadability of foamed mix is between 155 and 305 mm, varying accordingly to the surfactant type, content and w/c ratio (Brady et al. 2001). In this study, by using additional water (as detailed in Chapter 4) to adjust the workability of the

base binder, as indicated in Table 6-1, all the final foamed pastes achieve reasonable spreadability for casting.

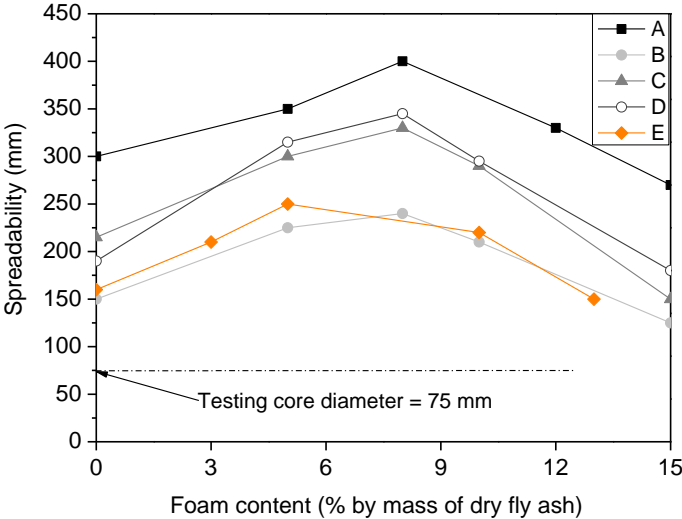


Figure 6-4. Spreadability of foamed geopolymer pastes.

Figure 6-4 also shows that mixing foam into the pre-mixed binder can improve the spreadability of the paste. This is because some of the bubbles will break and release H<sub>2</sub>O, causing a higher liquid/solid ratio. However, if foam content is higher than around 8 wt.%, the spreadability begins to decrease. Once the foam content is higher than 13 wt.%, the spreadability of foamed paste is even lower than the base binder without foam. This is because of the high cohesion force of the foam bubbles. Therefore, for foam geopolymer manufacture, it is recommended to use 0-10 wt.% foam as more foam will only cause a loss of workability as indicated by Figure 6-4.

It should be noted that the activator used includes 12M NaOH solution and liquid sodium silicate (LSS) and additional water if needed. The mixing sequence as recommended by Rattanasak and Chindaprasirt (2009) is: add NaOH solution into the fly ash first and mix for 5-10 min, and then add in LSS for another 5-10 min. This separate mixing will achieve high strength geopolymers with less LSS utilization because the leaching of fly ash under aqueous NaOH condition at the beginning is more intensive and releases more ions. In this study, it was found that for particular fly ashes, this separate mixing sequence could cause high liquid requirement. For example, fly ash A needs liquid/fly ash ratio of 0.3 while both B and E need >0.50. If the NaOH and LSS are mixed first and allowed to cool down, the total liquid requirement will be reduced: fly ash A needs 0.28 while B and E need 0.40 and 0.45 respectively. However, to keep consistency with the solid geopolymer binder synthesis, the same staged mixing sequence was adopted throughout this study.

The density of freshly foamed paste was also determined by taking the mean values of 3 tests, and the results are shown in Figure 6-5. When foam content is below 8 wt.%, the density mainly depends on the binder density and foam

content. Higher foam content amplifies the influence of bubble stability on the density. Foamed paste E was supposed to have the lowest density compared to the others at same foam content because of the lowest density of fly ash E and the highest liquid requirement, but the results shown in Figure 6-5 indicate that at foam content higher than 10 wt.%, it possesses higher density. This means the higher workability of paste A and B is beneficial in keeping the bubbles stable. Stiff mixing destroys the bubbles, making the paste denser. The higher workability of the paste, the more stable the freshly foamed paste.

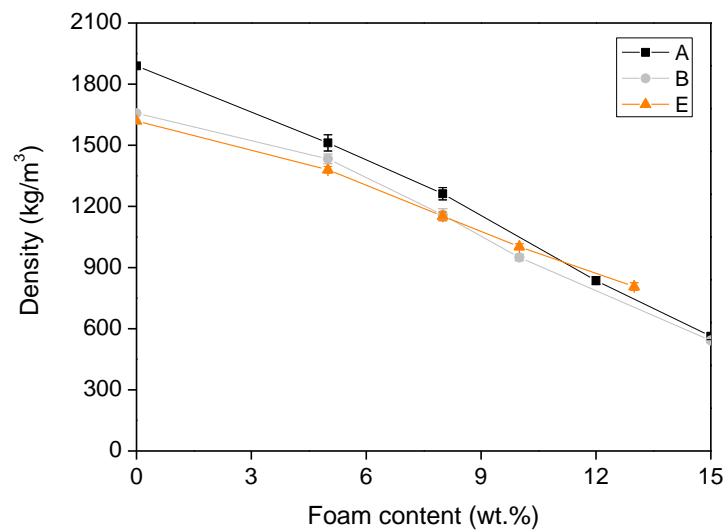
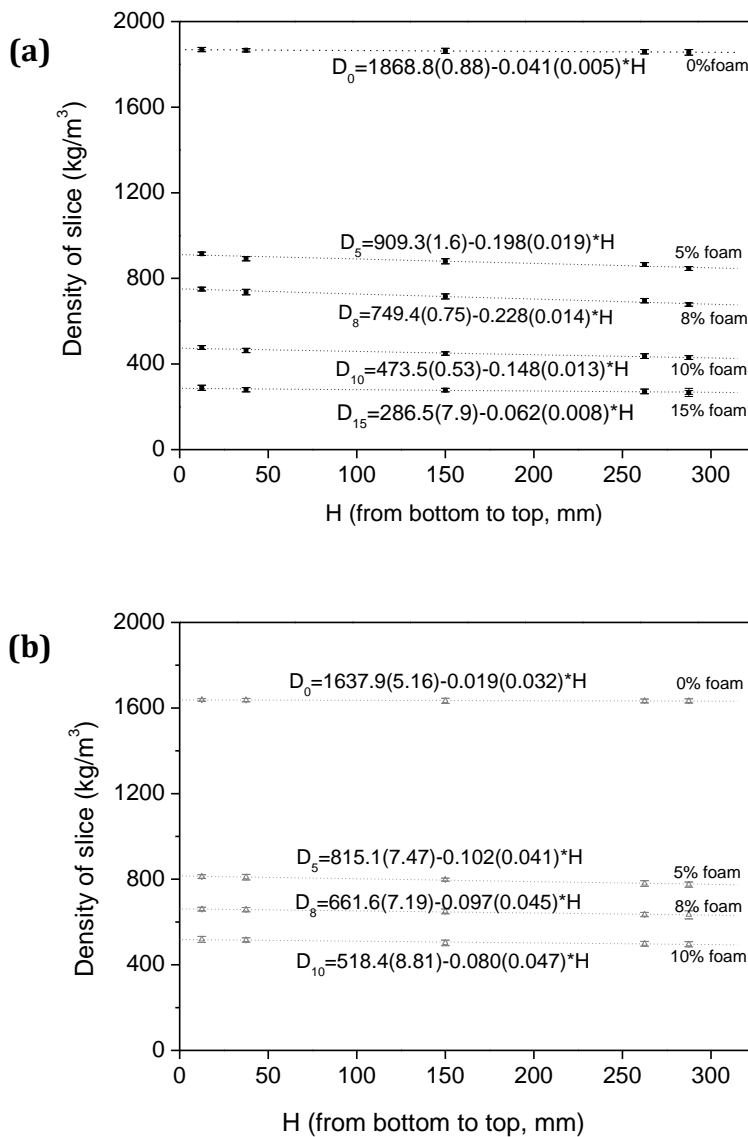


Figure 6-5. Density of freshly foamed geopolymer pastes.

### 6.3.2 Segregation of foamed pastes

Segregation is a very common problem for high workability foam concretes. After the foam is added into the binder and mixed, the individual bubbles tend to rise to the top and cause the top part of the hardened mix to be much more porous than the bottom part.

In this research, the segregation was quantified by comparison of oven-dried densities of the hardened GFC slices of 70 mm in diameter and 25 mm thick obtained from the top to the bottom of the cylindrical sample. The samples were cast in a  $\Phi 70$  mm $\times$ 300 mm PVC tubes and cured in an oven at 40°C for 24 h, and then aged at ambient conditions at room temperature for 7 days. The aged specimens were cut into 25 mm thick slices and oven dried at 105°C for 24 h. Geopolymer foam pastes derived from fly ash A and B, which had exhibited the highest and lowest workability at the given liquid/solid ratio as shown in Table 6-1, were examined because they represented the full spectrum. The density distributions vs. height (H) are shown in Figure 6-6 for a range of samples with foam content from 0 to 15 wt.%.



**Figure 6-6.** Segregation of GFCs: (a) derived from fly ash A; (b) derived from fly ash B.

The density variations between the bottom and top range from 20 to 72 kg/m<sup>3</sup> and 24 to 31 kg/m<sup>3</sup> for GFC A and B, respectively. According to the specification for foamed concrete, a density variation less than 50 kg/m<sup>3</sup> is usually required (Brady et al. 2001). From this point of view, the foamed pastes exhibit evaluated acceptable segregation resistance, except for foamed paste A with 5 and 8% foam addition, which demonstrated 60 and 68 kg/m<sup>3</sup>, respectively.

In terms of segregation resistance, fly ash A is not very suitable for manufacture of GFC at the studied liquid/solid ratio. However, segregation is not the only criteria for foam concrete synthesis. More important factors concerned in this study are the density and strength of foam concretes and these aspects are evaluated in more detail later.

### 6.3.3 Laboratory evaluation of strength and microstructure of GFCs

To examine the suitability of fly ash for GFC synthesis, the density and compressive strength of hardened GFCs were determined. The compositions of specimens were as shown in Table 6-1 and the foam content was set constant at 5 wt.% for the five mixes. The foamed pastes were cured in an oven immediately after casting, at 40°C for 24 h, and then allowed to cool down to room temperature and demoulded to age for another 6 days at room temperature. The diameter and length of each specimen were measured. After the testing of compressive strength, the fractured specimens were dried at 105°C for 24 h to calculate the oven dried density, and some were used for further FTIR and SEM analysis. Figure 6-7 shows the compressive strength and density of GFCs.

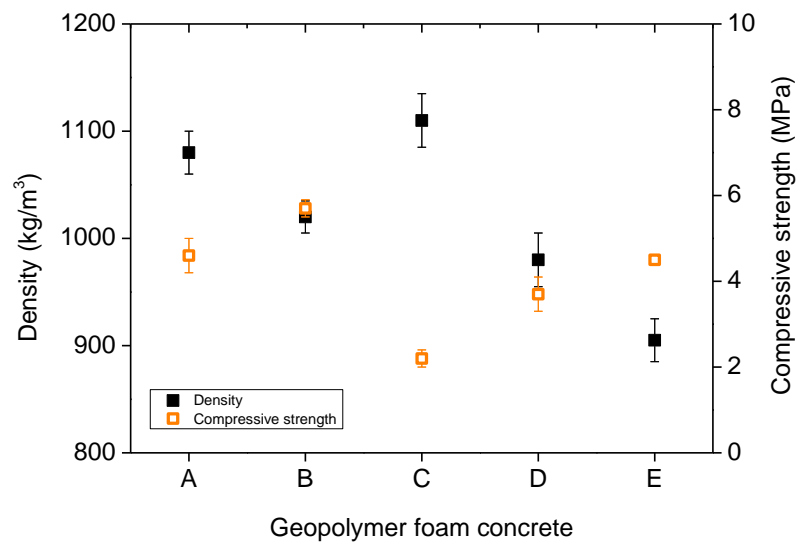


Figure 6-7. Density and compressive strength of GFCs.

Table 6-2: Compressive strengths and density of GFCs. Metakaolin and high Ca fly ash data from Arellano Aguilar et al. (2010) and Al Bakri Abdullah et al. (2012), respectively.

GFC	A	B	C	D	E	Metakaolin	High Ca fly ash
Compressive strength (MPa)	4.6	5.7	2.2	3.7	4.5	6-14	18
Density (kg/m <sup>3</sup> )	1080	1020	1110	980	905	900-1200	1650

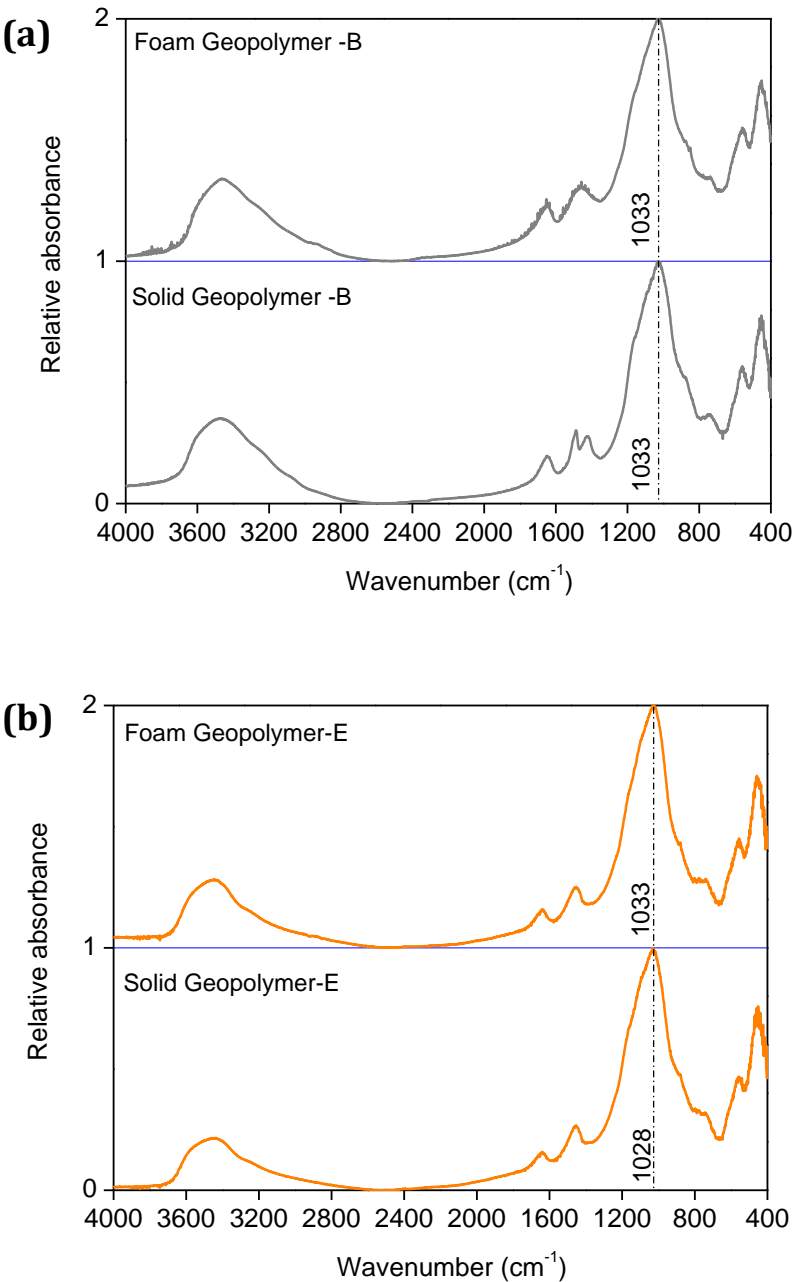
For the five GFCs derived from different fly ashes, the compressive strength varies in a range of 2 to 6 MPa, and the density is in a range of 900 to 1200 kg/m<sup>3</sup>. Table 6-2 compares the five GFCs with those obtained by activation of metakaolin by Arellano Aguilar et al. (2010) and high-Ca (CaO=21.6 wt.%) fly ash by Al Bakri Abdullah et al. (2012).

It is very interesting to note that geopolymer foam A does not exhibit the highest strength. In Chapter 4 & 5, it was confirmed by many techniques that fly ash A possesses the highest reactivity, while fly ash E possesses the lowest. Unexpectedly, geopolymer foam E shows relatively higher strength and lower density. The high strength of geopolymer foam E may be due to three possible

factors: (1) the higher activator content; (2) the foam addition significantly improved the reactivity of fly ash; and/or (3) it has a better microstructure.

The first factor appears relatively unimportant when the strength of GFC C is compared with that of GFC D, both of which have a activator/solid ratio of 0.35. More supporting evidences can be obtained by comparing the strength of GFC A and B, the latter which is activated with a lower concentrated activator when considering the dilution effect of additional water.

To examine the second factors, both the solid and GFC B and E were studied by FTIR deconvolution. Figure 6-8 shows the FTIR spectra of the solid and foamed geopolymers.

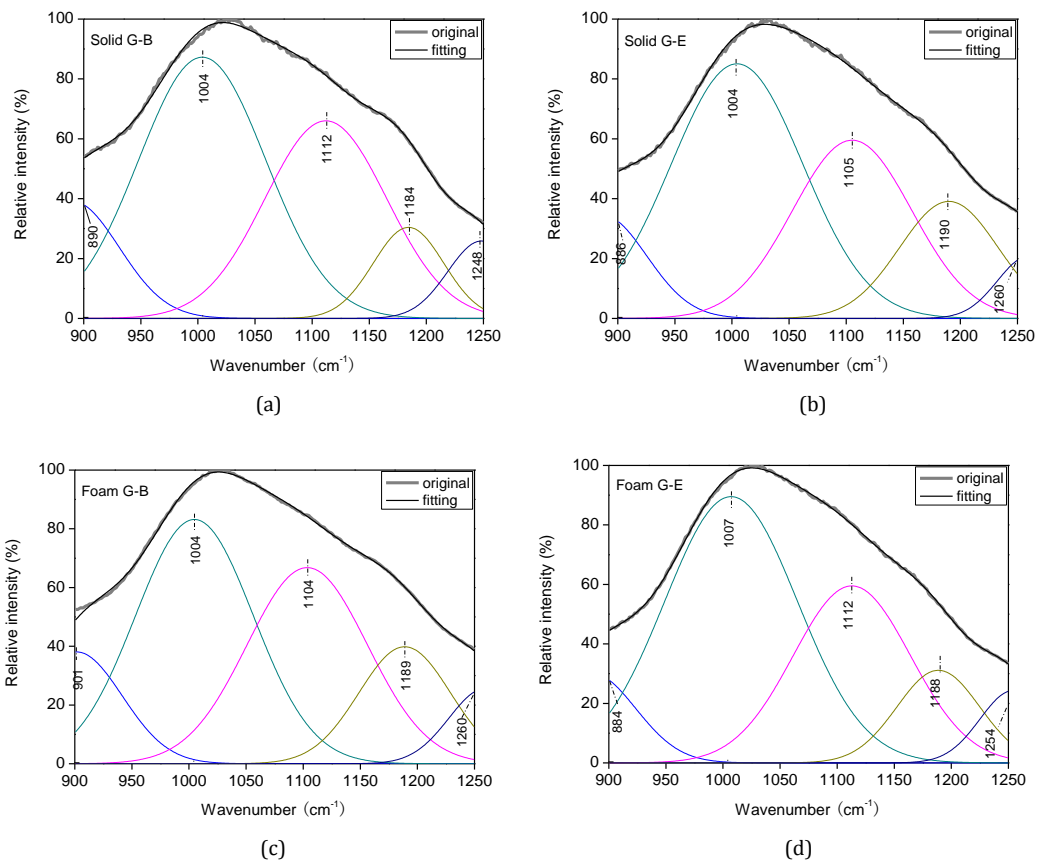


**Figure 6-8.** FTIR spectra of solid and foamed geopolymers at age of 28 d: (a) geopolymers from fly ash B and (b) geopolymers from fly ash E. The foam addition was 5 wt.% for GFCs.



The FTIR analysis is based on the findings in many other studies, that have shown that the relative area of band at  $1015\text{ cm}^{-1}$  due to the asymmetric stretch of the Si-O-T (T=Al and Si) bonds in the sodium aluminosilicate increases with time, and the frequency will shift towards higher region (Criado et al., 2007a). If the foam addition improved the reactivity of fly ash, the relative area of the characteristic band attributed to geopolymer gels centered near  $1015\text{ cm}^{-1}$  will increase in the geopolymer foam.

The spectra of foamed geopolymer are almost the same as that of the solid. The highest absorbance band at  $1033\text{ cm}^{-1}$  in solid geopolymer B does not change in foamed geopolymer B. The only notable change in the spectra is the bands at around  $1430\text{ cm}^{-1}$ , which is attributed to different vibration models of carbonates (Mozgawa and Deja 2009). It still centred at  $1430\text{ cm}^{-1}$  in the foamed geopolymer. The highest absorbance band shift from  $1028\text{ cm}^{-1}$  in solid geopolymer E to  $1033\text{ cm}^{-1}$  in foamed geopolymer E. This small difference may be due to a slightly higher reaction extent. A further deconvolution analysis on this band is shown in Figure 6-9.

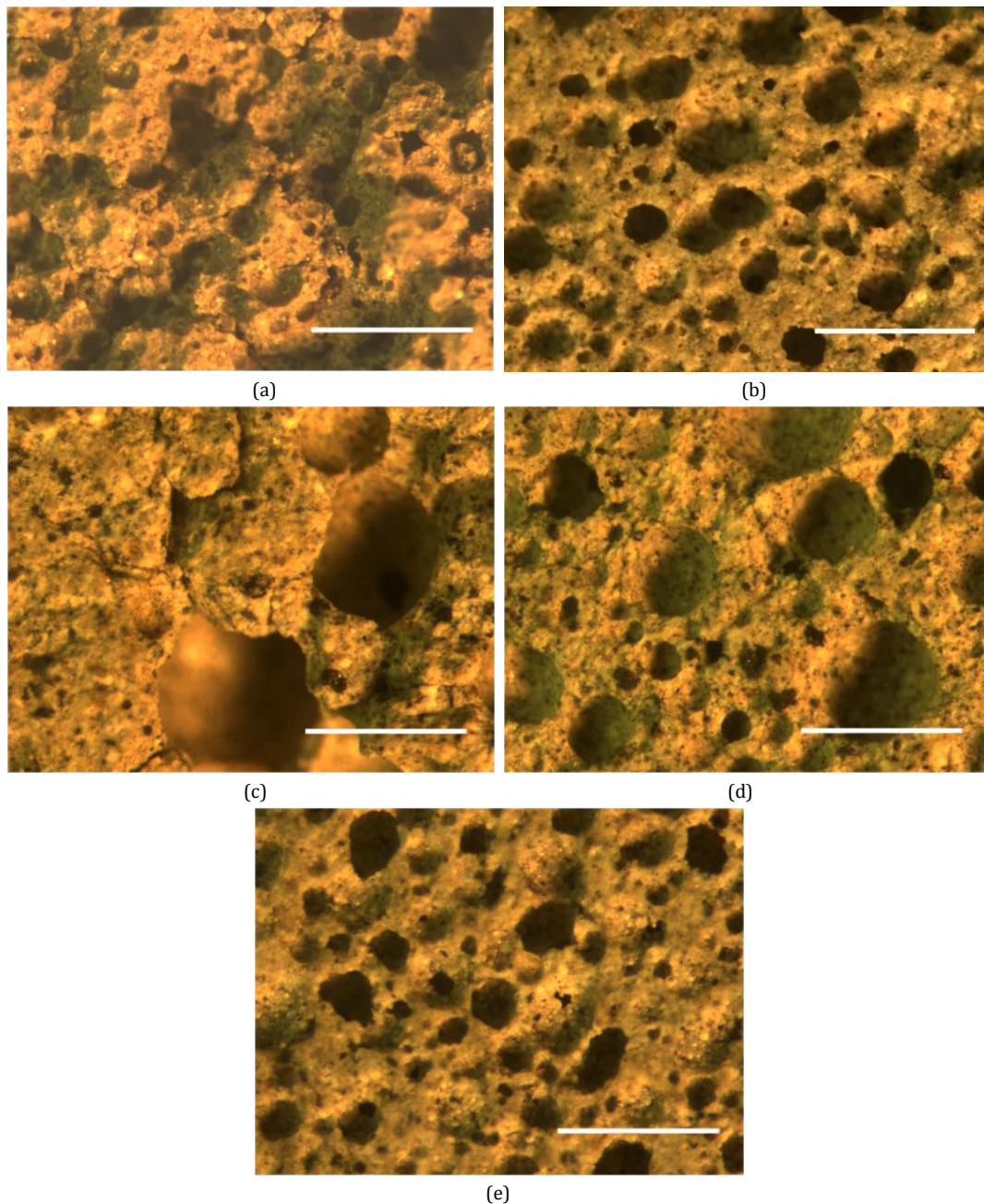


**Figure 6-9.** Deconvolution study of FTIR spectra of solid geopolymers B (a) and E (b) and foamed geopolymers B (c) and E (d).

The components shown in deconvolution spectra from low to high region are at  $\sim 900$ ,  $\sim 1000$ ,  $\sim 1100$ ,  $\sim 1180$  and  $\sim 1250\text{ cm}^{-1}$ . The first two can be attributed to the Si-O-(M, Me, Fe) stretching models and Si-O-T stretching models in geopolymer gels, respectively. The later three are mainly due to Si-O-T in undissolved fly ash. If it is assumed that the area of the first two bands at  $850$  to

1007  $\text{cm}^{-1}$  are proportional to the quantity of geopolymer gels, the analysis shows that the sum of area of the two bands keep constant ( $50\pm 5\%$ ) in the studied frequency range for both geopolymers B and E. It suggests that the foaming agent does not change the geopolymerization path of the fly ash. This will be further confirmed by XRD analysis on the slag-containing geopolymers in Chapter 7.

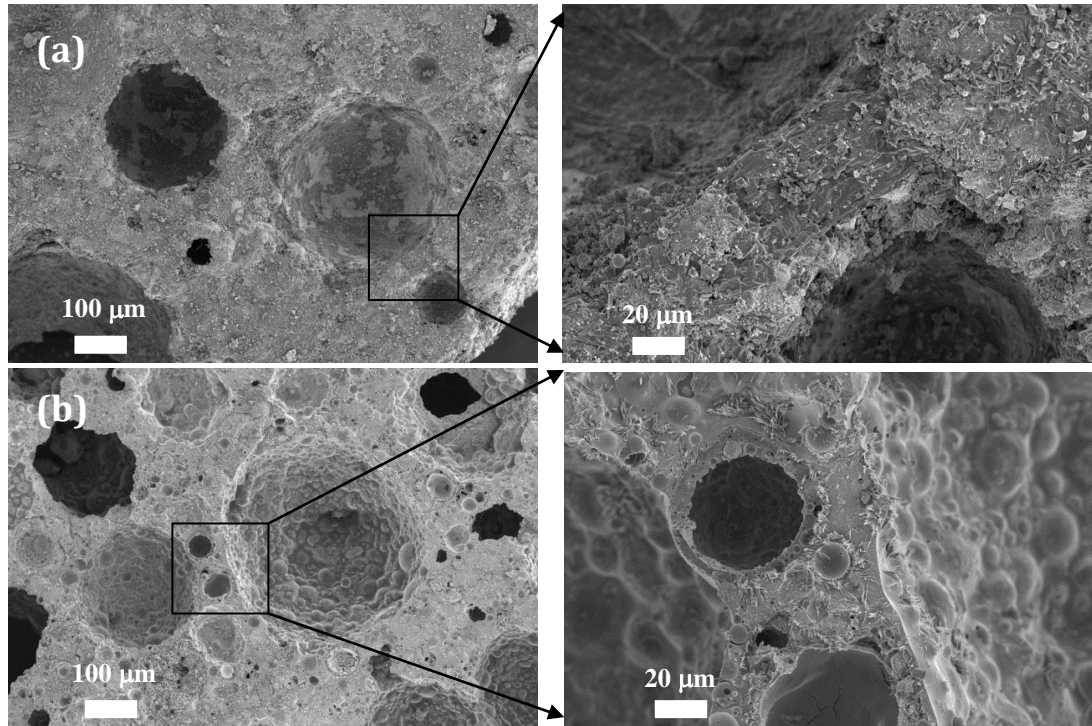
Regarding the third factor, the microstructure could be the most important factor that determine the strength and density of GFC. To examine this factor, relatively flat surfaces of fractured specimens were analysed using an optical microscope and SEM.



**Figure 6-10.** Pore structure of GFCs as observed by optical microscopy: (a) GFC A, (b) GFC B, (c) GFC C, (d) GFC D, and (e) GFC E. The scale bar is 1 mm.

Figure 6-10 presents the typical images obtained by optical microscope analysis. GFCs derived from different fly ashes exhibit significantly different pore structure. GFC A has more closed voids but connected by micro cracks; GFCs B and E have homogeneous pore structure, and most of the voids are connected pores; GFCs C and foam D have very large pores and the binder is compact. Large voids and micro cracks are apparently harmful to the compressive strength. The well distributed pores in GFCs B and E and the relatively narrow size distribution are the reasons why they possess higher strength than the other three.

Figure 6-11 presents higher-magnification images of GFCs A and E, obtained by SEM. The binder phase in GFC A is more compact than in GFC E. There are many small voids in a size of 10 to 100  $\mu\text{m}$  distributed in the binder. Many residual fly ash E particles assemble on the void wall to form a globular surface. The small voids and hollow particles present in the binder are two reasons why GFC E has the lowest density. Of course, the fly ash composition itself will affect the density of geopolymer foam to some extent.



**Figure 6-11.** SEM images of (a) GFC A and (b) GFC E.

From the microstructural observation, it can be speculated that the fine air bubbles introduced in paste are not stable. They tend to coalesce to form larger bubbles during mixing to decrease the surface energy, and tend to move up during setting. Due to the lower viscosity of the paste A, C and D, bubbles will move more easily. However, as fly ash A has the highest reactivity, the paste A solidifies faster than others, immobilising the bubbles quickly. Therefore, during mixing period, it is the paste properties (not only viscosity) that determine the air bubble movement. The large irregular fly ash particles in pastes B and E hinder the bubble from coalescing. From this point of view, fly ashes B and E are more suitable for GFC manufacture than the other fly ashes. This result is very

important because it indicates that fly ashes that appear unsuitable for solid geopolymer manufacture due to high liquid requirements or low reactivity may still be able to be used for GFC manufacture. For example, fly ash E is unsuitable for solid geopolymer manufacture; however, GFC E possesses well distributed air voids and acceptable strength. It means that GFC manufacture may bring geopolymer industry a better utilization of fly ash because it can effectively use 'low quality' fly ashes.

#### ***6.4. Effects of composition on the phase and microstructure of GFCs***

There is no doubt that the composition of the alkali activator and foam content will affect the phase and microstructure of GFC. These two factors will be further examined based on foam E in the following sections, to provide a more full understanding on the structure and property. The GFC E was selected for further investigation based on its good pore structure and more importantly the value of using fly ash E, which was evaluated as being unsuitable in solid geopolymer manufacture. The compressive strength of the GFC E is 4.5 MPa (Table 6-2), which is adequate for non-load bearing applications. However, it is not high enough for semi-structural purposes, which usually requires >10 MPa. An effective method to improve the strength is to partially substitute fly ash with more active aluminosilicate materials, such as slag and metakaolin. In this study, a ground granulated blast furnace slag was used.

##### **6.4.1 Orthogonal array study of composition factors**

The composition of the activator depends on the concentration of NaOH solution and the quantity of liquid sodium silicate (LSS) solution. As shown in Table 6-3, NaOH solution and LSS are taken as the two independent factors. This means that there are actually four factors to consider: slag, NaOH concentration, LSS and foam. To optimise the experimental process, an orthogonal array was designed for studying the four factors.

**Table 6-3:** Orthogonal array design of four composition factors.

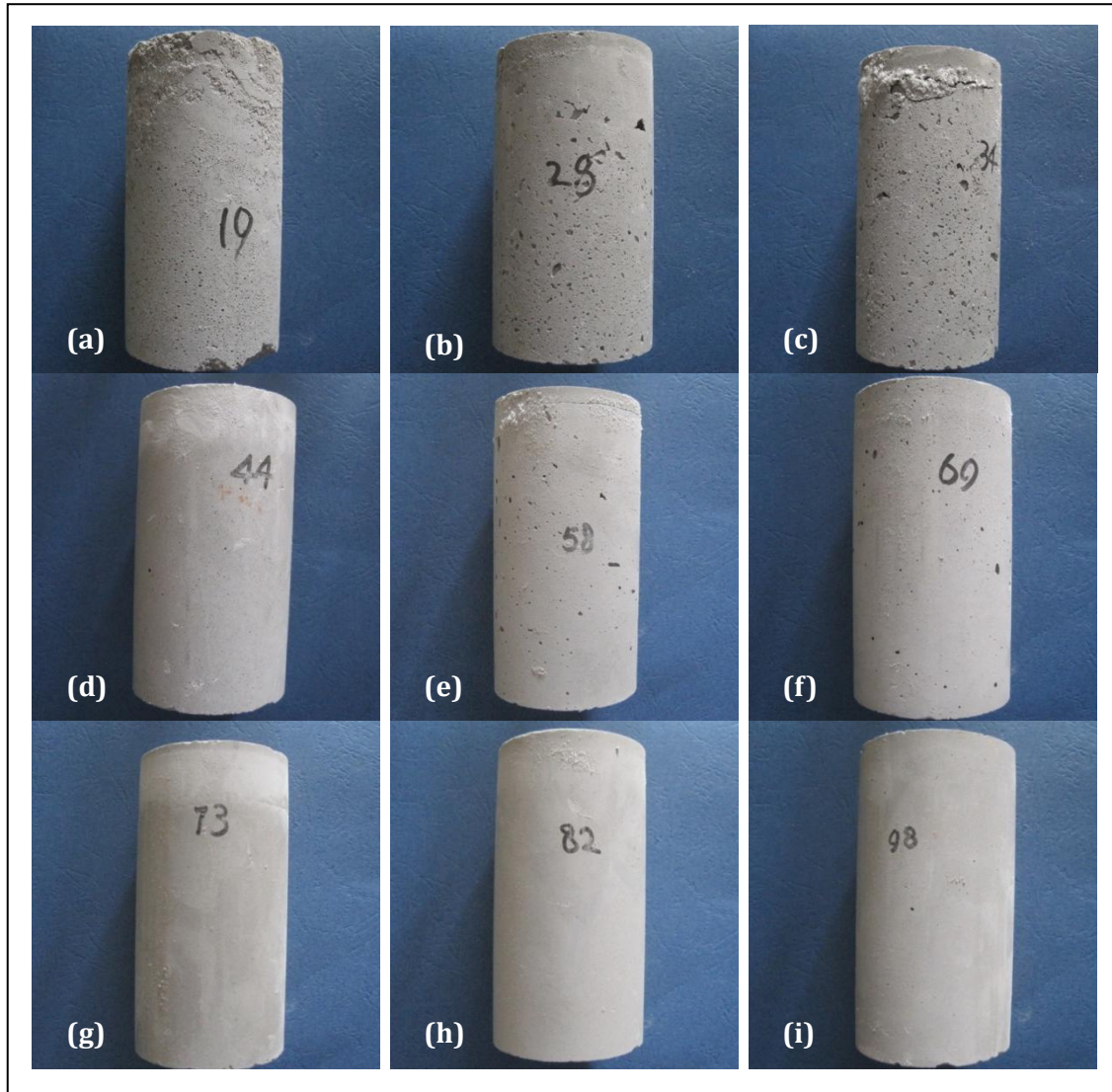
No.	Slag %	C <sub>NaOH</sub>	LSS	Foam	Result
1	A <sub>1</sub>	B <sub>1</sub>	C <sub>1</sub>	D <sub>1</sub>	y <sub>1</sub>
2	A <sub>1</sub>	B <sub>2</sub>	C <sub>2</sub>	D <sub>2</sub>	y <sub>2</sub>
3	A <sub>1</sub>	B <sub>3</sub>	C <sub>3</sub>	D <sub>3</sub>	y <sub>3</sub>
4	A <sub>2</sub>	B <sub>1</sub>	C <sub>2</sub>	D <sub>3</sub>	y <sub>4</sub>
5	A <sub>2</sub>	B <sub>2</sub>	C <sub>3</sub>	D <sub>1</sub>	y <sub>5</sub>
6	A <sub>2</sub>	B <sub>3</sub>	C <sub>1</sub>	D <sub>2</sub>	y <sub>6</sub>
7	A <sub>3</sub>	B <sub>1</sub>	C <sub>3</sub>	D <sub>2</sub>	y <sub>7</sub>
8	A <sub>3</sub>	B <sub>2</sub>	C <sub>1</sub>	D <sub>3</sub>	y <sub>8</sub>
9	A <sub>3</sub>	B <sub>3</sub>	C <sub>2</sub>	D <sub>1</sub>	y <sub>9</sub>
$\bar{I}_1$	$\bar{I}_{11} =$ $(y_1 + y_2 + y_3)/3$	$\bar{I}_{12} =$ $(y_1 + y_4 + y_7)/3$	$\bar{I}_{13} =$ $(y_1 + y_6 + y_8)/3$	$\bar{I}_{14} =$ $(y_1 + y_5 + y_9)/3$	Y =
$\bar{I}_2$	$\bar{I}_{21} =$ $(y_4 + y_5 + y_6)/3$	$\bar{I}_{22} =$ $(y_2 + y_5 + y_8)/3$	$\bar{I}_{23} =$ $(y_2 + y_4 + y_9)/3$	$\bar{I}_{24} =$ $(y_2 + y_6 + y_7)/3$	$1/9 \sum y_i$ i=1,2,3
$\bar{I}_3$	$\bar{I}_{31} =$ $(y_7 + y_8 + y_9)/3$	$\bar{I}_{32} =$ $(y_3 + y_6 + y_9)/3$	$\bar{I}_{33} =$ $(y_3 + y_5 + y_7)/3$	$\bar{I}_{34} =$ $(y_3 + y_4 + y_8)/3$	...9

Table 6-4 lists the composition and the compressive strength and air dried density testing results. Additional H<sub>2</sub>O was used to make all mixtures have a constant H<sub>2</sub>O/(fly ash + slag) ratio of 0.37. This is the minimum value at which all of the pre-mixed slurries are workable. After mixing with foam, the slurries exhibited good workability. The hardened specimens of each mix are shown in Figure 6-12.

**Table 6-4:** Composition and strength and air-dried (AD) density of GFCs (mean of 4 samples).

Mix	FA/g	Slag/g	C <sub>NaOH</sub> (270g)	LSS/g	Foam/g	H <sub>2</sub> O/g	Mean strength (MPa)	Mean AD density (kg/m <sup>3</sup> )
1	1500	0	9.6	300	60	131.1	4.1	855
2	1500	0	12	360	75	110.5	3.3	843
3	1500	0	14	420	90	86.2	3.6	785
4	1350	150	9.6	360	90	97.5	8.5	875
5	1350	150	12	420	60	76.7	15.4	1046
6	1350	150	14	300	75	153.3	14.0	961
7	1200	300	9.6	420	75	64	12.8	982
8	1200	300	12	300	90	143.8	11.0	949
9	1200	300	14	360	60	119.7	18.8	1110





**Figure 6-12.** Appearance of GFCs: (a) to (i) are mixture #1 to #9.

At a first glance, the compressive strengths of FGCs have a direct relationship with their densities. Viewing from the perspective of composition, the slag content plays the most important role. Specimens containing slag exhibit better workability and their surfaces are more homogeneous. To obtain a better understanding of each factor, the range analysis of the strength and density are as shown in Table 6-5.

In terms of compressive strength, the most important factor is slag. The second influencing factor is NaOH concentration, which determines the alkali content in geopolymerization systems.

To confirm this order in Table 6-5 an additional analysis on the variance of strength was performed and shown in Table 6-6. The analysis confirms that slag is the most important factor.

**Table 6-5:** Range analysis of factors affecting the strength and density.

Property	Factor	Level 1	Level 2	Level 3	R
Strength	Slag%	$D_{11}=\bar{1}_{11}-Y=-6.52$	$D_{21}=\bar{1}_{21}-Y=2.49$	$D_{31}=\bar{1}_{31}-Y=4.03$	10.55
	$C_{NaOH}$	$D_{12}=\bar{1}_{12}-Y=-1.68$	$D_{22}=\bar{1}_{22}-Y=-0.27$	$D_{32}=\bar{1}_{32}-Y=1.95$	3.63
	LSS	$D_{13}=\bar{1}_{13}-Y=-0.45$	$D_{23}=\bar{1}_{23}-Y=0.03$	$D_{33}=\bar{1}_{33}-Y=0.42$	0.87
	Foam	$D_{14}=\bar{1}_{14}-Y=0.01$	$D_{24}=\bar{1}_{24}-Y=-0.13$	$D_{34}=\bar{1}_{34}-Y=-2.46$	2.47
Density	Slag%	$D_{11}=-110.8$	$D_{21}=28.9$	$D_{31}=81.9$	192.7
	$C_{NaOH}$	$D_{12}=-27.8$	$D_{22}=7.5$	$D_{32}=20.2$	48
	LSS	$D_{13}=-10.1$	$D_{23}=4.2$	$D_{33}=5.9$	16
	Foam	$D_{14}=71.9$	$D_{24}=-9.8$	$D_{34}=-62.1$	134

**Table 6-6:** Variance analysis of factors affecting the strength.

Factor	Variance $S_i$	Degree of freedom $f_i$	Average variance $\hat{S}_i = S_i/f_i$	$F_i = \hat{S}_i/\hat{S}_E$	Significance
Slag%	194.82	2	97.41	87.13	>F0.05, No.1
$C_{NaOH}$	20.12	2	10.06	9.00	>F0.05, No.2
LSS	1.14	2	0.57	0.51	<F0.05, none
Foam	18.25	2	9.13	8.16	>F0.05, No.3
Error	20.12	18	1.12		

The NaOH concentration in combination with LSS content determines the modulus of alkali activator (Ms) and the Na<sub>2</sub>O content in geopolymer. Table 6-7 lists the Ms and Na<sub>2</sub>O content in each mix.

**Table 6-7:** Modulus (Ms) and alkali content in GFCs (Na<sub>2</sub>O/solid materials mass ratio).

Mix no.	1	2	3	4	5	6	7	8	9
Ms	0.90	0.91	0.93	0.98	0.98	0.76	1.08	0.81	0.85
Na <sub>2</sub> O (%)	6.73	8.05	9.13	7.32	8.64	7.95	7.91	7.46	8.54

It was observed that the pastes synthesised with 420 g LSS (Mix no.5 and no.7) exhibit high strength and good workability. This suggests that an alkali activator with Ms near 1.0 is preferred.

For density, there is no doubt that foam content will play a very important role. Generally, at the same conditions, the higher foam content will cause lower density, higher porosity and larger pore size (it is inevitable that air bubbles will coalesce). This trend is also shown in many OPC based foam concretes (Nambiar and Ramamurthy 2007). However, as shown in Table 6-4, the question then arises: why is slag apparently more important than foam content for density?

## 6.4.2 The effects of slag addition on the phase and pore structure of GFCs

### 6.4.2.1 Effect of slag addition on phase of geopolymers

To understand the mechanisms how slag addition can affect the strength and density of geopolymer foams, two batches of geopolymers containing 100-60% fly ash E and 0-40% slag were made and tested. From the results of the orthogonal array study, an optimal alkali activator was designed to be Ms=1.0 and Na<sub>2</sub>O=6.48% by mass of total solid content, including solid materials and Na<sub>2</sub>O and SiO<sub>2</sub> in activators.

Table 6-8 gives the composition of the mixtures and the strength and density of geopolymers. Selected samples were ground and dried at 105°C for at least 24 h for XRD and FTIR analysis.

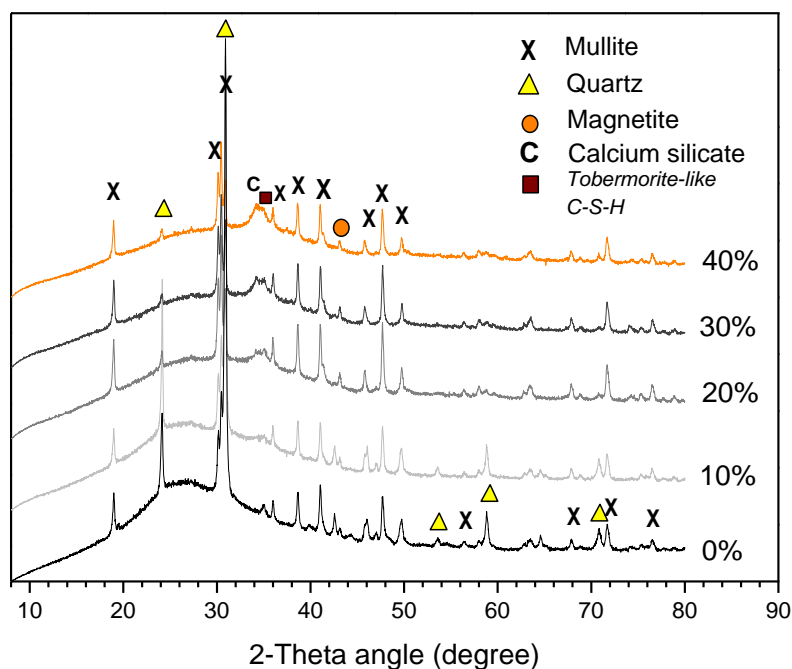
From Table 6-8, it can be seen that for the solid geopolymers, slag addition can effectively improve the compressive strength. As the slag content increases, the compressive strength increases consistently.

**Table 6-8:** Composition of slag containing geopolymers and the compressive strength at 28 d, AC-Density at 28 d ageing and oven-dried (OD) density after 60 d ageing (mean of 4 samples).

Type	Fly ash /g	Slag /g	NaOH (12M)/g	LSS /g	H <sub>2</sub> O /g	Foam /g	Mean strength /MPa	AC-density /kg/m <sup>3</sup>	OD-density kg/m <sup>3</sup>
Solid	1000	0	154.6	240	160	0	15.7	1515	1360
	900	100	154.6	240	145	0	28.5	1505	1300
	800	200	154.6	240	120	0	44.9	1445	1280
	700	300	154.6	240	100	0	48.6	1562	1373
	600	400	154.6	240	100	0	50.6	1629	1425
	Foam	1000	0	154.6	240	80	50	7.3	942
900		100	154.6	240	70	50	10.1	958	895
800		200	154.6	240	65	50	12.6	1052	988
700		300	154.6	240	60	50	11.3	1000	902
600		400	154.6	240	60	50	10.2	1047	975

To understand the strengthening mechanisms, XRD and FTIR analysis have been performed on the solid geopolymers, as shown in Figure 6-13 and Figure 6-14, respectively.





**Figure 6-13.** XRD patterns of solid geopolymers containing 0 to 40 wt.% slag after 40°C×24 h oven curing plus 27 d ageing at ambient conditions. The peaks labelled as tobermorite is calcium silicate hydrates (C-S-H) with tobermorite-like structure.

In the activation products, except for distinct crystalline phases originally present in fly ash E, two new crystalline phases, calcium silicate and tobermorite-like calcium silicate hydrates, are found in slag containing geopolymers. The calcium silicate is from the slag. The diffraction intensities of characteristic peaks corresponding to the two phases increase as slag content increases, implying the increased quantity of these phases. These phases were also observed in other alkali activated slag systems (Garcia-Lodeiro et al. 2011; Zhang et al. 2008). The improvement in strength seems to be closely related to the formation of calcium containing aluminosilicate hydration products (N-C-A-S-H) and alumina-substituted calcium silicate hydrates (A-C-S-H), which are expected as strengthening phases in geopolymer matrix (Yip et al. 2005; 2008).

These formed hydrates all contain calcium. The role of calcium cations in geopolymerization have been studied extensively. When the alkali activator contains soluble silicate, the calcium dissolved from the fly ash would likely form precipitates in the liquid phase, rather than on fly ash surface, thus promoting the dissolution of bulk particles (Lee and Van Deventer 2002b). The much higher reaction heat release rate for fly ashes containing higher CaO has been demonstrated (Winnefeld et al. 2010).

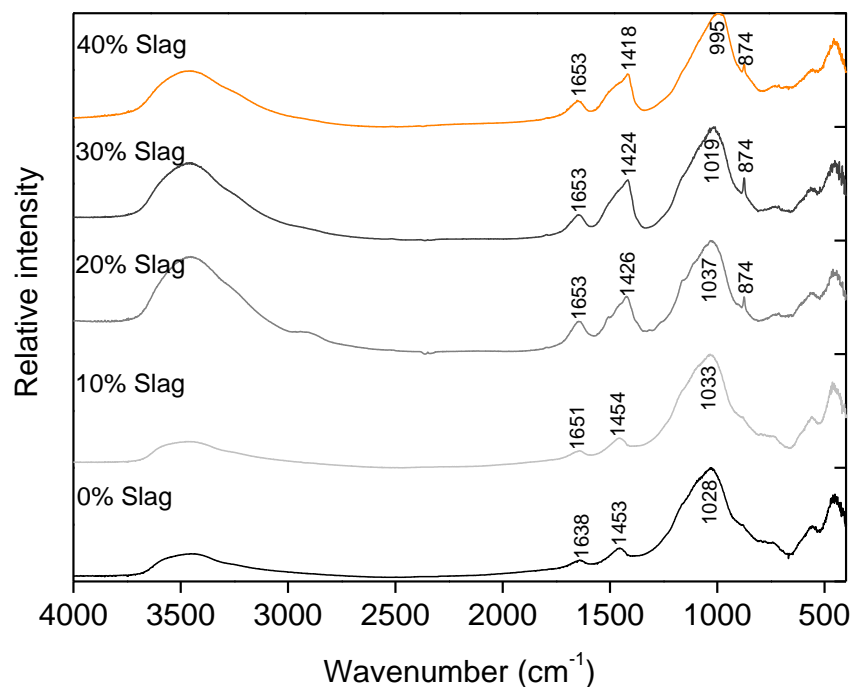
When calcium cations are dissolved from slag particles, the system will form more C-A-S-H. Some homogeneous but XRD amorphous sodium calcium aluminosilicates (N-C-A-S-H) were observed by SEM+EDS analysis (Yang et al. 2012), and recently observed by Ismail et al. (2014). These gels help to form a

more compact microstructure than when using fly ash as a single solid precursor. When calcium is sourced from chemical additives, such as  $\text{Ca}(\text{OH})_2$  and  $\text{CaO}$  (Temuujin and Van Riessen 2009), it will act as nucleating site in solution phases to form calcium containing aluminosilicates.

The hydration of these compounds leads to water deficiency and thus raises the alkalinity of the mixture. The increase in alkalinity promotes higher and faster dissolution of Si and Al species from the source material, increasing the rate of geopolymerization (Diaz-Loya et al. 2011). Therefore, the presence of calcium, either present in fly ash itself or by using slag or adding lime, contributes to the strengthening of hardened matrix not only by forming calcium containing aluminosilicates but also by enhancing the geopolymerization extent.

In this study, the more slag used, the less additional water was required, to achieve a workable paste. Besides the positive effects of lower porosity on the strength improvement as slag addition, although this point may be argued by different researchers (Yang et al. 2012; Ismail et al. 2014), less water will also increase the reaction extent. Less water will increase the alkalinity of the liquid phase, although it was separately added at the last step during mixing. The increased alkalinity of liquid phase promotes the dissolution of fly ash and slag and thus a higher reaction extent is achieved. This effect cannot be immediately distinguished in the mixtures studied here because they contain different amounts of slag. However, the FTIR spectra do provide some evidences that the fly ash has led to higher reaction extent in slag containing systems.

Figure 6-14 shows the FTIR spectra of the geopolymers. The increased relative absorbance intensity of bands centered at 1640 and 3450  $\text{cm}^{-1}$ , which are assigned to bending and stretching vibration of hydroxyl groups of chemically bound water in Al-substituted C-S-H (Yu et al. 1999) and/or sodium silicate gels (Dimas et al. 2009). It indicates higher quantities of hydration products that have been formed. This is in agreement with the above analysis. The asymmetrical bands between 1453 and 1418  $\text{cm}^{-1}$  are attributed to the asymmetric stretching mode of the O-C-O bonds of the carbonation products of  $\text{Ca}(\text{OH})_2$  and/or NaOH (Bernal et al. 2011c). The band appearing at 874  $\text{cm}^{-1}$  is due to the bending mode of C-O in the original slag (Appendix A3).

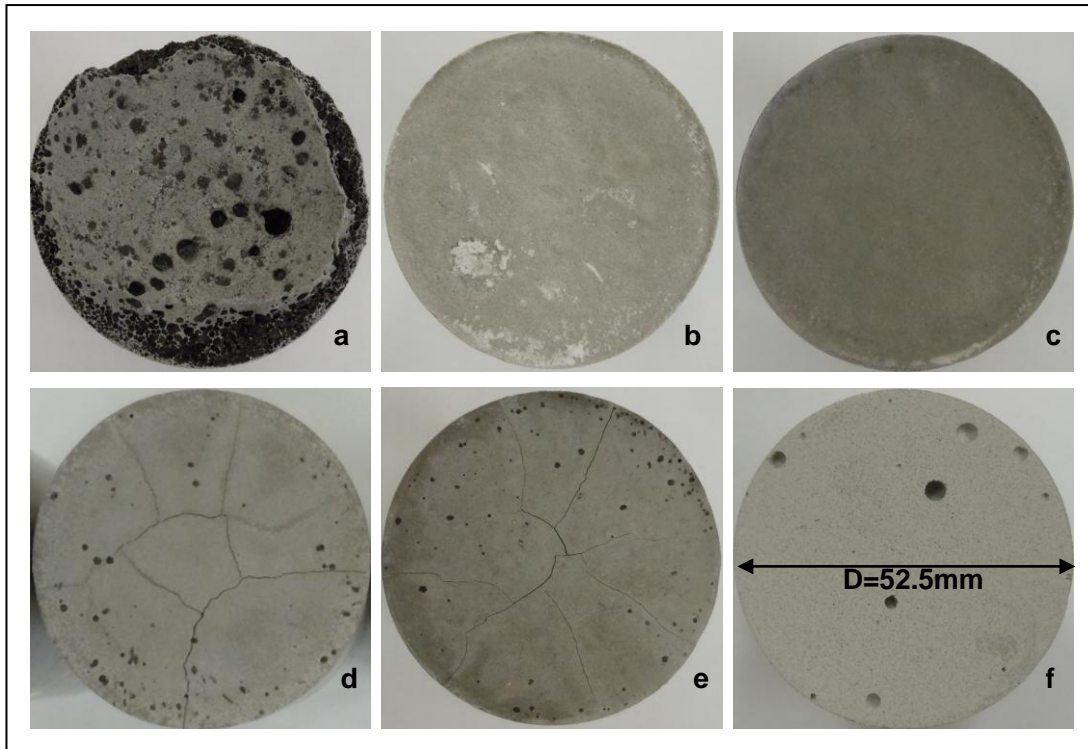


**Figure 6-14.** FTIR spectra of solid geopolymers containing 0 to 40 wt.% slag after 40°C×24 h oven curing plus 27 d ageing at ambient conditions.

The maximum absorbance band shifts from 1028  $\text{cm}^{-1}$  in the non-slag geopolymer to 1037  $\text{cm}^{-1}$  in the 20 wt.%-slag geopolymer and then shifts to 995  $\text{cm}^{-1}$  in the 40 wt.%-slag geopolymer. The first shift towards higher position is an indicator of higher atom weight of the chain or network of alkali activated products. This is because this band is ascribed to the average T-O stretching in N-A-S-H and other hydrates, like C-S-H and C-A-S-H. The shift towards higher wavenumber field indicates the heavier atomic molecular. The most likely reason is that the relatively more active slag, compared to fly ash, dissolves more Si in the alkaline solution and quickly form more cross linking structures. Another possible reason is that fly ash dissolves more Si. This is because the Si/Al molar ratio of the amorphous phase in fly ash is 7.08 while it is 2.0 in slag. If fly ash dissolves to the same extent, this band should have shifted towards the lower field consistently as slag content increases. Again, the reason that the fly ash processes higher dissolution is because of the higher alkalinity of the liquid phase as less additional water is used.

When slag content is higher than 20 wt.%, this band shifts towards lower fields. There are two possible factors: the first is the lower reaction extent of fly ash reduces the Si/Al ratio due to the competitive consumption of activator by slag; the second is that large quantities of calcium silicate hydrates are formed and the average polymerisation degree of dissolved silica is reduced ((Dimas et al. 2009), and also the Al and Ca-substitution in geopolymer network structures. It is very difficult to determine the exact reaction extent of fly ash and slag in the blended geopolymerization systems. However, it is more reasonable to ascribe the band shift towards lower field to be due to the second factor, which is more Ca and Al-substituted gels form. This aspect has been shown in many recent

observations in alkali activated slag and slag-fly ash blend (Yang et al. 2012; Ismail et al. 2014). As indicated by the XRD analysis that tobermorite-like structures are formed in the systems containing 20-40 wt.% slag, and these structures are recently described as calcium-sodium aluminosilicate hydrate gels, and are more cross-linked than those non-cross-linked tobermorite structures (Myers et al. 2013). These cross-linked tobermorite-like structures are formed due to Al substitution of Al in calcium silicate structures.



**Figure 6-15.** Appearance of top surfaces of solid geopolymers synthesised with 0 wt.% (a), 10 wt.% (b), 20 wt.% (c), 30 wt.% (d) and 40 wt.% (e) of slag and the surface after sanding (f).

The strength does not increase remarkably when slag content becomes higher than around 20 wt. %. This result agrees with the findings by other researchers (Kumar et al. 2010; Yang et al. 2012). Figure 6-15 may give one of the reasons why slag content  $\geq 30$  wt.% results in limited increase in strength. Samples with 30 wt.% and 40 wt.% slag content show cracks on the top surface. These cracks are formed due to the high drying shrinkage of the paste at the top due to the rapid loss of water. There could be micro-cracks in the geopolymer binders that cannot be observed by naked eye, though the visible cracks are not observed after sanding off the top surface (Figure 6-14f). Most of the published literatures have shown the presence of micro-cracks in alkali-activated slag binders (Puertas et al. 2006; Mozgawa and Deja 2009). The micro-cracks are believed due to the shrinkage nature of the alkali activated high-calcium containing materials, rather than due to the sampling process (Temuujin and Van Riessen 2009). These micro-cracks will lead to the loss of strength of solid geopolymers, even though they should be stronger as more slag was added. The other possible reason may lie on the compatibility of the calcium silicate hydrates with sodium aluminosilicate hydrates (N-A-S-H), mainly geopolymeric gels

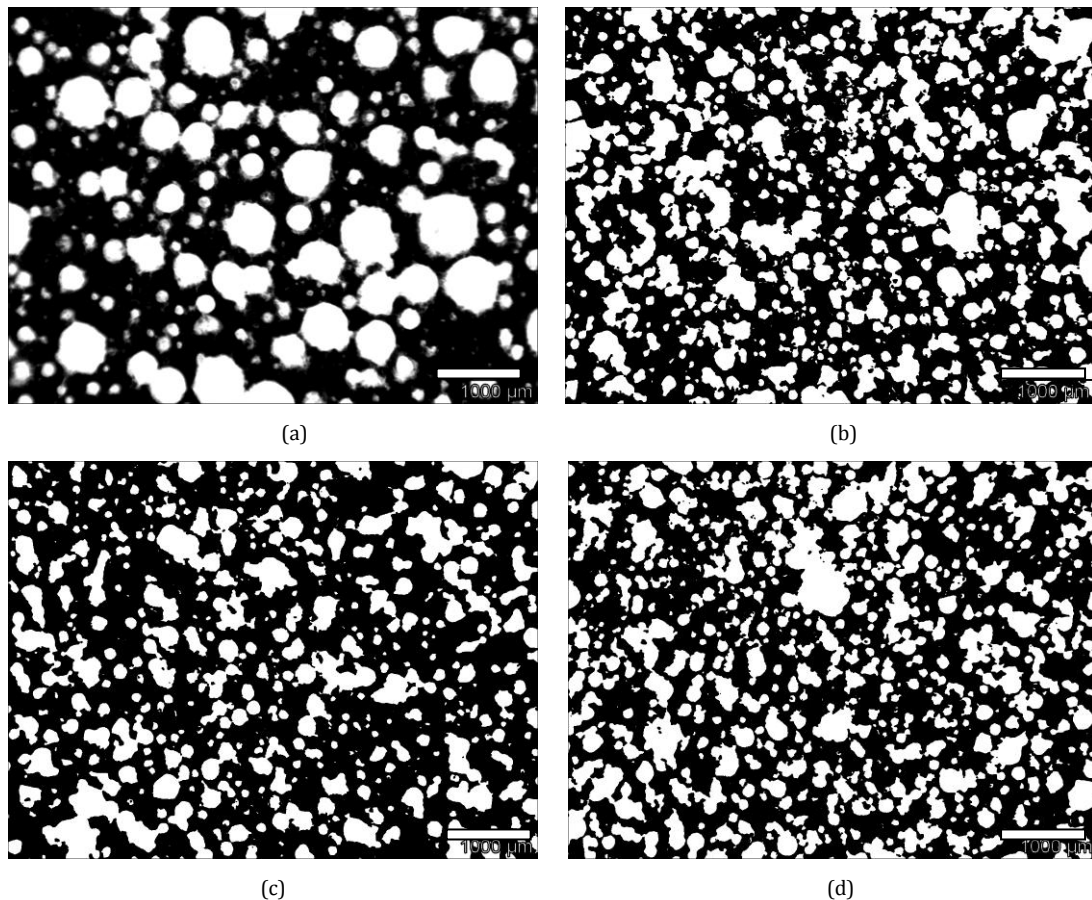
(Garcia-Lodeiro et al. 2011). This is beyond the scope of this study, but is worthy of further research in the future.

It is very interesting to note that the compressive strength of foamed geopolymers decreases as slag content increases from 20 to 40 wt.%, contrary to the trend of solid geopolymers. The reason behind this unexpected result, as presented below, is due to the microstructure change of foamed geopolymers as slag content increases.

#### 6.4.2.2 Effect of slag addition on pore structure of GFCs

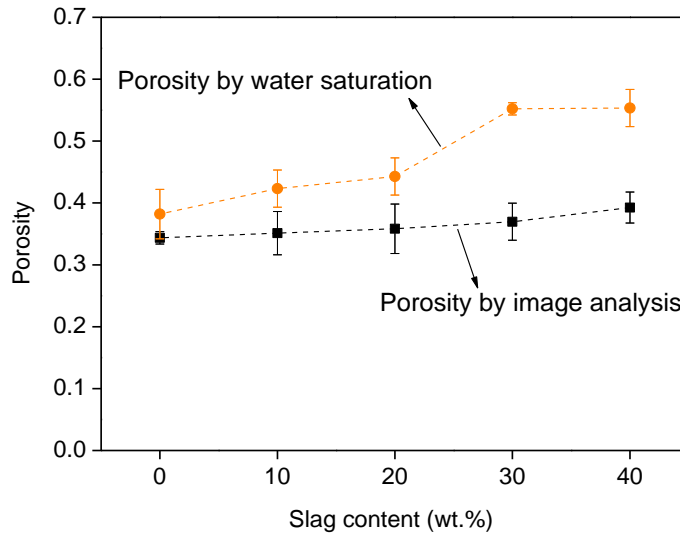
The pore size and porosity are certainly two of the most important factors determining the mechanical property and density of foam concrete. In this study, image analysis (IA) of the section of GFC was adopted to examine the pore structure and porosity. Since some of the small pores, particularly for the gel and capillary pores, are too small to be filled up with white powder and distinguished according to the method described in section 3.4.3.5, the porosity determined by this method might be lower than the real porosity. So a vacuum water absorption method was used to determine the water saturation porosity. Given the porous structure of foam concrete, this method will give porosity very close to the real porosity.

Figure 6-16 shows that with slag addition, the air voids become much finer.



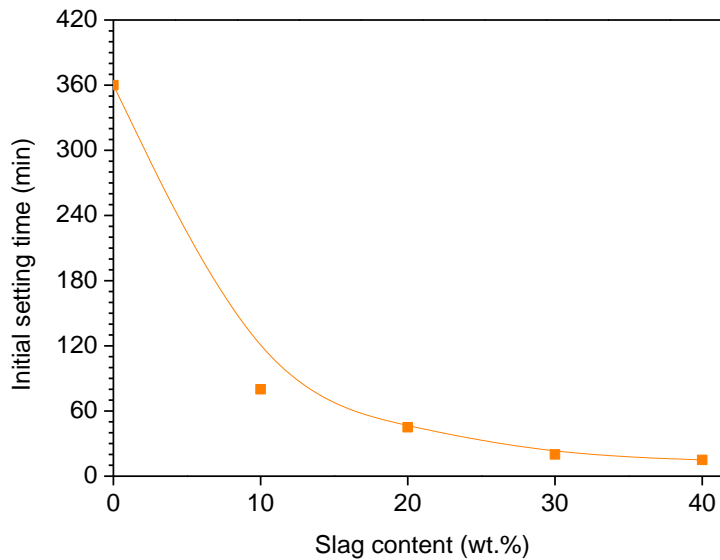
**Figure 6-16.** Typical optical images of GFCs with 0 wt.% (a), 20wt.% (b), 30 wt.% (c) and 40 wt.% (d) of slag. The white areas are pores and the black areas are binders. The scale bar is 1mm.

Figure 6-17 gives the porosity of the GFC determined by the two methods. As expected, the porosity obtained by IA is much lower than the porosity as determined by water saturation method. A general trend can be concluded that the porosity increases with slag addition increase.



**Figure 6-17.** Effect of slag addition on the porosity of GFCs. (The water saturation method uses 4 samples; the image analysis method uses 2 samples with 10-20 images for each sample).

One of the reasons that slag addition changes the pore structure and porosity is the fast setting of the paste. Figure 6-18 plots the setting time of solid geopolymer pastes. The pastes were put in an oven at 40°C. The paste without slag addition was measured at 20 min intervals using a Vicat Needle and the pastes containing slag were measured at 5 min intervals so as not to miss the initial setting.

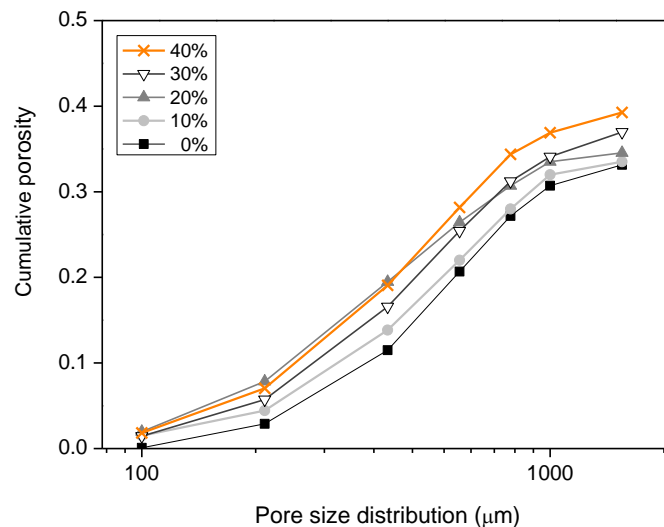


**Figure 6-18.** Effect of slag addition on the initial setting time of geopolymer.

The initial setting time of the geopolymer paste without slag addition at 40°C is 6 h. With slag addition, the setting time is greatly shortened. The initial setting time at room temperature was reported no shorter than 2 hours for low calcium fly ash (Hardjito et al. 2008) and around 1 hour for high calcium fly ash (Jumrat et al. 2011; Rattanasak et al. 2011) although it may be varied by changing other parameters. In comparison, the setting time of alkali activating GBFS was reported to be much shorter - around 1 hour at room temperature and shorter than 40 min at 60°C (Cheng and Chiu 2003). Apparently, the formation of calcium containing gels promotes the setting of paste.

Due to the quick setting of the foamed paste containing slag, there is less time for the air bubbles to coalesce, move and escape to the surface. The air bubbles remain small and separate and impact a final density.

The strength decreases by 10% as slag content increases from 30 wt.% to 40 wt.%. From the porosity measurements, the strength decrease when foamed geopolymers contain > 20 wt.% slag could be mainly due to the porosity increases. However, the porosities determined by water saturation method are constant. In comparison, the IA porosity, which focuses on large pores, seems more reasonable to explain the strength decrease. Therefore, the strength decrease could be related to the increased volume of large pores. Figure 6-19 shows the cumulative porosity of pores larger than 100 μm.



**Figure 6-19.** Effects of slag addition on the pore size distribution of GFCs by IA.

By image analysis, it was found that non-slag GFC contains 30% (in volume fraction of total porosity) pores with size <400 μm, while in slag containing geopolymers, it takes up more than 50%. The shift of pore size distribution towards smaller size region makes a positive contribution to the strength increase. However, as can be seen in Figure 6-18, GFC containing 40 wt.% slag has the highest volume of pores > 400 μm. This could be the reason why strength decreases.

It is well known that for cement-based materials, pore structure and porosity are very important to the mechanical properties and permeability. By selecting suitable fly ash and optimising the activator composition of the geopolymer binder, it is possible to produce high strength and durable binders. However, as shown above, for foam geopolymers, pore structure plays a key role affecting the mechanical properties. The negative effect of large pores could be the main reason of low strength.

The relationship between pore structure and properties, such as compressive strength and modulus, is unclear for GFCs. The only way to establish this relationship is to understand the effects of each aspect of pore structure, including porosity, pore size distribution and shape.

### ***6.5 Concluding remarks***

The chapter describes the successful manufacture of GFCs under laboratory conditions. The influences of several aspects of fresh and hardened GFCs have been examined, including segregation, workability, compressive strength and pore structure.

The foam generated with the foaming agent surfactant polypeptide-alkylene polyol used in this study is stable under high pH condition. This is particularly important to achieve stable foamed geopolymer pastes. The concentration of the foaming agent affects the stability of foam to a certain extent and an optimised concentration is around 1.5 wt.%. The foam density has little effect on its stability.

For the geopolymer pastes with a reasonable liquid/solid ratio (0.35-0.60), the workability of foamed geopolymer pastes mainly depends on the source of fly ash. The fresh foamed pastes manufactured with fly ash A, C and D exhibited higher workability than those manufactured with B and E. However, due to their higher workability, the hardened foam concretes also exhibited higher segregation. The GFC derived from A with 8% foam addition had the highest level of segregation.

The higher workability of the foamed paste A, C and D also allows the air bubbles to move and coalesce more easily. The large pore size distribution in their hardened state is the main factor contributing to their relatively lower compressive strength. In comparison, the well distributed pores in foams B and E and the relatively narrow size distribution appear to be the main reasons why they possess relatively higher compressive strength. It appears that fly ash physics play a more important role than fly ash chemistry in affecting the properties of GFCs.

The results indicate that a fly ash suitable for making high strength solid geopolymers is not necessarily suitable for GFC manufacture. Those fly ashes with lower particle density and irregular particle shape, such as fly ash E and B, appear best suited for the manufacture of foam geopolymers.



For a foamed paste derived from a specific fly ash, quick setting is a key property to achieve fine pore size and a homogeneous microstructure. The orthogonal array study conducted showed that slag addition is an effective method to control, and shorten the setting time of the foamed paste. The pore structure and porosity are also changed significantly and contribute to an increase in compressive strength. More detailed research into the critical characteristics of pore structure and their influences on mechanical and thermal properties is required, to understand the relationship between structure and properties of GFCs.

# **Chapter 7: The Influences of Pore Structure of GFCs on the Mechanical and Thermal Insulation Properties**

## ***7.1 Introduction***

The previous chapter described how GFCs were successfully manufactured in the laboratory using the pre-foaming technique. Blending a small amount of slag with foamed paste derived from less-reactive fly ash produces more desirable setting behaviour. The hardened products have good compressive strength and acceptably low density. The addition of slag not only changed the binder nature but also changed the pore (air void) structure and porosity. However, how the pore structure features, including porosity, pore size and distribution, affect the strength of GFC remains unclear. This is a fundamental issue for foam concrete and many other types of porous cement-based materials (Deo and Neithalath 2010).

This chapter describes the characterization of the pore structure features in geopolymer foam concrete, and their effects on their mechanical properties (including compressive strength and modulus) and thermal insulation, which is another area of concern for foam concretes. A better understanding of those relationships will provide critical information to enable better design and processing of foam concretes.

## ***7.2 Characterization of pore structure in GFCs***

When preformed air bubbles are introduced into a binder, some bubbles will be destroyed because of the mixing shear force while some will retain their original structure. Due to the tendency to coalesce, some of the introduced fine bubbles will interact with each other during mixing and setting to form larger bubbles. Consequently, the formed product is a porous structure composed of a geopolymer matrix and pores with a wide range of sizes and distribution. An effective characterization of the volume of pores, size and distribution, as well as their shape is a critical step towards the understanding of their effects on the properties of geopolymer foam concretes.

### **7.2.1 Density of GFCs**

To study the effects of pore structures, a set of GFCs were manufactured in the laboratory with different foam dosages. Table 7-1 gives the composition of the GFCs manufactured.

**Table 7-1:** Compositions of GFCs and the workability of the foamed pastes.

Mix	Fly ash E /g	Slag /g	NaOH(12M) /g	LSS /g	H <sub>2</sub> O /g	Foam/g (Volume/cm <sup>3</sup> )	Workability
GFC0	700	300	154.6	240	100	0(0)	Good
GFC1.3	700	300	154.6	240	100	13 (153)	Excellent
GFC3.3	700	300	154.6	240	80	33 (388)	Excellent
GFC5.0	700	300	154.6	240	60	50(588)	Good
GFC6.7	700	300	154.6	240	45	67 (788)	Good
GFC10	700	300	154.6	240	30	100 (1176)	Acceptable
GFC13	700	300	154.6	240	15	130 (1529)	Poor
GFC16	700	300	154.6	240	0	160 (1882)	Poor

The slag in the blend of solid precursors was set constant at 30%. This mixture was previously found to have a particularly low density (Table 6-7). Alkaline activators were separately mixed: firstly by adding NaOH solution and then LSS. This procedure is consistent with that used in the research outlined in previous chapters. According to the foam dosage, additional water was added after adding LSS, in order that all systems had similar alkalinity and H<sub>2</sub>O content. However, it was noted when foam was higher than 10% (mass ratio of foam to solid blend), the foamed pastes had poor workability although the additional water was used to keep the H<sub>2</sub>O at a constant ratio.

Fresh foamed pastes were cast in Ø 53×108 mm cylindrical moulds, followed by sealed curing at 40°C for 24 h. Demolded samples were allowed to age at laboratory conditions for 27 days and density and compressive strength were determined. Some specimens at 60 d were used for air-cured density and oven dried density measurement. Table 7-2 shows the densities and strengths of the GFCs.

**Table 7-2:** Effects of foam content on the density and strength (each mixture had ≥4 samples).

Mix	Foam/wt%	H <sub>2</sub> O/solid ratio	Air-cured density / kg/m <sup>3</sup>		Oven-dried density (60 d) / kg/m <sup>3</sup>	Compressive strength (28 d) / MPa
			28 d	60 d		
GFC0	0	0.30	1609±20	1562±26	1373±20	48.6±2.1
GFC1.3	1.33	0.32	1403±22	1353±27	1194±5	30.4±2.5
GFC3.3	3.33	0.32	1213±20	1166±26	1016±11	16.2±3.3
GFC5.0	5	0.31	1005±65	995±25	902±30	12.3±1.2
GFC6.7	6.67	0.32	982±60	917±40	817±45	9.1±1.2
GFC10	10	0.33	941±50	860±15	760±7	7.5±1.1
GFC13	13	0.34	746±10	683±6	608±7	4.5±0.6
GFC16	16	0.36	717±26	657±5	582±10	3.4±0.7

When foam dosage increases from 0 wt% to 16 wt%, the mean 28 d air-dried density decreases from 1609 to 717 kg /m<sup>3</sup>. The variation about the mean value

is <100 kg/m<sup>3</sup>. The 60 d air-dried and oven-dry densities are more consistent. Brady et al. (2001) suggested that ‘the variability of the dry density of the hardened foam concrete should not exceed ±100 kg/m<sup>3</sup> of the mean density’. Although the suggestion does not give any range of the density, the results of this research show that over a relatively large range, the density variation in each mixture is very small.

The density is one of the most important properties for foam concrete, therefore, a model relating the mixture and density will be useful for the synthesis of geopolymer foams. Based on the facts that the density is a function of the density of original binder (without foam) and the added foam content, a model is developed in the following format:

$$D = d_0 - A \cdot c^k \dots\dots\dots (7.1)$$

where *d*<sub>0</sub> is the density of original binder, *c* is the foam content, and *A* and *k* are empirical constants.

Using STATISTICA 10 with the least squares as loss functions at a 95% confidence limit (α=0.05), the power-law gave the best fit to the data. The regression formula has a R<sup>2</sup> value of 0.9536:

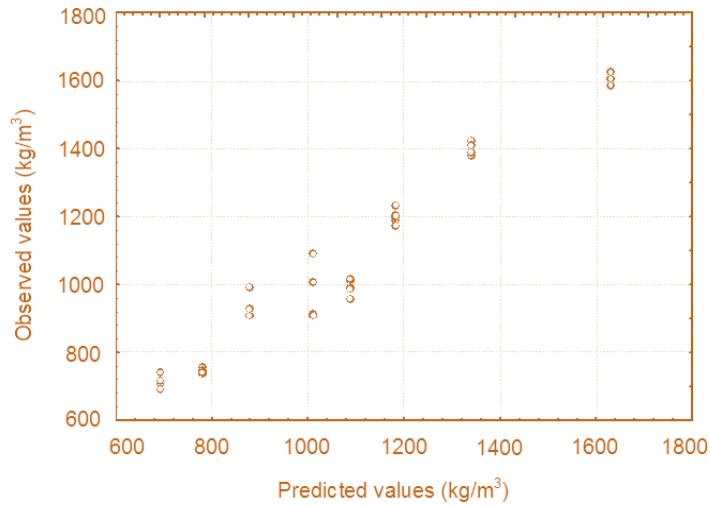
$$D_{28d} = 1628.8 - 252.9 \cdot c^{0.473} \dots\dots\dots (7.2)$$

The fitting parameters are summarised in Table 7-3.

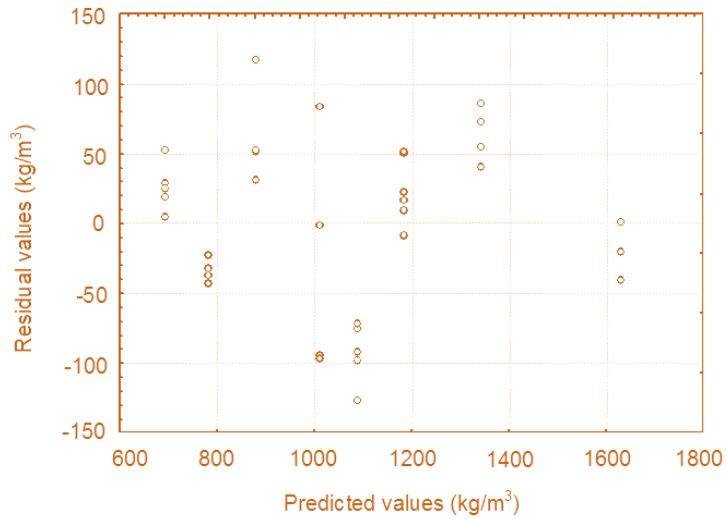
**Table 7-3:** Fitting results of 28 d air-cured density of geopolymer foam concretes.

Parameters	Estimate value	Standard error	t-value	p-level	Low Conf. limit	Up. Conf. limit
<i>d</i> <sub>0</sub>	1628.811	35.002	46.534	0.000	1557.598	1700.023
<i>A</i>	-252.899	32.919	-7.682	0.000	-319.874	-185.925
<i>k</i>	0.473	0.039	11.990	0.000	0.393	0.553

The differences between predicted and observed values are also shown in Figure 7-1. It can be seen that most residual values of predicted density compared to observed values are <50 kg/m<sup>3</sup>, which is comparable to the error by other prediction methods (Nambiar and Ramamurthy 2006b).



(a)



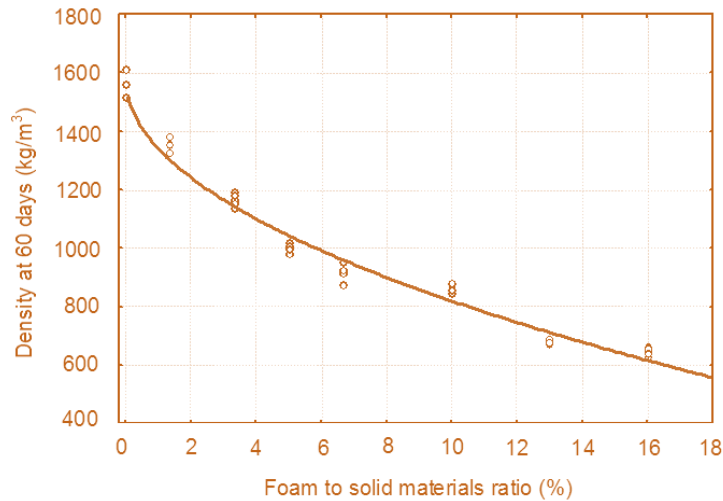
(b)

**Figure 7-1.** The difference between predicted and observed values: (a) predicted vs. observed; (b) residual analysis.

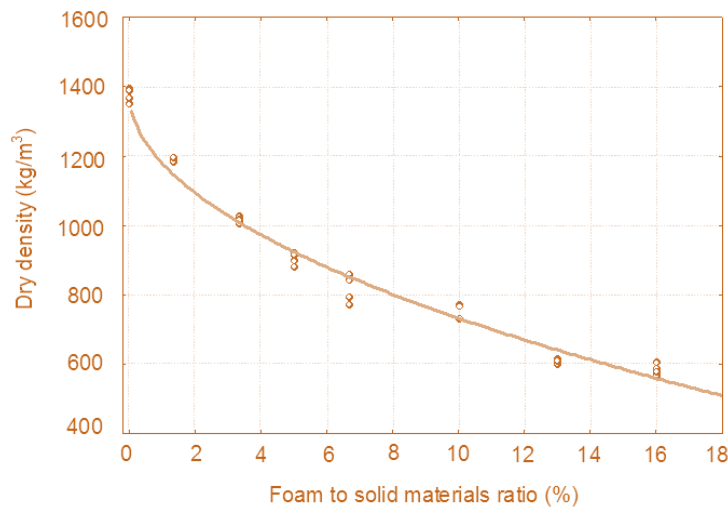
Using the same regression methods, the predicting formulas and curves for 60 d air-cured density and oven-dry density are given below:

$$D_{60d} = 1581.0 - 239.1 \cdot c^{0.503} \dots\dots\dots (7.3)$$

$$D_{\text{oven-dried}} = 1387.3 - 207.3 \cdot c^{0.499} \dots\dots\dots (7.4)$$



(a)



(b)

**Figure 7-2.** The relationship between foam content and the air-cured density at 60 d (a) and the oven-dried density (b).

Eq. 7.3 and Eq. 7.4 have a  $R^2$  of 0.9804 and 0.9843, respectively. It should be noted, however, that the three models are empirical and thus may not be suitable for predicting other systems, unless they have the same foaming conditions, alkaline activator and solid materials. Considering the volume of preformed foam, it is evident from Table 7-1 that some of the air bubbles have been destroyed during mixing. The mixing rate and duration are key factors that affect the stability of foam, and consequently affect the density of hardened geopolymer foams. In this project, the mixing followed a regime of 120 r/min  $\times$  1 min + 240 r/min  $\times$  1 min. The  $H_2O$ /solid ratio would also affect the density of original binder and the density of geopolymer foams. However, when the  $H_2O$ /solid ratio was analysed using STATISTICA 10, it was found that the fitted formulas have much lower  $R^2$ , which means the  $H_2O$ /solid ratio is not a suitable parameter to correlate with density. This is because it over emphasised the effects of additional water and/or alkaline solutions.

## 7.2.2 Porosity of GFCs

Two methods were used to determine the porosity: water saturation under vacuum conditions and mercury intrusion porosimetry (MIP). More detailed information about the processes of the two methods was provided earlier in Sections 3.2.3.4 and 3.2.3.5. Given that the high pressure of MIP may cause damage to the pore structure of low-strength geopolymer foams, only relatively strong foams (with lower porosity) were tested using this method. The porosities by the two methods are provided in Figure 7-3.

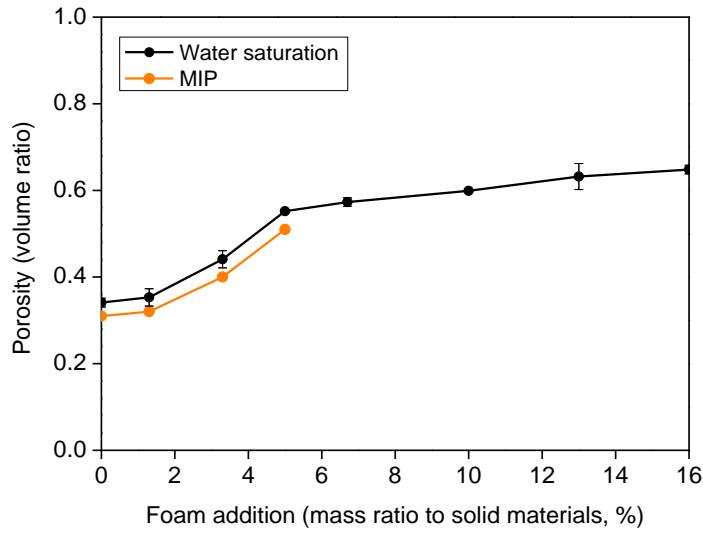


Figure 7-3. Effects of foam content on the porosity of GFCs.

Figure 7-3 shows that as foam dosage increases, the porosity measured either by water saturation or by MIP method both increases. The MIP measurement was performed under a maximum mercury-intrusion pressure of 141.3 MPa, which should be able to determine a minimal pore size of 10.4 nm in diameter. The pores smaller than this size theoretically are not be able to intruded. Due to this size limitation, the porosity by MIP should be lower than by water saturation method. The data in Figure 7-3 verified this where the MIP porosity is about 0.03-0.05 lower than the water-saturation porosity.

## 7.2.3 Pore sizes and distribution

Since foam concrete is a heterogeneous material, the porosity alone is insufficient to describe the effects of pore structure on properties. More pore features, such as pore sizes, distribution and shape factors (Nambiar and Ramamurthy 2007) are required to provide a comprehensive description of potential material performances. In this project, the effects of foam content on pore sizes and distribution, and their consequent influences on the properties of foam concrete are investigated.

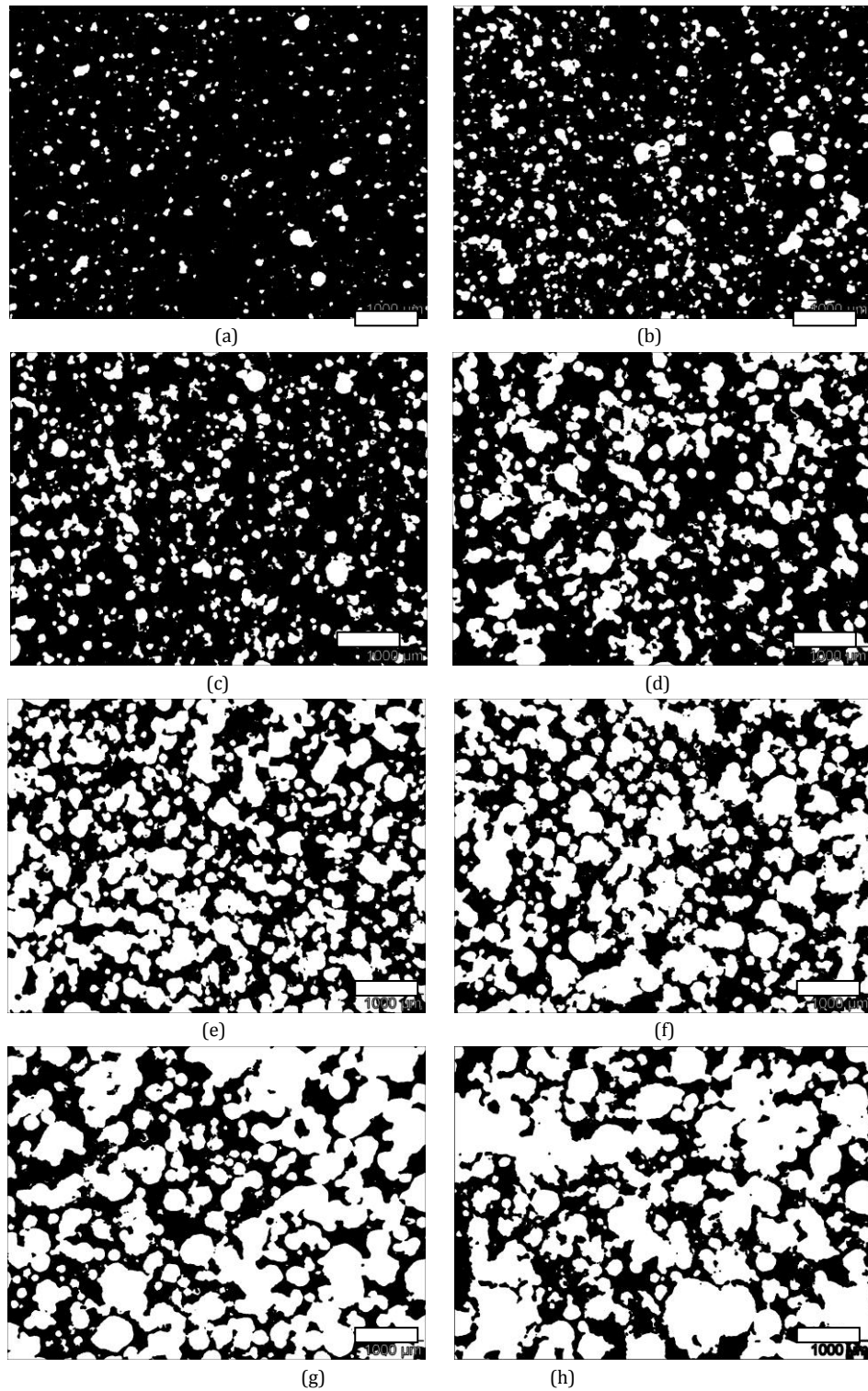
The connected pores in solid geopolymer binders can be determined by the MIP method. However, it is not a suitable method when considering the possible destruction by high mercury pressure of the integrity of geopolymer foams. The image analysis (IA) method developed by Nambiar and Ramamurthy (2007) is considered to be more suitable. Detailed information about sampling and imaging of this method was provided earlier in Section 3.2.3.6.

The larger the range of the characterized pores, the more important it becomes to more precisely describe the pore structure due to their impact on properties. One of the limitations of the imaging method is that only large pores can be effectively characterized. In this project, the void area of the smallest distinguishable pores was  $24.62 \mu\text{m}^2$ , and the corresponding equivalent circle diameter (ECD) is  $5.60 \mu\text{m}$ . Such an ECD is much smaller than the objective macropores ECD in the analysis of OPC foam concretes, which is usually  $50 \mu\text{m}$  (Nambiar and Ramamurthy 2007).

Typical binarized images of geopolymer foams with 0-16% foam addition are shown in Figure 7-4. In the solid geopolymer sample GFC0, pores  $>5.6 \mu\text{m}$  are also observed. Two possible reasons may cause these large pores in solid samples. The first reason is the introduction of air voids during mixing. This is inevitable under ambient conditions (vacuum mixing could avoid the pores). The second possible reason is that the unreacted fly ash particles in the hollow structure fall off from the shell during sampling. However, whether formed because of mixing or the detachment of unreacted particles, these pores are all weak regions in the structure.

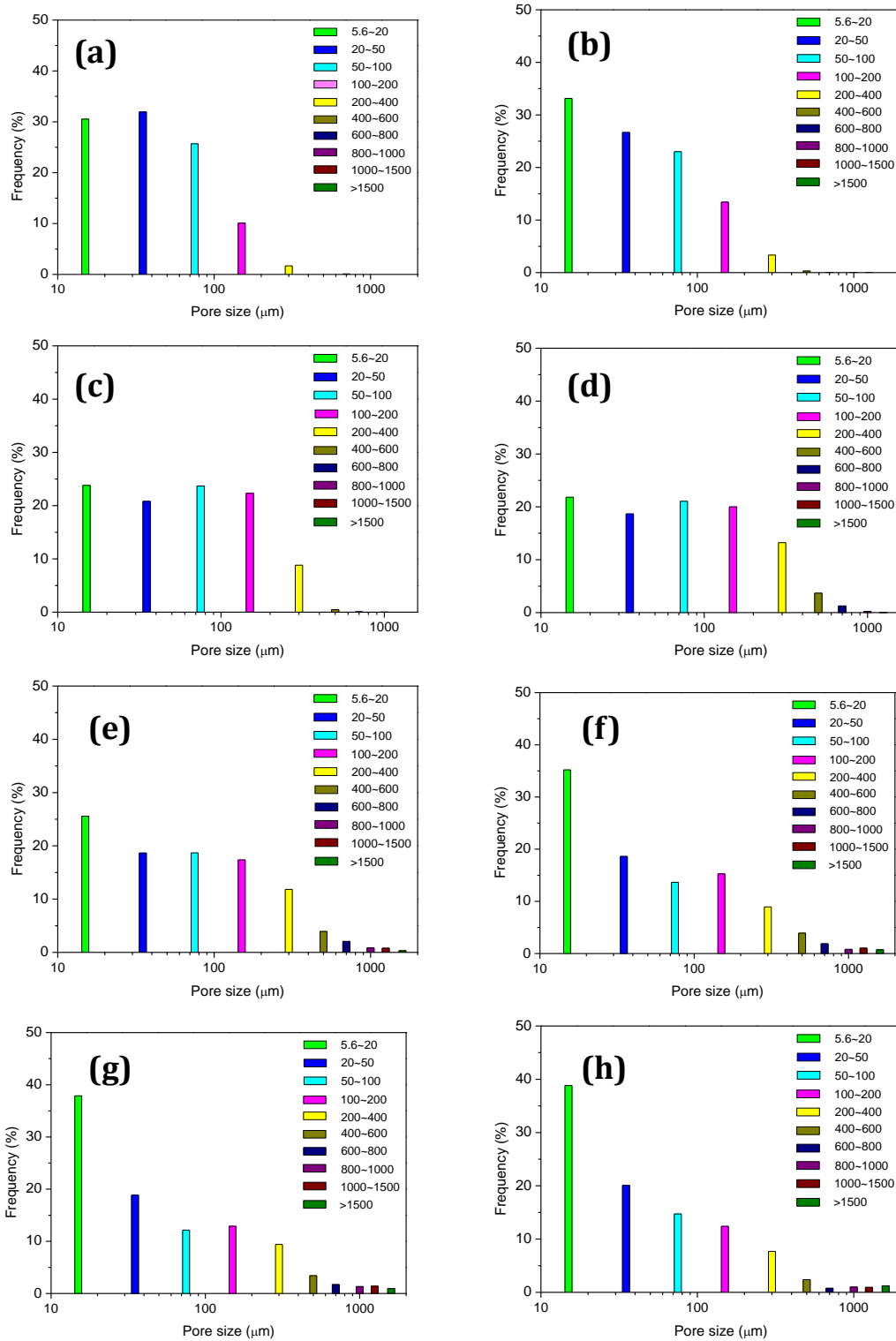
As expected, when foam is introduced, the pores become larger and more connected. When the foam dosage is higher than 5%, only a small number of pores remain small and isolated. Many pores connect with each other on their 'spherical' perimeter, forming large and irregular pores. The effects of this behaviour on the properties will be further quantified and discussed later.





**Figure 7-4.** Typical IA images of GFCs with 0 wt% (a), 1.3 wt% (b), 3.3 wt% (c), 5 wt% (d), 6.7 wt% (e), 10 wt% (f), 13 wt% (g) and 16 wt% (h) of foam addition. The white areas are pores and the black areas are geopolymer binder. The scale bar is 1 mm.

By analysing 15 to 20 images of each specimen, the frequency distribution of pores with different sizes is presented in Figure 7-5.



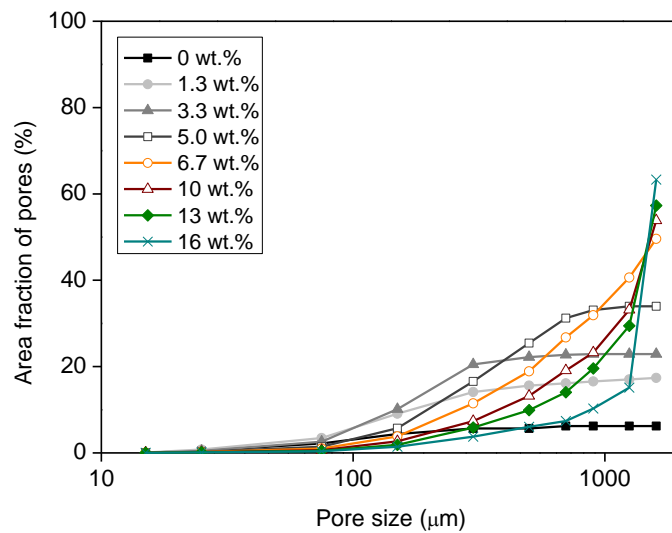
**Figure 7-5.** Frequency of pores in GFCs with 0 wt.% (a), 1.3 wt.% (b), 3.3 wt.% (c), 5 wt.% (d), 6.7 wt.% (e), 10 wt.% (f), 13 wt.% (g) and 16 wt.% (h) of foam addition.

It is seen that in the geopolymer GFC0, 85% of the detected pores are smaller than 100 μm. With an increased dosages of foam, the number of pores that are larger than 100 μm increases. However, when foam addition is higher than 10%,

the frequency of pores  $<100\ \mu\text{m}$  increases significantly. This is not because the number of fine pores becomes larger but because of the increased pore interruption, that is the total number of pores decreases. As a result, the total volume of large bubbles increases, which can be reflected by the distribution of area fraction of pores.

#### 7.2.4 Pore area fraction and pore shape

As foam dosages increases, large pores occupy more volume in GFCs. This overall trend is shown in Figure 7-6, noting that the actual shape of the trend lines change at a foam dosage of about 5 wt.%.



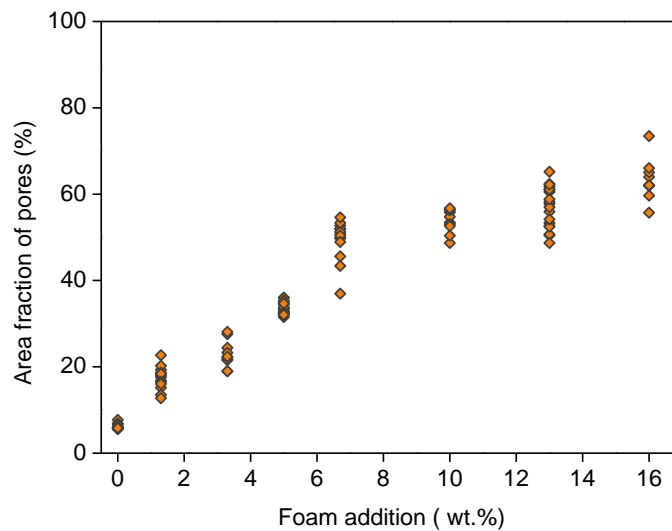
**Figure 7-6.** Cumulative distribution of area fraction of pores in GFCs. The legend shows the dosage of foam addition.

The absolute volume of pores in the tested size range decreases consistently when the dosage increases from 6.7 to 16 wt.%. This indicates that when the foam dosage is higher than around 5 wt.% only a small fraction of the finer air bubbles remain isolated. It would suggest that many of the bubbles tend to coalesce and form larger voids. The high volume of these larger voids could also be one of the reasons why the strength decreases dramatically when the dosage increases from 6.7 wt.% to 16 wt.%. This aspect needs to be further quantified.

The total area fraction of pores in each image is summarized in Table 7-4 and plotted in Figure 7-7. It can be seen that as the foam addition increase, the volume of large pores increases.

**Table 7-4:** Porosity measured by the IA method and the standard deviation (SD) and coefficients of variation (CV) (Each mixture had 2 samples).

Mix	Number of image	Mean porosity / %	SD	CV / %
GFC0	17	6.21	0.62	9.96
GFC1.3	19	17.25	2.24	12.97
GFC3.3	18	22.86	2.49	10.90
GFC5.0	19	33.63	1.37	4.08
GFC6.7	18	49.59	4.56	0.9
GFC10	18	53.78	3.03	5.64
GFC13	19	57.23	4.65	8.12
GFC16	16	63.72	4.09	6.41



**Figure 7-7.** Area fraction of pores in GFCs.

From Table 7-4 and Figure 7-7 it is noted that the standard deviations of the total area fraction for each specimen are <5%. The standard deviations in specimens containing >5 wt.% foam are relatively higher. This is because of the heterogeneous nature of the pore structure, and images taken from different part of the section may vary. However, their coefficients of variation are in the same range of the specimens with less foam addition. In another study of pervious concretes with pore area fraction between 20 to 30%, the IA method measured with an error of  $\pm 6\%$  (Sumanasooriya and Neithalath 2009). The error is one of the limitations of the IA, which was not indicated by Nambiar and Ramamurthy (2007).

As foam dosage increases, the pores tend to connect with each other, and seem more irregular (Figure 7-4). To quantify this feature, the shape factor of each pore is determined by the following equation:

$$SF = (\text{perimeter})^2 / 4\pi(\text{area}) \dots \dots \dots (7.5)$$

The shape factors in each mixture are averaged over a size range and plotted in Figure 7-8.

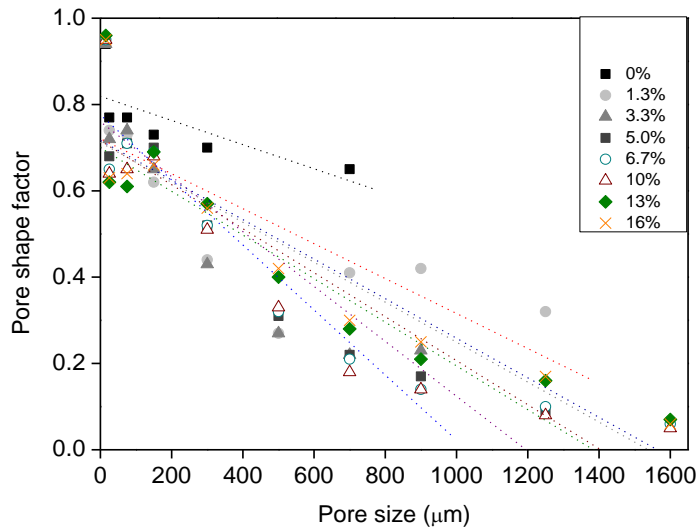


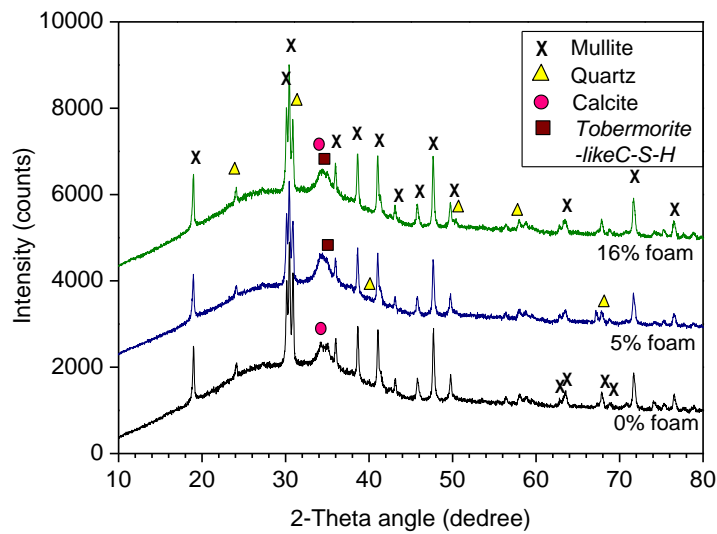
Figure 7-8. Shape factors of pores in geopolymer foams. The legend shows the dosage of foam addition.

As seen in Figure 7-8, the shape factor decreases in a roughly linear relation as function of the pore size. It is not necessary that the pore shape factor should be higher in the mixture at higher foam dosages. Nambiar and Ramamurthy (2007) suggested that the shape of pores has no influence on the properties of foam concrete, as the air voids are approximately the same shape and independent of foam volume. The effects of shape factor on the mechanical properties of geopolymer foam will not be investigated further in this research but is worthy of further consideration by future researchers.

### 7.3 Mechanical properties and pore structure

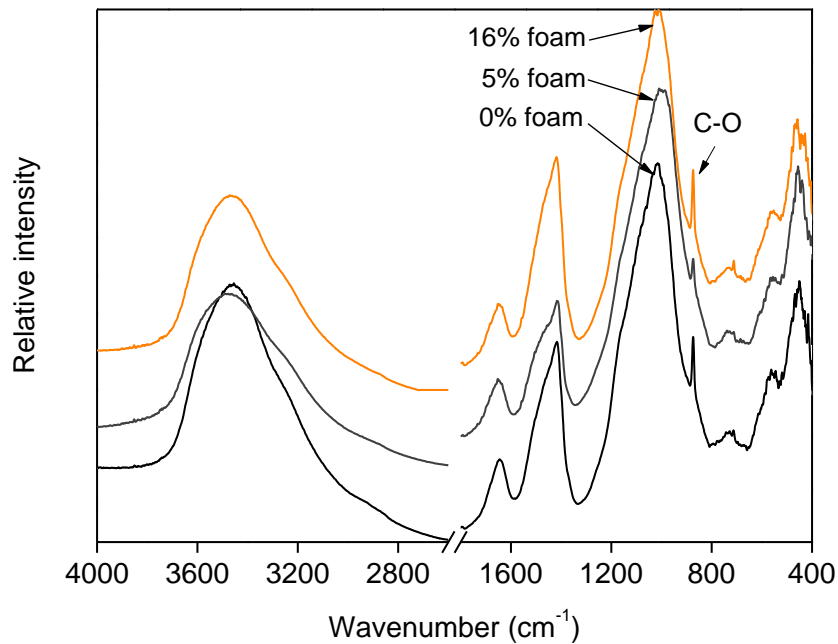
#### 7.3.1 The effects of foam addition on phases in geopolymers

Before modelling the relationship between mechanical properties and pore structure, it is important to examine the phase change in geopolymers as the foam content varies. In Figures 6-8 and 6-9 it was shown that in 100% fly ash geopolymers the mixing of 5 wt.% foam has little influence on the reaction paths and final phases of geopolymerization. Figures 7-9 and 7-10 present the XRD patterns and FTIR spectra of geopolymer foams that were manufactured in the laboratory with a blend of 70% fly ash (E) and 30% slag (see Table 7-1).



**Figure 7-9.** XRD patterns of geopolymers containing 0 to 16 wt.% of foam. Geopolymers were manufactured with a blend of 70 wt.% fly ash (E) and 30 wt.% slag.

In Figure 7-9, the broad diffraction humps indicate the major amorphous phases in the geopolymers, irrespective of the dosage of added foam. The diffraction intensities of the characteristic peaks of mullite and quartz remain nearly constant as foam dosage varies. It means the relative amounts of amorphous and crystalline phases do not change too much. One difference between the three patterns is the broad diffraction peaks that can be attributed to calcium silicate hydration products. The hydration product is a calcium silicate hydrate with low Ca/Si ratio, also described as tobermorite-like Al-substituted C-S-Hs (Ben Haha et al. 2012), as discussed in Section 6.4.2.1. The characteristic peak attributed to this C-(A)-S-H phase in solid geopolymers is relatively sharper than in these geopolymer foams. This is due to the slower evaporation of water in solid geopolymers, which provides a relatively longer hydration period for the slag. This is probably the reason that a trace amount of calcite is formed. However, in general, the differences between the three products are very small, particularly given any error in sampling and testing.



**Figure 7-10.** FTIR spectra of geopolymers containing 0 to 16 wt.% of foam. Geopolymers were manufactured with a blend of 70 wt.% fly ash and 30 wt.% slag.

In Figure 7-10, the three spectra in the region from 900 to 1200  $\text{cm}^{-1}$  that are assigned to the main stretching models of Si-O-T (T=Si and Al) structures are almost the same. Also the bending models of T-O in 400 to 800  $\text{cm}^{-1}$  are very similar. Comparing the relative absorbance intensities, the only notable difference is the bands that belong to C-O and O-H vibrations. The difference in the bands at 1430  $\text{cm}^{-1}$  and 875  $\text{cm}^{-1}$  assigned to C-O vibrations (Mozgawa and Deja 2009) is due to the different carbonation rate, as the pore structure and humidity inside are different. This difference cannot be regarded as the phase difference in geopolymer. The high absorption band at 1430  $\text{cm}^{-1}$  in the sample mixed with 16% foam may be also due to the presence of foaming agent, which is of very low concentration though (0.2% by mass of solid materials). The ultra high O-H stretching band from 3200 to 3600  $\text{cm}^{-1}$  in the spectra of solid geopolymers is due to the retained free water and bound water in C-(A)-S-Hs that has not been fully dried in sampling. In comparison, it is easier to remove free water from the porous geopolymers. In the three spectra, the O-H vibration intensities of molecular water at 1630  $\text{cm}^{-1}$  are the same, suggesting that the three hydration products contain equal amount of structural water or the mixtures have the same reaction degree.

In combination with the XRD analysis, it is reasonable to conclude that the addition of foam does not change the reaction degree or phase in the geopolymer which was formed with a blend of 70 wt.% fly ash and 30 wt.% slag as raw materials. The change of the strength of geopolymer foams is most likely due to the changed pore structure.

**7.3.2 Relationships between porosity and compressive strength and modulus of elasticity**

7.3.2.1 Relating the porosity and compressive strength

There have been many models developed (see Table 2-2) to predict the strength for foam concretes. The models are typically based on parameters used in cement based materials, such as water/cement ratio, filler/cement ratio and water/solid ratio. These parameters are not readily applicable in geopolymer manufacture, where alkaline solution/solid ratio, Na<sub>2</sub>O content and modulus of alkaline solution are more common. None of the existing models is readily applicable for geopolymer foam concretes.

The above specific parameters are important factors that determine the binder composition and property. For foam concretes with the same binder composition, foam content is the most important parameter that affects the strength and other properties via the pore features. Porosity is used as a single parameter in the basic Balshin exponential model, Ryshkevitch exponential model, Schiller logarithmic model and Hasselmann linear model to predict the strength of foam concretes (Kearsley and Wainwright 2002).

To examine the relevance of the existing models is the first step to relate porosity and compressive strength. It is noted that Ryshkevitch and Balshin models are shown to be more precise compared to other two models (Kearsley and Wainwright 2002). Table 7-5 summarizes the fitting results of those models with the data generated in this research.

**Table 7-5:** Fitting results of equations for the strength-porosity relationship of GFCs.

Model	Fitting for OPC foam concretes		Fitting for the GFCs in this research		
	Rößler and Odler (1985)	Kearsley and Wainwright (2002)	New relationship	R <sup>2</sup>	Correlation coefficient
Ryshkevitch	$f_c = 636e^{-17.04p}$	$f_c = 981e^{-7.43p}$	$y = 544.7e^{-7.52p}$	0.92	0.96
Balshin	$f_c = 540(1-p)^{14.47}$	$f_c = 321(1-p)^{3.6}$	$y = 216.7(1-p)^{3.99}$	0.90	0.95

If the correlation coefficient is considered, the two new relationships appear reasonable. They both indicate relatively strong relationships between the compressive strength and the porosity of the GFCs. Figure 7-11 plots the observed values and predicted curves by the two equations.



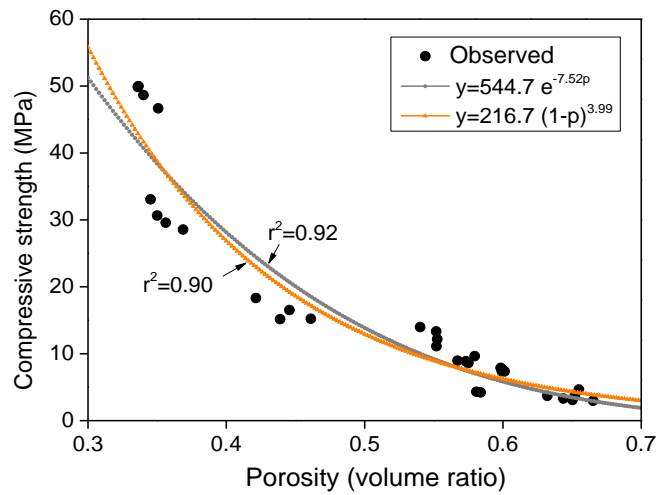


Figure 7-11. Experimental data correlation with the new relationships.

When the porosity is in the range from 0.55 to 0.7, the models fit well with the observed values. However, as porosity shifts towards lower region, the difference between predicted and observed values becomes larger, as shown in Figure 7-12.

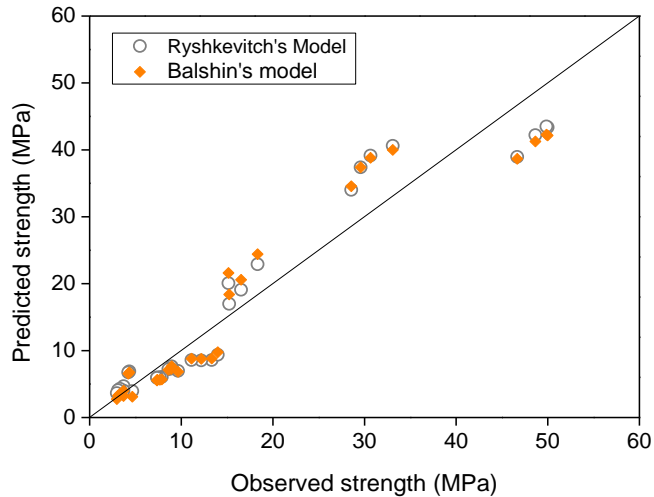


Figure 7-12. The differences between predicted values by Ryshkevitch's and Balshin's model and observed values.

The large difference in the low porosity region is expected to be due to the effects of pore size distribution on the strength being omitted in the two models. It is generally agreed that large pores or voids are more harmful to the structures than small pores in cement based materials (Neville 2011). In this research, at low porosity, there are more pores that can be ascribed to small pores (<5.6  $\mu\text{m}$ ). This can be seen by comparing the water saturation porosity

(Figure 7-4) and pore area fraction (Figure 7-7). As the pores are randomly distributed in foams, and the cross sections for image analysis are also random, the distribution by image analysis can be regarded as a 3-dimensional pore distribution. Therefore, the area fraction represents the volumetric porosity of pores >5.6 μm. This point is supported by the porosity measurements of pervious concretes (Deo and Neithalath 2010). Table 7-6 lists the volume of pores with different size ranges in the GFCs.

**Table 7-6:** Pore volumetric distribution in the GFCs (mean value of four samples for each mix).

Foam content ( wt.%)	0	1.3	3.3	5.0	6.7	10	13	16
p-Porosity by water saturation	34.1	35.3	44.1	55.2	57.3	59.9	63.2	64.8
p <sub>1</sub> -Porosity of large pores (d >5.6 μm)	6.2	17.4	22.9	34.0	49.6	53.8	57.4	63.1
p <sub>2</sub> -Porosity of small pores (d <5.6 μm)	27.9	17.9	21.2	21.2	7.7	6.1	5.8	1.7

Considering the effects of pore size, two new models based on Ryshkevitch’s and Balshin’s models were developed as follows:

**Model 1:**  $f_c = A \times e^{a \cdot p_1} + B \times e^{b \cdot p_2}$  ..... (7.6)

**Model 2:**  $f_c = C \times (1 - p_1)^c + D \times (1 - p_2)^d$  ..... (7.7)

In Model 1 and Model 2, the volume of small pores (d <5.6 μm) and the volume of large pores (d >5.6 μm) are treated separately. The empirical constants *a*, *b* in Eq. 7.6, and *c*, *d* in Eq. 7.7 indicate the relative impacts of small pores and large pores on the strength. *A*, *B*, *C* and *D* are fitting constants. The fitting results are shown in Table 7-7 and Figure 7-13.

**Table 7-7:** Fitting results of the new for the strength-porosity relationship of GFCs.

Model	Equations	R <sup>2</sup>	Correlation coefficient
Model 1	$y = 61.55e^{-4.396p_1} - 5.28e^{-280.15p_2}$	0.97	0.99
Model 2	$y = 56.11(1 - p_1)^{3.07} - 10.25(1 - p_2)^{207.50}$	0.97	0.98

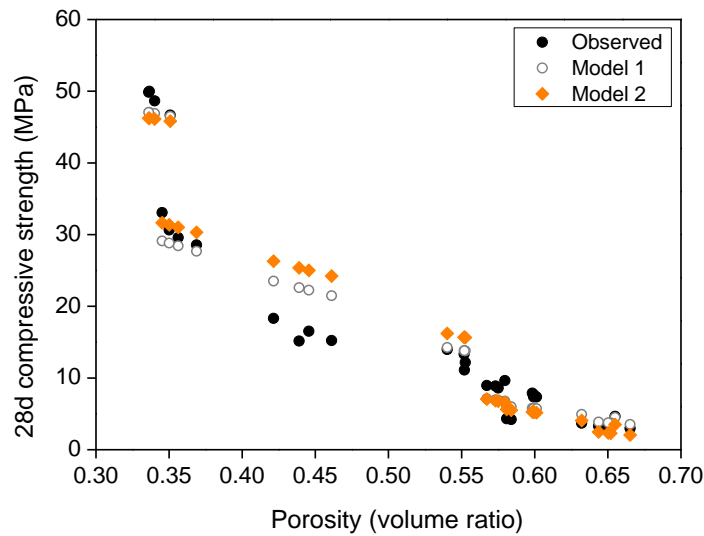


Figure 7-13. The predicted values of the Model1 and Model 2.

The correlation coefficient and  $R^2$  increase in the new models compared to the original fitted Ryshkevitch and Balshin models. It is clear that to treat different size pores separately is helpful in improving the fitting accuracy. In other words, the pores with different sizes contribute differently to the mechanical property of foam concrete. The porosity of large pores correlates with the strength very well, while the effect of small pores is very limited. It is indeed that the second parts of the two models both have very high exponents, which means that the terms of small pore contribute nearly zero to the whole equations.

Considering the effects of pore size distribution, a new model is proposed to treat the total porosity and the large pores separately. A critical diameter for the large pores is seen to be  $100 \mu\text{m}$ , as shown in Figure 7-6. This size was also selected by Schober (2011) to allocate the lower limited of air or gas pores (also regarded as macro-pores) in OPC foam concretes. In GFCs the void volumes were formed by voids  $>100 \mu\text{m}$ , by comparing the pore size frequency and volume before and after introducing the preformed foams into the binder. The proposed model is thus expressed as following:

$$\text{Model 3: } f_c = E \times e^{e p_c} + F \times e^{f p} \dots\dots\dots (7.8)$$

where,  $p_c$  is the porosity of pores larger than critical diameter ( $100 \mu\text{m}$ ),  $E$ ,  $e$ ,  $F$  and  $f$  are fitting parameters reflecting the relative influences of the large pores ( $>100 \mu\text{m}$ ) and total porosity ( $p$ ) on the strength.

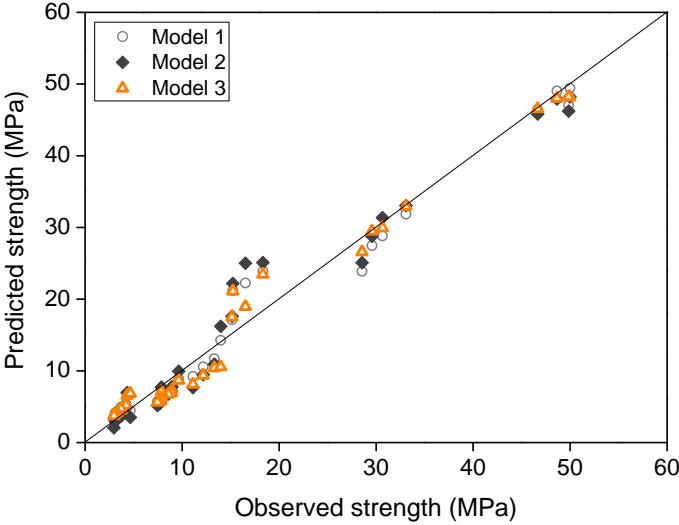
The fitting results for Model 3 are shown in Table 7-8. Using the porosity of large pores can more precisely predict the strength of GFC. The effect of total porosity decreases with the total porosity increasing as expected. It is consistent

with fact that as porosity increases the large voids become dominant. Comparing Model 3 with Model 1 and Model 2, the large pore model gives an even better fitting result, in terms of the increased  $R^2$  and correlation coefficient. Figure 7-14 shows the differences between predicted and observed values of the three models.

**Table 7-8:** Fitting results of Model 3 for the strength-porosity relationship of GFCs.

Model	Equations	R <sup>2</sup>	Correlation coefficient
Model 3-large pore model	$y=62.33e^{-4.307p_c}-6.31e^{-145.98P}$	0.98	0.99

It is again found that the second part that represents the contribution of total porosity has a very high exponent, which means that the effect of total porosity is very limited. It is worth to keep this part to obtain a precise prediction. However, for future industrial application, it is recommended to ignore the effect of total porosity while just consider the critical pores, i.e.  $y = 62.33e^{-4.307pc}$ , formally in the Ryshkevitch model but with a porosity of critical pore size.



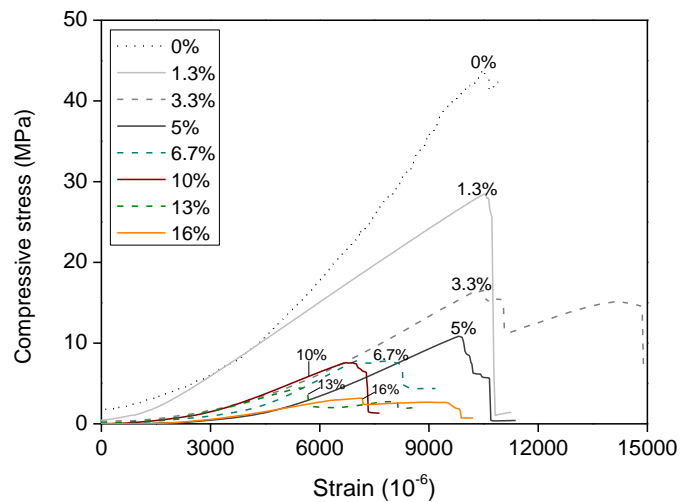
**Figure 7-14.** The differences between observed and predicted values by Model 1~3.

From the above fitting results, it is reasonable to conclude that in foamed concretes the large pores (mainly large voids) determine the compressive strength to a large extent. Due to this mechanism, two important guidelines for foam concrete synthesis can be extracted: (1) foaming agents, either used for pre-forming method or chemical mixing method, should be able to generate fine bubbles; (2) the fine air bubbles introduced into the paste should be kept stable to avoid the formation of large pores.

### 7.3.2.2 Modulus of compression elasticity

The modulus of elasticity is one of the key mechanical properties of concrete that determine the strain and creep behaviour. The relationship between strain and stress over their full range is of vital importance in structural design. To develop GFCs for structural or semi-structural applications, understanding their compression elastic modulus is an important aspect.

Figure 7-15 shows the representative strain-stress curves of the GFCs manufactured with different quantities of foam addition.



**Figure 7-15.** Representative stress-strain curves of the GFCs.

Note: the curves show the whole deformation history from the beginning of loading, rather than from a minimum stress that to fix the cylinder, as per BS 1881-121:1983 or ASTM C 469-02.

Compared to the typical stress-strain curves of solid OPC concrete (Neville 2011) and geopolymer concretes (Hardjito et al. 2005), the geopolymer binder (0%) exhibits much higher strain under the same compression loading. This is because of the absence of aggregates in the binder. In comparison with foamed OPC concrete (Mydin and Wang 2012), the GFC at a similar density also shows higher strain. More importantly, the deformation under loading is more linear as shown by the stress-strain curves, which means that they are in elastic state below maximum loading.

Table 7-9 summarises the average compression modulus of elasticity of geopolymer foams. The average values are calculated in the range of 20 to 60% of maximum stress and are based on four samples of each mix.

**Table 7-9:** Compression modulus of elasticity of GFCs (mean value of 4 samples of each mix).

Foam content (%)	0	1.3	3.3	5	6.7	10	13	16
Average (GPa)	5.4	3.2	2.3	2.1	2.0	1.5	1.1	0.7

The modulus of elasticity decreases with an increase in the foam content or porosity. Several models have been developed to correlate the modulus of elasticity with compressive strength for aerated concretes (Narayanan and Ramamurthy 2000). Two general forms of the models are shown below:

$$E_c = a \cdot f_c^b \dots\dots\dots (7.9)$$

$$E_c = a \cdot \rho \cdot f_c^{0.5} \dots\dots\dots (7.10)$$

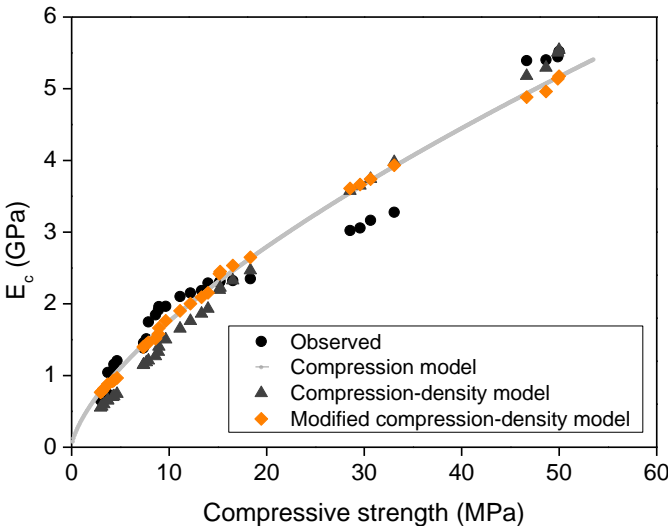
in which, *a*, and *b* are fitting constants,  $\rho$  is density (usually oven-dried density, kg/m<sup>3</sup>), *f<sub>c</sub>* is compressive strength, MPa.

Eq. 7.9 uses the compressive strength as the sole independent parameter. Eq. 7.10 is recommended by the CEB manual of design and technology (1978) for autoclaved aerated concrete, where the constant *a* usually ranges from 1.5 to 2.0. A model that can be regarded as a modified CEB model has been developed to describe the modulus of elasticity of EPS lightweight concretes (Saradhibabu et al. 2005):

$$E_c = a \cdot \rho^b \cdot f_c^c \dots\dots\dots (7.11)$$

in which, *a* varies from 0.043 to 1.146, *b* ranges from 1.1 to 1.53 and *c* usually equals to 0.25 or 0.5 according to different systems (Saradhibabu et al. 2005).

To obtain the relationship between the compressive strength and density and the modulus of elasticity of geopolymer foam concretes, the three models are all examined by fitting with observed data, as shown in Figure 7-16.



**Figure 7-16.** The relationship between the modulus of the GFCs and compressive strength.

**Table 7-10:** The fitting results of models predicting modulus of elasticity.

Model	Equations	R <sup>2</sup>	Correlation coefficient
Compression model	$E_c=0.3743 \cdot f_c^{0.671}$	0.95	0.98
Compression-density model	$E_c=0.561 \times 10^{-3} \cdot \rho \cdot f_c^{0.5}$	0.92	0.96
Modified Compression-density model	$E_c=0.902 \times 10^{-3} \cdot \rho \cdot f_c^{0.361}$	0.94	0.97

In general, the three models all give acceptable predicting capabilities over the testing range. The compression model with the compressive strength as the sole variable has the best fitting result, in terms of the highest R<sup>2</sup>.

However, it is observed that the compression model and modified compression-density model underestimate the modulus at high strength, while the compression-density model underestimate at low strength. Therefore, it is more precise if different models are used at different strength ranges:

$$E_c = \begin{cases} 0.3743 \cdot f_c^{0.671} & f_c \leq 25 \text{ MPa}; \dots\dots\dots (7.12) \\ 0.561 \times 10^{-3} \cdot \rho \cdot f_c^{0.5} & f_c \geq 25 \text{ Mpa} \dots\dots\dots (7.13) \end{cases}$$

The breaks of 25 MPa were selected based on the experimental results in this research (Figure 7-16) and the models could be separated at a different point within 20-30 MPa.

### 7.3.2.3 Validation of the mechanical property models

To validate the above proposed mechanical property models for geopolymer foam concretes, four more batches are fabricated and tested. The mixing composition is shown in Table 7-11.

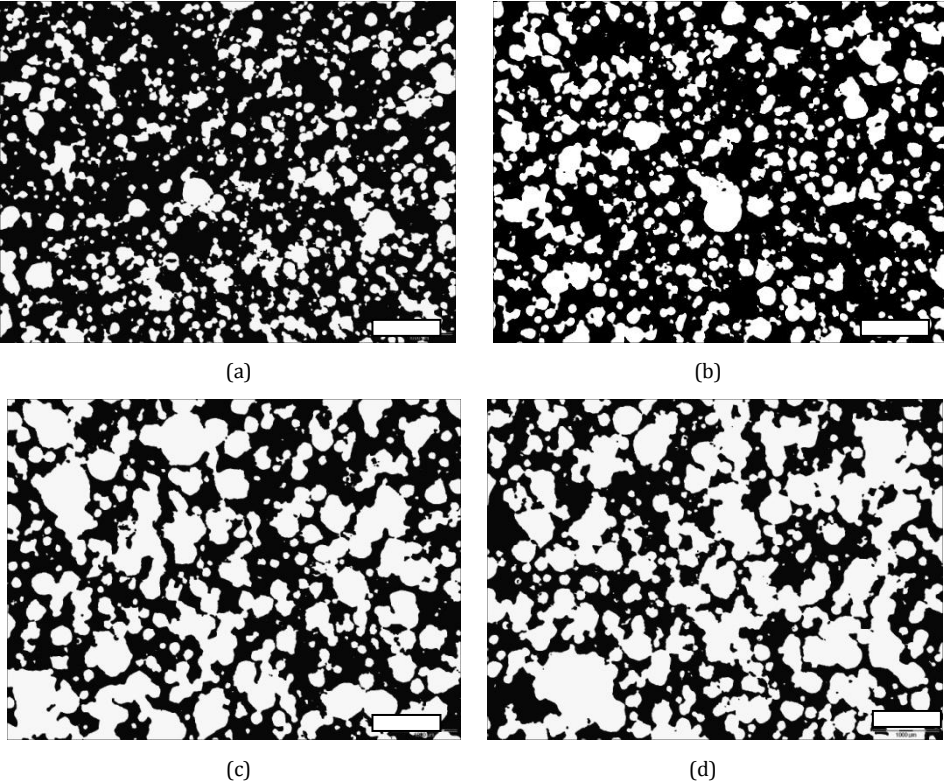
**Table 7-11:** Composition of GFCs with varied foam size and content.

Mix	Fly ash E/g	Slag/g	NaOH(12M)/g	LSS/g	H <sub>2</sub> O/g	Big foam /g	Fine foam/g
GFC'3.3	700	300	154.6	240	80	23.3	10
GFC'5.0	700	300	154.6	240	60	16.7	33.3
GFC'10	700	300	154.6	240	30	50	50
GFC'15	700	300	154.6	240	0	50	100

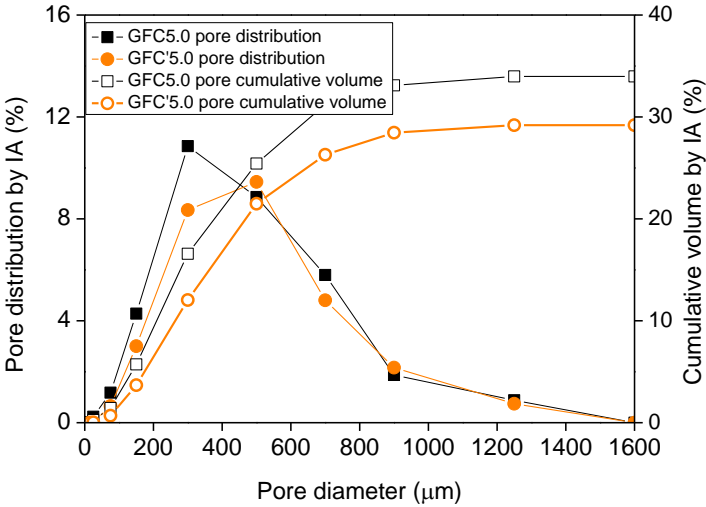
The difference between these four mixtures and those listed in Table 7-1 lies in the foam size. The *big foam* used here refers to the foam that has been allowed to set for 5 min after being generated while the *fine foam* is the foam mixed immediately after being generated. It was observed that air bubbles become larger and larger due to coalesce during setting in a container. Therefore, by changing the foam setting time, it is possible to adjust the sizes of air bubbles, and thus design the pore structure of GFCs. However, it does not mean that this method is able to precisely control the pore size in the hardened products, as the air bubbles also change (break and coalesce) during mixing and setting of

the paste. The pore structures of the four GFCs as determined by IA are shown in Figure 7-17.

It was observed that the foam that was allowed to set for 5 min suffered a loss of large pores because the air bubble walls were so thin that the bubbles collapsed during mixing. The consequence was that the hardened samples contained less large pores and lower porosity than in the fine foams, see Figure 7-18.



**Figure 7-17.** Typical IA images of GFCs with 3.3 wt% (a), 5 wt% (b), and 10 wt% (c) and 15 wt% foam addition. The scale bar is 1 mm.



**Figure 7-18.** The pore size distribution and pore volume fraction of in the GFC5.0 and GFC'5.0.



The oven-dried density, porosity and pore structure features of the four batches of GFCs were analyzed using the same procedures as described in the above sections. The compressive strength and modulus were predicted by the models and were determined by mechanical testing. The predicted and measured results are shown in Table 7-12. The two models are able to predict the strength and modulus within an average error of 15%.

**Table 7-12:** Validation of the mechanical property models (each mix has  $\geq 4$  samples).

Mix	Oven-dried density	Porosity <sup>a</sup>		Compressive strength (MPa)		Modulus of elasticity (GPa)	
		Water saturation	Pores >100 $\mu\text{m}$	Predicted (byModel3)	Measured	Predicted <sup>b</sup>	Measured
GFC'3.3	1107	0.40	0.27	19.7	16.2	2.8	2.6
GFC'5.0	944	0.50	0.347	15.5	11.9	2.4	2.0
GFC'10	805	0.56	0.51	7.0	7.6	1.4	1.4
GFC'15	684	0.63	0.60	4.7	4.5	1.0	0.9

a: The porosity is an average value, so the predicted compressive strength and modulus are actually average values. b: The predicted values of modulus of elasticity are based on the predicted strength values.

The over-estimation of the strength and modulus at high density is believed to be due to a strength loss in the binder. When large bubbles collapse during mixing, the foaming solution acts as part of the activator liquid. As a result, the volume and size of gel pores increase. Figure 7-18 shows that the pore size distribution has shifted toward a larger region in GFC'5.0. Therefore, the models need to be modified by adding the parameters of pore size distribution to gain a more precise prediction. However, as indicated by the average error (15%), the two models are both considered as effective.

## ***7.4 Modelling of the thermal insulation property of GFCs***

### **7.4.1 Thermal conductivity measurement**

Good thermal insulation is another attractive property for foam concretes, in addition to the lightweight and acceptable mechanical properties. The most widely used parameter to quantify thermal insulation property is thermal conductivity, which is defined as a material's ability to conduct heat. The thermal conductivity predicts the rate of energy loss (in watts, W) through a material, mathematically multiplied by a temperature difference (in kelvin, K) and area (in square meter,  $\text{m}^2$ ) and divided by thickness (in meters, m). For the insulating construction materials, the lower thermal conductivity, the better their thermal insulation. It means that the building needs less energy for cooling in summer or heating in winter.

There are a number of ways to measure thermal conductivity, depending on the thermal properties and the medium temperature. In this study, the measurement of thermal conductivity of GFCs was performed using the transient plane source (TPS) technique. The advantage of this technique is the

ability to move quickly undertake measurements compared to steady-state techniques, which usually need a well-engineered experimental setup and need a certain period to reach a steady state at a given temperature. The theoretical considerations of TPS method and its principles in determining have been summarized and discussed by Gustafsson (1991) and He (1995).

Table 7-13 lists the thermal conductivity of GFCs measured in this project (the detailed experimental conditions are described in Section 3.4.3.2). In general, the thermal conductivity of GFCs decreases with increasing of foam content.

**Table 7-13:** Thermal conductivity of GFCs (mean of 4 values).

Foam content (wt.%)	0	1.3	3.3	5.0	6.7	10	13	16
Conductivity (W/(m·K))	0.479	0.325	0.314	0.239	0.217	0.187	0.162	0.152
	±0.012	±0.003	±0.008	±0.009	±0.008	±0.005	±0.004	±0.002


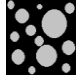
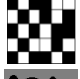


The thermal conductivity of GFCs in the current study is in the same range of the geopolymer foams derived from metakaolin with Al powder as foaming agent (Kamseu et al. 2011). In comparison with the OPC foam concretes as shown in Figure 2-2, the GFCs have a similar thermal conductivity as OPC foam concretes in the dry density range from 500 to 1200 kg/m<sup>3</sup>. The geopolymer binder GFC0 has a thermal conductivity of 0.479 W/(m·K), which is in the measured range of OPC foam concrete with the same dry density (Figure 2-2), regardless of the foaming methods. These results suggest that GFCs have similar thermal insulation properties as OPC foam concretes, as a function of density, if the thermal conductivity is regarded as index.

## 7.4.2 The relationship of thermal conductivity with porosity and density

### 7.4.2.1 Re-consideration of the classic models for the prediction of the thermal conductivity of foam concretes

The measured thermal conductivity of a heterogeneous or composite material is a complex function of the continuous phase and the dispersed phase. Numerous modelling approaches for predicting the thermal conductivity of heterogeneous material have been proposed, either purely empirical or theoretically based on physical models (Behrens 1968; Progelhof et al. 1976; Bauer 1993; Gonzo 2002). For two-phase materials with simple physical structures, the effective thermal conductivity can be modelled using five fundamental structural models, which have been summarised in Table 7-14.

**Table 7-14:** The five fundamental structure effective thermal conductivity models for two phase materials (Carson et al. 2005; Wang et al. 2008). In the formulas,  $v$  and  $k$  are their phase volume ratio and thermal conductivity, respectively.

Model	$K_e =$	Structure
Parallel	$(1-v_2)k_1 + v_2k_2$	
ME1	$k_1 (2k_1+k_2-2(k_1-k_2)v_2)/(2k_1+k_2+(k_1-k_2)v_2)$	
EMT	$\frac{3}{4}((3v_2-1)k_2+[3(1-v_2)-1]k_1+((3v_2-1)k_2+[3(1-v_2)-1]k_1)^2+8k_1k_2)^{0.5})$	
ME2	$k_2 (2k_2+k_1-2(k_2-k_1)(1-v_2))/(2k_2+k_1+(k_2-k_1)(1-v_2))$	
Series model	$1/((1-v_2)/k_1+v_2/k_2)$	

To predict the effective thermal conductivity of geopolymer foams as a whole structure, it needs the real thermal conductivity of the geopolymer binder. However, the geopolymer binder itself is heterogeneous. As shown in Figure 4-11 and Figure 6-11, the binder consists of a considerable amount of residual fly ash particles and micro size pores. Moreover, there will be residual slag particles embedded in the geopolymeric gels when slag is used as setting accelerator and strengthening admixture. It is difficult to obtain the ‘real’ thermal conductivity of geopolymer because “it is impossible to synthesize fully dense geopolymer gel” (Duxson et al. 2006a). The thermal conductivity of geopolymer binder can only be obtained by theoretical deduction with the measured values of geopolymer binders under certain assumed conditions.

According to the theoretical depiction by Carson et al. (2005), “the heat conduction pathway is dependent on whether the thermal conductivity of the dispersed phase is higher or lower than the thermal conductivity of the continuous phase: if  $k_{cont} > k_{disp}$  the heat flow essentially avoids the dispersed phase; if  $k_{cont} < k_{disp}$  the heat flow involves the dispersed phase as much as possible”. If consider the geopolymeric gels has a higher thermal conductivity than hollow fly ash particles and pores, which is probably true, the heat flow essentially avoids the hollow residual fly ash particles and micro size pores. In contrast, if the residual slag particles and solid fly ash particles have higher conductivity than gels, the heat flow will involve the embedded solid slag and fly ash particles as much as possible. Here it is not possible to give a direct comparison of the thermal conductivity between these phases without experimental work. However, it is reasonable to treat the geopolymeric gels including the residual phases as a whole while the pores as another phase with lower thermal conductivity, supposing that the pores are fully dried (no moisture in pores).

If it is assumed that the temperature distribution caused by individual inclusions can be averaged over a sufficiently large volume, it is most likely suitable to use the EMT (Table 7-14) model for the geopolymer binder. It treats geopolymer binder as a uniform temperature distributor. The ‘average’ thermal

conductivity of geopolymer binder can be approximated by Eq. 7.14, which is derived from the equation of EMT model:

$$k_b = 3k_m \cdot (1 - P(k_a - k_m)(1 - P)^{-1}(k_a + 2k_m)^{-1})^{-1} - 2k_m \dots \dots \dots (7.14)$$

in which  $k_b$  is the ‘average’ thermal conductivity of geopolymer binder,  $k_m$  is the measured value of solid geopolymer paste GFC0, and  $k_a$  is the thermal conductivity of air in pores.

Assuming that the humidity inside of pores is zero, which is probably hard to reach, and the thermal conductivity of air to be 0.024 W/(m·K) and using the measured value  $k_m = 0.469$  W/(m·K), Eq.7.14 yields  $k_b = 0.91$  W/(m·K). Table 7-15 lists the calculated thermal conductivities of geopolymers in this research and by other researchers (Duxson et al. 2006a; Kamseu et al. 2011).

**Table 7-15:** Calculated theoretical thermal conductivity of geopolymeric gels.

Mix	Raw materials	Si/Al	Alkali type	Thermal conductivity/ W/(m·K)
Current research	Fly ash	2.6	Na	0.91
Duxson et al. (2006a)	Metakaolin	2.15	Na	1.15
Kamseu et al. (2011)	Metakaolin	2.42	K+Na	0.98

The value obtained in this research is very close to the calculated value of the Na-based geopolymers (Duxson et al. 2006a), particularly given the overall Si/Al ratio in GFC0 is 2.6. This is despite the fact that the raw materials for geopolymer synthesis and the Si/Al ratio and nanostructure are different. It is also close to the values calculated using the reported results by Kamseu et al. (2011). Therefore, it appears reasonable to use this ‘average’ conductivity as  $k_2$  in the existing models for predicting the thermal conductivity of geopolymer foams.

Figure 7-19 shows the predicted results for the five classic simplified models. It is evident that the EMT model fits well with the observed results ( $R^2=0.94$ ). In comparison, the parallel and ME1 models overestimate the thermal conductivity while the ME2 and series models underestimate. The results further indicate that heat transfer follows the EMT model, which means that the temperature distribution within GFCs could be approximated by a material having a uniform temperature distribution and thermal conductivity.

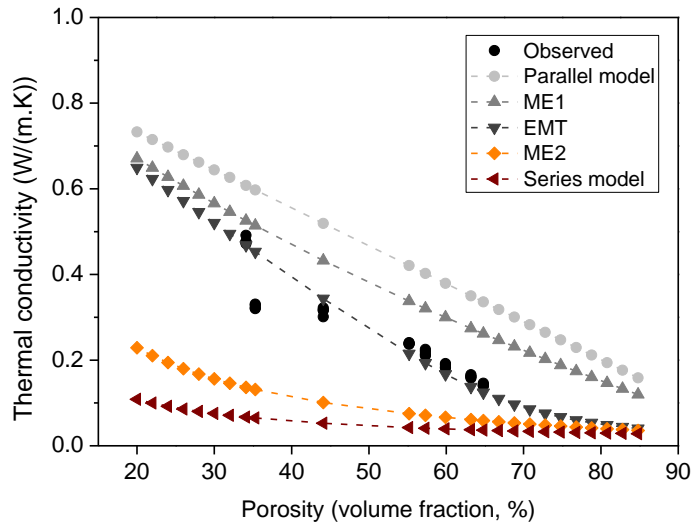


Figure 7-19. The predicting results for the five classic simplified models.

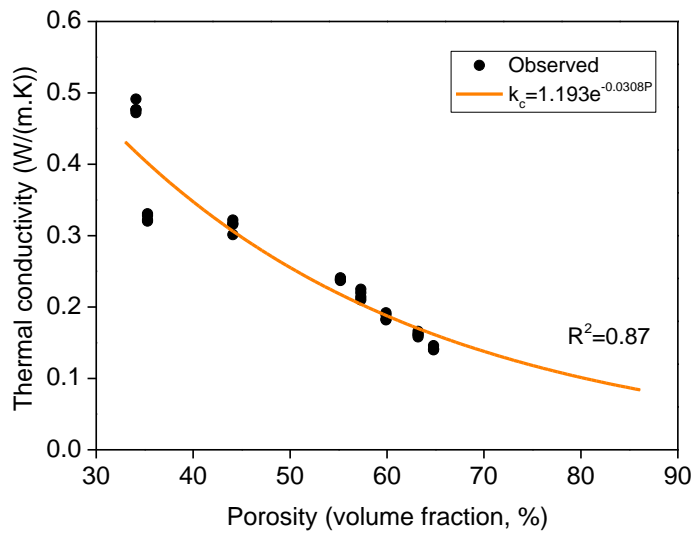
#### 7.4.2.2 The relationship of thermal conductivity and porosity

Kamseu et al. (2011) developed a mathematical model to relate the thermal conductivity of metakaolin-based geopolymer foams as a function of porosity:

$$k_c = a \cdot e^{-b \cdot P} \dots\dots\dots (7.15)$$

in which,  $a$  and  $b$  are fitting parameters,  $P$  is the porosity as determined by MIP in volume fraction of pores, %.

However, in this study, the MIP was only adopted to analyse the relatively strong foams (Figure 7-1). Using the porosity determined by the water saturation method could be an alternative way. Figure 7-20 shows the fitting results for this type of model, which provides an acceptable predicting capability.



**Figure 7-20.** The relationship between the porosity and thermal conductivity of GFCs.

### 7.3.2.3 Relating the thermal conductivity and density

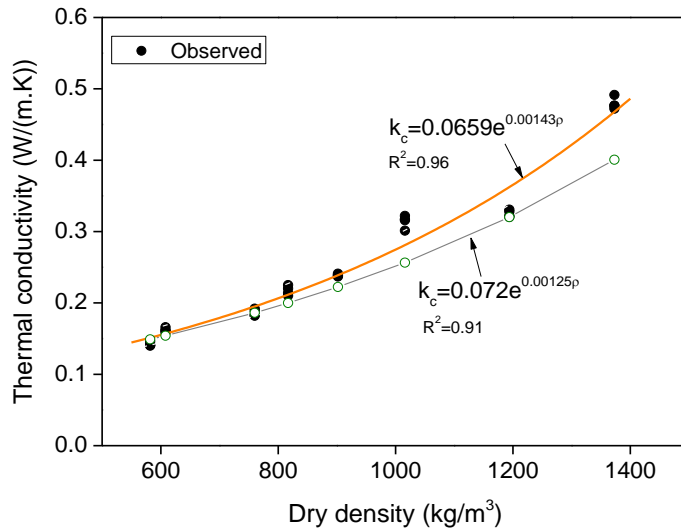
Valore (1980) plotted oven-dry density of concrete as a function of the logarithm of thermal conductivity, developing the model below:

$$k_c = 0.072 \cdot e^{0.00125\rho} \dots\dots\dots (7.16)$$

in which  $k_c$  is thermal conductivity, W/(m·K);  $\rho$  is the dry density, kg/m<sup>3</sup>.

For the neat cement paste and foam concretes, this model fits very well with the experimental results over a density range from 320 to 1600 kg/m<sup>3</sup>; however, the error is relatively large outside this range, particularly when different fillers or aggregates are used (ACI 122R-02).

To correlate the thermal conductivity of GFCs with their density, a mathematical model with a similar format to Valore’s model (Eq. 7.16) is shown in Figure 7-21:



**Figure 7-21.** The relationship between the density and thermal conductivity of GFCs.

The fitting results demonstrate that, in general, for this research, the new model correlates the thermal conductivity with density better than the original Valore's model.

#### 7.4.2.3 Validation of the thermal conductivity models

The thermal conductivities of the four samples GFC'3.3, GFC'5.0, GFC'10 and GFC'15 are listed in Table 7-16, as determined using the TPS method.

**Table 7-16:** Validation of the thermal conductivity models.

Mix	$\rho$ -Dry density/ kg/m <sup>3</sup>	P-Water saturation porosity/ %	Measured/ W/(m·K)	EMT	$k_c = 1.193 \cdot e^{-0.0308P}$	
					W/(m·K)	
GFC'3.3	1107	40.19	0.36	0.39	0.35	0.32
GFC'5.0	944	49.58	0.27	0.28	0.26	0.25
GFC'10	805	55.65	0.20	0.21	0.21	0.21
GFC'15	684	62.82	0.17	0.14	0.17	0.17

The validation results show that the EMT model fits well at the low porosity range but with a large difference for GFC'15, which has an average porosity of 62.8%. This is because of the effects of the large pores in the materials. As discussed above, EMT model regards the pores to be so fine that they will not affect the temperature distribution. However, when the porosity reaches a certain value, for example, in GFC'15, the effects of the large pores becomes so significant that they cannot be ignored. It seems more suitable to describe the materials as a 'co-continuous' structure between the ME1 structure and the

EMT structure at large porosity region (Wang et al. 2008). In conclusion, the two simple mathematical models obtained by fitting the measured conductivity with porosity and dry density both show a relatively accurate prediction.

### ***7.5 Concluding remarks***

The pore features in GFCs manufactured in the laboratory with a range of foam additions were examined using mercury intrusion porosimetry (MIP), water saturation and conventional image analysis (IA). The porosity, pore size distribution, and pore shape were obtained and that information was used to understand and build new relationships for mechanical and thermal insulation properties. Methodologically, the IA method provides a more suitable approach to obtain the information of large pores, which are more critical in affecting the strength of GFC.

The density of GFCs decreases exponentially with foam content. The relationship between porosity and the mixed foam volume indicates that many of the air bubbles are destroyed during mixing. The liquid due to the broken bubbles has very limited effect on geopolymerization pathways for the GFCs in the range studied. In addition, as foam increases, the pore shape factors in different foams are in the same range as a function of pore size, which means that the pore shape is not a significant factor for the structure.

The pore size distribution in GFC affects the compressive strength to a large extent, particularly at high porosity. The analysis of the Ryshkevitch and Balshin models and their modified variants, which consider small pores and large pores separately, demonstrated that the large pores have a significant effect on the compressive strength. Based on this, a new model was developed, called the “large void model”, which treats the porosity of critical size pores ( $>100\ \mu\text{m}$ ) and total porosity separately. A simple compression-modulus model and a compression-density-modulus model are recommended for predicting the compression modulus elasticity at low strength ( $f_c < 25\ \text{MPa}$ ) and high strength ( $f_c > 25\ \text{MPa}$ ) respectively.

The modelling of the thermal conductivity reveals that heat transfer follows the EMT model, the temperature distribution within GFCs, can be approximated by a material having a uniform temperature distribution and thermal conductivity. Geopolymer foams can be treated as a “continuous” porous material. However, at high porosity, for example,  $>60\ \text{vol.}\%$ , the large pores make the foam behave more like the ME1 model. Two mathematical models relating the measured conductivity with porosity and dry density were successfully developed.



## Chapter 8: Conclusions and Recommendations

### 8.1 Conclusions

The aim of this thesis was to develop the geopolymer foam concretes (GFCs) by alkali-activation of fly ash and the foam concrete technique. The research works included understanding fly ash physics and chemistry and their effects on the geopolymerization reactivity, the effects of fly ash features on the GFC manufacture and the relationship between the pore structure of the GFCs and their mechanical and thermal properties.

The first key outcome of this research was the discovery of the relationship between the fly ash reactivity of geopolymerization and its particle surface and glass chemistry. Based on this work, a comprehensive index was formulated, which was proven to be useful in evaluating the reactivity of fly ashes, which may be not only applicable to fly ashes. The second key outcome was the discovery of the importance of fly ash particle physics in GFCs manufacture, which answered a set of questions concerning which fly ash is most suitable and why.

In Chapter 4, five Class F coal fly ashes denoted as A, B, C, D and E sourced from power stations around Australia were selected for a series of characterisations, including particle morphology and size, surface area, particle density and residual carbon in each fly ash sample. The five fly ashes exhibited substantially different physical properties. The inter-particle volume of fly ash particles was found to determine the liquid requirement, which further affected the porosity of hardened binders. By examining the compressive strengths of the solid geopolymer binders derived from the five fly ashes, fly ash A exhibited the highest reactivity while fly ash E was the most inactive.

By analysing the porosities and phases in the geopolymer binders, it was found that the extremely low strength of binder E resulted from the higher porosity, the higher volume of large pores and the relatively less gels. The former two factors were due to its relatively higher liquid requirement (related to the particle physical properties), while the last factor was due the lower reaction extent of fly ash under the activation conditions. This was related to the lower reactivity of fly ash E, in particular the lower concentration of network-modifying cations in its glassy phases.

In Chapter 5, the fly ash glass chemistry was investigated by quantifying the glassy phase, compositions and mineral components in each sample. With the understanding of the roles of the alkali and alkali earth metals (Na, K, Mg and Ca), the Fe cations and the Ti cations in aluminosilicate glasses, in combination with the effects of surface area of fly ash on its 'apparent reactivity' as indicated by the compressive strength, an reactivity index was built up for evaluating the fly ash reactivity under geopolymerization conditions. The reactivity index took the concentration of 5-coordinated iron cations ( $[^5]\text{Fe}^{2+}$  and  $[^5]\text{Fe}^{3+}$ ) as glass network modifiers, in addition to  $\text{Na}^+$ ,  $\text{K}^+$ ,  $\text{Mg}^{2+}$  and  $\text{Ca}^{2+}$ . The reactivity index perfectly explained the reactivity order of the fly ashes studied and some other fly ashes reported by other researchers.

To verify the proposed reactivity index, a series of dissolution experiments on fly ashes A, B and E were conducted under different liquid/solid conditions. The dissolution experiments confirmed that mullite and quartz phases present in fly ash were much less reactive than glassy phases but also suffered attack, particularly for the 'impure' crystals. A certain concentration of soluble silicate in the alkaline solution improved the dissolution rate. This means that it is beneficial to use silicate containing activators for geopolymer manufacture. The early dissolution at the stage when the rate was controlled by the glass network dissolution was very important in determining the total reaction extent of fly ash under geopolymerization conditions. The dissolution results supported the reactivity index from the perspective of reaction extent of the fly ashes.

Chapter 6 investigated the suitability of the selected five fly ashes for GFCs manufacture by development of a wide range of trial mixtures, based on the understanding of fly ash physics and chemistry. It was shown that the particle density and morphology played more important roles in affecting the stability of fresh foamed pastes and the compressive strength than the fly ash chemistry. The foamed pastes derived from fly ashes A, C and D that had higher densities and lower inter-particle volumes had higher workability than foamed pastes B and E. The higher workability of the foamed pastes A, C and D also allowed the air bubbles to move and coalesce more easily. The large pore size distribution in their hardened concretes was the main factor causing their relatively lower strengths. In comparison, the well distributed pores in the foam B and E and the relatively narrow size distribution appeared to be the main reasons why they possessed relatively higher strength.

This finding is very meaningful for geopolymer manufacture and the utilization of fly ash. It indicates that those fly ashes that are unsuitable for solid geopolymer manufacture due to their high liquid requirements or low reactivity may still be able to be used in GFC manufacture. For example, fly ash E is 'undesirable' for solid geopolymer manufacture because of its low reactivity; however, GFC E possesses well distributed air voids and appreciable strength. It means that GFC manufacture may bring geopolymer industry a real 'valuable use' of fly ash because it can effectively use the 'low quality' fly ashes.

Using fly ash E and its geopolymer foams, further investigations used slag to shorten the setting time and increase the compressive strength. The addition of appropriate slag (10-30 wt.%) was proven to be an effective method to compensate the drawback of low reactivity of the fly ash. The pore structure and porosity also changed significantly with the addition of slag and contributed to an increase in compressive strength.

Finally, Chapter 7 investigated the relationship between the pore structure of fly ash E-based GFCs and their mechanical and thermal insulation properties, including compressive strength, compression modulus and thermal conductivity. A series of GFCs with dry density from 1370 to 580 kg/m<sup>3</sup> and compressive strength of 48.6 MPa to 4.6 MPa were successfully manufactured at laboratory conditions.

The pore sizes, distribution and shape were investigated by image analysis (IA). The pore size distribution in geopolymer foam concrete was found to affect the

compressive strength to a large extent, particularly at high porosity. The comparison and analysis of the Ryshkevitch and Balshin models, which are two classic models relating strength and porosity for normal concrete, and their modified variants considering small pores and large pores separately, demonstrated that the large pores played a determining role in affecting the compressive strength. Based on the calculated results, a new model was developed, called 'large void model', which treated the porosity of critical size pores >100 mm and total porosity separately. This model had the best fitting results and was proven to have fairly good predicting capability. A simple compression-modulus model and a compression-density-modulus model were recommended for predicting the compression modulus elasticity.

The modelling of the thermal conductivity revealed that heat transfer followed the EMT model, where the temperature distribution within geopolymer foam concretes is uniform. Two mathematical models by fitting the measured conductivity with porosity and dry density both showed acceptable prediction capabilities. Based on the fitting and modelling results, two important guidelines for GFC manufacture were extracted: (1) foaming agents should be able to generate fine bubbles; and (2) the fine air bubbles introduced into the paste should be stable to avoid the formation of large pores.

## ***8.2 Current issues in the development and applications of GFCs***

This research successfully manufactured a series of fly ash-based GFCs with a wide range of densities and strengths under laboratory conditions. In the research two important issues were noted: the high shrinkage of GFCs and the high efflorescence potential.

### **8.2.1 Shrinkage of fly ash-based GFCs**

Foam concrete usually exhibits much higher shrinkage than normal weight concrete, as discussed in Section 2.3.2.3. In this study, the solid and foamed geopolymers with a size of Ø53×108 mm did not exhibit notable shrinkage under laboratory conditions. However, it was noted that the trial mixture of GFC panels of 150 × 200 × 850 mm that manufactured at ambient conditions showed large shrinkage, which led to cracks on the surface (Appendix A4). This problem was believed to be due to the lack of aggregates and the different curing conditions from the laboratory conditions.

The GFCs manufactured in this research did not contain any sand or other fillers. This is one of the reasons for the large shrinkage. The small cylindrical samples were cured sealedly for 24 h, followed by room temperature curing. In comparison, the relatively large panel samples were cured at ambient conditions, without any sealing or high temperature curing. The quick loss of water after casting caused large drying shrinkage before the GFCs gained high enough strength, consequently leading to the cracks on the surface.

### **8.2.2 The potential efflorescence of GFCs**

Efflorescence is the formation of white salt deposits on or near the surface of concrete. For OPC concrete, efflorescence forms due to the reaction of  $\text{Ca}(\text{OH})_2$

with water and CO<sub>2</sub>, and is generally harmless except for the discolouration. However, for geopolymers, as they contain much higher soluble alkali metal concentrations than conventional cement, efflorescence could be a significant issue when the products are exposed to humid air or in contact with water. The GFCs manufactured at laboratory conditions did not show efflorescence under ambient conditions. However, when the samples contacted water, efflorescence products appear on the surface immediately (Appendix A5). The white efflorescence products were collected and analysed by XRD and it showed that they were mainly hydrous alkali carbonate (Na<sub>2</sub>CO<sub>3</sub>·7H<sub>2</sub>O) (Appendix A6). The formation of the carbonate caused flaking of the surface. The efflorescence is harmful to the integrity of GFC structure. The GFCs seem suitable for applications under dry conditions only.

### ***8.3 Recommendations for the future research***

Based on the outcomes of the work undertaken in this research and the issues that found related to the GFCs, at least four areas need further investigations, as recommended in the following sections, before GFC manufacture can be fully controlled and to be ready in applications.

#### **8.3.1 Research of the dissolution behaviour of glass phases in fly ash**

The reactivity index proposed in this research was based on one of the assumptions that in the glass phases 'the Si-O, Al-O, Fe-O and Ti-O bonds linked with network modifiers are much weaker (more reactive) than Si-O and Al-O in Si-O-Si and Si-O-Al'. This assumption only categorised the bonds into two general classes: the strong bonds of Si-O·Si and Si-O·Al and the weak bonds of Si(Al)-O·M, where M is a network modifier. This categorisation ignored the reactivity differences of the 'weak bonds', as they were supposed to be dissolved equally at high pH conditions. This may be not the fact under the geopolymerization conditions, but this is not clear yet.

It is recommended to perform research on synthetic glasses with similar composition to the glass in fly ashes, for a better understanding of their dissolution behaviour. A more rigorous examination of the dissolution rate of synthetic Si-Al-Fe-Na-K-Ca-Mg-O glasses under different liquid/solid ratios could be the best method. This will provide a quantitative description 'how weak' of the active bonds, and based on this a more precise reactivity index may be proposed. Eventually, by establishing the dissolution kinetics, it is possible to build up a prediction model for the final composition of geopolymer gels at different activation conditions.

#### **8.3.2 Evaluation of the pore size effects on the strength of GFCs**

The relationship between the compressive strength and the porosity has shown that the pore size had significant effects on the compressive strength. The 'large void model' proposed in this research regarded the porosity into two categories: the porosity of pores that are >100 μm and the total porosity. The porosity of large pores played the main role of determining the strength and the effect of

total porosity was very limited. This model had fairly good capability of predicting the strength of the GFCs; however, it is possible to improve the predicting accuracy by considering the contribution of pores more finely. It is recommended to add influencing factors to each size range, for example, <10  $\mu\text{m}$ , 10-20  $\mu\text{m}$ , 20-30  $\mu\text{m}$ ..., to establish new models. This work is important for a better understanding of the relationship between the pore structure and the mechanical properties of foam concretes. It is also useful for the industry to select suitable foaming agents, foaming methods and optimise the rheology properties of geopolymer binders.

### **8.3.3 Research into GFC shrinkage control**

The large shrinkage of the GFCs manufactured at room temperature is one of the problems that need to be solved. Some trial experiments in this research (not shown here) conducted by the author of this thesis showed that at elevated temperatures and sealed conditions the shrinkage was much smaller. However, high temperature curing is energy-intensive. For this reason, it is recommended to carry out a series of research trials to understand the main reasons causing shrinkage at different stages, so as to solve this technical problem in practice.

From the trial experiment results and the current understanding in the literature (Wallah and Rangan 2006; Dimas et al. 2009; Chindaprasirt et al. 2011; Kuenzel et al. 2011; Vasconcelos et al. 2011), it is recommended to: (1) use a certain amount of suitable fillers to reduce the total chemical shrinkage of the gels; (2) use expansive chemical additives such as MgO to compensate partial shrinkage; (3) use water absorbent to reduce drying shrinkage at early ages after casting and (4) use alkali-resistant short fibres to increase the long-term volume stability of GFCs. The selection of fillers, chemical additives and fibres should be based on a chemical level understanding, and the achievement of their optimal dosages needs systematic investigations.

### **8.3.4 Research into GFC efflorescence control**

Efflorescence occurred quickly on the surface when the GFCs contacted with water at the bottom. This efflorescence could be a critical challenge for geopolymer applications, although its effects on mechanical and chemical stability have not yet been examined. Efflorescence is a complex function of the penetration rate of water into the geopolymer matrix, the dissolution rate of  $\text{CO}_2$  into the aqueous phase, the leaching rate of alkali and the crystallization-dissolution balance of carbonates. This is further related to the alkali type and stability, pore size and distribution in geopolymers and the chemistry of the aluminosilicate phases. It is recommended to perform fundamental research in this aspect to understand the efflorescence rate-controlling factors, so as to prevent, or at least reduce, the efflorescence rate under wet air conditions. This work is not only important for the application of GFCs but also important for the applications of solid geopolymer concretes, particularly under outdoor conditions.

## References

- Arellano Aguilar R, Burciaga Díaz O, Escalante García JI. Lightweight concretes of activated metakaolin–fly ash binders, with blast furnace slag aggregates. *Constr Build Mater* 2010; 24: 1166–75.
- Ahmaruzzaman M. A review on the utilization of fly ash. *Prog Energy Comb Sci* 2010; 36(3): 327–63.
- Akthar FK, Evans JRG. High porosity (>90%) cementitious foams. *Cem Concr Res* 2010; 40: 352–8.
- Alam J, Akhtar MN. Fly ash utilization in different sectors in Indian scenario. *Int J Emerg Trends Eng Develop* 2011; 1(1): 1–14.
- Al Bakri Abdullah MM, Hussin K, Bnhussain M, Ismail KN, Yahya Z, Razak, RA. Fly ash–based geopolymer lightweight concrete using foaming agent. *Int J Mol Sci* 2012; 13(6): 7186–98.
- Al–Jabri KS, Hago AW, Al–Nuaimi AS, Al–Saidy AH, 2005. Concrete blocks for thermal insulation in hot climate. *Cem Concr Res* 2005; 35(8): 1472–9.
- Álvarez–Ayuso E, Querol X, Plana F, Alastuey A, Morenoa N, Izquierdo M, Font O, Morenoa T, Diez S, Vázquez E, Barra M. Environmental, physical and structural characterisation of geopolymer matrixes synthesised from coal (co–)combustion fly ashes. *J Hazard Mater* 2008; 154: 175–83.
- Aparicio P, Galán E, Valdrè G, Moro D. Effect of pressure on kaolinite nanomorphology under wet and dry conditions, Correlation with other kaolinite properties. *Appl Clay Sci* 2009; 46: 202–8.
- API 10B-2. Recommended practice for testing well cements. 1<sup>st</sup> edition. *Globe Engineering Document*; 2005.
- Andini S, Cioffi R, Colangelo F, Grieco T, Montagnaro F, Santoro L. Coal fly ash as raw material for the manufacture of geopolymer–based products. *Waste Manage* 2008; 28: 416–23.
- ASTM C 796, 1997. Standard test method for foaming agents for use in producing cellular concrete using preformed foam. *ASTM International*.
- ASTM C 496/C 496M – 04, 2004. Standard test method for splitting tensile strength of cylindrical concrete specimens. *ASTM International*.
- ASTM C 495–07, 2007. Standard test method for compressive strength of lightweight insulating concrete. *ASTM International*.
- ASTM C 1446–07, 2007. Standard Test Method for measuring consistency of self–flowing castable refractories. *ASTM International*.
- ASTM C 230/C 230M–08, 2008. Standard specification for flow table for use in tests of hydraulic cement. *ASTM International*.
- Australasian (Iron & Steel) Slag Association (ASA). 2011a. Blast furnace slag cements properties, characteristics and applications (ASA– Reference Data Sheet 1).
- Australasian (Iron & Steel) Slag Association (ASA). 2011b. Blast furnace slag cements properties, characteristics and applications (ASA– Reference Data Sheet 3).

- Aydın S, Baradan B. Effect of pumice and fly ash incorporation on high temperature resistance of cement based mortars. *Cem Concr Res* 2007; 37(6): 988–95.
- Bakharev T. Thermal behaviour of geopolymers prepared using class F fly ash and elevated temperature curing. *Cem Concr Res* 2006; 36:1134–47.
- Bauer TH. A general analytical approach toward the thermal conductivity of porous media. *Int J Heat Mass Transfer* 1993; 36: 4181–91.
- Bayukov OA, Anshits NN, Balaev AD, Sharonova OM, Rabchevskii EV, Petrov MI, Anshits AG. Mössbauer study of magnetic microspheres isolated from power plant fly ash. *Inorg Mater* 2005; 41(1): 50–59.
- Bazant ZP, Kaplan MF. *Concrete at High Temperatures*. Longman, London.1996.
- Bean DL, Malone PG. Alkali-activated glassy silicate formed concrete. 1997; US Patent 5605570.
- Behrens E. Thermal conductivities of composite materials. *J Compos Mater* 1968; 2: 2–17.
- Bell JL, Kriven WM. Preparation of ceramic foams from metakaolin-based geopolymer gels. In (Hua-Tay Lin IER, Koumoto K, Kriven WM, Norton DP, Garcia E Ed.) *Developments in Strategic Materials: Ceramic Engineering and Science Proceedings*, 2008; 29(10): 97–111.
- Bell JL, Sarin P, Provis JL, Haggerty RP, Driemeyer PE, Chupas PJ, Van Deventer, JSJ, Kriven WM. Atomic structure of a cesium aluminosilicate geopolymer: A pair distribution function study. *Chem Mater* 2008a; 20(14): 4768–76.
- Bell JL, Sarin P, Driemeyer PE, Haggerty RP, Chupas PJ, Kriven W. X-ray pair distribution function analysis of a metakaolin-based,  $KAlSi_2O_6 \cdot 5.5H_2O$  inorganic polymer (geopolymer). *J Mater Chem* 2008b; 18: 5974–81.
- Ben Haha M, De Weerd K, Lothenbach B. Quantification of the degree of reaction of fly ash. *Cem Concr Res* 2010; 40: 1620–9.
- Ben Haha M, Lothenbach B, Le Saout G, Winnerfeld F. Influence of slag chemistry on the hydration of alkali-activated blast-furnace slag — Part II: Effect of  $Al_2O_3$ . *Cem Concr Res* 2012; 42: 74–83.
- Benazzouk A, Douzane O, Mezreb K, Laidoudi B, Quéneudec M. Thermal conductivity of cement composites containing rubber waste particles: Experimental study and modeling. *Constr Build Mater* 2008; 22: 573–9.
- Bentz DP, Peltz MA, Durán-Herrera A, Valdez P, Juárez CA. Thermal properties of high-volume fly ash mortars and concretes. *J Build Phys* 2011; 34(3): 263–75.
- Bernal SA, Rodríguez ED, Mejía de Gutiérrez R, Gordillo M, Provis JL. Mechanical and thermal characterisation of geopolymers based on silicate-activated metakaolin/slag blends. *J Mater Sci* 2011a; 46(16): 5477–86.
- Bernal SA, Mejía de Gutiérrez R, Pedraza AL, Provis JL, Rodríguez ED, Delvasto S. Effect of binder content on the performance of alkali-activated slag concretes. *Cem Concr Res* 2011b; 41(1): 1–8.

Bernal S, Provis JL, Rose V, Mejía de Gutiérrez, R. Evolution of binder structure in sodium silicate-activated slag-metakaolin blends. *Cem Concr Compos* 2011c; 33(1): 46-54.

Bernal SA, Mejía de Gutiérrez R, Ruiz F, Quiñones H, Provis JL. Desempeño a temperaturas altas de morteros y hormigones basados en mezclas de escoria/metacaolín activadas alcalinamente (High-temperature performance of mortars and concretes based on alkali-activated slag/metakaolin blends). *Mater Constr* 2012; 308(62): 471-88.

Bing C, Zhen W, Ning L. Experimental research on properties of high-strength foamed concrete, *J Mater Civil Eng* 2012; 24(1): 113-8.

Birch GD. Cellular cementitious composition. 2012 United States Patent. US 8,167,994 B2.

Bleszynski R, Hooton RD, Thomas MDA, Rogers CA. Durability of ternary blend concrete with silica fume and blast-furnace slag, laboratory and outdoor exposure site studies. *ACI Mater J* 2002; 99(5): 499-508.

Boldyrev VV. Mechanochemistry and mechanical activation of solids. *Russ. Chem. Rev.* 2006; 75: 177-189.

Bondar D, Lynsdale CJ, Milestone NB, Hassani N, Ramezani-pour AA. Effect of type, form and dosage of activators on strength of alkali-activated natural pozzolans. *Cem Concr Compos* 2011; 33(2): 251-60.

Brady K, Watts G, Jones MR. Specification for foamed concrete. Highways agency and TRL application guide AG 39. 2001.

Brunauer S, Emmett PH, Teller E. Adsorption of gases in multimolecular layers. *J Am Chem Soc* 1938; 60: 309-19.

Brouwers H, Van Eijk RJ. Reactivity of fly ash: extension and application of a shrinking core model. *Concr Sci Eng* 2002; 4(14): 106-13.

Bumrongjaroen W, Muller I, Schweitzer J, Livingston RA. Application of glass corrosion tests to the reactivity of fly ash. 2007 World of Coal Ash (WOCA) (Paper 146#) Northern Kentucky, USA. Available: [www.flyash.info/2007/146bumron.pdf](http://www.flyash.info/2007/146bumron.pdf). [05/06/2013]

Buchwald A, Oesterheld R, Hilbig H. Incorporation of aluminate into silicate gels and its effect on the foamability and water resistance. *J Am Ceram Soc* 2010; 93(10): 3370-6.

Bui TH. Lightweight structural concrete provided with various wood properties. 2010; U.S. Patent, 7736431B2,

Cao D, Selic E, Herbell J. Utilization of fly ash from coal-fired power plants in China. *J Zhejiang Uni Sci A*, 2008; 9(5): 681-7.

Carson JK, Lovatt SJ, Tanner DJ, Cleland A C. Thermal conductivity bounds for isotropic, porous materials. *Int J Heat Mass Transf* 2005; 48: 2150-8.

CCM - China Commodity Marketplace, 2011. Policy of China cement industry in the first year of 12th Five Year Plan. <http://www.chinaccm.com/07/0720/072001/news/20110308/161130.asp>. [2011-3-8]



CEB manual of design and technology. Autoclaved aerated concrete. The construction press. 1978.

CEMBUREAU, 2008; 2009. 2000–2008 Cement production proportion in the world (in Chinese). <http://www.okokok.com.cn/Htmls/GenCharts/080421/8484.html>. [2008–04–21] <http://www.okokok.com.cn/Htmls/GenCharts/090313/16021.html>. [2009–3–13]

Chan YN, Luo X, Sun W. Compressive strength and pore structure of high-performance concrete after exposure to high temperature up to 800°C. *Cem Concr Res* 2000; 30: 247–51.

Chen B, Liu J. Properties of lightweight expanded polystyrene concrete reinforced with steel fiber. *Cem Concr Res* 2004; 34: 1259–63.

Chen C, Gong W, Lutze W, Pegg IL, Zhai J. Kinetics of fly ash leaching in strongly alkaline solutions. *J Mater Sci* 2011; 46: 590–7.

Chindaprasirt P, Rattanasak U, Jaturapitakkul C. Utilization of fly ash blends from pulverized coal and fluidized bed combustions in geopolymeric materials. *Cem Concr Compos* 2011; 33(1): 55–60.

Choo, T. K., Song, Y., Zhang, L., Selomulya, C., & Zhang, L. (2013). Metal extraction by acid leaching of yallourn brown coal fly ash. In *Chemica 2013*, 29 Sep.-2 Oct., Brisbane, Australia. (Available: <http://www.conference.net.au/chemeca2013/papers/26746.pdf>)

Çolak A. Density and strength characteristics of foamed gypsum. *Cem Concr Compos* 2000; 22(3): 193–200.

Corinaldesi V, Moriconi G. Behaviour of cementitious mortars containing different kinds of recycled aggregate. *Constr Build Mater* 2009; 23(1): 289–94.

Cormier L, Calas G, Cuello G. (2010). Structural study of Ca-Mg and K-Mg mixing in silicate glasses by neutron diffraction. *J Non-Crystal Solid* 2010; 356: 2327-31.

Criado M, Palomo A, Fernández-Jiménez A. Alkali activation of fly ashes. Part 1: Effect of curing conditions on the carbonation of the reaction products. *Fuel* 2005; 84: 2048–54.

Criado M, Fernández-Jiménez A, De la Torre A, Aranda M, Palomo A. An XRD study of the effect of the SiO<sub>2</sub>/Na<sub>2</sub>O ratio on the alkali activation of fly ash. *Cem Concr Res* 2007b; 37(5): 671–9.

Criado M, Fernández-Jiménez A, Palomo A. Alkali activation of fly ash: Effect of the SiO<sub>2</sub>/Na<sub>2</sub>O ratio Part I: FTIR study. *Microporous Mesoporous Mater* 2007a; 106: 180–91.

Criado M, Fernández-Jiménez A, Palomo A, Sobrados I, Sanz J. Effect of the SiO<sub>2</sub>/Na<sub>2</sub>O ratio on the alkali activation of fly ash. Part II: <sup>29</sup>Si MAS-NMR Survey. *Microporous Mesoporous Mater* 2008; 109: 525–34.

Damtoft JS, Lukasik J, Herfort, Sorrentino D, Gartner EM. Sustainable development and climate change initiatives. *Cem Concr Res* 2008; 38: 115–27.

Davidovits J. *Geopolymer Chemistry and Applications*. Saint-Quentin, France, Institut Géopolymère; 2008.

- Davidovits J. Mineral polymers and methods of making them. 1982; U.S. Patent, 4 349 386.
- Davidovits J. Geopolymers: inorganic polymeric new materials. *J Therm Anal* 1991; 37: 1622–56.
- Davidovits J. 30 Years of Successes and Failures in Geopolymer Applications. Market Trends and Potential Breakthroughs. Keynote speech on Geopolymer 2002 Conference, Melbourne, Australia.
- De La Torre AG, Bruque S, Aranda M A. Rietveld quantitative amorphous content analysis. *J Appl Crystal* 2001; 34: 196–202.
- De Silva P, Sagoe-Crentsil K. Medium-term phase stability of  $\text{Na}_2\text{O}-\text{Al}_2\text{O}_3-\text{SiO}_2-\text{H}_2\text{O}$  geopolymer systems. *Cem Concr Res* 2008; 38(6): 870–6.
- Delair S, Prud'homme É, Peyratout C, Smith A, Michaud P, Eloy L, Joussein E. Durability of inorganic foam in solution: The role of alkali elements in the geopolymer network. *Corros Sci* 2012; 59: 213–21.
- Deo O, Neithalath N. 2010. Compressive behaviour of pervious concretes and a quantification of the influence of random pore structure features. *Mater Sci Eng A* 2010; 528(1): 402–12.
- Diaz-Loya EI, Allouche EN, Vaidya S. Mechanical properties of fly-ash-based geopolymer concrete. *ACI Mater J*, 2011; 108(3): 300–6.
- Diamond S. Particle morphologies in fly ash. *Cem Concr Res* 1986; 16(4): 569–79.
- Dimas D, Giannopoulou I, Papias D. Polymerization in sodium silicate solutions: a fundamental process in geopolymerization technology. *J Mater Sci* 2009; 44(14): 3719–30.
- Douglas R, El-Shamy T. Reactions of glasses with aqueous solutions. *J Am Ceram Soc* 1967; 50(1): 1–8.
- Dove P, Han N, Wallace A. Kinetics of amorphous silica dissolution and the paradox of the silica polymorphs. *Proc Nat Acad Sci USA* 2008; 105(29): 9903–8.
- Duchesne J, Duong L, Bostrom T, Frost R. Microstructure study of early in situ reaction of fly ash geopolymer observed by environmental scanning electron microscopy (ESEM). *Waste Biomass Valoriz* 2010; 1: 367–77.
- Dudas MJ, Warren CJ. Submicroscopic model of fly ash particles. *Geoderma* 1987; 40(1-2): 101–14.
- Duxson P, Lukey GC, Van Deventer JSJ. Thermal conductivity of metakaolin geopolymers used as a first approximation for determining gel interconnectivity. *Ind Eng Chem Res* 2006a; 45: 7781–8.
- Duxson P, Provis JL. Designing precursors for geopolymer cements. *J Am Ceram Soc* 2008; 91(12): 3864–9.
- Duxson P, Lukey GC, Van Deventer JSJ. Evolution of gel structure during thermal processing of Na-geopolymer gels. *Langmuir* 2006b; 22(21): 8750–7.
- Duxson P, Provis JL, Lukey GC, Mallicoat SW, Kriven WM, Van Deventer JSJ. Understanding the relationship between geopolymer composition,

microstructure and mechanical properties. *Colloids Surface A* 2005; 269(1-3): 47-58.

Duxson P, Provis JL, Lukey GC, Van Deventer JSJ. The role of inorganic polymer technology in the development of 'green concrete'. *Cem Concr Res* 2007; 37: 1590-7.

EAEP- Energy and environmental profile of the U.S. Chemical Industry. Chapter 6. The Chlor-alkali industry, Incorporated U.S. Department Of Energy Office Of Industrial Technologies. 1999; pp:175-200.

Ehrman S, Friedlander S, Zachariash M. Phase segregation in binary SiO<sub>2</sub>/TiO<sub>2</sub> and SiO<sub>2</sub>/Fe<sub>2</sub>O<sub>3</sub> nanoparticle aerosols formed in a premixed flame. *J Mater Res* 1999; 14(12): 4551-61.

Fawer M, Concannon M, Rieber W. Life cycle inventories for the production of sodium silicates. *Int J Life Cycle Ass* 1999; 4: 207-12.

Feng D, Provis JL, van Deventer JSJ. Thermal activation of albite for the synthesis of one-part mix geopolymers. *J Am Ceram Soc* 2012; 95(2): 565-72.

Fernandez NP. The influence of construction materials on life-cycle energy use and carbon dioxide emissions of medium size commercial buildings. Master degree thesis. 2008; Victoria University of Wellington.

Fernández-Jiménez A, de la Torre AG, Palomo A, López-Olmo G, Alonso MM, Arand MAG. Quantitative determination of phases in the alkali activation of fly ash. Part I. Potential ash reactivity. *Fuel* 2006a; 85: 625-34.

Fernández-Jiménez A, de la Torre AG, Palomo A, López-Olmo G, Alonso MM, Arand MAG. Quantitative determination of phases in the alkaline activation of fly ash. Part II: Degree of reaction. *Fuel* 2006b; 85: 1960-9.

Fernández-Jiménez A, Palomo A. Composition and microstructure of alkali activated fly ash binder: Effect of the activator. *Cem Concr Res* 2005; 35: 1984-92.

Fernández-Jiménez A, Palomo A, Criado M. Microstructure development of alkali-activated fly ash cement: a descriptive model. *Cem Concr Res* 2005; 35: 1204-9.

Fernández-Jiménez A, Palomo A, Pastor J, Martín A. New cementitious materials based on alkali-activated fly ash: performance at high temperatures, *J Am Ceram Soc* 2008; 91(10): 3308-14.

Fisher GL, Prentice BA, Sllberman D, Ondovl JM, Biermannl AH, Richard C, Mcfarland AR. Physical and morphological studies of size-classified coal fly ash. *Environ Sci Technol* 1978; 12(4): 447-51.

Fletcher RA, MacKenzie KJD, Nicholson CL, Shimada S. The composition range of aluminosilicate geopolymers. *J Eur Ceram Soc* 2005; 25(9): 1471-7.

Flower D, Sanjayan J. Greenhouse gas emissions due to concrete manufacture. *Int J Life Cycle Ass* 2007; 12: 282-8.

Font O, Moreno N, Querol X, Izquierdo M, Alvarez E, Diez S, Elvira J, Antenucci D, Nugteren H, Plana F, López A, Coca P, Peña FG. X-ray powder diffraction-based method for the determination of the glass content and mineralogy of coal (co)-combustion fly ashes. *Fuel* 2010; 89(10): 2971-6.

- Fouad FH. Cellular concrete. In Lamond JF and Pielert JH (Eds) *Significance of Tests and Properties of Concrete and Concrete Making Materials*. ASTM International; p: 561–9, 2006.
- Francl J, Kingery WD. Thermal conductivity: IX. Experimental investigation of effect of porosity on thermal conductivity. *J Am Ceram Soc* 1954; 37: 99–107.
- Fu K, Lu M, Zhu T, Zhang Q. Alkali activates fly ash to produce cementitious materials and its growth mechanism (in Chinese). *Multipurpose Utilization of Mineral Resources* 2007; 6: 40–3.
- Furuya K, Miyajima Y, Chiba T, Klkuchl T. Elemental characterization of particle size–density separated coal fly ash by spectrophotometry inductively coupled plasma emission spectrometry, and scanning electron microscopy–energy dispersive X-ray analysis. *Environ Sci Technol* 1987; 21(9): 898–903.
- Gallé C. Effect of drying on cement–based materials pore structure as identified by mercury intrusion porosimetry: a comparative study between oven– vacuum and freeze–drying. *Cem Concr Res* 2001; 31 (10): 1467–77.
- Garcia-Lodeiro I, Palomo A, Fernández-Jiménez A, Macphee DE. Compatibility studies between N-A-S-H and C-A-S-H gels. Study in the ternary diagram  $\text{Na}_2\text{O}-\text{CaO}-\text{Al}_2\text{O}_3-\text{SiO}_2-\text{H}_2\text{O}$ . *Cem Concr Res* 2011; 41(9): 1-9.
- Gartner EM, Macphee DE. A physico–chemical basis for novel cementitious binders. *Cem Concr Res* 2011; 41: 736–49.
- Gervais F, Blin A, Massiot D, Coutures J, Chopinet M, Naudin F. Infrared reflectivity spectroscopy of silicate glasses. *J Non Cryst Solids* 1987; 89(3): 384–401.
- Georgiades A, Ftikos Ch, Marinos J. Effect of micropore structure on autoclaved aerated concrete shrinkage. *Cem Concr Res* 1991; 21(4): 655–62.
- Ghosal S, Self S. Particle size–density relation and cenosphere content of coal fly ash. *Fuel* 1995; 74(4): 522–9
- Gomes S, Francois M. Characterisation of mullite in silicoaluminous fly ash by XRD, TEM, and  $^{29}\text{Si}$  MAS NMR. *Cem Concr Res* 2000; 30: 175–81.
- Gomes S, François M, Abdelmoula M, Refait Ph, Pellissier C, Evrard O. Characterization of magnetite in silico-aluminous fly ash by SEM, TEM, XRD, magnetic susceptibility, and Mössbauer spectroscopy. *Cem Concr Res* 1999; 29: 1705–11.
- Gonzo EE. Estimating correlations for the effective thermal conductivity of granular materials. *Chem Eng J* 2002; 90: 299–302.
- Gouny F, Fouchal F, Maillard P, Rossignol S. A geopolymer mortar for wood and earth structures. *Constr Build Mater* 2012; 36: 188–95.
- Guillot B, Sator N. A computer simulation study of natural silicate melts. Part I: Low pressure properties. *Geochim Cosmochim Acta* 2007; 71: 1249-65.
- Gustafsson SE. Transient plane source techniques for thermal conductivity and thermal diffusivity measurements of solid materials. *Rev Sci Instr* 1991; 62: 797–804.

- Hajimohammadi A, Provis JL, Van Deventer JSJ. One-part geopolymer mixes from geothermal silica and sodium aluminate. *Ind Eng Chem Res* 2008; 47(23): 9396-405.
- Hajimohammadi A, Provis JL, Van Deventer JSJ. Effect of alumina release rate on the mechanism of geopolymer gel formation. *Chem Mater* 2010; 22(18): 5199-208.
- Haque M, Langan B, Ward M. High fly ash concretes. *ACI Mater J* 1984: 54-60.
- Hardjito D, Cheak CC, Lee Ing CH. Strength and setting times of low calcium fly ash-based geopolymer mortar. *Modern Appl Sci* 2008; 2(4): 4-11.
- Hasegawa I, Sakka S, Kuroda K, Kato C. The effect of sodium ions on the distribution of silicate anions in tetramethylammonium silicate aqueous solutions, *Bull. Inst. Chem. Res. (Kyoto Univ.)* 1987, 65 (5-6): 192-196.
- He Y. Rapid thermal conductivity measurement with a hot disk sensor Part 1. Theoretical considerations. *Thermochimica Acta* 2005; 436: 122-9.
- He Y. The importance of cement grinding aids and concrete admixture in cement and concrete production (in Chinese). Available: <http://tech.sg8.cc/czzn/2010/1130/34639.html>. [2010-11-30]
- Henderson G, Fleet ME. The structure of titanium silicate glasses investigated by Si K-edge X-ray absorption spectroscopy. *J Non Cryst Solids* 1997; 211: 214-21.
- Henderson G, Liu X, Fleet M. A Ti L-edge X-ray absorption study of Ti-silicate glasses. *Physic Chem Miner* 2002; 29: 32-42.
- Heidrich C. Ash utilisation – an Australian perspective. 2003 International Ash Utilization Symposium. University of Kentucky, U.S.A. Paper #3.
- Hendriks CA, Worrell E, Jager D de, Blok K, Riemer P. Emission reduction of greenhouse gases from the cement industry. Available: <http://www.ieagreen.org.uk/prghgt42.htm>. [2004-08-23]
- Henon J, Alzina A, Absi J, Smith D, Rossignol S. Porosity control of cold consolidated geomaterial foam: Temperature effect. *Ceram Int* 2012; 38: 77-84.
- Hewlett PC. *Lea's Chemistry of Cement and Concrete*. Elsevier Science & Technology Books. 2004.
- Hoff GC. Porosity-strength consideration for cellular concrete. *Cem Concr Res* 1972; 2: 91-100.
- Hou Y, Wang D, Li Q. Effects of activator on compressive strength of fly ash-based geopolymers (in Chinese). *J Build Mater* 2007; 10(2): 214-8.
- Huang J, Liu K. Mechanical properties of cement foams in shear. *J Mater Sci* 2001; 36: 771-7.
- Hunaiti VM. Strength of composite sections with foam and lightweight aggregate concrete. *J Mater Civil Eng* 1997; 9(2): 58-61.
- Hwang JY, Sun X, Li Z. Residual carbon in fly ash for mercury adsorption: I. Separation and characterization of unburned carbon. *J Miner Mater Character Eng* 2002; 1(1): 39-60.

Iglesias E, Anderez J, Forgiarini A, Salager J-L. A new method to estimate the stability of short-life foams. *Colloid Surf A: Physicochem Eng Aspects* 1995; 98(1-2): 167-74.

Ismail I, Bernal S, Provis JL, San Nicolas R, Hamdan S, Van Deventer JSJ. Modification of phase evolution in alkali-activated blast furnace slag by the incorporation of fly ash. *Cem Concr Com*, 2014, 45: 125–35.

Jolicoeur C, To TC, Benoît É, Hill R, Zhang Z, Pagé M. Fly Ash–Carbon Effects on Concrete Air Entrainment : Fundamental Studies on their Origin and Chemical Mitigation. 2009 World of Coal Ash (WOCA) Conference (Paper 68#). Lexington, KY. Available: <http://www.flyash.info/2009/068-jolicoeur2009.pdf> [05/06/2013]

Jones MR, McCarthy A. Utilising unprocessed low–lime coal fly ash in foamed concrete. *Fuel* 2005a; 84: 1398–409.

Jones MR, McCarthy MJ, McCarthy A. Moving fly ash utilisation in concrete forward : A UK perspective. International Ash Utilization Symposium, Center for Applied Energy Research, University of Kentucky, 2003; Paper#113.

Jones MR, McCarthy A. Preliminary views on the potential of foamed concrete as a structural material. *Mag Concr Res* 2005b; 57(1): 21–31.

Jones MR, McCarthy A. Heat of hydration in foamed concrete: effect of mix constituents and plastic density. *Cem Concr Res* 2006; 36(6): 1032–41.

Just A, Middendorf B. Microstructure of high–strength foam concrete. *Mater Charact* 2009; 60: 741–8.

Juenger MCG, Winnefeld F, Provis JL, Ideker JH. Advances in alternative cementitious binders, *Cem Concr Res* 2011; 4: 1232–43.

Jumrat S, Chatveera B, Rattanadecho P. Dielectric properties and temperature profile of fly ash-based geopolymer mortar. *Int Commun Heat Mass Trans* 2011; 38: 242–8.

Just A, Middendorf B. Microstructure of high–strength foam concrete. *Mater Character* 2009; 60: 741–748.

Justnes H, Ardoullie B, Hendrix E, Sellevold EJ, van Gemert D. The chemical shrinkage of pozzolanic reaction products. 6th CANMET Conference on Fly Ash, Silica Fume, Slag, and Natural Pozzolans in Concrete, Bangkok, Thailand; 1998; ACI SP178.

Kamseu E, Ceron B, Tobias H, Leonelli E, Bignozzi MC, Muscio A, Libbra A. Insulating behaviour of metakaolin–based geopolymer materials assess with heat flux meter and laser flash techniques. *J Therm Anal Calorim* 2011; 108(3): 1189–99.

Kamseu E, Nait–Ali B, Bignozzi MC, Leonelli C, Rossignol S, Smith DS. Bulk composition and microstructure dependence of effective thermal conductivity of porous inorganic polymer cements. *J Eur Ceram Soc* 2012; 32(8): 1593–603.

Kani E, Allahverdi A, Provis JL. Efflorescence control in geopolymer binders based on natural pozzolan. *Cem Concr Compos* 2011; 34: 25–33.

Kearsley EP, Wainwright PJ. The effect of high fly ash content on the compressive strength of foamed concrete. *Cem Concr Res* 2001; 31: 105–112.

Kearsley EP, Wainwright PJ. The effect of porosity on the strength of foamed concrete. *Cem Concr Res* 2002; 32(2): 233–9.

Keertana B, Mani SS, Thenmozhi M. Utilization of Ecosand and fly ash in aerated concrete for a richest mix design. *Int J Eng Sci Tech* 2011; 3(1): 299–304.

Keyte L. What's wrong with Tarong? The importance of coal fly ash glass chemistry in inorganic polymer synthesis. PhD thesis. 2008; The University of Melbourne.

Kirschner A, Harmuth H. Investigation of geopolymer binder with respect to their application for building materials. *Ceram-Silikáty* 2004; 48(3): 117–20.

Koloušek D, Brus J, Urbanova M, Andertova J, Hulinsky V, Vorel J. Preparation, structure and hydrothermal stability of alternative (sodium silicate-free) geopolymers. *J Mater Sci* 2007; 42(22): 9267–75.

Kouassi SS, Tognonvi MT, Soro J, Rossignol S. Consolidation mechanism of materials obtained from sodium silicate solution and silica-based aggregates. *J Non Cryst Solids* 2011; 357(15): 3013–21.

Kovalchuk G, Krivenko PV. Producing fire- and heat-resistant geopolymers, in JL Provis & JSJ Van Deventer, Eds. *Geopolymers: Structure, Processing, Properties and Industrial Applications*. Woodhead, Cambridge, UK. 2009; pp: 227–66.

Kong D, Sanjayan JG, Sagoe-Crentsil K. The behaviour of geopolymer paste and concrete at elevated temperatures. In proceedings of the International Conference on Pozzolan, Concrete and Geopolymer, 24–25 May 2006, Khon Kaen, Thailand, pp: 105–19.

Kong DLY, Sanjayan JG, Sagoe-Crentsil K. Comparative performance of geopolymers made with metakaolin and fly ash after exposure to elevated temperatures. *Cem Concr Res* 2007; 37(12): 1583–9.

Kong DLY, Sanjayan JG, Sagoe-Crentsil K. Factors affecting the performance of metakaolin geopolymers exposed to elevated temperatures. *J Mater Sci* 2008; 43(3): 824–31.

Kovalchuk G, Fernández-Jiménez A, Palomo A. Alkali-activated fly ash: Effect of thermal curing conditions on mechanical and microstructural development. Part II. *Fuel* 2007; 86: 315–22.

Kovalchuk G, Krivenko PV. Producing fire- and heat-resistance geopolymers, in Provis & Van Deventer Ed. *Geopolymers: Structure, processing, properties and industrial applications*. CRC press, NW. 2009; pp:227–66.

Kreft O, Hausmann J, Hubálková J, Aneziris CG, Steaube B, Schoch T. Pore size distribution effects on the thermal conductivity of light weight autolaved aerated concrete, in 5th International Conference on Autoclaved Aerated Concrete, Bydgoszcz, Poland; 2011; pp: 257–64.

Kroehong W, Sinsiri T, Jaturapitakkul C, Chindaprasirt P. Effect of palm oil fuel ash fineness on the microstructure of blended cement paste. *Constr Build Mater* 2011; 25(11): 4095–104.

Kuenzel C, Li F, Cheeseman CR, Vandeperre L, Donatello S, Boccaccini AR. Drying shrinkage in metakaolin based geopolymers mortars, in: C. Cheeseman (Ed.)

Proceedings of the 31<sup>st</sup> Conference on Cement and Concrete Science. Imperial College London, 2011.

Kumar S, Kumar R. Mechanical activation of fly ash: Effect on reaction, structure and properties of resulting geopolymer. *Ceram Int* 2011; 37(2): 533–41.

Kumar S, Kumar R, Mehrotra SP. Influence of granulated blast furnace slag on the reaction, structure and properties of fly ash based geopolymer. *J Mater Sci* 2010; 45: 607–15.

Laperche V, Bigham J. Quantitative, chemical, and mineralogical characterization of flue gas desulfurization by-products. *J Environ Qual* 2002; 31: 979–88.

Laukaitis A, Žurauskas R, Kerienė J. The effect of foam polystyrene granules on cement composite properties. *Cem Concr Compos* 2005; 27: 41–7.

Łaźniewska-Piekarczyk B, Szwabowski J. Anti-foaming admixture (AFA) and its influences on the properties of a fresh self-compacting concrete mix. *J Civil Eng Manag* 2012; 18(2): 151–7.

Lee WKW, Van Deventer, JSJ. Structural reorganisation of class F fly ash in alkaline silicate solutions. *Colloid Surf A: Physicochem* 2002a; 211: 49–66.

Lee WKW, Van Deventer JSJ. Effects of anions on the formation of aluminosilicate gel in geopolymers. *Ind Eng Chem Res* 2002b. 41(18): 4550–8.

Lee WKW, Van Deventer JSJ. Use of infrared spectroscopy to study geopolymerization of heterogeneous amorphous aluminosilicates. *Langmuir* 2003; 19(21): 8726–34.

Lemougna PN, MacKenzie KJD, Melo UFC. Synthesis and thermal properties of inorganic polymers (geopolymers) for structural and refractory applications from volcanic ash. *Ceram Int* 2011; 37(8): 3011–8.

Lloyd RR. Accelerated aging of geopolymers, in Provis & Van Deventer Ed. *Geopolymers: Structure, processing, properties and industrial applications*. CRC press, NW. 2009. pp: 139–66.

Lloyd RR, Provis JL, Van Deventer JSJ. Microscopy and microanalysis of inorganic polymer cements. 1: remnant fly ash particles. *J Mater Sci* 2009a; 44: 608–19.

Lloyd RR, Provis JL, Van Deventer JSJ. Microscopy and microanalysis of inorganic polymer cements. 2: the gel binder. *J Mater Sci* 2009b; 44: 620–31.

Lloyd RR, Provis JL, Van Deventer JSJ. Pore solution composition and alkali diffusion in inorganic polymer cement. *Cem Concr Res* 2010; 40: 1386–92.

MacKenzie KJD, Smith ME, Rahner N, Wong A. Calcium-containing inorganic polymers as potential bioactive materials. *J Mater Sci* 2010; 45(4): 999–1007.

McLellan BC, Williams RP, Lay J, Van Riessen A, Corder GD. Costs and carbon emissions for geopolymer pastes in comparison to ordinary portland cement, *J Clean Prod* 2011; 19: 1080–90.

Mehta PK. Sustainable cements and concrete for the climate change Era—A review. In (Zachar J, Claisse P, Naik TR And Ganjian E Ed) *proceedings of second international conference on sustainable construction materials and technologies*. 2010. ISBN 978–1–4507–1490–7.



- Mehta PK, Monteiro PJM. Concrete: Microstructure, Properties and Materials, 3rd Ed. New York, McGraw-Hill; 2006.
- Merzbacher C, White WB. Structure of Na in aluminosilicate glasses: a far-infrared reflectance spectroscopic study. *Am Mineralog* 1988; 73: 1089–94.
- Midorikawa T, Pelova G, Walraven J. Application of the water layer model to self-compacting mortar with different size distributions of fine aggregate. *HERON – Concr Tech* 2009; 54(2): 73–100.
- Mostafa NY. Influence of air-cooled slag on physicochemical properties of autoclaved aerated concrete. *Cem Concr Res* 2005; 35: 1349–57.
- Mozgawa W, Deja J. Spectroscopic studies of alkaline activated slag geopolymers. *J Mol Struct* 2009; 924: 434–41.
- Mydin MAO, Wang YC. 2012. Mechanical properties of foamed concrete exposed to high temperatures. *Constr Build Mater* 2012; 26(1): 638–54.
- Myers RJ, Bernal SA, Nicolas RS, Provis JL. Generalized structural description of calcium–sodium aluminosilicate hydrate gels: The cross-linked substituted tobermorite model. *Langmuir*, 2013, 29 (17): 5294-306.
- Mysen BO, Virgo D, Scarfe CM, Cronin DJ. Viscosity and structure of iron- and aluminum-bearing calcium silicate melts at 1 atm. *Am Mineralog* 1985; 70: 487–95.
- Nair BG, Zhao Q, Cooper RF. Geopolymer matrices with improved hydrothermal corrosion resistance for high-temperature applications. *J Mater Sci* 2007; 42: 3083–91.
- Nambiar EKK, Ramamurthy K. Air-void characterisation of foam concrete. *Cem Concr Res* 2007; 37: 221–30.
- Nambiar EKK, Ramamurthy K. Influence of filler type on the properties of foam concrete. *Cem Concr Compos* 2006a; 28: 475–80.
- Nambiar EKK, Ramamurthy K. Models relating mixture composition to the density and strength of foam concrete using response surface methodology. *Cem Concr Compos* 2006b; 28: 752–60.
- Nambiar, EKK, Ramamurthy K. Shrinkage behaviour of foam concrete. *J Mater Civil Eng*, 2009; 21(11): 631–6.
- Narayanan N, Ramamurthy K. Microstructural investigations on aerated concrete. *Cem Concr Res* 2000a; 30: 457–64.
- Narayanan N, Ramamurthy K. Structure and properties of aerated concrete: a review. *Cem Concr Compos* 2000b; 22(5): 321–9.
- Neville AM. Properties of concrete (5th edition). Pearson, London, UK. 2011.
- Newman J, Owens P, Properties of lightweight concrete, in: J Newman and RS Choo (Eds) *Advanced Concrete Technology Part 3: Process*. Butterworth-Heinemann Press; 2003. p: 2/7–2/9.
- Ngu L, Wu H, Zhang D. Characterization of ash cenospheres in fly ash from Australian power stations. *Energy & Fuels* 2007; 21: 3437–45.

- Nieto P, Zanni H. Polymerization of alkaline-calcium-silicate hydrates obtained by interaction between alkali-silica solutions and calcium compounds. A  $^{29}\text{Si}$  nuclear magnetic resonance study. *J Mater Sci* 1997; 32: 3419–25.
- Nyale SM, Babajide OO, Birch GD, Böke N, Petrik LF, Synthesis and characterization of coal fly ash-based foamed geopolymer. *Proc Environ Sci* 2013; 18: 722 – 30.
- Okada K, Ooyama A, Isobe T, Kameshima Y, Nakajima A, MacKenzie KJD. Water retention properties of porous geopolymers for use in cooling applications. *J Eur Ceram Soc* 2009; 29: 1917–23.
- Olivier JGK, Janssens–Maenhout G, Peters JAHW. Trends in global CO<sub>2</sub> emissions; 2012 report. PBL Netherlands Environmental Assessment Agency, The Hague, Netherlands, 2012.
- Olympus Product, Analysis FIVE. Available [http://www.olympusaustralia.com.au /Product/Detail/399/Analysis-FIVE](http://www.olympusaustralia.com.au/Product/Detail/399/Analysis-FIVE) [available 2013-07-20]
- Othuman MA, Wang YC. Elevated-temperature thermal properties of lightweight foamed concrete. *Constr Build Mater* 2011; 25(2): 705–16.
- Pacheco-Torgal F, Abdollahnejad Z, Camões AF, Jamshidi M, Ding Y. Durability of alkali-activated binders: A clear advantage over Portland cement or an unproven issue? *Constr Build Mater* 2012; 30: 400–5.
- Pacheco-Torgal F, Moura D, Ding Y, Jalali S. Composition, strength and workability of alkali-activated metakaolin based mortars. *Constr Build Mater* 2011; 25(9):3732–45.
- Pacheco-Torgal F, Castro-Gomes J, Jalali S. Alkali-activated binders: A review. Part 2. About materials and binders manufacture. *Constr Build Mater* 2008; 22(7): 1315–22.
- Palomo A, Grutzeck MW, Blanco MT. Alkali-activated fly ashes A cement for the future. *Cem Concr Res* 1999; 29(29): 1323–9.
- Pan Z, Hiromi F, Tionghuan W. Preparation of high performance foamed concrete from cement, sand and mineral admixtures. *J Wuhan Uni Tech-Mater Sci Ed* 2007; 22(2): 295–8.
- Panias D, Giannopoulou IP, Perraki T. Effect of synthesis parameters on the mechanical properties of fly ash-based geopolymers. *Colloid Surf A: Physicochem Eng Aspect* 2007; 301: 245–54.
- Park H, Englezos P. Thermodynamic modeling of sodium aluminosilicate formation in aqueous alkaline solutions. *Ind Eng Chem Res* 1999; 38(12): 4959–65.
- Pera J, Boumaza R, Ambroise J. Development of a pozzolanic pigment from red mud. *Cem Concr Res* 1997; 27(10):1513–22.
- Piasta J, Sawicz Z, Rudzinski L. Changes in the structure of hardened cement paste due to high temperature. *Matériaux et Constructions* 1984; 17(4): 291–6.
- Pietersen H, Fraay A, Bijen J. Reactivity of fly ash at high pH. *MRS Proceed*, 1990; 178: 139–57.

- Pimraksa K, Chindaprasirt P, Rungchet A, Sagoe-Crentsil K, Sato T. Lightweight geopolymer made of highly porous siliceous materials with various  $\text{Na}_2\text{O}/\text{Al}_2\text{O}_3$  and  $\text{SiO}_2/\text{Al}_2\text{O}_3$  ratios. *Mater Sci Eng A* 2011; 528(21): 6616–23.
- Progelhof RC, Throne JL, Reutsch RR. Methods for predicting the thermal conductivity of composite systems: A review. *Polym Eng Sci* 1976; 16: 615–25.
- Provis JL. Modelling the formation of geopolymers. PhD thesis. 2006; The University of Melbourne.
- Provis JL, Harrex RM, Bernal SA, Duxson P, Van Deventer JSJ. Dilatometry of geopolymers as a means of selecting desirable fly ash sources. *J Non Cryst Solids* 2012; 358(16): 1930–7.
- Provis JL, Lukey GC, Van Deventer JSJ. Do geopolymers actually contain nanocrystalline zeolites? A reexamination of existing results. *Chem Mater* 2005; 17(12): 3075–85.
- Provis JL, Myers RJ, White CE, Rose V, Van Deventer JSJ. X-ray microtomography shows pore structure and tortuosity in alkali-activated binders. *Cem Concr Res* 2012; 42: 855–64.
- Provis JL, Van Deventer JSJ. Introduction to geopolymers, in Provis & Van Deventer Ed. *Geopolymers: Structure, processing, properties and industrial applications*. CRC press. NW. 2009a. pp: 1–7.
- Provis JL, Duxson P, Harrex RM, Yong C, Van Deventer, JSJ. Valorisation of fly ashes by geopolymerization. *Global NEST Journal*, 2009c; 11(2): 147–54.
- Provis JL, Duxson P, Van Deventer JSJ. The role of particle technology in developing sustainable construction materials. *Adv Powder Technol* 2010; 21(1): 2–7.
- Provis JL, Yong C, Duxson P, Van Deventer JSJ. Correlating mechanical and thermal properties of sodium silicate–fly ash geopolymers. *Colloid Surface A* 2009b; 336(1–3): 57–63.
- Provis JL, Rose V, Winarski RP, Van Deventer JSJ. Hard X-ray nanotomography of amorphous aluminosilicate cements. *Scripta Mater* 2011; 65(4): 316–9.
- Prud'homme E, Michaud P. Silica fume as porogent agent in geo-materials at low temperature. *J Eur Ceram Soc* 2010; 30: 1641–8.
- Prud'homme E, Michaud P, Joussein E, Peyratout C, Smith A, Rossignol S. In situ inorganic foams prepared from various clays at low temperature. *Appl Clay Sci* 2011; 51(1–2): 15–22.
- Pullen S. Energy used in the construction and operation of houses. *Architect Sci Rev* 2000; 43(2): 87–94.
- Purnell P. Material nature versus structural nurture: the embodied carbon of fundamental structural elements. *Environ. Sci. Technol.* 2012; 46: 454–61.
- Puertas F, Palacios M, Vázquez T. Carbonation process of alkali-activated slag mortars. *J Mater Sci* 2006; 41(10): 3071–82.
- Phair JW, Van Deventer JSJ. Effect of silicate activator pH on the leaching and materials characteristics of waste-based inorganic polymers. *Miner Eng* 2001;14(3):289–304.

- Rahier H, Denayer J, Van Mele B. Low-temperature synthesized aluminosilicate glasses Part IV Modulated DSC study on the effect of particle size of metakaolinite on the production of inorganic polymer glasses. *J Mater Sci* 2003; 38(14): 3131-6.
- Rahier H, Wastiels J, Biesemans M. Reaction mechanism, kinetics and high temperature transformations of geopolymers. *J Mater Sci* 2007;42:2982-96.
- Ramamurthy K, Nambiar EKK, Ranjani GIS. A classification of studies on properties of foam concrete. *Cem Concr Compos* 2009; 31: 388-96.
- Ramamurthy K, Narayanan N. Influence of composition and curing on drying shrinkage of aerated concrete. *Mater Struct* 2000; 33(4): 243-50.
- Rao JB, Narayanaswami P, Prasad KS. (2010). Thermal stability of nano structured fly ash synthesized by high energy ball milling. *Int J Eng Sci Tech* 2010; 2(5): 284-99.
- Rashad AM, Zeedan SR. The effect of activator concentration on the residual strength of alkali-activated fly ash pastes subjected to thermal load. *Constr Build Mater* 2011; 25(7): 3098-107.
- Rattanasak U, Chindaprasirt P. Influence of NaOH solution on the synthesis of fly ash geopolymer. *Miner Eng* 2009; 22: 1073-8.
- Rattanasak U, Pankhet K, Chindaprasirt P. Effect of chemical admixtures on properties of high-calcium fly ash geopolymer. *Intl J Miner Metal Mater* 2011; 18(3): 364-369.
- Rees CA, Provis JL, Lukey GC, Van Deventer JSJ. In situ ATR-FTIR study of the early stages of fly ash geopolymer gel formation. *Langmuir* 2007; 23: 9076-82.
- Rees CA, Provis JL, Lukey GC, Van Deventer JSJ. The mechanism of geopolymer gel formation investigated through seeded nucleation. *Colloid Surface A* 2008; 318: 97-105.
- Rickard WDA, Van Riessen A, Walls P. Thermal character of geopolymers synthesized from Class F fly ash containing high concentrations of iron and alpha-quartz. *Int J Appl Ceram Tech* 2010; 7(1): 81-8.
- Rickard WDA, Williams R, Temuujin J, Van Riessen A. Assessing the suitability of three Australian fly ashes as an aluminosilicate source for geopolymers in high temperature applications. *Mater Sci Eng A* 2011; 528(9): 3390-7.
- Rietveld H. A profile refinement method for nuclear and magnetic structures. *J Appl Cryst* 1969; 2: 65-71.
- Pipilikaki P, Beazi-Katsioti M. The assessment of porosity and pore size distribution of limestone Portland cement pastes. *Constr Build Mater* 2009; 23(5): 1966-70.
- Rößler M, Odler I. Investigations on the relationship between porosity, structure and strength of hydrated Portland cement pastes: I. Effect of porosity. *Cem Concr Res* 1985; 15: 320-30.
- Rovnaník P. Effect of curing temperature on the development of hard structure of metakaolin-based geopolymer. *Constr Build Mater* 2010; 24(7): 1176-83.

- Saradhibabu D, Ganeshbabu K, Wee T. Properties of lightweight expanded polystyrene aggregate concretes containing fly ash. *Cem Concr Res* 2005; 35(6): 1218–23.
- Scarano D, Zecchina A, Bordiga S, Geobaldo F, Spoto G, Pertrini G, Leofanti G, Padovan M, Tozzola G. Fourier-transform infrared and Raman spectra of pure of and Al-,B-, Ti- and Fe-substituted silicalites: stretching-mode region. *J Chem Soc Faraday Trans* 1993; 89(22): 4123–30.
- Schneider M, Romer M, Tschudin M, Bolio H. Sustainable cement production—present and future. *Cem Concr Res* 2011; 41(7): 642–50.
- Schober G. Porosity in autoclaved aerated concrete (AAC): A review on pore structure, types of porosity, measurement methods and effects of porosity on properties, in 5th International Conference on Autoclaved Aerated Concrete, Bydgoszcz, Poland; 2011. pp: 351–9.
- Shi C. Composition of materials for use in cellular lightweight concrete and method thereof. U.S. 2002; Patent, 6488762 B1.
- Shi C, Krivenko PV, Roy DM. Alkali-activated cements and concrete. Taylor & Francis, Abingdon. 2006.
- Shirai H, Ikeda M, Tanno K. Factors affecting the density and specific surface area (blaine value) of fly ash from pulverized coal combustion. *Energy Fuel* 2011; 25(12): 5700–6.
- Silva de Vargas A, Dal Molin DCC, Vilela ACF, José da Silva F, Pavão B, Veit H. The effects of Na<sub>2</sub>O/SiO<sub>2</sub> molar ratio, curing temperature and age on compressive strength, morphology and microstructure of alkali-activated fly ash-based geopolymers. *Cem Concr Compos* 2011; 33: 653–60.
- Sindhunata, Provis JL, Lukey GC, Xu H, Van Deventer JSJ. Structural evolution of fly ash-based geopolymers in alkaline environments. *Ind. Eng Chem Res* 2008; 47: 2991–9.
- Singh P, Trigg M, Burgar I. Geopolymer formation processes at room temperature studied by <sup>29</sup>Si and <sup>27</sup>Al MAS-NMR. *Mater Sci Eng A* 2005;3 96: 392–402.
- Sinoma. China National Development and Reform Commission: cement production in 2010 increased by 15.5%. Available: <http://www.sinoma.cn/news/ShowArticle.asp?ArticleID=6595>. [2011–1–30]
- Škvára F, Kopecký L, Šmilauer V, Alberovská L, Vinšová L. Aluminosilicate polymers – influence of elevated temperatures, efflorescence. *Ceram-Silikaty* 2009; 53: 276–82.
- Somna K, Jaturapitakkul C, Kajitvichyanukul P, Chindaprasirt P. NaOH-activated ground fly ash geopolymer cured at ambient temperature. *Fuel* 2011; 90(6): 2118–24.
- Sorrentino F. Chemistry and engineering of the production process: State of the art. *Cem Concr Res* 2011; 41: 616–23.
- Spinney SC. Cellular concrete. U.S. Patent, 1993, 5183505A.

- Stengel T, Reger J, Heinz D. Life cycle assessment of geopolymer concrete – What is the environmental benefit? Concrete Solutions 09: Proceedings of the 24th Biennial Conference of the Concrete Institute of Australia, Sydney, 2009.
- Sumanasooriya MS, Neithalath N. Stereology- and morphology-based pore structure descriptors of enhanced porosity (pervious) concretes. ACI Mater J 2009; 106(5): 429–38.
- Sun X, Qiao Y. Effect of different factors on oil-absorbing, water-holding and foaming capacities of ginko protein. Food and Machinery (In Chinese) 2012; 28(3): 17-20.
- Tam CT, Lim TY, Lee SL. Relationship between strength and volumetric composition of moist-cured cellular concrete. Mag Concr Res 1987; 39(138): 12–8.
- Tan SN, Pugh RJ, Fornasiero D, Sedev R, Ralston J. Foaming of polypropylene glycols and glycol/MIBC mixtures. Miner Eng 2005; 18: 179–88.
- Tang M. State of art and prospect of cement and concrete industries in China (In Chinese). J Southeast Uni (Natural Sci Ed) 2006; 36 sup(II): 1–6.
- Taylor WR. (1990). Application of infrared spectroscopy to studies of silicate glass structure: Examples from the melilite glasses and the systems  $\text{Na}_2\text{O}-\text{SiO}_2$  and  $\text{Na}_2\text{O}-\text{Al}_2\text{O}_3-\text{SiO}_2$ . Proc Indian Acad Sci (Earth Planet. Sci.) 1990; 99(1): 99–117.
- Taylor HFW. Cement chemistry. Thomas Telford Services Ltd. 1997.
- Temuujin J, Williams R, Van Riessen A. Effect of mechanical activation of fly ash on the properties of geopolymer cured at ambient temperature. J Mater Proc Technol 2009a; 209: 5276–80.
- Temuujin J, Van Riessen A, Williams R. Influence of calcium compounds on the mechanical properties of fly ash geopolymer pastes. J Hazard Mater 2009b; 167: 82–8.
- Thornton SD, Radke CJ. Dissolution and condensation kinetics of silica in alkaline solution. SPE Reservoir Engineering 1988: 743-752.
- Tuchman DP. Research toward direct analysis of quartz dust on filters using FTIR spectroscopy. In: US Department of the Interior, Bureau of Mines. 1992. Available: <http://www.cdc.gov/Niosh/mining/pubs/pdfs/ic9309.pdf>
- UNIDO. Cement production in Vertical Shaft kilns in China – status and opportunities for improvement. A report to the United Nations Industrial Development Organization, 2006.
- Uygunoğlu T, Keçebaş A. LCC analysis for energy-saving in residential buildings with different types of construction masonry blocks. Energ Buildings, 2011; 43(9): 2077–85.
- Valcke SLA, Sarabèr AJ, Pipilikaki P, Fischer HR, Nugteren HW. Screening coal combustion fly ashes for application in geopolymers. Fuel, 2013; 106: 490–7.
- Valore RC. Foam and gas concrete. In Structural foams, Proceedings of a conference presented as part of the 1960 Fall Conference of the Building Research Institute. National Academy of Sciences – National Research Council, publication 892, 1961.

- Valore RC. Calculation of U-values of hollow concrete masonry. *Concr Int* 1980; 2(2): 40-63.
- Van Deventer JSJ, Duxson P, Provis JL, Brice DG. Chemical research and climate change as drivers in the commercial adoption of alkali activated materials. *Waste Biomass Valor* 2010; 1: 145-55.
- Van Deventer JSJ, Provis JL, Duxson P. Technical and commercial progress in the adoption of geopolymers. *Miner Eng* 2012; 29: 89-104.
- Van Jaarsveld JSJ, Van Deventer JSJ. Effect of the alkali metal activator on the properties of fly ash-based geopolymers. *Ind Eng Chem Res* 1999; 38(10): 3932-41.
- Van Jaarsveld JSJ, Van Deventer JSJ, Lukey GC. The effect of composition and temperature on the properties of fly ash- and kaolinite-based geopolymers. *Chem Eng J* 2002; 89(1-3): 63-73.
- Vasconcelos E, Fernandes S, Barroso de Aguiar JL, Pacheco-Torgal F. Concrete retrofitting using metakaolin geopolymer mortars and CFRP. *Constr Build Mater* 2011; 25: 3213-21.
- Velbel M. Bond strength and the relative weathering rates of simple orthosilicates. *American Journal of Science*, 1999; 299: 679-96.
- Vereshchagina TA, Anshits NN, Maksimov NG, Vereshchagin SN, Bayukov OA, Anshits AG. The nature and properties of iron-containing nanoparticles dispersed in an aluminosilicate matrix of cenospheres. *Glass Phys Chem* 2004; 30(3): 247-56.
- Visagie M, Kearsely EP. Properties of foamed concrete as influenced by air-void parameters, *Concrete Beton* 2002; 101: 8-14.
- Voll D, Lengauer C, Beran A, Schneider H. Infrared band assignment and structural refinement of Al-Si, Al-Ge, and Ga-Ge mullites. *Eur J Mineral* 2001; 13: 591-604.
- Wallah SE, Rangan BV. Low-calcium fly ash-based geopolymer concrete: Long-term properties. Research report GC2. Curtin University of Technology, 2006.
- Wan L, Meng Y, Zhao X. Mechanism study on stability of foam fluid. *Journal of Xinjiang Petroleum Institute (In Chinese)* 2003; 15(1): 70-3.
- Wang J, Carson JK, North MF, Cleland DJ. A new structural model of effective thermal conductivity for heterogeneous materials with co-continuous phases. *Int J Heat Mass Transf* 2008; 51: 2389-97.
- Wang L, Cui Y. The application and development of fly ash in China. *World of Coal Ash*. May 7-10, 2007, Northern Kentucky, U.S.A. Paper #99.
- Wang MR, Jia DC, He PG, Zhou Y. Microstructural and mechanical characterization of fly ash cenosphere/metakaolin-based geopolymeric composites. *Ceram Int* 2011; 37(5): 1661-6.
- Wang SD, Scrivener KL. Hydration products of alkali activated slag cement. *Cem Concr Res* 1995; 25(3): 561-71.
- Ward C, French D. Characteristics of Australian fly ashes. A technical note of Cooperative Research Centre for coal in sustainable development, established

and supported under the Australian Government's Cooperative Research Centres Program, 2003.

Wee TH, Babu DS, Tamilselvan T, Lin HS. Air-void systems of foamed concrete and its effect on mechanical properties. *ACI Mater J* 2006; 103(1): 45–52.

Weigel C, Cormier L, Calas G, Galois L, Bowron DT. Intermediate-range order in the silicate network glasses  $\text{NaFe}_x\text{Al}_{1-x}\text{Si}_2\text{O}_6$  ( $x=0, 0.5, 0.8, 1$ ): A neutron diffraction and empirical potential structure refinement modeling investigation. *Phys Rev B* 2008; 78: 064202-064212.

Weigler H, Karl S. Structural lightweight aggregate concrete with reduced density—Lightweight aggregate foamed concrete. *Int J Light Concr* 1980; 2(2): 101–4.

Weng L, Sagoe-Crentsil K. (2007). Dissolution processes, hydrolysis and condensation reactions during geopolymer synthesis: Part I—Low Si /Al ratio systems. *J Mater Sci* 2007; 42(9): 2997–3006.

White CE, Provis JL, Proffen T, Riley D, Van Deventer JSJ. Combining density functional theory (DFT) and pair distribution function (PDF) analysis to solve the structure of metastable materials: the case of metakaolin. *Phys Chem Chem Phys* 2010a; 12: 3239–45.

White CE, Provis JL, Proffen T, Van Deventer JSJ. The effects of temperature on the local structure of metakaolin-based geopolymer binder: A neutron pair distribution function investigation. *J Am Ceram Soc* 2010b; 93(10): 3486–92.

White CE, Provis JL, Llobet A, Proffen T, Van Deventer JSJ. Evolution of local structure in geopolymer gels: an in situ neutron pair distribution function analysis. *J Am Ceram Soc* 2011; 94(10): 3532–9.

White CE, Provis JL, Proffen T, Van Deventer JSJ. Molecular mechanisms responsible for the structural changes occurring during geopolymerization: Multiscale simulation. *AIChE Journal*, 2012; 58(7): 2242–53.

Williams R, Van Riessen A. Effect of mechanical activation of fly ash on the properties of geopolymer cured at ambient temperature. *J Mater Pro Tech* 2009a; 209: 5276–80.

Williams R, Van Riessen A. Determination of the reactive component of fly ashes for geopolymer production using XRF and XRD. *Fuel* 2010; 89: 3683–92.

Winnefeld F, Leemann A, Lucuk M, Svoboda P, Neuroth M. 2010. Assessment of phase formation in alkali activated low and high calcium fly ashes in building materials. *Constr Build Mater* 2010; 24(6):1086–93.

World Commission on Environment and Development. *Our Common Future*. Chapter 2: Towards sustainable development. 1987; Oxford: Oxford University Press.

Worrell E, Van Heijningen RJJ, de Castro JFM, Hazewinkel JHO, de Beer JG, Faau APC, Vringer K. New gross energy requirement figures for material production. *Energy* 1994; 19(6): 627–40.

Xu H, Lukey GC, Van Deventer JSJ. The activation of Class C-, Class F- fly ash and blast furnace slag using geopolymerization. In 2004 the Proceedings of 8th CANMET/ACI International Conference on Fly Ash, Silica Fume, Slag and natural



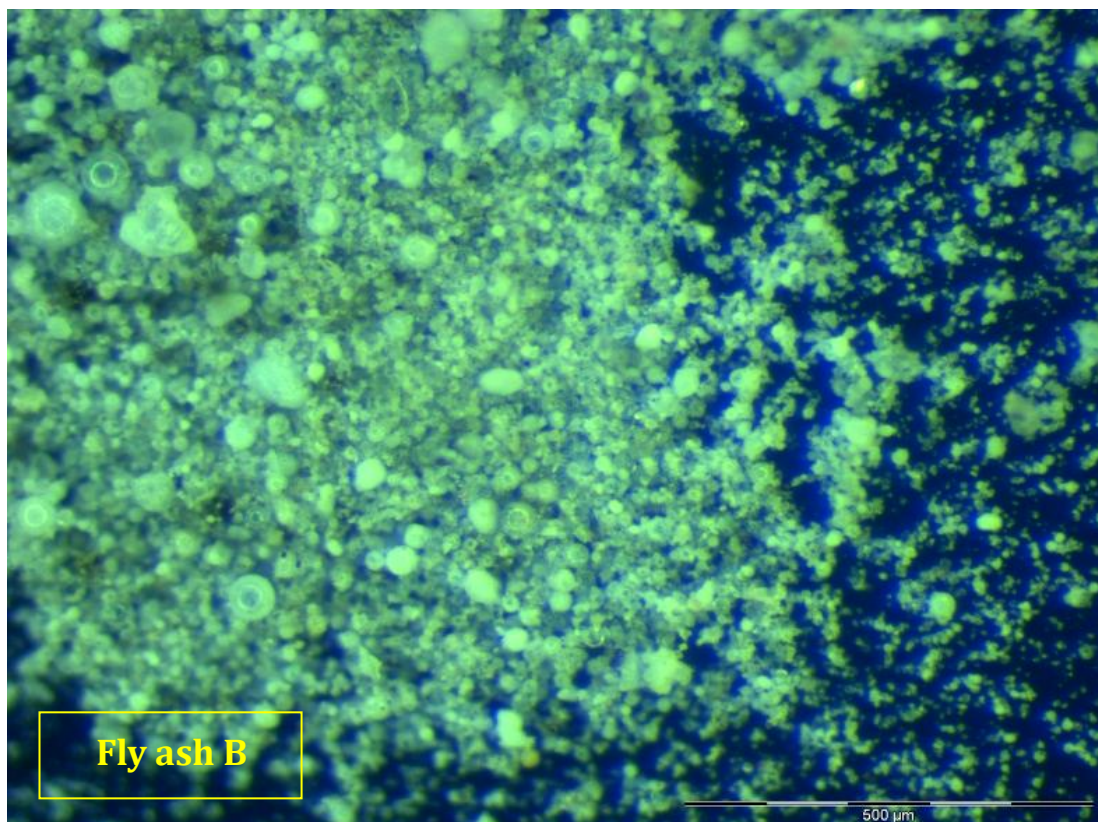
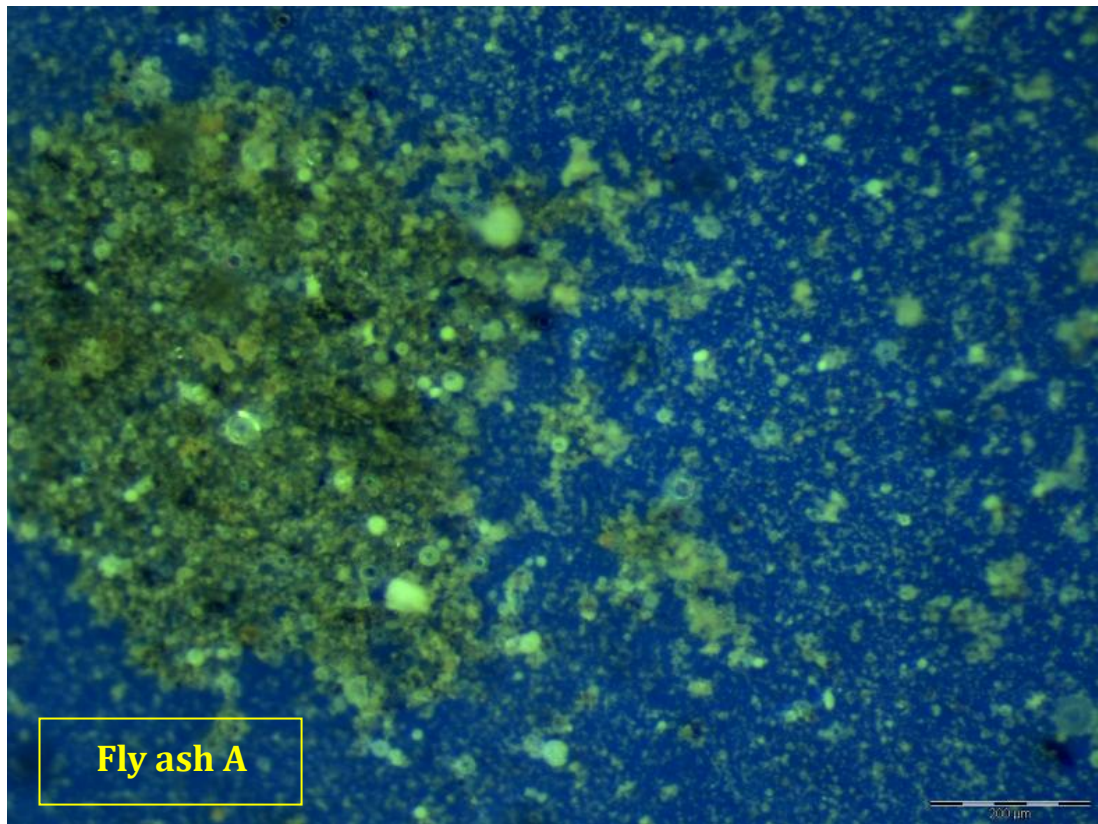
- Pozzolans in Concrete. Editor: V. Mohan Malhotra, American Concrete Institute, pp: 797-819.
- Yang CC. On the relationship between pore structure and chloride diffusivity from accelerated chloride migration test in cement-based materials. *Cem Concr Res* 2006; 36(7): 1304–11.
- Yang N, Yue W. The handbook of inorganic metalloid materials atlas. Wuhan University of Technology Press, Wuhan (in Chinese). 2000; pp: 277.
- Yang T, Yao X, Zhang Z, Wang H. 2012. “Mechanical property and structure of alkali-activated fly ash and slag blends.” *Journal of Sustainable Cement-Based Materials* 1(4):167-178
- Yang X, Zhu W, Yang Q. The viscosity properties of sodium silicate solutions. *J Sol Chem* 2008; 37: 73–83.
- Yao X, Zhang Z, Zhu H, Chen Y. Geopolymerization process of alkali-metakaolinite characterized by isothermal calorimetry. *Thermochim Acta* 2009; 493: 49–54.
- Yip CK, Lukey GC, Provis JL, Van Deventer JSJ. Effect of calcium silicate sources on geopolymerization. *Cem Concr Res* 2008; 38(4): 554–64.
- Yip CK, Lukey GC, Van Deventer JSJ. The coexistence of geopolymeric gel and calcium silicate hydrate at the early stage of alkaline activation. *Cem Concr Res* 2005; 35(9):1688–97.
- Yu P, Kirkpatrick RJ, Poe B, McMillan FP, Cong X. 1999. Structure of calcium silicate hydrate (C-S-H): Near-, Mid-, and Far-infrared spectroscopy. *J Am Ceram Soc* 1999; 82(3): 742-8.
- Zawada JM, Mont A. Lightweight, waterproof, insulating, cementitious composition. 1998; U.S. Patent 5,782,970.
- Zhang Q, Dong J, Jing S, Wu Y, Pei M. 2006. Effect of pH value on the foaming properties of oleic acid. *J Jinan Uni (Sci & Tech)* (In Chinese) 2006; 20(1): 31-4.
- Zhang Z, Yao X, Zhu H, Activating process of geopolymer source material: kaolinite, *J. Wuhan Univ. Tech (Mater Sci Ed)* 2009a; 24(1): 132–6.
- Zuhua Z, Xiao Y, Zhu H, Chen Y. Role of water in the synthesis of calcined kaolin-based geopolymer. *Applied Clay Science*, 2009b; 43: 218–23.
- Zhang Z, Wang H, Provis JL. Quantitative study of the reactivity of fly ash in geopolymerization by FTIR. *J Sustain Cem-Based Mater* 2012a; 1(4): 154–66.
- Zhang Z, Wang H, Yao X, Zhu Y. Effects of halloysite in kaolin on the formation and properties of geopolymers. *Cem Concr Compos* 2012b; 34: 709–15.
- Zhang Z, Wang H, Provis JL, Bullen F, Reid A, Zhu Y. Quantitative kinetic and structural analysis of geopolymers. Part 1. The activation of metakaolin with sodium hydroxide. *Thermochim Acta* 2012c; 539: 23–33.
- Zhang Z, Provis JL, Wang H, Reid A. Geopolymer foam concrete: an emerging material for sustainable construction. *Cem Concr Compos* 2013 (under review).
- Zhao Y, Ye J, Lu X, Liu M, Lin Y, Gong W, Ning G. Preparation of sintered foam materials by alkali-activated coal fly ash. *J Hazard Mater* 2010; 174: 108–12.

Zibouche F, Kerdjoudj H, de Lacaillerie J-B d'Espinose, Van Damme H. Geopolymers from Algerian metakaolin. Influence of secondary minerals. *Appl Clay Sci* 2009; 43: 453–8.

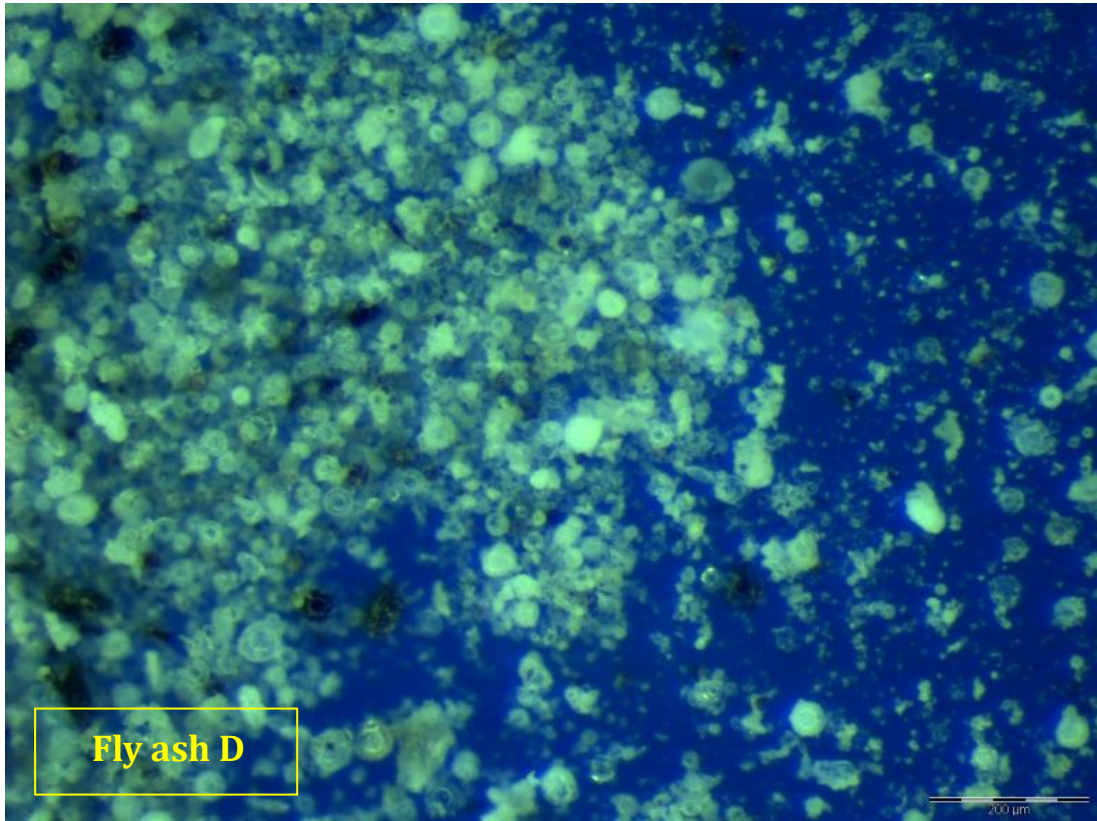
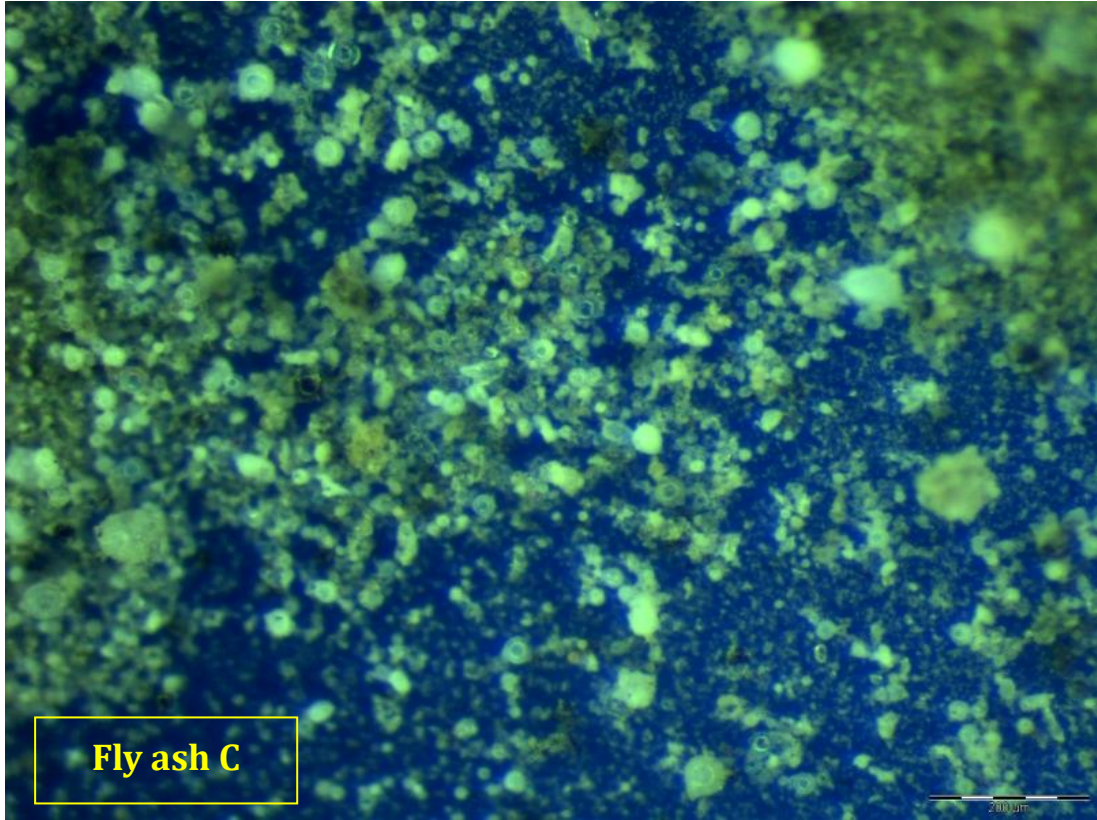
Živica V, Balkovic S, Drabik M. Properties of metakaolin geopolymer hardened paste prepared by high-pressure compaction. *Constr Build Mater* 2011; 25(5): 2206–13.

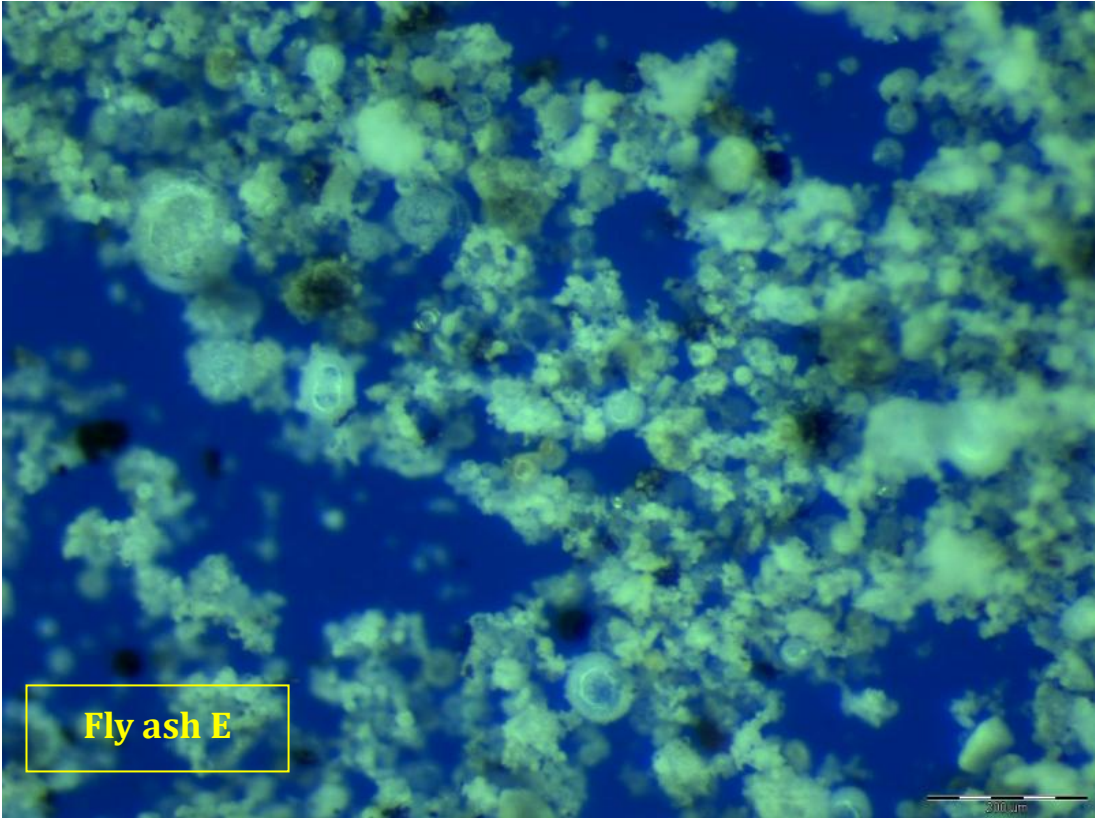
## Appendix

### *A1. Optical microscopy images of the fly ash samples*

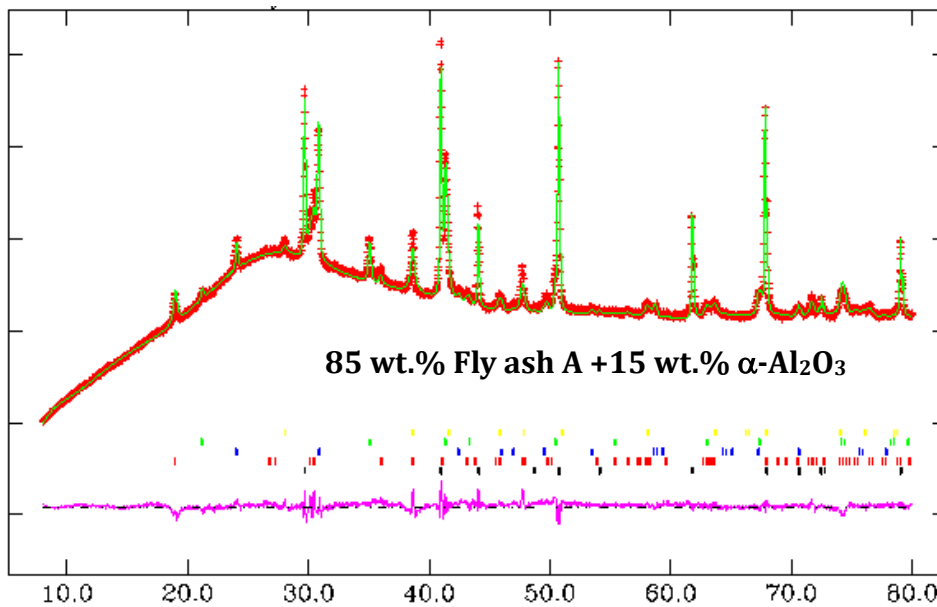
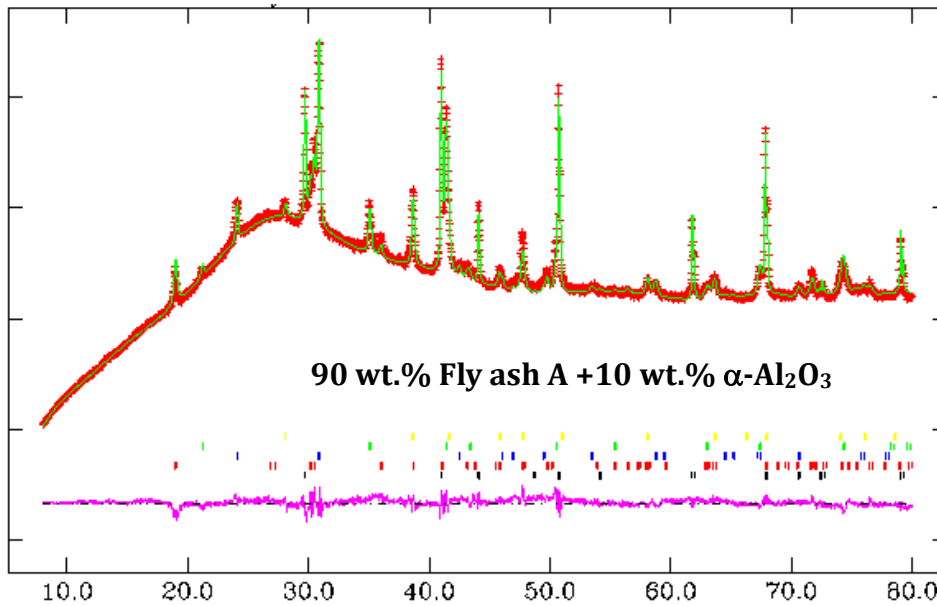




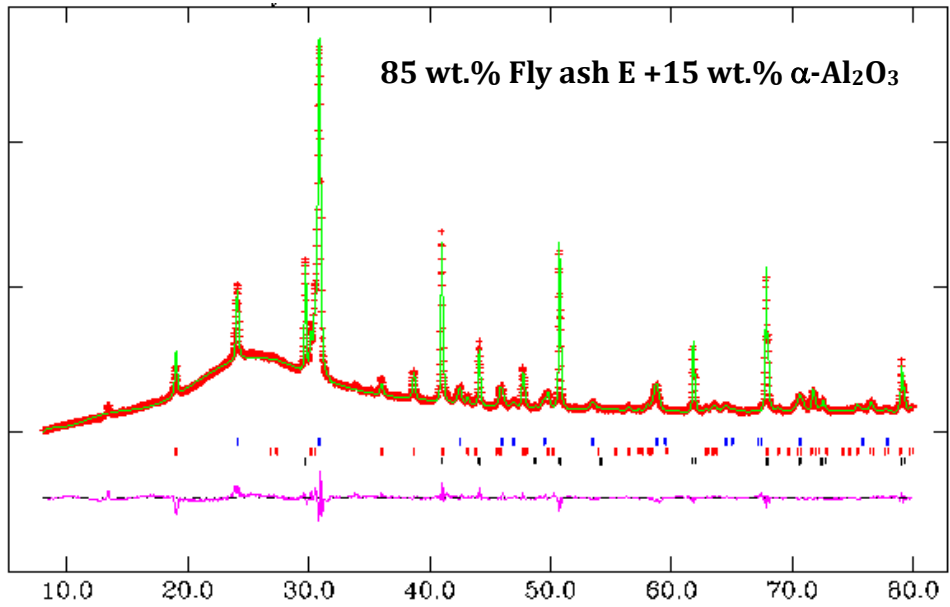
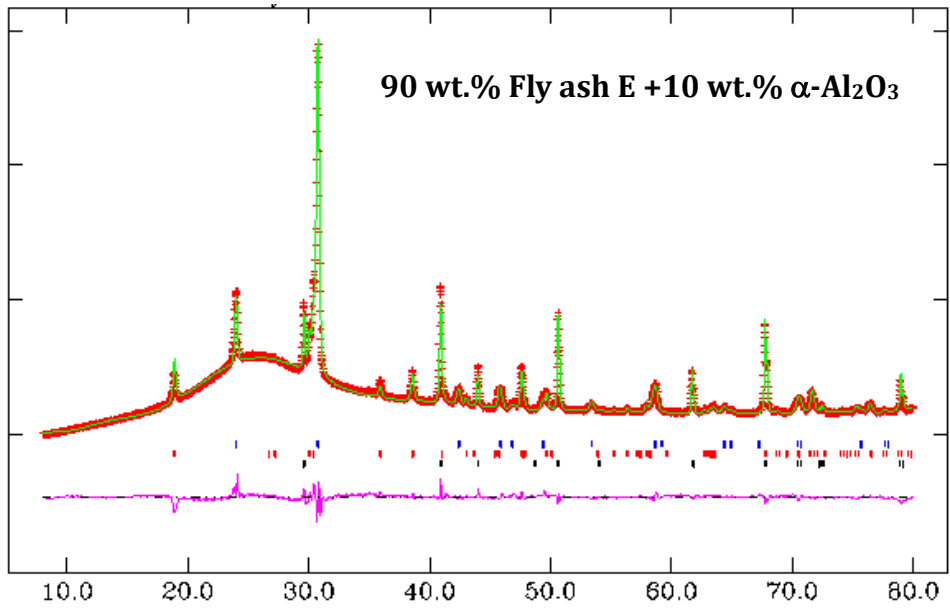




**A2. RQXRD analysis of fly ashes A and E mixed with 10 wt.% and 15 wt.%  $\alpha$ -Al<sub>2</sub>O<sub>3</sub>**

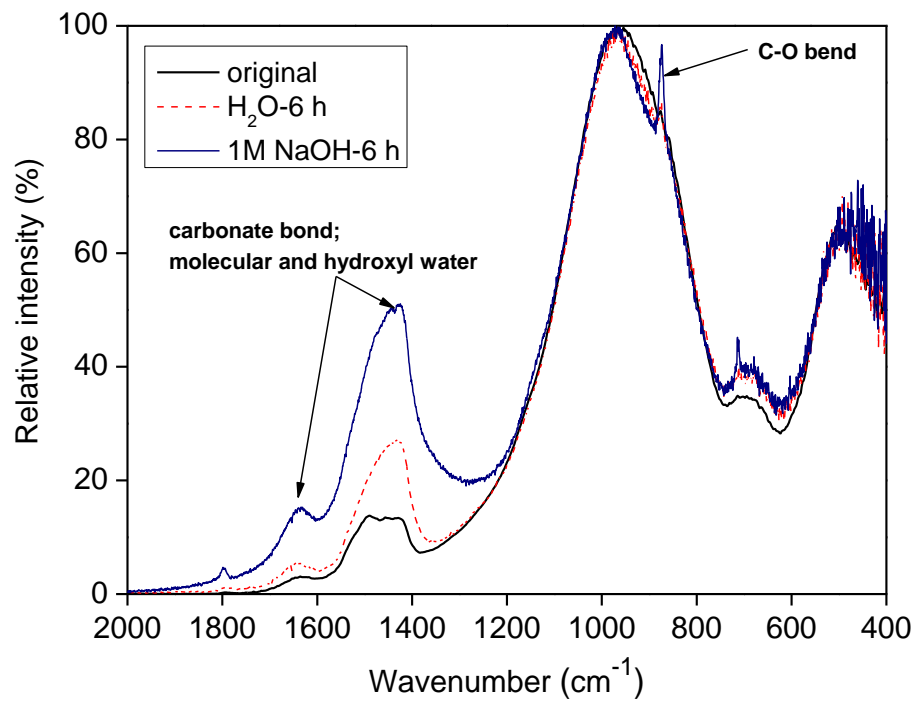


Components (ICSD)	10%	15%	20%	Mean	± Error %
Mullite (66448)	17.9	18.4	19.8	18.7	5.9
Quartz (89280)	3.1	2.9	3.4	3.1	8.6
Magnetite (43001)	2.6	2.6	2.3	2.5	8.0
Hematite (15840)	1.5	1.5	1.4	1.5	4.8
Amorphous	74.9	74.6	73.1	74.2	1.3



Componets (ICSD)	10 wt.%	15 wt.%	20 wt.%	Mean	± Error %
Mullite (66448)	28.2	22.4	21.6	24.1	17.0
Quartz (89280)	13.6	13.5	12.2	13.1	6.9
Amorphous	58.2	64.2	66.2	62.9	7.1

### A3. FTIR spectra of slag
















***A4. The shrinkage of large geopolymer foam concrete sample***



**A5. Efflorescence of geopolymer binders contacted with water**

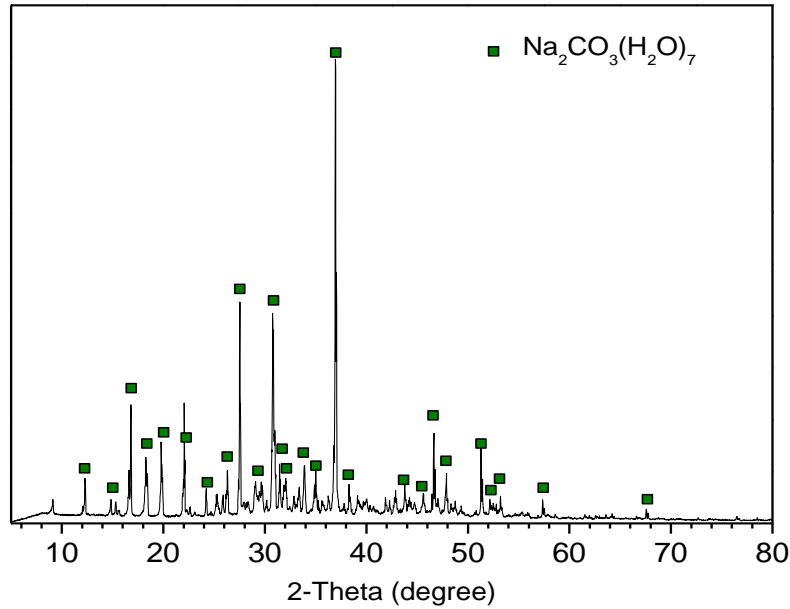
Dry			
Wet-3 h			
Wet-6 h			
Wet-12 h			
Wet-24 h			
	NS-FA100-80°C	N-FA100-80°C	NS-FA80SL20-80°C

Samples manufactured by 80°C curing for 90 d: 'SN' means the activator is sodium silicate and 'N' means NaOH solution, 'FA100' means that the solid precursor is 100% fly ash and 'FA80SL20' means a blend of 80 wt.% fly ash and 20 wt.% slag.

Dry			
Wet-3 h			
Wet-6 h			
Wet-12 h			
Wet-24 h			
	NS-FA100-20°C	N-FA100-20°C	NS-FA80SL20-20°C

Samples manufactured by 20°C curing for 90 d: 'SN' means the activator is sodium silicate and 'N' means NaOH solution, 'FA100' means that the solid precursor is 100% fly ash and 'FA80SL20' means a blend of 80 wt.% fly ash and 20 wt.% slag.

***A6. XRD analysis of the efflorescence product (the white product collected from the surface)***



The efflorescence product is a hydrous alkali carbonate,  $\text{Na}_2\text{CO}_3 \cdot 7\text{H}_2\text{O}$ . Some minor diffraction peaks are not identifiable, which may be due to some particles of geopolymer gel and/or fly ash present in the sample. The carbonate should crystallize from inside pores and grow outside the specimens. The availability of sodium cations is the main reason for the efflorescence growth.